EXAMINATION OF OXIDE AND HYDROXIDE FILMS GROWN ON ALUMINIUM AND SOME ALUMINIUM ALLOYS

by

AMARJIT SINGH REHAL

A thesis submitted to the UNIVERSITY OF ASTON IN BIRMINGHAM for the Degree of

DOCTOR OF PHILOSOPHY

September 1978

DEPARTMENT OF PHYSICS

SUMMARY

Examination of oxide and hydroxide films grown on aluminium and some aluminium alloys.

Amarjit Singh Rehal

Doctor of Philosophy

1978

Aluminium oxide and hydroxide films grown on aluminium sheet and evaporated aluminium films were studied using a number of techniques. Electron Spectroscopy for Chemical Analysis (ESCA), Ellipsometry and a combination of Transmission Electron Microscopy TEM, Scanning Transmission Electron Microscopy STEM and Scanning Electron microscopy SEM, known as (TEMSCAN).

For a radiation wavelength of 549 nm the refractive index for aluminium hydroxide films less than 80 nm was found to be $n = 1.58 \pm 0.03$. For thicker films it was necessary to assume a k value of 0.0009 rather than zero.

There were discrepancies between aluminium oxide and hydroxide film thicknesses as measured by ESCA, using the ratio of chemically shifted and unshifted peaks. This discrepancy is explained by assuming that the oxide and hydroxide film grows in islands and the height of these islands is greater than the escape depth of the electron. The ESCA technique therefore was not detecting oxide or hydroxide at the base of the islands.

Examination of electron transparent specimens after exposure to water vapour saturated air (WVSA) at 70° C in the SEM mode, revealed reaction sites in the forms of blisters. Examination of the same area in STEM, only showed the underlying microstructure due to the fact that blistering is a surface phenomenon. Electron transparent specimens prepared from sheets of aluminium alloy (Al5%/Mg) and (Al5%/Zn), exposed to WVSA for 10 minutes were examined in TEM, STEM and SEM specimens prepared from sheets heated at 350° C and 450° C showed reaction sites along the grain boundary surface interface whereas specimens prepared from 550° C heated sheets showed randomly distributed reaction sites. Closer examination (in TEM mode) of the grain boundary surface interface revealed hydrogen bubbles which could be viewed by their stress field contrast.

Ellipsometry/ESCA/TEMSCAN/Aluminium/Corrosion/.

INDEX

page

CHAPTER 5 - EXPERIMENTAL RESULTS AND DISCUSSION

CHAPTER 1

INTRODUCTION

The occurrence of stress-corrosion susceptibility in Aluminium-zinc-magnesium alloys restrict their widespread use. Much research is being carried out on the mechanism of stress-corrosion cracking[1-5]. The main objective in the present work was to obtain insight into the mechanism. To this end the structure and rate of growth of aluminium oxide and aluminium hydroxide films grown on pure aluminium, aluminium-magnesium and aluminium-zinc alloys under different conditions were studied.

The reaction of aluminium with water at 70°C produces a duplex film consisting of pseudoboehmite, on aluminium oxyhydroxide similar to boehmite (AlOOH) but containing more water and bayerite ($Al(OH)_3$)[6]. Both forms of hydrous oxide have characteristic morphologies, bayerite crystals taking the form of pillars or cones and pseudo-boehmite appearing as needles when viewed by transmission electron microscopy or platelets when viewed by scanning electron microscopy.

However the reaction of aluminium with water vapour saturated air as opposed to liquid water has received little attention. The structure of aluminium oxide and aluminium hydroxide films formed at low exposures have also received very little attention. These experiments can only be carried in under ultra-high-vacuum and the techniques used should be surface sensitive. The techniques used in this present work were in this context, ellipsometry and Electron spectroscopy for Chemical Analysis (ESCA). Both these techniques, although fundamentally different, can measure the growth of oxide or hydroxide films at low exposures. These techniques can also be used to study thick films, for this to be possible ion etching is

necessary in the case of ESCA but not ellipsometry for non absorbing films.

Ellipsometry and ESCA are techniques which over a given area. In order to study the effect of underlying microstructure on the location of reaction, use was made of a new microscope which combines transmission electron microscopy (CTEM) scanning transmission electron microscopy (STEM) and scanning electron microscopy. TEMSCAN JEM 100C is one such microscope. The important feature of this type of microscope is that comparison of precisely located areas in the (STEM) and (SEM) modes allows direct correlation of surface features with underlying microstructure Obviously such a technique is limited to electron-transparent specimens, but the secondary electron detector can be used to examine surfaces at high resolution.

By using a combination of the above techniques for surface investigation it was hoped to elucidate mechanism and structure of corrosive layers in the early stages of growth.

1.1 Ellipsometry

Interest in the optical study of surface films is not a recent phenomenon There are many optical techniques available for measuring various parameters, e.g. the use of multiple beam interferometry developed by Tolanski[8]. Knowing the thickness one could determine the optical constants by measuring the intensities of the light transmitted and reflected from both sides of the film as proposed by Murmann[9]. It is desirable to measure n, k and t simultaneously because thin films can differ in density from bulk material so that a separate measurement of geometric thickness may not correspond to the thickness. These and other optical techniques are summarised and discussed by Heavens[10].

The optical technique used in the present work was ellipsometry

which involves the measurement of the change in the state of polarisation of a beam of light after reflection. The incident polarised light can be resolved into components parallel and perpendicular to the plane of incidence and one usually denoted by r_p and r_s, are reflection coefficients respectively. In the case of a clean surface these coefficients can be derived from the electromagnetic theory in terms of refractive index and angle of incidence.

The foundations of ellipsometry were laid at the end of the last century by Rayleigh and Drude[11-12]. Drude derived the fundamental equation of ellipsometry from Maxwell's equations with suitable boundary conditions but was unable to solve the equation explicitly for n, k and t but obtained approximate solutions for films of thickness small compared to the wavelength of light used.

Although the optical properties of metals were studied by means of reflectivity measurement few specific references to the use of ellipsometry were made in succeeding years, probably because of the development of other methods of determinations of film thickness.

The first detailed experimental work using the Drude technique was by Tronstad[13-15] who investigated the chemically-produced passivity of iron and steel mirrors. Tronstad also investigated the optical constants of a mercury surface which he used as a standard surface for the calibration and adjustment of the ellipsometer. Since it was found to give more reproducible results than any surface produced by mechanical polishing.

Lebernight and Lustman[16] investigated the oxidation of iron and nickel and verified Drude's equations for thinner films. Until about 1940 the instruments used were often normal spectrometers, modified to carry polarising and analysing prisms and a quarter were plate. Detection was by eye using half-shade devices. The introduction of photomultiplier detection made possible great

improvements in sensitivity and accuracy, and also enabled measurements to be made over a wider range of wavelengths.

Rother[17] and later Rothen and Hanson[18] were responsible for the term "ellipsometry". They developed the technique of calibration of an ellipsometer using a surface coated with a known number of barium stearate monolayers.

In 1955, in the extensive review by Winterbottom[19] results of optical constants for bulk metals were presented for the visible region of spectrum. The development of polarising devices for the infra-red region of the spectrum made possible the development by Beattie[20] of an ellipsometric technique for studying metals using radiation extending to 12 microns wavelength. Although there were serious theoretical limitations on the accuracy of such measurements as shown by Beattie and Conn. Infra-red measurements on metals are extremely important in order to assess the validity of the Drude-Zener theory.

Hayfield and White[21] adopted the ideas initiated by Beattie and Conn, in a study of corrosion and oxidation in metals. But in this work the compensator method, for the visible wavelengths, of McCrackin was adopted. The instrument is comparatively simple and inexpensive and used in conjunction with an ultra-high vacuum system.

Work on the general technique of ellipsometry was continued by McCrackin[22] et al. Who reviewed the procedure for alignment and calculation of results, and by Archer[23] who made extensive studies of silicon surfaces using the exact theoretical equations.

More recent developments have lead to some sophisticated instruments employing the Faraday effect. This idea was developed by Gilham[24].

The 'magneto-optic' or 'Faraday' effect is observable as a rotation of the plane of polarisation when light passes through a

dielectric in the presence of a magnetic field. Gilham employed lead-zinc borate glass in the form of cylindrical rods 10cm in length overwound with a copper coil carrying an alternating current of 1 amp at 50 H_z with this arrangement the plane of polarisation was arranged to oscillate at 50 H_z through 6 degrees. When this light passed through the analyser prism on to the photomultiplier, an alternating intensity of light was received, resulting in a convenient output signal.

Several instruments have been developed on the basic design of Gilham, for example that of Seward[25] which as well as accurate mechanical parts and Glan-Foucoult prism polarisers, employed a detection system using two Faraday cells, M and C, as shown in Figure 1. The first cell is fed with a constant alternating current signal of frequency f, which causes the plane of polarisation to oscillate at the same frequency f. The light then passes through the second cell C and an analysing prism A on to a photomultiplier. The photomultiplier produces an asymmetrical signal which has a basic 2f component with an f component superimposed. An electronic analysis unit detects the f component and feeds into the compensator cell C a suitable current to reduce the f component to zero. The value of this current is proportional to the angular difference between the actual analyser azimuth and the azimuth at which it would be 'crossed' with respect to the incoming polarised light. In this way, the analyser can be set accurately to $\pm$ 5 seconds of angle.

1.1.1 Automatic Ellipsometers

Although automatic ellipsometers have been used prior to 1969 Cahan and Spanier[26] gave a very good description of a high speed automatic instrument. Since the early work with increasing interest in measuring reaction rates and following film growth with

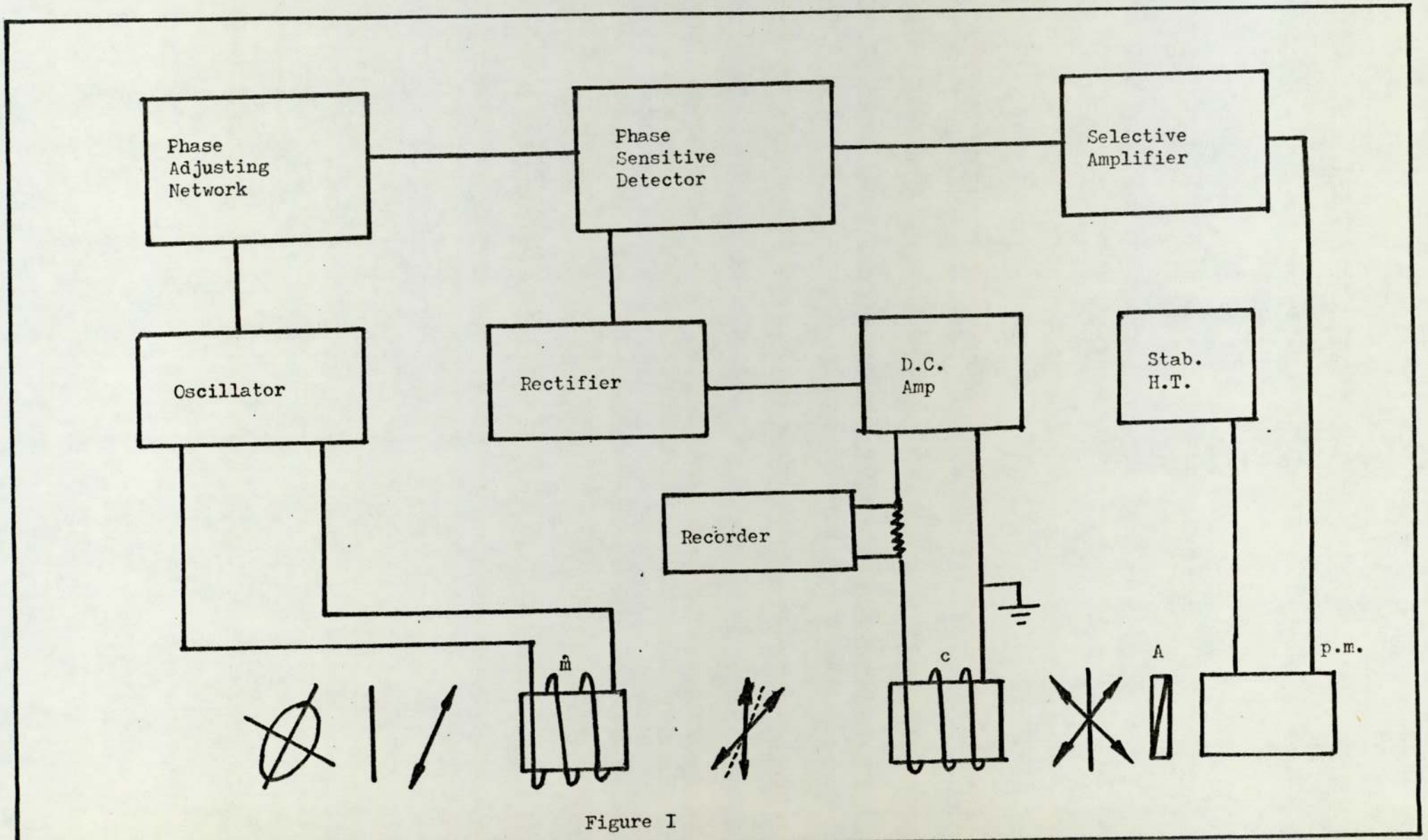
Phase
Adjusting
Network
Phase
Sensitive
Detector
Selective
Amplifier
Oscillator
Rectifier
D.C.
Amp
Stab.
H.T.
Recorder
m
c
A
p.m.

Figure I

increasing speed and accuracy, there have been reports of many modifications. One such is that of modulated ellipsometry by Jasperson, Burge and O'Handley[27] for studying thin layer optical properties and surface dynamics and by Cahan, Horkans and Yeager[28] who studied the electrode-electrolyte interface with platinum and gold electrodes.

In modulated ellipsometry, quantities related to the parameters Ψ and Δ are extracted simultaneously by synchronous detection of reflected light intensities in two frequency channels. Signal processing is completed by an on-line computer which samples the data at a repetition rate of approximately one a second. Once the optical system is aligned all elements remain rigidly in place so that precision and stability are high. For Ψ and Δ precision of the order of 0.001° and stability of the order of 0.01° over a period of one hour can be achieved.

During the last two or three years interest in automatic instruments has still further increased. Muller and Mathiew[29] outlined a series of tests for checking the fine characteristic parameters of automatic ellipsometers which they felt were appropriate.

More recently Muller[30] has given a further comprehensive report on the classification of different types of automatic ellipsometers into compensating and non-compensating instruments and compare their performances.

1.1.2 Ellipsometry as a technique complementary to other techniques for surface examination

Where there is a need for examination of surfaces or surface layers, there is a whole array of techniques such as low energy electron diffraction, Auger electron spectroscopy, electron spectroscopy for chemical analysis, field emission microscopy and

ellipsometry. To some extent the method is badly named in that the word 'ellipsometry' does not indicate the function as do the names given to many other techniques. Neal[31] has recently suggested more appropriate names, such as optical surface spectrometer (O.S.S.) or surface optical spectrometer (S.O.S.). However, Ellipsometry has been used as a complementary technique, an interesting application of combined ellipsometric and Auger electron spectrometry techniques have been made by Allen[32]. Simultaneous studies were made on the elemental chemical composition and optical properties of clean and contaminated aluminium surfaces under vacuum. Another example of the application of the complementary techniques of Auger spectroscopy and ellipsometry was demonstrated in the work of Chou, Van der Nuelen, Hammer and Cahill[33].

Latham and Brah[34] have used ellipsometry both to characterise the surfaces and to study the influence of surface oxidation on charge reversal on microspheres which occurs during a rebounding impact with negatively charged copper and stainless steel electrodes. This is also the aim in this work to use ellipsometry, as a complementary technique, in conjunction with Electron spectroscopy for chemical analysis ESCA.

1.2 Electron spectroscopy for Chemical Analysis (ESCA)

The technique is based on a magnetic or electrical analysis of high resolution of the electrons which are emitted from a substance on irradiation with X-rays. The technique reproduces directly the electronic level structure, from the innermost shells to the atomic surface. All elements from Lithium to the heaviest ones can be studied even if the element occurs together with several other elements and represents only a small part of the chemical compound.

Shifts of inner levels due to chemical structure effects are

characteristic features, and ESCA provides information on the chemical bonding in elements.

From the turn of this century to the middle of the nineteen thirties some research workers, Robinson and de Broglie[35-38], have investigated the energy distribution of electrons in various elements irradiated with X-rays Only few further attempts have been made to extend the early works of Robinson and de Broglie, but these experiments meet with limited success.

The different ways of using X-rays for gaining information on atomic structure are illustrated in Figure 2. A specimen is irradiated with X-rays. The upper branch is the X-ray fluorescence and X-ray absorption spectroscopy. The lower branch represents electron spectroscopy as the alternative source of information. There were many problems to solve, for example, the electrons adsorption in the material will destroy any precise information originally contained in the spectrum. This is because the energy and the intensity of electrons produced inside the material by the X-radiation would be expected to diminish considerably on their way out. The early studies in fact confirmed this general behaviour and the difficulty of getting precise energy limited electron spectroscopy as a competitor to X-ray spectroscopy.

In 1951 Kai Siegbahn started a research programme aimed at the very high resolution study of the energy spectrum of electrons expelled by X-rays. There were two main problems to be solved. The first is the problem of shaping the magnetic field according to the $1/_{e}$ form required for double focussing. Fortunately, it was found that the same field would be obtained over a limited region if coil arrangement consisting of two co-axial coils of special dimensions[40-42]. The second problem was to obtain an efficient geometry for the X-ray tube and in addition high transmission and

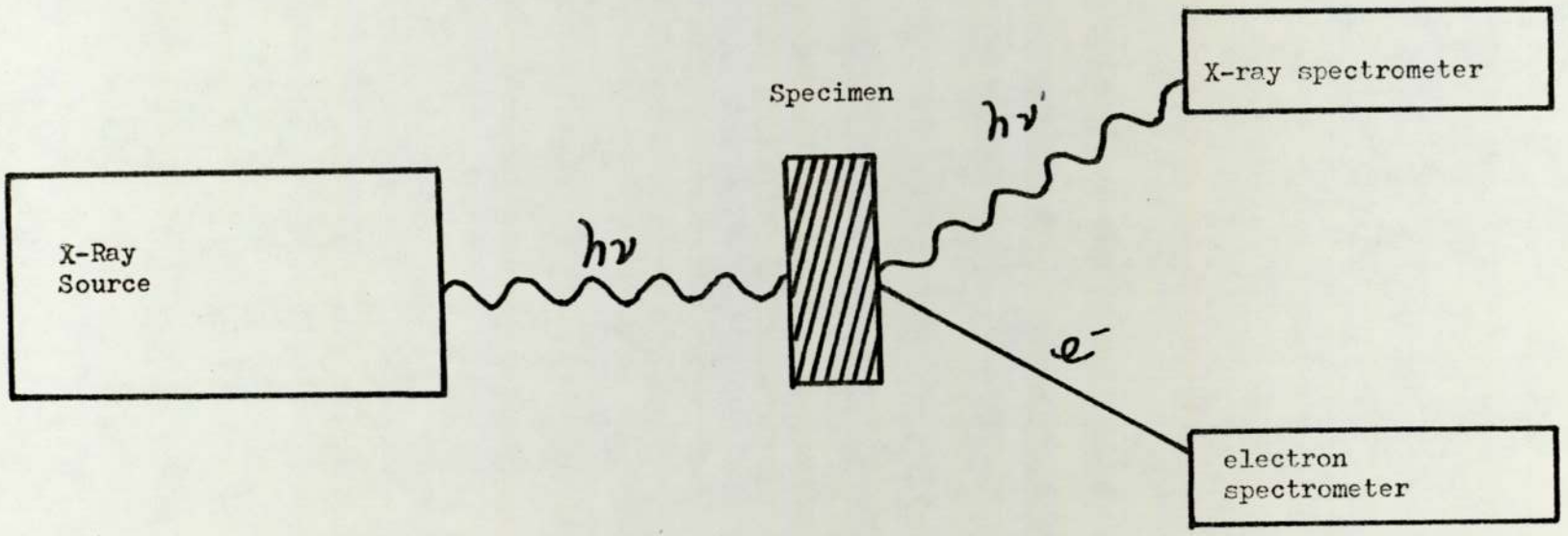
X-Ray
Source
hν
Specimen
hν'
X-ray spectrometer
e⁻
electron
spectrometer

Figure 2

large dispersion of the electron spectrometer were needed.

Compensation has to be made for all external magnetic fields including the earth's field. It took three years to build and test the first iron-free double focussing magnetic spectrometer. The electrons used were obtained from radioactive sources. That is the reason why the first part of the work, described in a paper[39] was entitled "Beta ray spectroscopy in the precision range".

In 1954 the first instrument was ready and attempts were made to record at high resolution photoelectron spectra produced by X-rays. A new observation then changed the course of the future development of the method. This was the appearance of a very sharp line which could be resolved from the edge of each electron line.

A more detailed study of a photoelectron line obtained with the ESCA method showed that it consisted of the principal line together with a more or less continuous energy distribution immediately to the left of the line and with the resolution now obtainable this can be distinguished from the principal line by an intensity minimum. This minimum occurs because electrons passing through the specimen can only lose energy in certain discreet amounts, a phenomenon which had been observed earlier in another connection[43] but had not previously been observed in connection with ESCA work. The discreet energy losses are due to so called plasmon excitations of the electron plasma in the specimen. Collective electron vibrations in the plasma plus ionisation, and excitation in interband transitions. In ESCA only the following factors contribute to the line width.

(1) The natural width of the incident X-ray line.

(2) The width of the atomic level from which electrons are ejected.

(3) The aberration of the spectrometer[44].

The choice of anode material is dependent on the binding energy of the particular atomic shell studied. In majority of cases one should use anode material from the light elements exception would be those cases where inner levels of higher Z elements are being studied. In the present work, Magnesium was chosen as the anode material. There are number of advantages in useing soft X-radiation.

(1) The inherent widths of the levels of light elements are smaller, so that they contribute less to the line width of the resulting electron line.

(2) The energy of the electron is lower which means a high resolution on an absolute scale.

The electron lines produced by softer X-rays completely extended over the low energy region. In fact, the resulting electron spectra look very similar to the line spectra obtained in, for example, X-ray emission spectroscopy.

During the ten years of development following the resolution and recording of the first ESCA spectra a large body of data on the electron binding energies of most elements from lithium to plutonium has been accumulated and systematised. It has been found that, accuracy of the binding energies is consistently higher than that offered by the X-ray absorption method. In order to obtain electron spectra from the inner levels of heavier elements, one must use anode materials of higher Z values like molybdenum and tungsten. If one uses the lighter elements like sodium, magnesium or aluminium as anodes, one finds that ESCA can be used to study the band structure in metals and alloys more effectively.

As an analytical method, ESCA can be applied over the whole periodic system. For the light elements, like carbon, nitrogen and oxygen ESCA gives excellent signals. The sensitivity of ESCA is high.

Only a very thin surface layer of around 5 nm of the sample is utilized for the analysis.

Photoelectrons emitted from atoms further down, deeper into the material, lose energy and are therefore removed from the electron line spectra. Gases adsorbed on the surface of a foil yield spectra of good intensity.

Oxide films formed at the surface of most metals are seen in ESCA spectra, both as an oxygen line and as a shifted line situated near the line from the unoxidized metal. ESCA can be used to examine materials which are normally liquid or gaseous, if they are first solidified by freezing.

1.3 Electron microscopy

Electron microscopes are finding increasing application at all levels of science and technology. A wide range of instruments are now available and these are enabling physicists, metallurgists and crystallographers to work together in solving problems not only of atomic structure but of chemical composition and surface morphology[46-61].

The rapid development of integrated circuits and the evolution of computers have provided a powerful tool for electron microscopists in handling the vast amount of data that can now be extracted from a modern electron microscope[62-66]. In view of these new technologies the design of the electron microscope has and is undergoing a radical change. New instruments, such as the scanning transmission electron microscope (STEM), and the manner in which its image is formed have been reexamined[67-69]. The basic assumptions behind the theory of image formation has in turn, led designers to realize more clearly the limitations of traditional instruments. In many cases the limitations are placed by the state of technology. As the technology improves, new possibilities are opened up for the microscopy and

micro-analysis of specimens. It is not possible to assess the relative merits of the TEM and STEM because neither instrument has, reached the limit of technological perfection. The strong competition, both commercial and scientific between these two instruments, have resulted in designs which try to combine the best features of both instruments. JECL 100C TEMSCAN electron microscope is one of these instruments which combines TEM and STEM. To buy one of these instruments is an expensive undertaking and in the particular circumstances of an individual laboratory it may be necessary to decide in advance what are the important points that are required of the microscope and to accept compromise in areas of less importance.

1.3.1 Scanning electron microscopes

Scanning electron microscopes (SEM) were first introduced into the market a decade ago and they have probably already exceeded the total number of TEM installations in materials laboratories throughout the world. The current SEM output, in terms of conference and journal publications, textbooks, substantially exceeds that based on TEM. In its present form SEM is a sophisticated instrument, easy to operate useful for fractograph work, microanalysis, and more recently, crystallographic studies and image analysis.

The recent development of the combined TEM and STEM + SEM systems has been an important development. The higher brightness gun and better lens design of TEM, combined with the bean focussing and superior image processing facilities of SEM result in a number of advantages over both individual SEM and TEM instruments while retaining few of their disadvantages. JEM 100C electron microscope is one such instrument which combines TEM, STEM and SEM systems. In studies of Aluminium oxide and Aluminium hydroxide films all three systems were used.

CHAPTER 2

SURVEY OF THE PUBLISHED LITERATURE

2.1 The oxidation of metals

2.1.1 The initial stages of oxidation: Adsorption

The interaction of gases with metal surfaces may be classified in terms of physical adsorption, chemisorption, solution or bulk compound formation. Review articles (Hayward 1971[70], Culver and Tompkins 1959[71] and a number of books (Bond 1962[72], Hayward and Trapnell 1964[73]) have discussed in detail the theories and experimental data on adsorption. If chemisorption experiments are to produce meaningful results clean surfaces are essential. Because of the problem of producing clean surface much of the data in the literature is difficult to interpret[74].

In the interaction of oxygen with metal surface the rate at which the molecules strike the unit surface being given by kinetic theory as

$$P/(2\pi mkT)^{\frac{1}{2}}$$

where P is the gas pressure

m the mass of the gas molecule

k the Boltzmann constant

T the absolute temperature

A monolayer of absorbed gas forms on the surface in one second at room temperature for a gas pressure of 10^{-6} torr if we assumed the adherence probability is unity.

Distinction between physical adsorption and chemisorption is not always possible. When adsorption takes place there is a decrease

in free energy and since entropy decreases because of the loss of degrees of freedom, the heat of adsorption has to decrease and adsorption is always exothermic. To distinguish between physical adsorption and chemisorption, measurements of heats of adsorption have been used because in the case of physical adsorption values are low (10 k cal mole^{-1}) and higher for chemisorption, but in many cases the heat of chemisorption may be quite low (Hayward and Trapnell 1964[73]) so it is not always possible to distinguish between the two types of adsorption. It was usually considered that chemisorption required activation energy, but it has now been shown that, in many cases, chemisorption may occur in the absence of an activation barrier (Ehrlich 1965[75]).

When chemisorption takes place (chemical reaction) there is a rearrangement of valence electrons of the metal and the gas. Even though chemical reactions at surfaces have been studied extensively, the mechanism of such interactions is still not well understood (Culver and Tompkins 1959[72]) illustrated the interaction of a bimolecular molecule such as H_2 or O_2 with a metal surface by a potential energy diagram shown in Figure 3. Curve (1) represents the potential energy of the molecule as it is attracted to the surface by long-range forces, Curve II represents the potential energy curve for a molecule which was dissociated into atoms prior to chemisorption. Curve I may intersect Curve II at a point either above or below the zero of potential energy depending on the particular gas-metal combination. If point P is above zero an energy E_A will be required for the molecule to switch to Curve II and become chemisorbed If the intersection point P is below the zero, chemisorption becomes non-activated.

Incorporation of oxygen has been studied by some works, (Roberts and Wells 1966,[76-78])(Huber and Kirk 1966[79]) in an

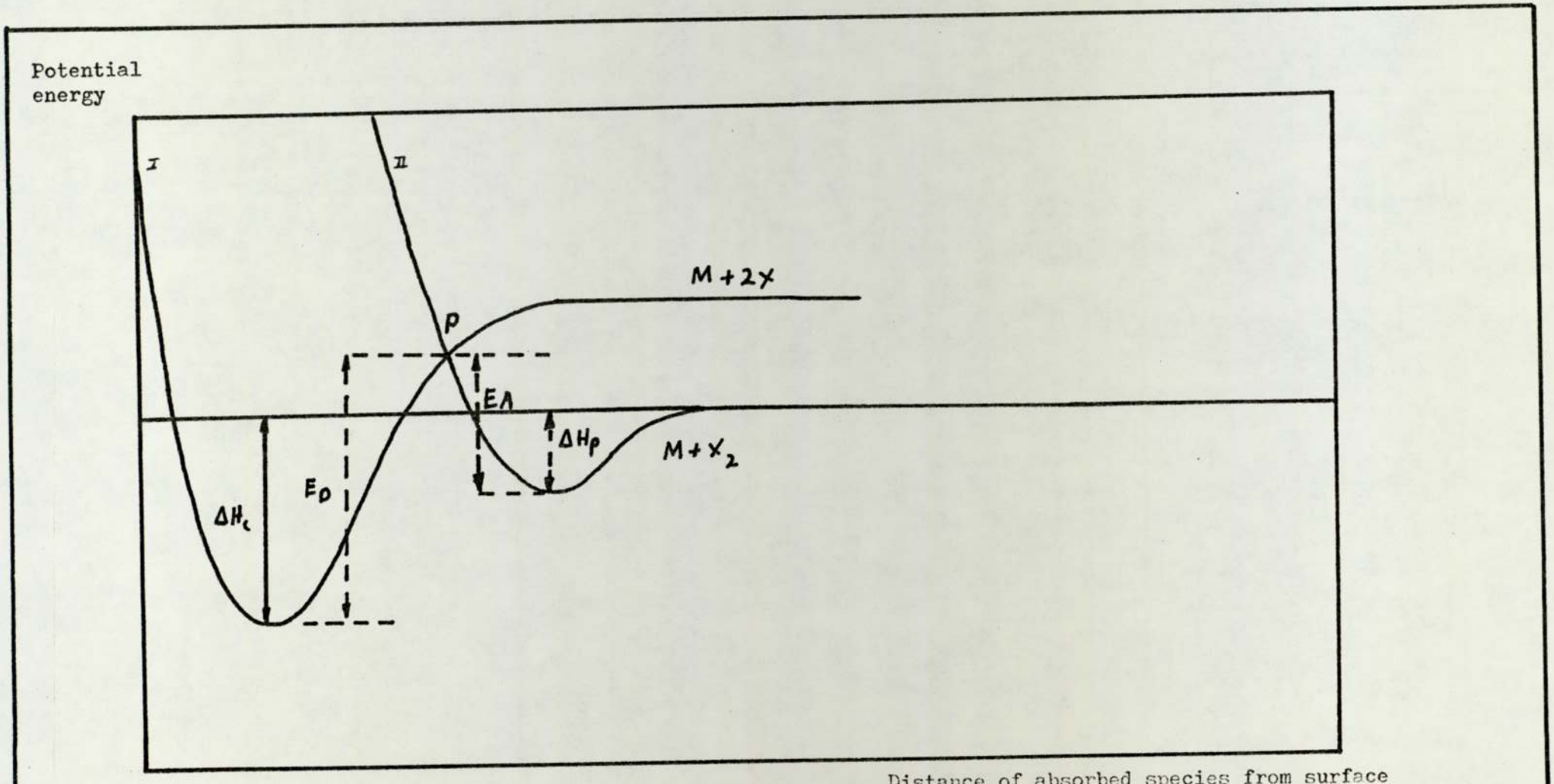

Figure 3: Schematic potential energy diagram for the interaction of a bomolecular gas with a metal substrate

attempt to understand the nature of adsorbed layers of oxygen on metal surfaces. The technique they used was the measurement of changes in work function. Culver and Tompkins (1959) have shown that the change in work function $\Delta\phi$ on adsorption is given by:

$$\Delta\phi = 4\, n_s \pi \theta m$$

where n_s is the number of adsorption sites per cm^2 of surface

θ is the fractional coverage of the surface by adsorbate

m is the dipolemoment.

If there is an increase of $\Delta\phi$, which means a decrease in surface potential. This is a measure of the magnitude of the negative charge at the adsorbed layer-gas interface. This technique should give a good indication of what happens to the oxygen on the surface, whether the absorbed oxygen remains on the surface as ions or is converted to oxide, but in practice, the extreme sensitivity of work function to surface contamination, crystallographic orientation and general heterogeneities have led to considerable controversy regarding the interpretation of results.

Some metals, like aluminium show an uptake of oxygen at room temperature which is much greater than the monolayer value and heats of adsorption that are comparable with the bulk heats of formation of the oxide[80]. A large amount of data on the structure of metal after exposure to low oxygen pressures is now available, primarily from low energy electron diffraction (LEED) investigation, but also from high energy electron diffraction (HEED). The interpretation of the data is the subject of much controversy in the literature (Germer, Bauer[81-84]). A chemisorbed layer may be pictorially represented either in terms of a classical model in which the adsorbed ions are located at potential minima on the surface of

the metal with a minimum amount of displacement of the metal atoms, or in terms of a reconstruction or rearrangement model in which the surface layer consists of both metal ions and oxygen ions.

The reconstruction is a necessary step in the ultimate development of a three-dimensional oxide even though the first stage may be the development of two-dimensional 'oxide' structures which bear little direct relationship to the three-dimensional structures. In order to explain the uptake of a second monolayer of oxygen, Lanyson and Trapnell[85] suggested a mechanism of interchange of adsorbed oxygen atoms with underlying metal atoms, this mechanism is commonly called 'place exchange'. Several different mechanisms are possible depending on whether the surface is perfect or contains defects. The two possible mechanisms are illustrated in Figure 4a.

In this model it is assumed that oxygen is in the gas phase, and that the liberation of the heat of chemisorption of the oxygen molecule assists the exchange.

May[86] has suggested another model for surface reconstruction in which place exchange provides one possible mechanism. In this model a part of the heat of chemisorption is available to form excited oxide molecules - with high kinetic energy parallel to the surface. This energy can provide transport of metal atoms over considerable distances on a smooth surface. Two possible mechanisms are illustrated in Figure 4b. A place-exchange mechanism leads to the formation of an excited molecule which can move along the surface to contribute to the formation of islands of reconstructed structure.

2.1.2 Oxygen solubility in metals

The solubility of oxygen in various solid metals varies markedly from very small mounts to 20-30%. It has been shown that

even small amounts of dissolved oxygen play an important role in the early stages of oxidation[87-88]. The solubility of oxygen in a metal varies greatly with temperature and the available data have been collected and summarized by Hansen and Anderko[89]. Reports of oxygen solubility show lack of agreement and no data is available at relatively low temperatures (room temperature). The available diffusion data have been discussed by Kofstad[90].

2.1.3 The formation of oxide films

When a thin continuous film of oxide has been formed on a metal surface. The metal and gaseous reactants are separated by a barrier and the reaction can continue only if cations, anions or both and electrons diffuse through the oxide layer. The rate which determines the oxidation reaction may be mass or charge transport through the oxide layer. This is shown in Figure 4c[9]. A large number of theories and models have been proposed to explain the formation of thin oxide films. Some of the mechanisms proposed include quantum mechanical tunnelling of electrons (Mott[92]), cation diffusion in a large space charge field (Cabrera and Mott[93-94]), place exchange (Eley and Wilkinson[95]). These try to explain the various forms of the logarithmic law. All these mechanisms and others have been discussed in a recent review by Lawless[96].

2.1.4 Chemisorption on oxide films

When an oxide film is present on the surface of a metal, the chemical reaction between the solid and a gas is initiated by chemisorption of the gas on the oxide. Since most oxides are semiconductors[92], the process of chemisorption is generally very complex and must be treated as a three-dimensional process (Vol'Kenshtein[97]). Chemisorption will generally be influenced by the presence of lattice defects, the distribution of electrons and

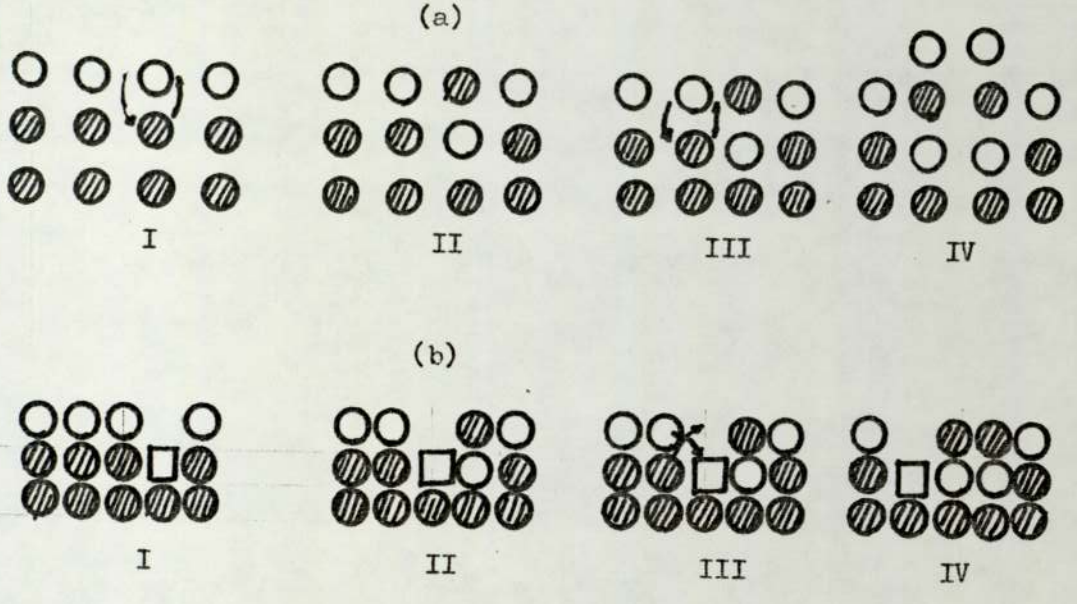

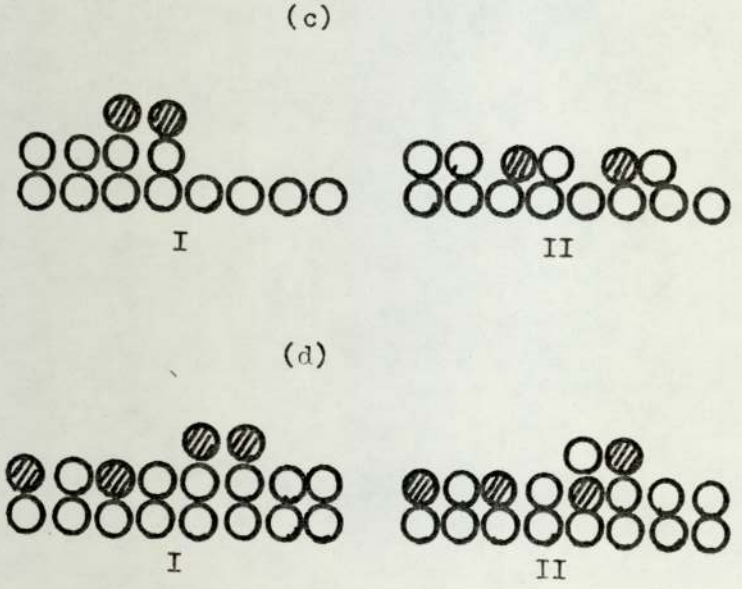

Figure 4: Schematic representation of place-exchange process in the presence of gaseous oxygen

(a) Surface free of defects

(b) Surface contains vacancy defects

(c) Reaction of a surface step

(d) Simple place exchange (after May 1969)

holes, as well as electron traps in and near the surface of the oxide. Since the oxygen molecule has an attraction for electrons, it is natural to expect oxygen to be adsorbed as negative ions. There is considerable speculation as to whether the adsorbed ions are O^-, O^{2-} or O_2^-. Barry and Stone[99] suggested that either O^- or O_2^- are prevalent at room temperature, but for higher temperature 100°C to 400°C O^{2-} predominated.

As more oxygen atoms are adsorbed, more electrons must be transferred and these must come from deeper levels in the oxide. This process causes the build-up of a space charge boundary layer and the development of a potential. The space-charge-layer theory of chemisorption has been discussed in detail by Hauffe and Engell[100].

2.1.5 Theory of Fehlner and Mott

Low temperature oxidation, room temperature has been discussed intensively by Fehlner and Mott[101]. An evaluation of Cabrera-Mott (1948-49)[94] theory is given by Lawless and modifications suggested in the light of recent experimental results. The low temperature oxidation is considered to go through a period of fast, linear oxidation followed by a slow logarithmic reaction, which may under certain conditions be followed by a rate increase and a second logarithmic stage. The initial linear oxidation is considered as a continuation of the chemisorption process by a place exchange mechanism.

Once a stable oxide has formed, it is assumed that oxygen ions formed on the surface by dissociation of oxygen molecules and capture of tunnelling electrons are partially incorporated in the oxide surface. A potential is thus set up across the film which provides a driving force for continued oxidation. The field created across the oxide lowers the potential barriers to ion migrations which

exist for anions at the oxide-oxygen interface and for cations at the metal-oxide interface. Fehlner and Mott differ from Cabrera and Mott, in that they consider anion as well as cation migration. The basic assumptions in the theory for the case of cation migration are the same as those used by Cabrera and Mott, but for the case of anion migration it is necessary to replace the assumption of a constant potential across the oxide by that of a constant field.

The assumption that very thin oxide films, formed by exposure of a metal surface to gaseous oxygen, are amorphous is certainly too general, even for low temperature oxidation. The experimental determination of the structure of very thin oxide films is rather difficult and reliable data is rare in the literature. Beck et al[102] have shown that low temperature oxide, room temperature, films on aluminium are amorphous. Additional data on the detailed structure of thin oxide films is badly needed since the transport of ions through such thin films is critical for the oxidation process.

The evidence used by Fehlner and Mott for the importance of anion migration in low temperature oxide films is primarily from studies of anodic oxidation in aqueous solution (Davies et al[103]). Heine and Pryor[104] have pointed out, that the defect structures of anodic and thermal oxide films are quite different. Pryor has criticized the theory, on the basis that it is by no means universally accepted that anionic transport is important, even for films formed in aqueous solutions.

There is not enough data to evaluate the effects of crystallographic orientation. Hart[105] has reported no orientation dependence for the low temperature oxidation of aluminium. The effect of oxygen pressure in the low temperature oxidation is not very well understood. Rhodin[106] found no pressure dependence, but Krishnamoorthy and Sircar[107] found the rate to be pressure

dependent. Kirk and Huber[79] found low temperature oxidation for aluminium to be pressure dependent.

2.2 The Aluminium-water system: Hydroxide film

When aluminium reacts, an electrochemical process provides the driving force for film growth. The anodic and cathodic half-cell reactions can be written[108]

$$\text{Anodic } Al + \begin{bmatrix} 3H_2O & Al(OH)_3 \\ 2H_2O \rightarrow & AlOOH \\ \frac{3}{2}H_2O & \frac{1}{2}Al_2O_3 \end{bmatrix} + 3H^+ + 3e$$

$$\text{Cathodic } 3H_2O + 3e \rightarrow \frac{3}{2}H_2 + 3OH^-$$

According to Alwitt the anodic reaction takes place over almost the full surface with the cathodic reaction occurring only at impurities and grain boundaries. Vedder and Vermilyea[109].

Films formed at less that 90°C have a duplex structure, with an outer layer of bayerite crystals on an inner layer of pseudo-boehmite. Bayerite is consistently present below 70°C, Hart[110], Alwitt[111], and Kawasaki[112].

Film growth proceeds in three stages. At first little change in the initial surface can be observed, Vedder and Vermilyea refer to this as the induction period. The second stage is the formation of the pseudoboehmite layer and the final stage is crystallization of bayerite. Alwitt suggests that the last two stages may overlap.

2.2.1 Pseudoboehmite layer

Hart has shown that the pseudoboehmite crystallites increase in size from about 2nm to several hundred nm at the start of growth. The low temperature, below 90°C, pseudoboehmite is preferentially

orientated so that the hydrogenbond channels of the boehmite structure are perpendicular to the surface Hart.[110]

There are important differences between the films formed at high and low temperatures. The low temperature films are more porous and the porosity decreases with increasing thickness. The other difference is low-temperature film is brittle. Perhaps the most significant difference between the two films is the distribution of porosity within the film. This may be associated with the poorer crystallinity of the low-temperature films.

2.2.3 Bayerite Crystal layer

Alwitt[108] reports, bayerite crystals are observed on the surface while the pseudoboehmite layer is still growing. Crystal nucleation and growth continues until the surface is completely covered. The pseudoboehmite rapidly reaches a limiting thickness and maintains that thickness throughout subsequent bayerite crystallization.

The bayerite crystals are not embedded in the surface nor joined to the pseudoboehmite crystals. They are easily removed by mechanical means or with adhesive tape. The cones and somatoids are the shapes most commonly reported for bayerite, but these apparently grow into cylinders.

2.3 Oxidation in humid oxygen atmospheres

In 1948 Podgurski[113] investigated oxidation in humid oxygen, but he could not obtain consistent results. Morize and Lacombe[114] studied the oxidation of electropolished aluminium in both dry and humid air at room temperature by measuring solution potentials. They found that films are formed appreciably thicker in humid air than in dry air. The oxidation rate was also found to increase with increasing humidity. The important feature of Morize and Lacombe's,

graphs on oxidation, is that even after very long exposures the curves still slope gently upwards. From this it is evident that film growth does not come virtually to a stop as indicated by the results of Podgurski. Hass[115] reported that the film formed on aluminium in air at room temperature quickly thickens to about 2 nm. However it does not stop here but continues at a very much reduced rate until a thickness of about 5 nm is reached after one month's exposure. These experiments were carried out in ordinary air, which no doubt contained some water vapour, on the other hand, the experiments of Cabrera[116] and co-workers were carried out in dried air and also humid air. In dry air a film thickness of 1.5 nm was rapidly reached increasing to about 2 nm after 25 days. The final growth rate was 0.2 to 0.3 nm/month. Cabrera also found that water vapour had a considerable effect on the growth rate and also that the oxidation rate is a function of the water-vapour pressure. Specimens which had been oxidized 10 hours in saturated air at 10°C were 4.0 nm thick.

2.4 Chemisorption of water vapour on clean surfaces (Vacuum)

Previous investigators, Hackerman, Wüstenhagen, Grunberg, Fianda and Müller,[117-123] of aluminium interaction with water vapour did not have the benefit of ultra-high vacuum systems therefore fresh films were deposited at pressures in excess of 1×10^{-6} torr . A monolayer of a gas with a sticking coefficient of unity can form in less than two seconds at these pressures and hence these earlier studies are particularly subject to contamination effects which could not be taken into account.

Huber and Kirk[124] were one of the first workers to evaporate aluminium in ultra-high-vacuum, and followed the adsorption of water vapour by granvimetric and work function measurements. Their study was made at room temperature and its purpose was to show that water

contamination could cause the lowered work functions obtained by other authors for the oxygen-aluminium system. They showed that exposure of a fresh aluminium film to water vapour at 25°C caused the work function to decrease by 1.1 eV after an exposure of about 5×10^{-5} torr-min. It then remained constant.

Batt and Mee[125] obtained similar results with photoelectric work function measurements on evaporated aluminium films. In addition, they found that with much larger exposures the work function dropped further to a minimum value of about 1.4 eV below the clean metal work function and then increased by about 0.5 eV.

Huber and Kirk[124] also found that water vapour lowered the work function of both the fresh surface and an oxygen exposed surface by 1 eV. The 1 eV lowering is consistent with the polar nature of water, assuming either H_2O or OH groups chemisorbed on the metal oxide surface with the hydrogen outward. Their microbalance and work function data indicated that water initially reacts with a fresh metal surface to produce a monolayer of oxide before forming the hydrogen outward dipole layer.

Fort and Wells[126] also studied the reaction of water vapour on clean aluminium by measurement of work function changes. In their experiment clean surfaces were produced on bulk aluminium samples by a cutting procedure inside an ultra-high vacuum system. They reproduced 'Huber and Kirk's results and also found the amount of adsorption at equilibrium to be independent of pressure in the range from 10^{-5} to 10^{-8} torr. The temperature dependence of the adsorption of water on aluminium was contrary to Langmuir's classical theory for chemisorption. According to Langmuir's classical theory the rate of chemisorption is determined by the rate at which molecules from the gas phase have favourable collisions with vacant sites on the metal surface. Thus the rate should decrease as the surface is

covered instead of remaining constant. Huber and Kirk also studied the reaction of water vapour at higher pressures and found that, as the water vapour was slowly let in to 4.56 torr the change of work function difference first decreased from its equilibrium value of - 1.19 to a minimum value of - 1.425 eV and then began to rise. These higher pressure results are very similar to those obtained by Batt and Mee[125], on evaporated aluminium films. Fuggle et al have also examined the reaction of aluminium films with water vapour. The technique they used was X-ray photoelectron spectroscopy (XPS) or ESCA. Their results indicated that aluminium formed oxidised layers with water vapour and oxygen. They observed an initial high sticking coefficient which reached a maximum when the oxidized layer was approximately 60% complete. Krueger and Pollack[128] did not observe the initial high sticking coefficient. This may be due to the probability that samples were not completely clean. With the exception of this initial region there was qualitative agreement between the results.

Fuggle et al tried to measure the ratio of oxide to hydroxide after 10^{-2} torr sec. exposure to water vapour, but found it difficult to reproduce. The ratio varied from 6:1 to 10:1. However, they concluded that 90% of the available hydrogen was lost from the oxidised surface compared with not more than 60% in the similar experiments of Krueger and Pollack. Eley and Wilkinson[129] found that approximately 70% of the available hydrogen was liberated. Their studies were done in a low vacuum and the measurements probably start close to the stage where Fuggle et al finish in terms of exposure. The results suggest that initially almost all of the hydrogen is lost, but during later stages of reaction more hydroxide, or hydrated oxide is formed.

2.5 The Hydrogen Problem

When aluminium reacts with a humid oxygen environment, at temperature less than 90°C, the reaction produces bayerite, pseudoboehmite and also hydrogen. What happens to hydrogen is of great importance because it can produce degradation of mechanical properties of many alloys and elements. There are many ways by which hydrogen can produce degradation and one is by hydrogen embrittlement, (Bernstin, McLright[130,131]).

The fundamental understanding of hydrogen embrittlement and of the associated areas of hydrogen diffusion and solubility including interaction with defects, is advancing. However, much controversy remains for embrittlement mechanism where some completely opposing models are still being supported.

There are phenomenological differences in Hydrogen Embrittlement depending on whether the source of the hydrogen is internal or external. In some cases dramatic differences are observed in the response of a material to internal and external hydrogen. For example, some alloys (Rene 41 and Inconel 718) are embrittled by high pressure external hydrogen, Jewett et al[132] but are unaffected under loading after rather severe electrolytic charging (Groenevelt and Fletcher[133]). It is difficult to be certain where different embrittlement mechanisms are operative.

The role of hydrogen, in Hydrogen Embrittlement, is that it influences the atomic bond breaking at the tip of a crack and hence can be related to effects on the interatomic cohesive force. This concept was introduced by Troiano[134] and is the basis of a theory by Oriani[135].

Much research is being carried out on the mechanism of Hydrogen Embrittlement. The results obtained by Scaman, Montgrain and Swann[5] on A1-2n-Mg alloys show hydrogen penetration of grain boundaries

resulting in a loss of grain-boundary adhesive strength. Since it is important to establish the form and morphology of the hydrogen on the boundary, Scaman has demonstrated that high-pressure hydrogen-filled bubbles can be formed on grain boundaries. These bubbles were formed by the combined effect of a changed state of elastic stress in the thin foil specimen and electron beam heating rapidly results in bubble formation. Scaman has observed that, molecular hydrogen within the bubble generates a significant stress to exceed the yield stress of the surrounding matrix and this leads to the generation and propagation of dislocations.

For a hydrogen bubble to be formed it is necessary that the chemisorbed hydrogen be recombined to form molecular hydrogen. From Scamans work, the activation barrier for this process must clearly be small because of the ease of bubble formation under the stimulation of a 120 kV electron beam, because of the bubble association with the grain-boundaries. The grain-boundary chemical composition is very important. The role of grain-boundary precipitates is also of interest. Again Scaman has demonstrated that the hydrogen bubbles interact both with the grain boundary precipitate and with intermetallic particles formed either during casting or during homogenization. Addition of small quantities of chromium and possibly manganese to aluminium alloys have beneficial results.

CHAPTER 3

ESSENTIAL THEORY

3.1 Principle of Electron Spectroscopy for Chemical Analysis (ESCA)

When a surface is irradiated with photons (X-rays) electrons are emitted from atoms in the surface layers. ESCA reproduces directly the electronic level structure. All elements heavier than lithium can be studied even if an element occurs together with several other elements and represents only a small part of a chemical compound.

The ejected electrons can arise from two processes in the atom as shown in Figure 5. In the first, direct photoionisation takes place to give an electron with an energy E_e

$$E_e = E_{x\text{-ray}} - E_{B1} \qquad \ldots\ldots 3.1$$

where E_{B1} is the binding energy of the electron in the atom and $E_{x\text{-ray}}$ the energy of the incident radiation. The second process takes place in the ionised atom, when an electron drops from a higher energy level L_2 in the atom to fill the vacancy left by the emitted electron. Instead of emitting a secondary photon all the energy of this transition is given to a third electron, generally known as an Auger electron, which is then emitted. For analytical purposes the importance of both types of electrons are that they have energies which are characteristic of the atoms from which they have been emitted for a given incident photon energy.

3.1.1 Calculation of Binding Energies from ESCA spectra

The kinetic energy K^1_{kin} of the photoelectron is given by

$$K^1_{kin} = E_{x\text{-ray}} - E_{B1} - E_r \qquad \ldots\ldots 3.2$$

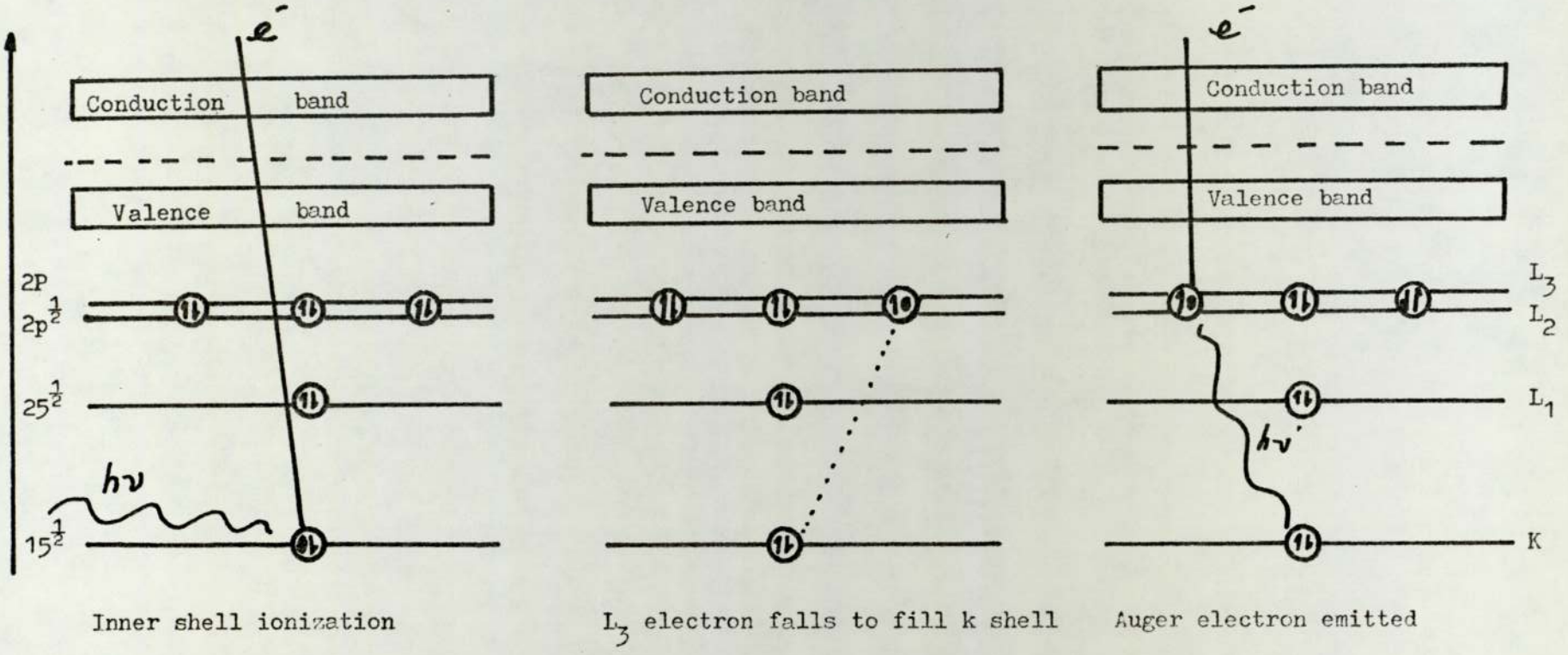

Inner shell ionization

L_3 electron falls to fill k shell

Auger electron emitted

Figure 5

Here $E_{X\text{-ray}}$ is the quantum energy of the X-ray photon, E_{B1} is the energy of liberation for the electron and E_r is the recoil energy. By using the law of conservation of momentum for the case when the recoil is in the direction of the incoming photon there is an upper limit for the recoil energy

$$E_r = E_{X\text{-ray}} \frac{m}{M} \frac{E'_{kin}}{E_{X\text{-ray}}} + \frac{2 E_{kin}}{mc^2}^{\frac{1}{2}} + \frac{E_{X\text{-ray}}}{2mc^2} \quad \ldots\ldots 3.3$$

M and m are the masses of the recoiling atom and the photoelectron, (non-relativistic calculation) by using the equation 3.3. The maximum recoil energy for the photoelectric ejection of a valence electron is calculated. In most cases it is less than one electron volt in magnitude and with suitable choice of X-radiation the recoil energy becomes negligibly small.

Nearly always there exists a small electric field in the space between the source and the entrance slit to the spectrometer even if both are grounded. This is because grounding the source and the spectrometer material means that their Fermi levels are the same. Any difference in work function of the source material and the spectrometer material thus gives a difference in macro-potential and therefore an electric field in the space between source and spectrometer chamber. The kinetic energy E_{kin} of the electron when it enters the spectrometer chamber is thus slightly different from the energy E'_{kin} which it has on emerging from the source. It is the kinetic energy E'_{kin} that is measured. The Fermi level is chosen as a reference level for bulk materials.

$$E_b = E_{X\text{-ray}} - E_{kin} - \phi_{sp} \quad \ldots\ldots 3.4$$

where E_b is the electron binding energy and ϕ_{sp} is the work function

of the spectrometer material. It should be noticed that the term ϕ_{sp} does not depend on the source material and as long as it does not vary with time, then the same work function correction can be applied to all measurements.

3.1.2 The inherent level widths and energy separations

When an inner electron shell is ionized, the vacancy is filled by outer electrons within a time interval of the order of 10^{-16} seconds. The principle of uncertainty shows that there is a lack of definition in the energy level of the order of a few electron volts. This is the inherent width of the level, which defines an upper limit for the accuracy with which atomic level energies can be measured. With ESCA machines this limit can actually be reached.

As is shown in the Figure 6 the width of each level decreases with decreasing atomic number. In the case of aluminium both the k and L_{III} widths are only a few tenths of an electron volt[137].

3.1.3 Electron escape

It is important to calculate the number of photoelectrons[138-140] dN that: (a) are emitted per second from a given nL (or nlj) subshell of certain atoms contained in a differential volume element of thickness dZ at a distance Z below the specimen surface, (b) escape from points on the surface that are somewhere within the projection of the spectrometer entrance aperture of effective area A_o without being inelastically scattered, (c) enter the spectrometer with velocity vectors within the geometrical acceptance solid angle Ω_o of the spectrometer, and (d) are finally detected so as to contribute to the resulting no-loss photoelectron peak. The initial kinetic energy just after leaving the specimen surface is E_1 and the final kinetic energy during analysis is E_o equal to or smaller than EA_o, and Ω_o determines the relative energy resolution $\Delta E/E_o$ Figure 7.

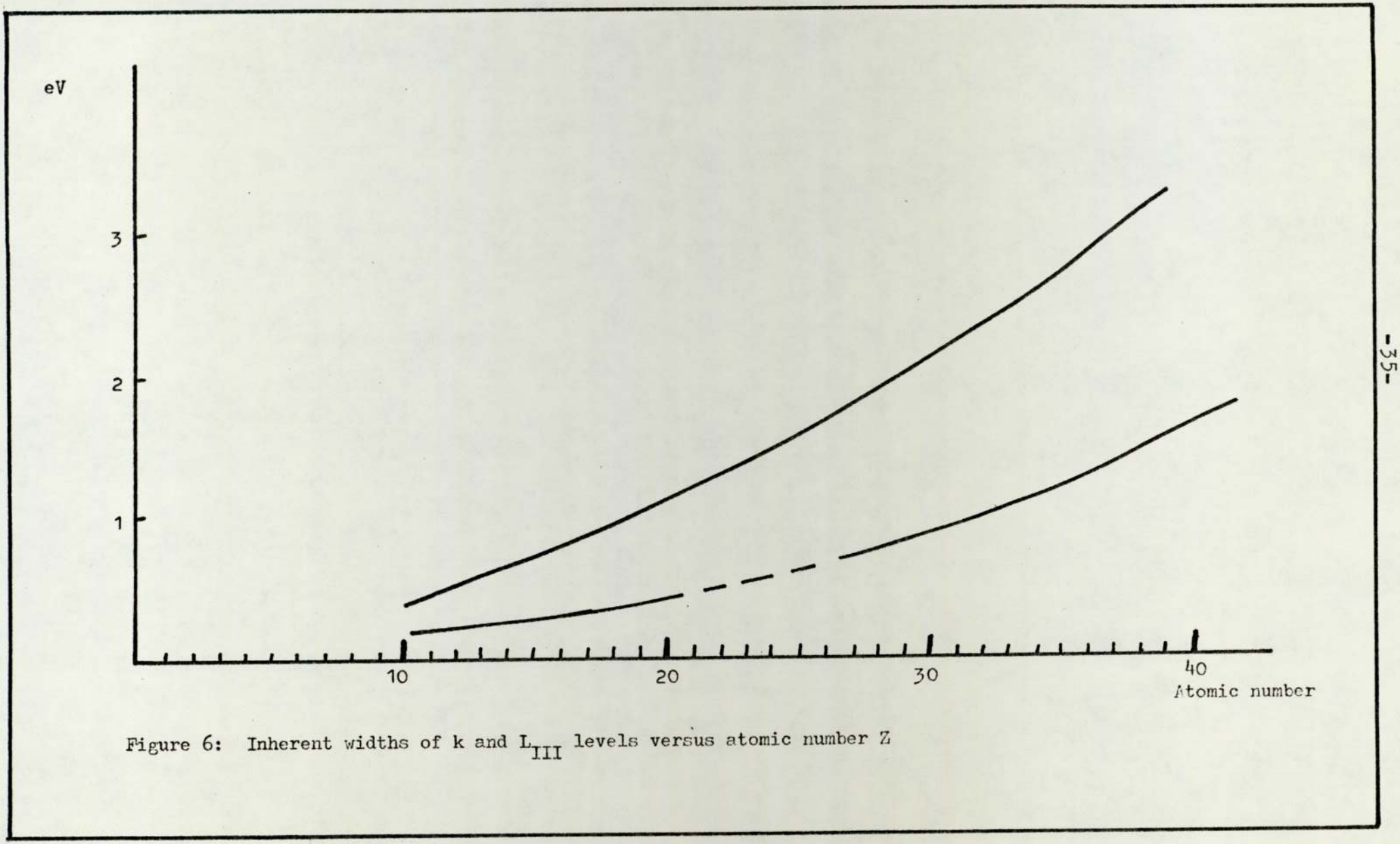

Figure 6: Inherent widths of k and L_{III} levels versus atomic number Z

The basic assumption utilized in connection with this model are listed.

(1) The specimen surface is assumed to be perfectly planar on an atomic scale.

(2) The specimen is assumed to be amorphous or to be composed of randomly-oriented crystallites with characteristic dimensions very small in comparison to those of A_o. In this way all effects due to diffraction or channeling of X-rays or electrons within the specimen can be neglected.

(3) The X-ray flux I_o incident upon the specimen is assumed to be uniform and is represented by a plane wave.

(4) The refraction and reflection of X-rays at the surface are described in terms of classical electromagnetic theory.

(5) Both X-ray and photoelectron attenuation within the specimen are assumed to follow an exponential decoy along their path lengths. The characteristic attenuation lengths written as (mean free paths) Λ_x for X-rays and Λ_e for electrons.

(6) The attenuation length for X-rays, although dependent on the X-ray wave-length λ_x is assumed to be independent of the angle of incidence ϕ. This assumption appears to be adequate for X-rays of approximately 1 Kev.

(7) Although the electron attenuation length Λ_e is known to be a strong function of the photoelectron kinetic energy E. It is assumed to be independent of Θ, the angle of escape relative to the surface.

(8) The acceptance of electrons into the spectrometer for energy analysis is assumed to be governed by a constant solid angle Ω_o acting over the projection of an effective aperture area

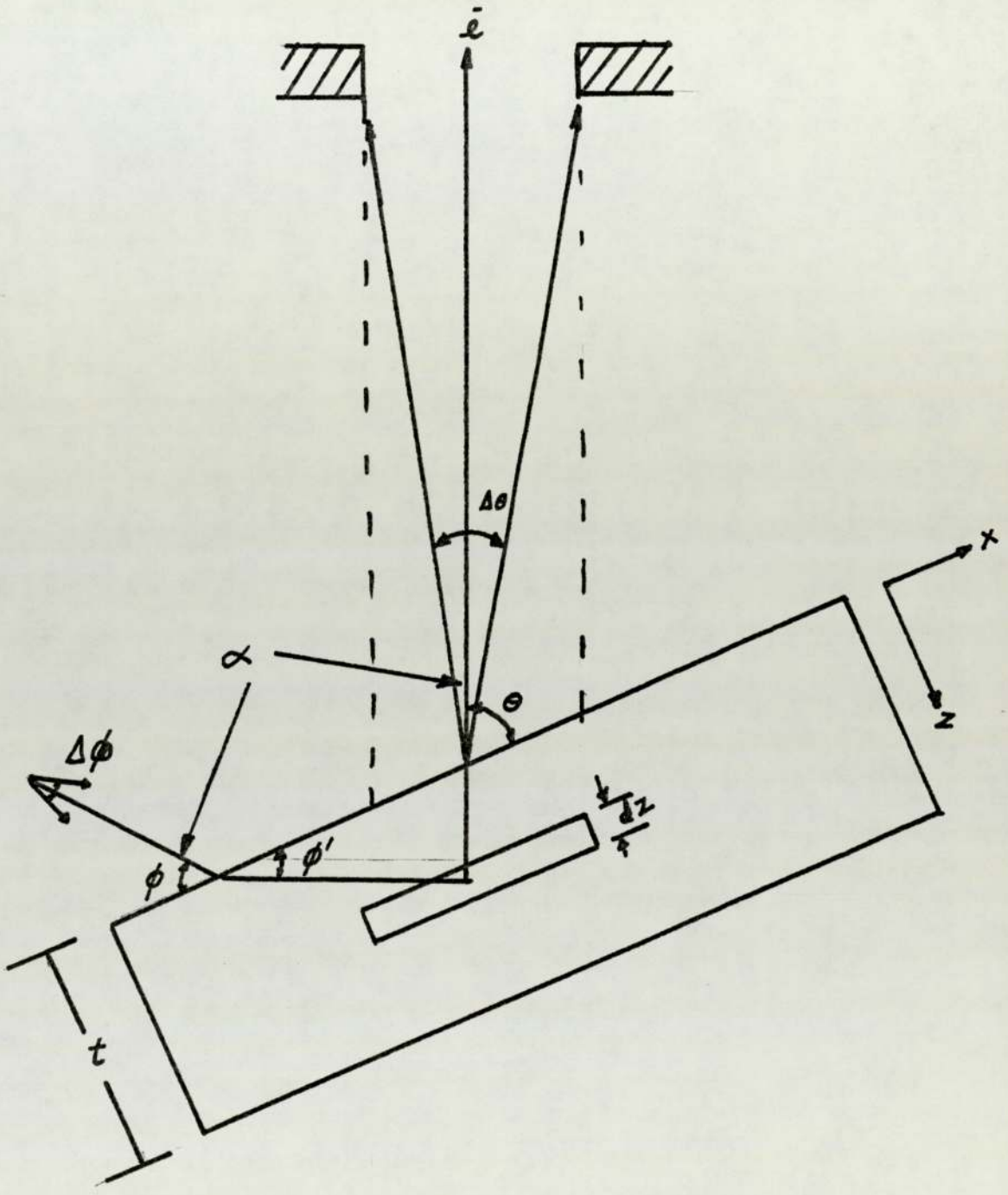

Figure 7: Schematic drawing of an arbitrary spectrometer geometry, with the nomenclature for various quantities indicated (Fadley et al) [140]

A_o onto the sample surface. With these assumptions, the general expression for the number of photoelectrons dN is given by Fadley as

$$dN(\Theta) = \left[\begin{matrix}\text{X-ray flux}\\ \text{at depth Z}\end{matrix}\right] \cdot \left[\begin{matrix}\text{number of atoms}\\ \text{in volume element}\end{matrix}\right] \cdot \left[\begin{matrix}\text{probability for}\\ \text{nl emission into}\,\Omega_o\end{matrix}\right]$$

$$\left[\begin{matrix}\text{fraction escaping}\\ \text{in no-loss peak}\end{matrix}\right] \cdot \left[\begin{matrix}\text{intensity loss factor}\\ \text{due to retardation}\end{matrix}\right] \cdot \left[\begin{matrix}\text{detection}\\ \text{efficiency}\end{matrix}\right]$$

$$dN(\Theta) = \left[I_o(1-R)\,\frac{\text{Sin}\,\phi}{\text{Sin}\,\phi}\,\exp\,-\frac{Z}{\Lambda_x \text{Sin}\,\phi}\right] \cdot \left[\rho\,\frac{A_o}{\text{Sin}\,\Theta}\,d_Z \cdot \frac{d\sigma_{nl}}{d\Omega}\Omega_o\right]$$

$$\cdot \left[\exp\,\frac{Z}{\Lambda_e(E)\sin\,\Theta}\right] \cdot \left[F\,\frac{E_o}{E}\right] \cdot \left[D_o\right] \qquad \ldots\ldots\ 3.5$$

R represents the X-ray reflection coefficient, ρ is the number density of the atom under consideration, $A_o/\sin\,\Theta$ is the effective specimen area seen by the projected spectrometer aperture; $d\sigma_{nl}/d\Omega$ is the differential photoelectric cross-section for the nl subshell; $Z/\text{Sin}\,\phi$ and $Z/\text{Sin}\,\Theta$ are the path lengths within the specimen for X-rays and electrons - respectively; $F(E_o/E)$ represents a function describing the intensity loss caused by retardation; and D_o is an overall detector efficiency.

An important special case of this model is shown schematically in Figure 8. Consider a single uniform surface layer of thickness t', with characteristic parameters ρ', $\Lambda_e{}'E'$ and $d\sigma_{n'l'}/d\Omega$ that need not equal the corresponding values in the thick underlying substrate. The kinetic energy E' will depend on the subshell $n'l'$ from which the photoelectron is emitted. This model is thus relevant to such experimental situations as chemisorbed layers, oxide layers. As t' is not too many times larger than Λ_e' so that photoelectrons from the

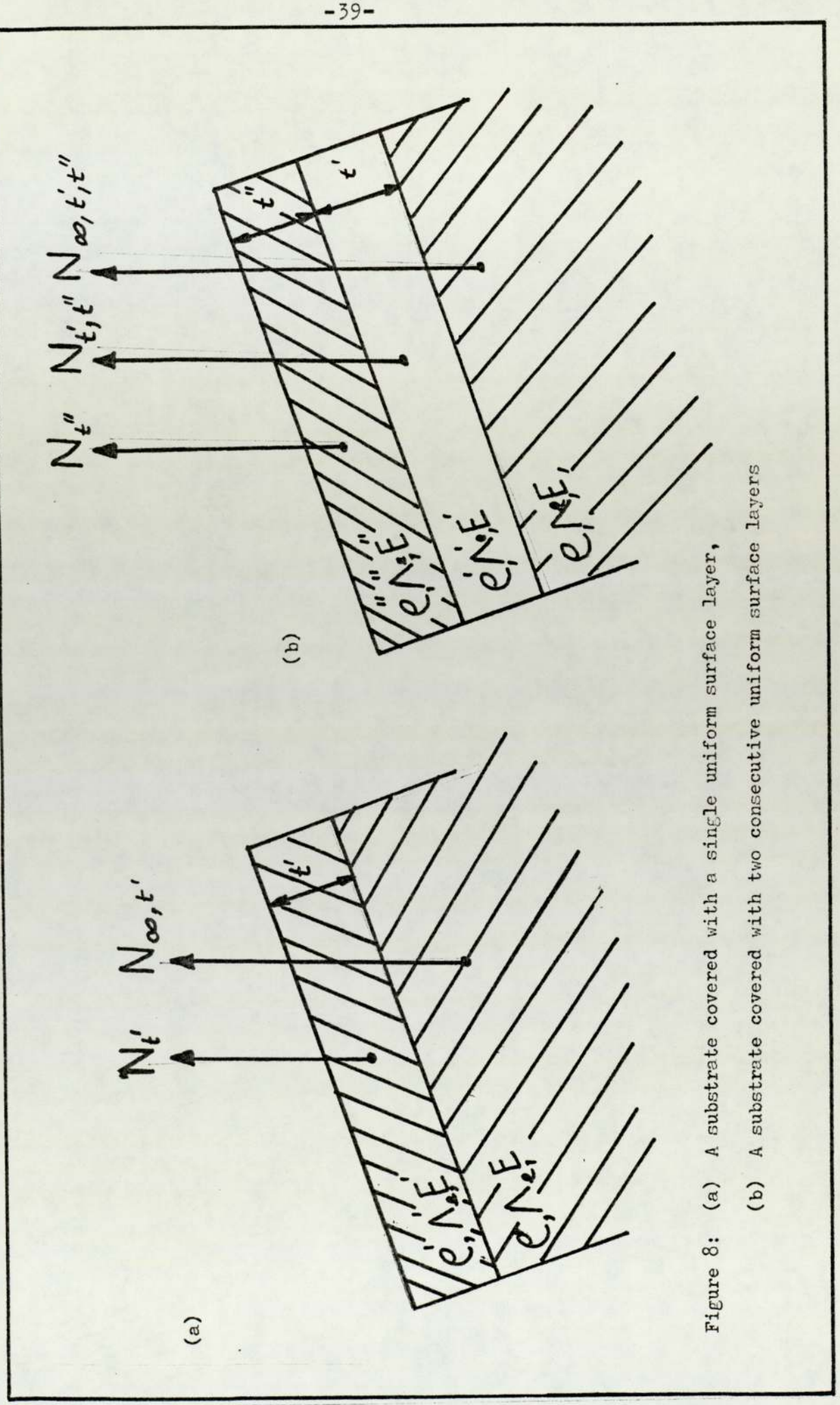

Figure 8: (a) A substrate covered with a single uniform surface layer,

(b) A substrate covered with two consecutive uniform surface layers

substrate can still escape through the surface layer without inelastic scattering to a sufficient degree to be detected. The intensity of a given photoelectron peak originating in the surface layer will be given by:

$$N_t'(\Theta) = C_o \frac{E_o'}{E'} \rho' \frac{d\sigma' n' l'}{d\Omega} \Lambda'_e(E) \left[1 - \exp - \frac{t}{\Lambda'_e(E) \sin \Theta}\right] \quad \ldots. 3.6$$

and the intensities from the substrate

$$N_\infty t(\Theta) = C_o \frac{E_o}{E} \rho \frac{d\, nl}{d} \Lambda_e(E) \exp\left[-\frac{t}{\Lambda_e(E) \sin \Theta}\right] \quad \ldots. 3.7$$

A useful specialization of this one-layer model is the substrate and the nl photoelectron peaks of this atom are chemically shifted from one another by a sufficient amount to enable measuring angular distributions of each peak separately. This system has been studied recently by Carlon and McGuire. For such a system equation reduces to:

$$\frac{N_t'(\Theta)\rho}{N\ t(\Theta)\rho} = \frac{\Lambda'_e(E)}{\Lambda_e(E)} \exp\left[\frac{t}{\Lambda'_e(E) \sin \Theta}\right]\left[1 - \exp - \frac{t}{\Lambda'_e(E) \sin \Theta}\right] \quad \ldots. 3.8$$

which can further be simplified to:

$$\ln\left[\frac{N_t'(\Theta)}{N\ (\Theta)} \frac{\Lambda_e(E)\ (Al)}{\Lambda'_e(E)\ (Al_2O_3)} + 1\right] \Lambda'_e(E)(Al_2O_3) \sin \Theta = t \quad \ldots. 3.9$$

3.1.4 Effects of surface roughness

As in most experimental situations, it is difficult to satisfy the assumption of an atomically flat surface; it is of interest to

determine at least qualitatively what the effects of surface roughness will be on angular distributions. A rough surface is any surface deviating from atomically flat roughness will affect the photoemission process in basically two ways, (1) a given point on the surface may be shaded for either the incident X-rays or the escaping electrons by adjacent roughness, (2) the true X-ray incidence and electron escape-angles will, in general, be different from the corresponding flat surface values at any point on a rough surface. Significant X-ray shading will occur only if the characteristic dimensions of the roughness are of the order of Λ_x. Electron shading correspondingly need only be considered with roughness dimensions of the order of Λ_e or larger.

In figure 9 the cross-section of an arbitrary rough surface is shown. The overall incidence and escape angles ϕ and Θ are defined relative to the planar average of the roughness. The true X-ray incidence angle on an arbitrary differential element of area dA on the surface is indicated by ϕ'', the true refraction angle by ϕ''', and the true electron escape angle by Θ'.

Provident that the characteristic dimensions of the roughness are much larger than either Λ_x or Λ_e, we can approximate that volume element generated by projecting each unshaded dA anti-parallel to dA and into the surface as a single flat specimen of cross-sectional area dA. A differential volume element of such a specimen at a distance Z below the surface will produce a number of photoelectrons given

$$dN(\Theta) = C_o \frac{E_o}{E} (1-R) \rho \frac{d\sigma n l}{d\Omega} \frac{\sin \phi}{\sin \phi} \frac{dA}{A_o} \exp\left[-Z\left[\frac{1}{\Lambda_x \sin \phi'''} + \frac{1}{\Lambda_e \sin \Theta}\right]\right] dZ \quad \ldots\ldots 3.10$$

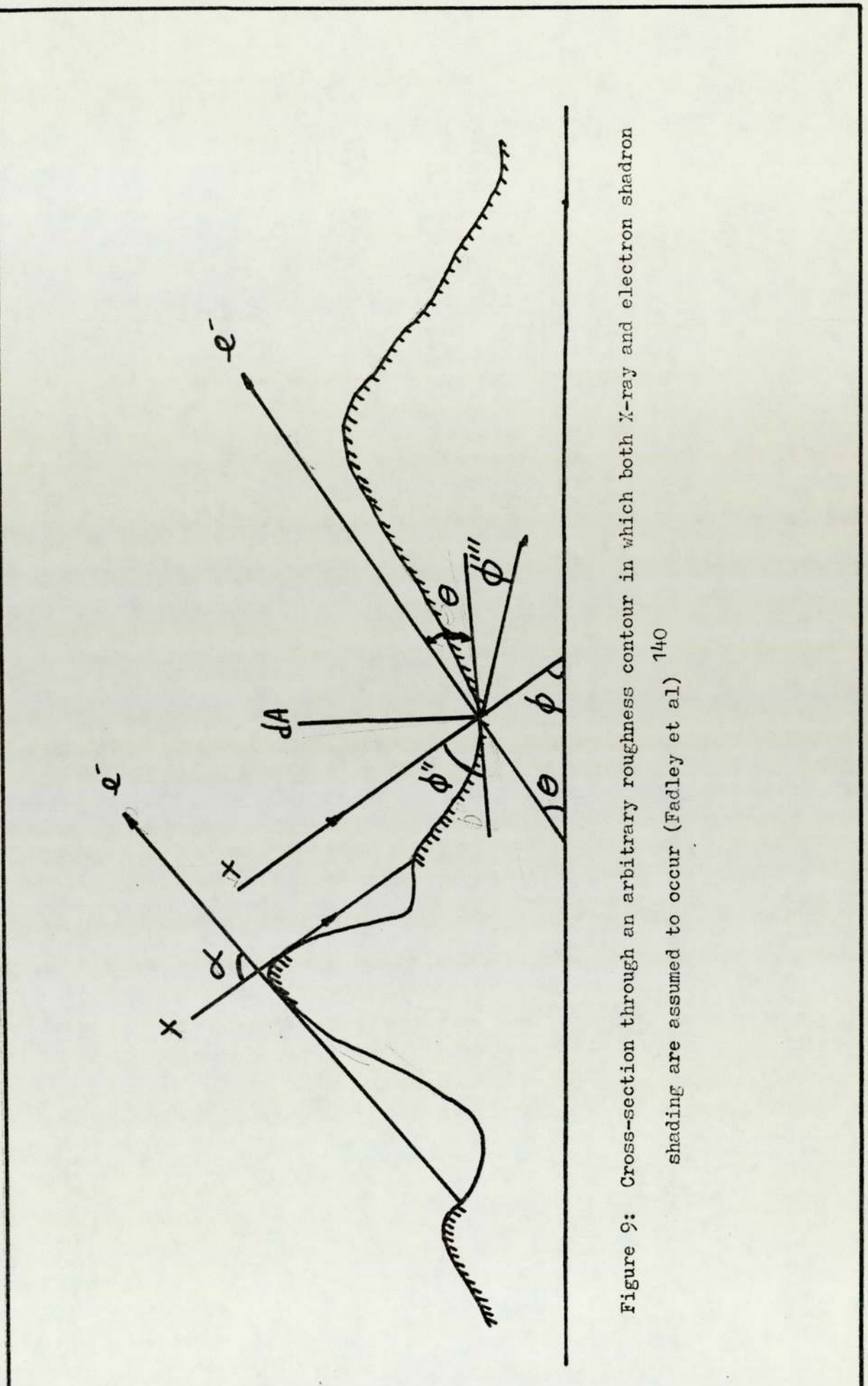

Figure 9: Cross-section through an arbitrary roughness contour in which both X-ray and electron shadron shading are assumed to occur (Fadley et al) [140]

This is for a specimen of cross-section dA that is entirely in view of the spectrometer aperture and for which the planar surface angles ϕ, ϕ' and θ are replaced by the values ϕ'', ϕ''' and θ' respectively describing the orientation of the arbitrary surface elements.

Although total intensities from rough surfaces may equal those from smooth surfaces, the average angle of emission $\langle\theta'\rangle$ need not be equal to θ. Thus, the average depth of emission compared with that from a smooth surface, will be correctly given by $\Lambda_e \langle \sin\theta' \rangle \approx \Lambda_e \sin\langle\theta'\rangle$. This also affects the oxide and hydroxide films.

The behaviour of a rough surface covered with a layer of uniform thickness t is also rather important from an experimental point of view. It is convenient to write the relevant expressions as ratios of the rough surface total intensities with a surface layer to the anologous smooth surface intensities with the same surface layer:

$$\frac{N_t^R(\theta)}{N_{t'}(\theta)} = \frac{\left\langle \left[1-\exp\left(-t'/\Lambda'_e(E)\sin\theta\right)\right]\sin\theta \right\rangle}{\left[1-\exp\left(-t'/\Lambda'_e(E)\sin\theta\right)\right]\sin\theta} \frac{A^R(\theta)}{A} \qquad \ldots\ldots 3.11$$

$$\frac{N_\infty^R t(\theta)}{N_\infty t(\theta)} = \frac{\left\langle \exp\left(-t/\Lambda'_e(E)\sin(\theta)\right)\right\rangle}{\exp\left(-t/\Lambda'_e(E)\sin\theta\right)\sin\theta} \frac{A^R(\theta)}{A} \qquad \ldots\ldots 3.12$$

Here $A^R(\theta)/A$ can be treated as a single quantity representing the ratio of total unshaded rough surface area to the total area of a smooth planar surface of the same overall dimensions. In the same notation:

$$\frac{N_{\infty}^{R}(\theta)}{N_{\infty}(\theta)} = \frac{\langle \sin \theta' \rangle}{\sin \theta} \frac{A^{R}(\theta)}{A} = f_{x}(\theta(\phi)) \qquad \ldots\ldots 3.13$$

As a detailed illustration of this type of analysis Fadley [141] carried out numerical calculations for an idealized sinusoidal model of surface roughness. The model surface he used is indicated in Figure 10a. It is assumed to have a constant sinusoidal cross-section in any plane parallel to the x-Z plane and thus can be characterized as a 'one-dimensional' roughness.

The form of the surface is thus:

$$Z = (a/Z) \sin (2 x/\lambda) \qquad \ldots\ldots 3.14$$

The only other study of a specific model for surface roughness in connection with X.P.S. was carried out by Ebel et al [143], who considered a one-dimensional triangular roughness such as that shown in Figure 10b for the special case of right triangles and for fixed $\phi = \theta = 45$. This study was primarily concerned with the effect of cube size on intensities through X-ray shading, and did not consider the forms of angular distributions from such surfaces.

In the work of Fadely et al [141] the average rough-surface escape angles $\langle \theta' \rangle$ were plotted against the flat-surface escape angle θ for different values of a/λ; these results can be explained very simply. For θ near 90°, the entire surface is unshaded and a considerable fraction of the emission is from the sloping sides of the sinusoidal surface for which $\theta < 90^{\circ}$. Thus for any non-zero value of a/λ $\langle \theta' \rangle$ will be less than θ for $\theta = 90^{\circ}$. Also as a/λ becomes larger, the slopes become larger and $\langle \theta' \rangle$ becomes smaller near 90°. For small values of θ, on the other hand, the curve for each a/λ displays a region for which $\langle \theta' \rangle > \theta$. This

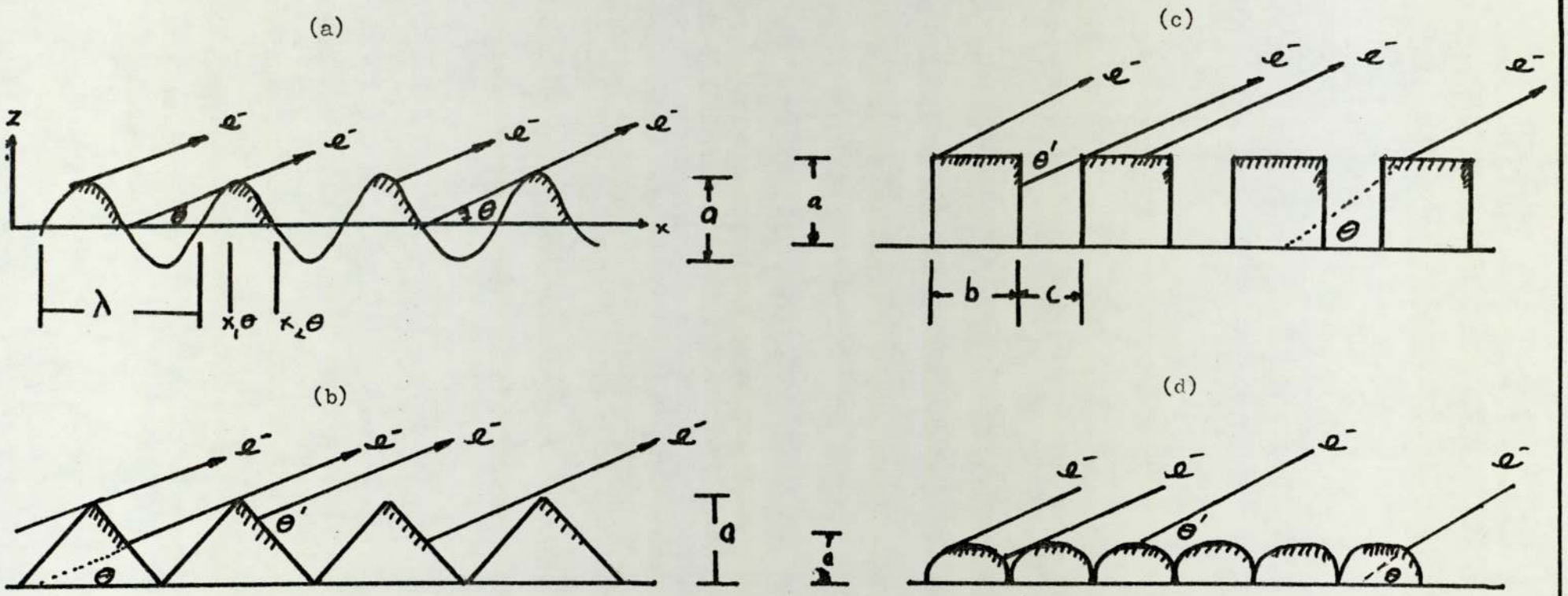

Figure 10: (a) Sinusaidal roughness, electron shading only

(b) Triangular roughness, electron shading only

(c) Rectangular roughness, electron shading only

(d) Hemespherical roughness, electron shading only

is due to the fact that only the uppermost rounded portions of the sinusoidal surface are unshaded and these in general will have a range of θ' values from zero to considerably above θ.

Thus, for any non-zero value of a/λ $\langle \theta' \rangle$ will be less than θ for $\theta \lesssim 90^{\circ}$. Also as a/λ becomes larger the slopes become larger and $\langle \theta \rangle$ becomes smaller near 90°.

In this model it appears that relatively smooth surfaces with $a/\lambda = 0.318$ will behave essentially as flat surfaces over a region symmetric about 45°. This suggests that experimental surfaces with very low, but non-zero, roughness might be expected to conform most closely to the flat surface model in some region of θ near 45° and that deviations from this model would occur on either the low-angle or high sides of this region.

3.2 The Theory of Ellipsometry

The amplitude and phase of a beam of light reflected or transmitted by a thin film, or combination, may be obtained by solving Maxwell's equation with the appropriate boundary condition. The problem is considerably simplified by the use of Fresnel coefficients R and T where R is the ratio of reflected to incident amplitudes and T is the ratio of transmitted to incident amplitude.

The notation used here for different boundaries between media is adopted from that of Abele's [144] and used by Heavens [10]. A superscript + or - indicates the direction of propogation with respect to the normal to the film. The direction of the plane of polarization of any orientation is specified with respect to the plane of incidence.

The wave vectors are resolved into components parallel and perpendicular to the plane of incidence and are denoted by a

subscript (p) and (s) respectively. The media are numbered and the material identified by this number. For an absorbing medium, the refractive index is a complex quantity N = n - ik. The imaginary part is related to the absorption of energy by the medium. For non-normal incidence, the angles of refraction become complex quantities. The physical interpretation of this lies in the fact that the planes of equal phase are no longer parallel to the planes of equal amplitude (Vasiak) [145]. It may be shown that the Fresnel coefficients are given by

$$R_{12(P)} = \frac{E_{1p}^{-}}{E_{10}^{+}} = \frac{N_1 \cos \phi_2 - N_2 \cos \phi_1}{N_1 \cos \phi_1 + N_2 \cos \phi_1} \quad \ldots\ldots 3.15$$

$$R_{12(S)} = \frac{E_{13}^{-}}{E_{13}^{+}} = \frac{N_1 \cos \phi_1 - N_2 \cos \phi_2}{N_1 \cos \phi_1 + N_2 \cos \phi_2} \quad \ldots\ldots 3.16$$

For light travelling from medium 1 to medium 2 having an angle of incidence ϕ_1 and angle of refraction ϕ_2. Similar expressions exist for the transmitted (P) and (S) components.

The above equations may be applied to a single film, which is assumed to be homogeneous and isotropic and to have parallel plane boundaries as indicated in Figure 11. This represents a parallel beam of plane polarized light of unit amplitude and wavelength λ falling on an absorbing film of thickness t and complex refractive index N_2 supported on an absorbing substrate of index N_3.

The complex amplitudes of the successive beams reflected and transmitted by the film are shown in Figure 11 in which δ_2 represents the amplitude and phase change in traversing the film once

$$\delta_2 = \frac{2\pi}{\lambda} N_2 + \cos \phi_2 \quad \ldots\ldots 3.17$$

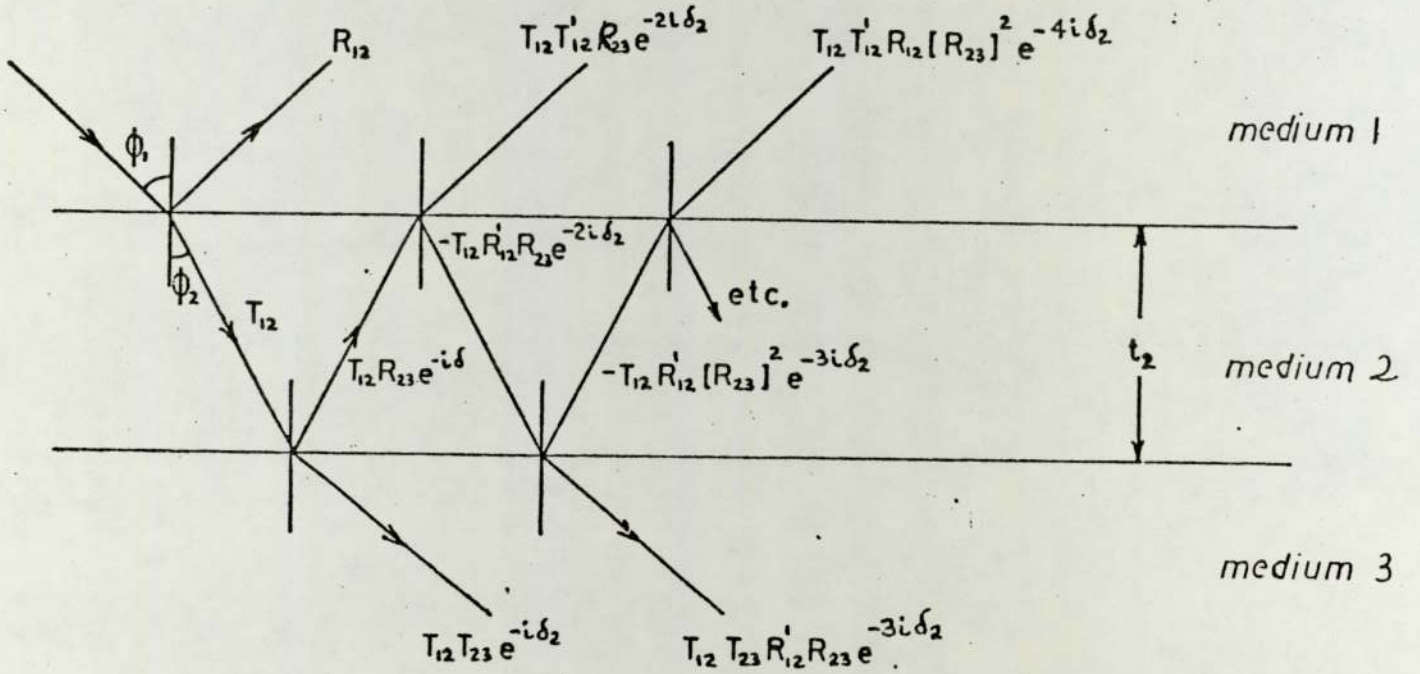

FIG.11.- COMPLEX AMPLITUDES OF THE SUCCESSIVE BEAMS REFLECTED AND TRANSMITTED BY A SINGLE FILM.

The reflected amplitude from the whole system is thus given by the infinite series

$$R_{13} = R_{12} + T_{12}\,T_{12}\,R_{23}\,e^{-2i\delta_2} - T_{12}\,T_{12}\,R_{12}\left[R_{13}\right]^2 e^{-4i\delta_2} + \quad \ldots. \quad 3.18$$

which can be summed to give

$$R_{12} = R_{12} + \frac{T_{12}\,T_{12}\,R_{23}\,e^{-2i\delta_2}}{1 + R_{12}\,R_{23}\,e^{-2i\delta_2}} \qquad \ldots. \quad 3.19$$

It follows from the conservation of energy that $T_{12}\,T_{12} = 1 - \left[R_{12}\right]^2$ and substituting this into the previous expressions, the reflected amplitude becomes

$$R_{13} = \frac{R_{12} + R_{23}\,e^{-2i\delta_2}}{1 + R_{12}\,R_{23}\,e^{-2i\delta_2}} = \rho\, e^{i\Delta} \qquad \ldots. \quad 3.20$$

where ρ is the amplitude ratio and Δ is the difference in phase of the reflected light compared to the incident light. Two identical expressions exist for the (R) and (S) components, although the numerical values are different.

The ratio of amplitude changes for the (P) and (S) components is given by

$$\frac{R_{12}\,(P)}{R_{12}\,(S)} = \frac{\rho_{(P)}\,e^{i\Delta P}}{\rho_{(S)}\,e^{i\Delta S}} = \frac{(P)}{(S)}\,e^{\,i(\Delta_p - \Delta_s)} \qquad \ldots. \quad 3.21$$

As shall be shown, the ellipsometer measures $\mathrm{Tan}\,\Psi$ the relative amplitude reduction, and Δ, the difference in phase change for the (P) and (S) components. The parameters Ψ and Δ are

thus related, through the Fresnel coefficient, to the refractive index and thickness of the film, and the angle of incidence. The derivation of n and k for the film from the measured values of Ψ and Δ is extremely laborious, so that an electronic computer is very essential. For a clean opaque film surface, n and k are related to the instrument reading Ψ and Δ through equations and are given in a form suitable for computation by Ditchburn as [145]

$$n^2-k^2 = \frac{\sin^2\phi_1 \tan^2\phi_1 (\cos^2\psi - \sin^2 2\Psi \sin^2\Delta) + \sin^2\phi}{(1 + \sin^2\Psi \cos\Delta)^2} \quad \ldots. 3.22$$

$$2nk = \frac{\sin^2\phi_1 \tan^2\phi_1, \sin\Psi \sin\Delta}{(1 + \sin^2\Psi \cos\Delta)^2} \quad \ldots. 3.23$$

The extension of the calculations to several layers is possible since a single film, bounded by two surfaces, has an effective reflection coefficient and phase change. Such a film may be replaced by a single surface having the same properties as indicated in Figure 11.

In this way, it is possible to start at the supporting substrate and work upwards through each layer to the surface as performed by Rouard [146] or to start at the surface and work downwards towards the substrate, as proposed by Vasicek [147]. For an oxidized surface, the angles Ψ and Δ are changed from the values for a clean surface. If the optical constants of the oxide-free surface are known, then any subsequent changes of the instrument angles Ψ and Δ can be used to determine the thickness of the oxide film formed.

Two Algol programmes were used in this work. The first computed values of n and k for a range of values of Ψ and Δ at a given angle of incidence. These computed values are pseudo-constants (for a surface with a superimposed, i.e. a clean surface is assumed). The second programme was used to predict values of Ψ and

Δ for a range of values of n and k for the film whose thickness was measured in a subsidiary experiment. The true values of n and k were then found by inspection by finding consistency between values of n, R, d, Ψ and Δ .

3.2.1 The compensator method

In this work most of the ellipsometry was done by using a compensator method and the principle of the compensator [148] method is illustrated in Figure 12. Plane polarized light, produced by the polarizer P_1 is incident on the specimen with azimuth Ψ i.e. its plane of polarization inclined at an angle Ψ to the plane of incidence. Conventionally, inclinations are considered positive if anti-clockwise from the plane of incidence, looking towards the oncoming light. On reflection from the specimen the difference in amplitude ratio and the difference in phase change between the (P) and (S) components - ensures that the reflected light is, in general, elliptically polarized, i.e. the tip of the electric vector moves in an ellipse with azimuth of the major axis χ and ellipticity (ratio of minor to major axes) γ . This elliptically polarized light then passes through the compensator which consists of a bi-refringent sheet of mica.

If the fast axis of the compensator is arranged to be parallel to the major axis of the reflected ellipse, the vibrations along the major and minor axis of the ellipse (for which a phase difference of 90 degrees exists) are again brought into phase, and plane polarized light results. The azimuth of this 'compensated' plane polarized light will be at an angle χ to the major axis of the ellipse (See Figure 13).

Finally the light passes through the analysing polaroid A_1 which may be rotated until its transmission axis is perpendicular to the plane of viberation. In this condition, and only in this

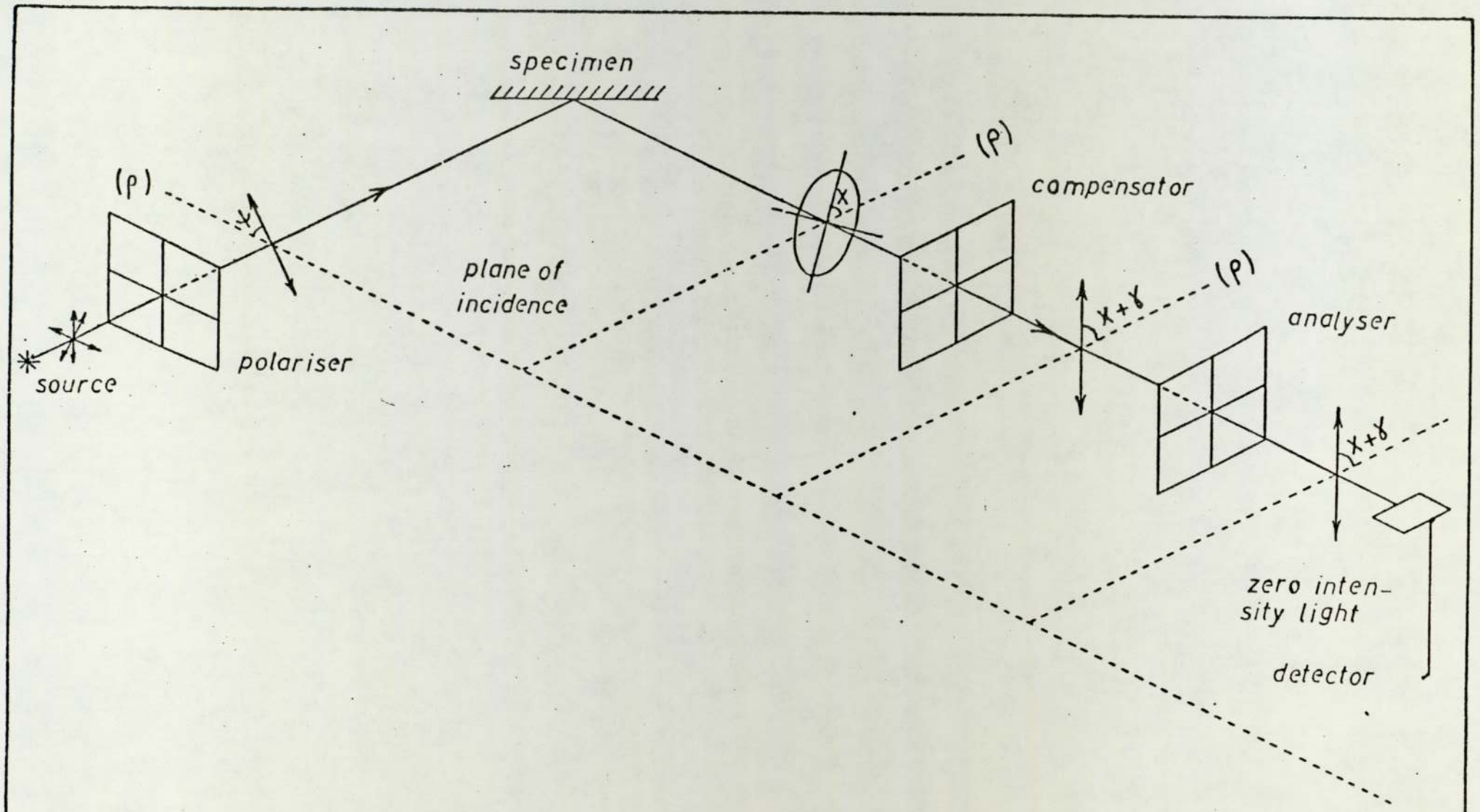

FIG.12.- BASIS OF THE COMPENSATOR METHOD OF ELLIPSOMETRY.

condition, the light intensity received by the photomultiplier detector is zero.

The experimental procedure is considerably simplified if the compensator is first located with its fast axis at exactly 45° to the plane of incidence.

The polarizer and analyser are then adjusted for minimum light intensity received by the photomultiplier. The situation then corresponds to that shown in Figure 13. The azimuth of the reflected ellipse is always 45°, or in other words, the amplitudes of the reflected (P) and (S) components are equal i.e. E_p^- and E_S^- are equal.

The azimuth Ψ of the polarizer is then equal to the parameter ψ mentioned previously

$$\text{Tan } \psi = \frac{E_s^+}{E_p^+} \qquad \ldots\ldots 3.24$$

But

$$\tan \Psi = \frac{\varrho(p)}{\varrho(s)} = \frac{\dfrac{E_p^-}{E_p^+}}{\dfrac{E_s^-}{E_2^+}} = \frac{\dfrac{E_p^-}{E_s^-}}{\dfrac{E_p^+}{E_s^+}} \qquad \ldots\ldots 3.25$$

Since from above

$$\frac{E_p^-}{E_s^-} = 1.00 \qquad \ldots\ldots 3.26$$

then

$$\tan \Psi = \frac{1}{\dfrac{E_p^+}{E_s^+}} = \frac{E_s^+}{E_p^+} \qquad \ldots\ldots 3.27$$

Hence from 2.10

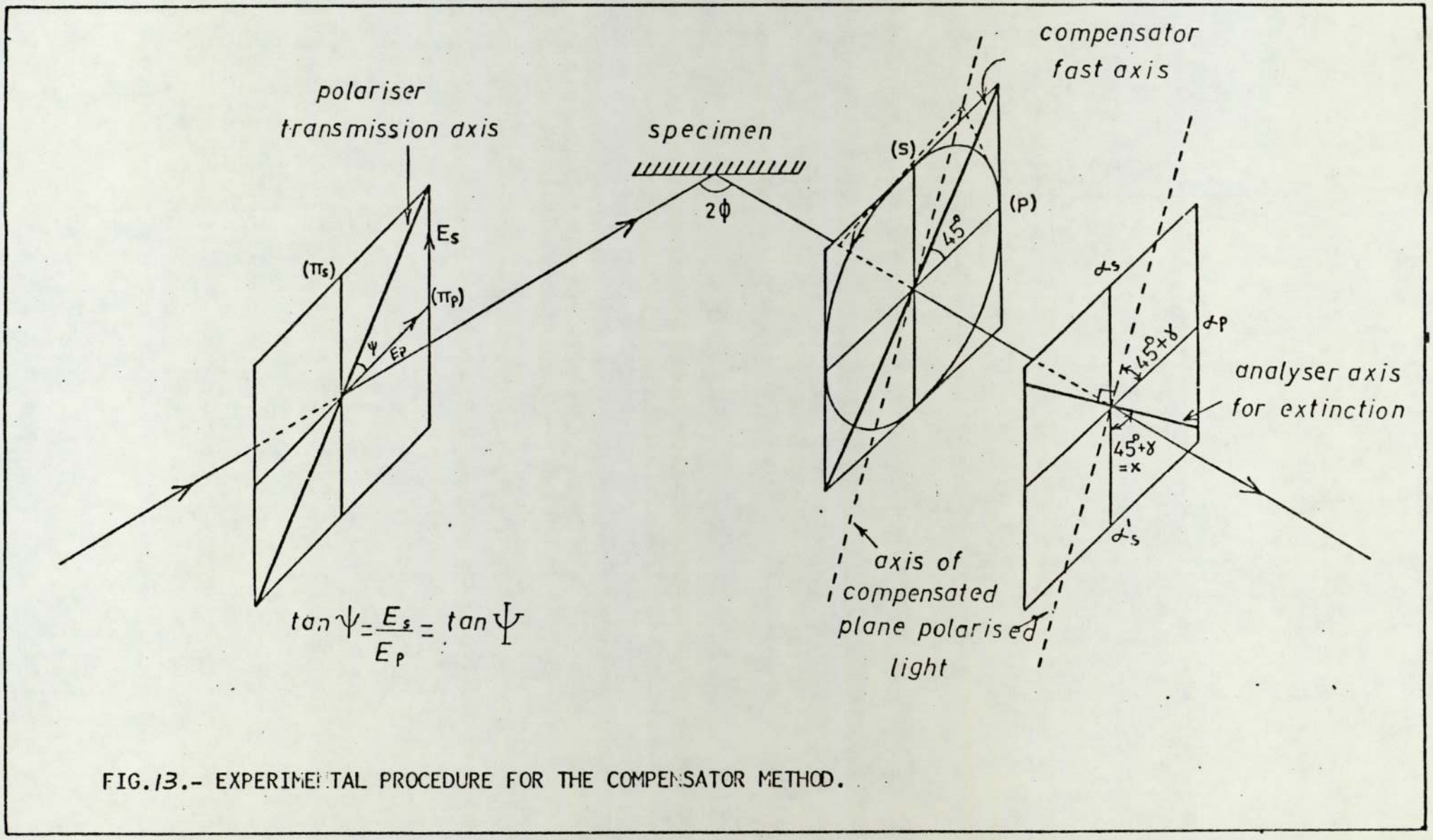

FIG. 13.- EXPERIMENTAL PROCEDURE FOR THE COMPENSATOR METHOD.

$$\tan \Psi = \tan \tilde{\Psi}$$

$$\Psi = \tilde{\Psi} \qquad \ldots\ldots 3.28$$

The ellipticity γ is related to the phase difference Δ between the (p) and (s) components. In general, it may be shown that:

$$\tan \Delta = \frac{\tan 2\gamma}{\sin 2\chi}$$

Since, from above $\chi = 45^\circ$, $\sin 2\chi = 1.00$ and

$$\tan \Delta = \tan 2\gamma \quad ; \quad \Delta = 2\gamma \qquad \ldots\ldots 3.29$$

The ellipticity γ and hence the phase difference Δ is determined from the analyser azimuth, as shown in Figure 13. The azimuth of the compensated light is $45^\circ + \gamma$, so that the azimuth at the analyser in its extinction position will be $45^\circ + \gamma$ with respect to α the perpendicular to the plane of incidence. It is this quantity marked X on Figure 13 which is measured experimentally

$$\text{Since } X = 45^\circ + \gamma = 45^\circ + \Delta/2$$

$$\text{then } \Delta = 2X - 90^\circ \qquad \ldots\ldots 3.30$$

In general, pairs of polarizer and analyser azimuths for extinction occur which fall into four zones. MacCrakin [149] gives a detailed explanation of the effect.

The total 32 pairs of polarizer and analyser positions for extinction can be understood in a methodical fashion by respresenting the state of polarization of light by means of the Poincare sphere

3.3 Principles of Scanning Transmission Electron Microscopy (STEM)

The basic electron optical and instrumental elements required by a high resolution (STEM), such as strong, electrically stable, probe-

forming lenses,a beam deflection system, and specimen manipulation facilities of high mechanical stability are components which are already in a highly developed state in a conventional high resolution (TEM). In a STEM system the beam is focussed to a fine probe and scanned over the sample as in scanning electron microscope. Electrons which pass through the sample are collected and processed as in a SEM system. In a STEM system the detector is beneath the specimen. If another detector is placed above the sample, the microscope can also be used as a high resolution SEM • JEM 100C is one such system which combines STEM and SEM modes.

The resolution of STEM is determined by the probe size used. The size of probe (d) obtained is controlled by such factors as the gun brightness (β), the current (I) and the beam convergence ($2\alpha_o$). The relationship between the probe size and these parameters is given by the expression:

$$d = (41/\beta\pi^2\alpha^2)^{\frac{1}{3}} \qquad \ldots\ldots 3.31$$

3.3.1 Theory of STEM

Using the coordinate system shown in Figure (14) the electron wave function in the object is

$$\psi_o(e) = \int G(\alpha) \exp\{ik(\alpha.e)\}\, d\alpha \qquad \ldots\ldots 3.32$$

where $G(\alpha)$ is the angular variation of the incoming conical illumination. It is given by

$$G(\alpha) = \exp\{iW(\alpha, Z)\} \quad \alpha \leq \alpha_o$$

$$= 0 \qquad \alpha > \alpha_o$$

with $W(\alpha Z) = -K(C_s\alpha^4/4 + \Delta Z\alpha^2/2)$ 3.33

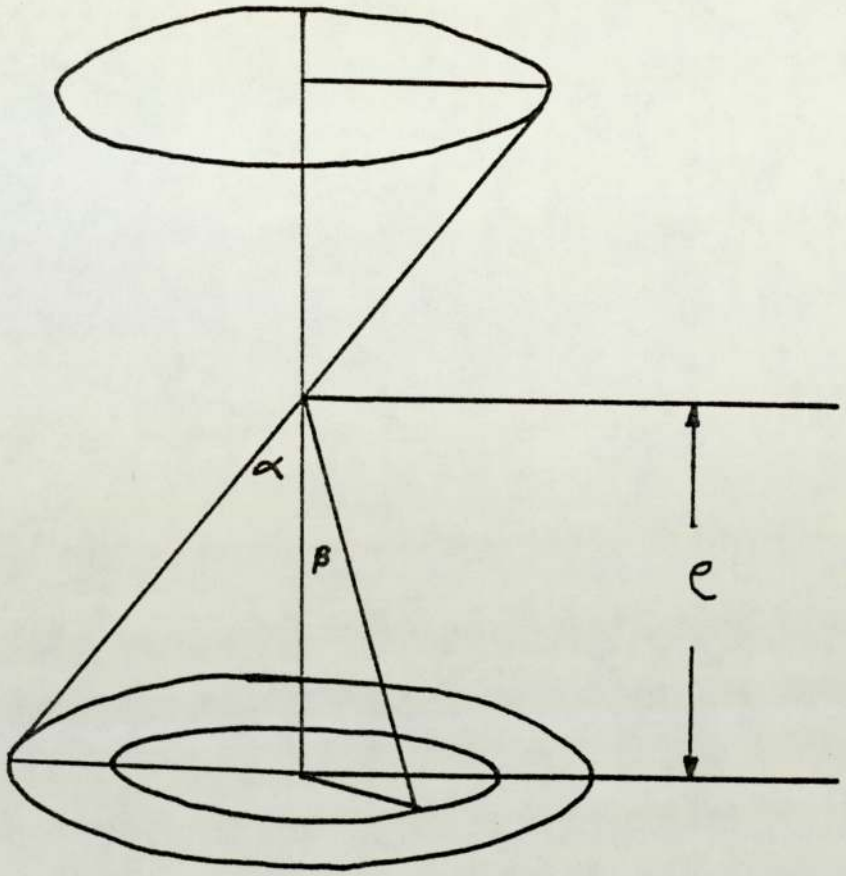

The system of coordinates Figure 14

C_s spherical aberration, C_s.

The wave function in the detector plane is obtained by a Fourier transform after the interaction with the specimen

$$\Psi(\beta) = \int T(\alpha)\, G(\alpha-\beta)\, d\alpha \qquad \ldots\ldots 3.34$$

where $T(\alpha)$ is the scattering amplitude of the specimen. The wave function can be split into two parts. One from the unscattered beam ($G(\beta)$, with $|G| = 1$ in this case) and one from the scattered wave ($\Psi_2(\beta)$), so

$$\Psi(\beta) = G(\beta) + \Psi_2(\beta)$$

The detector plane intensity is then

$$\Psi\Psi^* = 1 + G\Psi^* + G^*\Psi_2 + \Psi_2\Psi_2^* \qquad \beta \leq \alpha_o$$
$$= \Psi_2\Psi_2^* \qquad \ldots\ldots 3.35$$

where * denotes a complex conjugate.

The term $(G\Psi_2^* + G^*\Psi_2)$ is linearly related to the object scattering amplitude, and this is the dominant term in the formation of a bright-field phase contrast image. The term $\Psi_2\Psi_2^*$ is an additional nonlinear component. The final intensity is found by integrating over the azimuth and phase of β is appropriate for the detector. Complete details of this calculation are given by Ref 150-151 .

3.3.2 Scanning Electron Microscopy (SEM)

The electron optical column contains an electron gun and a series of electron lenses which focus a fine beam of electrons onto the specimen surface. This electron beam is scanned across the specimen surface in a rectangular raster in Synchrony with the electron beam in the cathode ray tube (CRT). As the beam scans the specimen surface, secondary electrons are generated at the specimen surface; the secondary electron current varies according to the local properties of the specimen surface. This current is amplified to form the video signal which governs the brightness in the CRT; the displayed image represents a picture of the specimen. Figure 15. If the scanned area in the CRT is the same as that on the specimen surface, the magnification is unity; but by reducing the scanned area on the specimen, the magnification is increased. The usual range for a commercial SEM is between 20 and 50,000.

3.3.3 Resolving Power

In the absence of aberrations, the beam diameter is related to the source diameter by magnification as follows:

$$d_o = \frac{D_o}{M} \qquad \ldots\ldots 3.36$$

where d_o is Aberration less beam diameter

D_o Diameter of the source

M Magnification

The final beam current is

$$i = \frac{\pi}{6} d_o^2 J_c \frac{eV}{kT} \alpha^2 \qquad \ldots\ldots 3.37$$

J_c Beam current density, A cm^{-2}

e Charge on an electron, coulombs

V Accelerating voltage of primary beam, volts

T Temperature

Semi-angle of convergence of the beam

To get finer resolving power, the final beam diameter has to be reduced. This can be done by increasing the magnification, but this will also decrease the final beam current i. In practice, the aberrations of the final lens will make the total beam diameter d larger than d_o. The spherical aberration gives circle of least confusion given as

$$d_s = \frac{1}{2} C_s \alpha^2 \qquad \ldots\ldots 3.38$$

Where C_s is the spherical aberration constant.

For a well-designed lens C_s is of the order of a focal length of the lens.

In chromatic aberration the electrons of higher energy come to

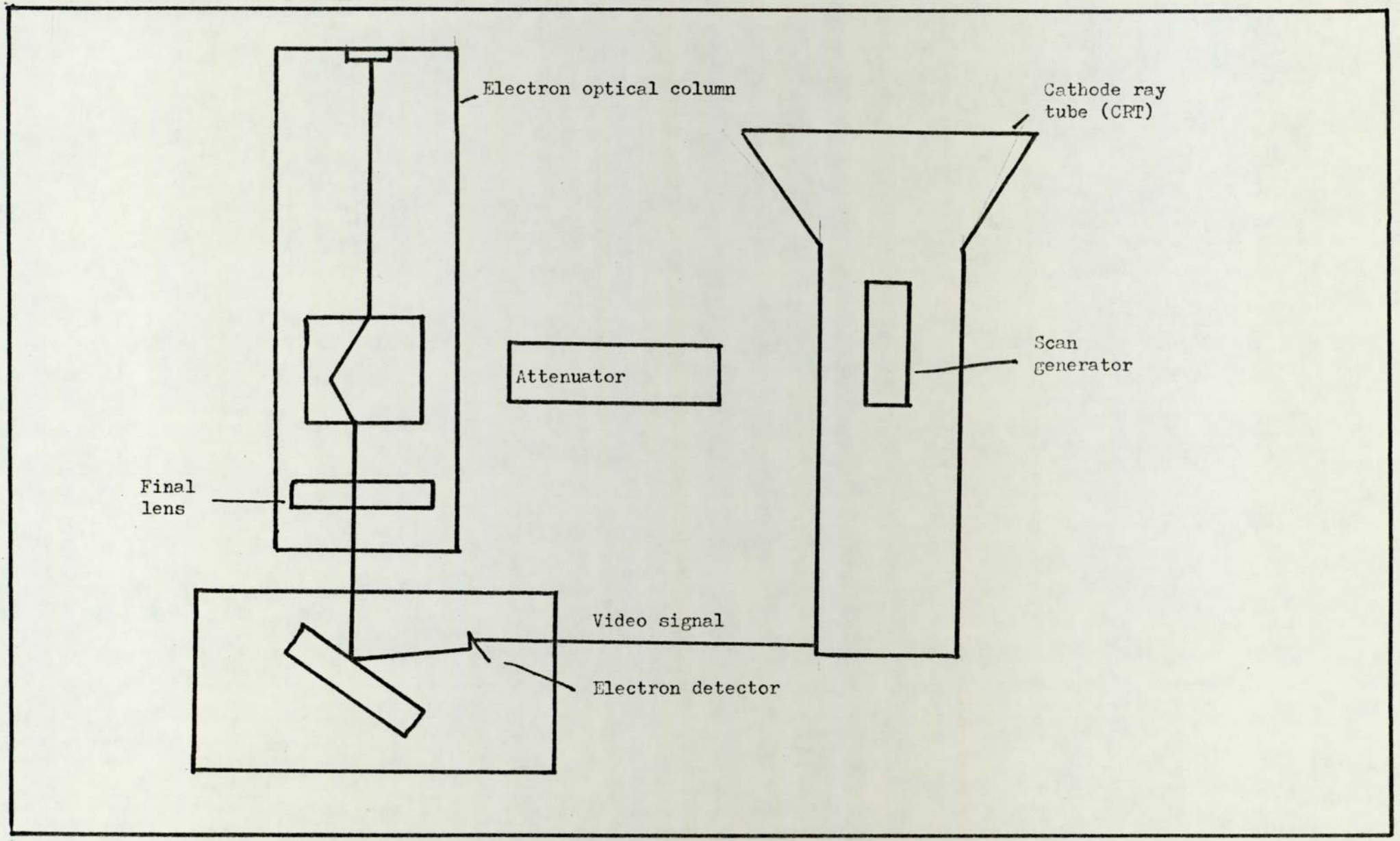
Electron optical column
Cathode ray tube (CRT)
Attenuator
Scan generator
Final lens
Video signal
Electron detector

Figure 15

a focus farther from the lens. This circle of least confusion has a diameter

$$d_c = \frac{\Delta V}{V} C_c \alpha \qquad \ldots\ldots 3.39$$

C_c Chromatic aberration constant.

Diffraction also contributes an airy circle of diameter

$$d_f = \frac{15}{\alpha} V^{-\frac{1}{2}} \times 10^{-8} \qquad \ldots\ldots 3.40$$

The total beam diameter d is usually estimated by adding in quadratu e the various components

$$d^2 = d_o^2 + d_s^2 + d_c^2 + d_f^2 \qquad \ldots\ldots 3.41$$

For a transmission electron microscope (TEM) operating at V = 100 Kv and $\Delta v \approx 1v$ he aberrations are small, and the typical resolving power works out to be in the region of 0.7 nm. This has also been achieved for special SEM. The reason why commercial available SEM machines are so much worse is that commercial SEM machines are made primarily to examine surfaces of bulk specimens by collecting the low-energy (about 4 eV) secondary electrons from the specimen surface, and this requires that the specimen surface be outside the magnetic field of the final lens (otherwise, the low energy electrons are trapped in the flux). This restriction increases the focal length, with a resultant increase in d.

The second reason is that the terms involving d_o are more important in SEM than in TEM.

The third reason is, in examining a bulk specimen, penetration of the electron is restricted. In order to achieve this, the accelerating voltage is kept low (values of 10 to 20 kV are typical

for an SEM). Unfortunately, lowering the value of $\forall$ will increase the values of d_s, d_c and d_f.

3.3.4 Contrast Formation

The advantage of SEM (over TEM) is the wide variety of contrast mechanisms. This advantage arises from the fact that the focussing operation and the contrast formation are now separated. The information used to build up the image need not be focused. Any measurable interaction can be used to build up a picture of the specimen. The interpretation depends on the interaction used to form the image. For example measurable X-rays, which cannot be focused, can be used to build up a picture of the elemental content of the specimen surface. Another mode of operation is the secondary electron collection to generate the video signal. The pictures obtained give a most realistic presentation of the geometry of the specimen surface.

3.4 Ion Bombardment

The study of the interaction of ions with surfaces has a long history, but with the introduction of ultra-high-vacuum techniques the whole field of surface investigation, including particle interactions with surfaces really started, and in the past decade a vast improvement in our understanding has resulted. Almen and Bruce [152] laid the foundation of the experimental data on sputtering which are still unchallenged but a detailed understanding of the sputtering process still remains to be explored. Recently a very good review by McCracken [153] has appeared on the behaviour of surfaces under ion bombardment.

3.4.1 Types of interaction

When an ion first interacts with the surface the incident ion

will transfer energy to the solid. Lindhard and Scharff [154] divided the process into two parts, electronic collisions and nuclear collisions. The first process is the interaction of the fast ion with the lattice electrons resulting in excitation and ionization, and it is almost entirely inelastic. As the density of electrons is high the collisions are so numerous that the process can normally be regarded as one of continuous energy loss. This process has been described in detail by (Whaling, Lindhard and Scharff [154]). The second process by which an ion loss energy is by nuclear loss. This results from collisions between the incident ion and the lattice atoms. It can normally be considered to be described by a two-body collision in which the normal laws of conservation of energy and momentum applies. At high energies they can be accurately described by Rutherford scattering and at medium energies by screened Coulomb scattering.

The interactions with electrons lead to secondary electron emission, emission of characteristic X-rays, and optical photon emission. Interactions with the lattice lead to displacement of lattice atoms, formation of point defects, and, in cases where the energy is transferred back to the surface, erosion of the target by sputtering.

The interaction of the incident ion with electrons can be thought of in terms of overlapping of electron shells. It causes direct excitation of electrons in both the incident and the target atoms.

CHAPTER 4

EXPERIMENTAL PROCEDURE AND EQUIPMENT

4.1 Preparation of aluminium sheets for ellipsometric experiments

Two groups of aluminium samples of different purity (99.3% and 99.99%) were prepared. First, half of the samples from each group were given heat treatment at 300°C for 10 minutes and the rest of the samples were given heat treatment at 200°C for 10 minutes. These two different heat treatments gave different degrees of crystalisation. The samples were then cooled in air.

All the samples were chemically polished by Phosbrite for 25 seconds at 100°C and cleaned in (HNO_3) nitric acid followed by distilled water. A hydroxide film was grown on these samples by placing them vertically in a humidity chamber at 70°C at 100% humidity. At fixed times the samples were taken out of the humidity chamber and the ellipsometer readings taken at a wavelength λ 540 nm. After the readings were taken the samples were returned to the humidity chamber.

4.2 Preparation of aluminium hydroxide films on glass substrate

Glass substrate which were cut from microscope slides were cleaned by immersing in 3% detergent solution in an ultrasonic bath, followed by repeated cleaning in distilled water in an ultrasonic bath. Finally the substrates were boiled in isopropyl alcohol and dried by withdrawing through the vapour.

Aluminium films were deposited onto glass substrates under high vacuum and ultra-high vacuum conditions, 10^{-6} torr and 10^{-9} torr respectively. The thickness of each film was measured by interferometry (Tolansky) after which the film was placed in the

humidity chamber and the time noted down. The film was examined after every 15 min. and after a certain length of time the film became transparent and again the time was noted.

The precise time when the film became transparent was important, so the technique was refined. An apparatus was arranged as shown in Figure 16. The aluminium film was placed between the light source and the photodiode. The time was noted and the chart recorder started. When all the aluminium had been reacted to become aluminium hydroxide, the film became transparent and a higher voltage reading was recorded on the chart recorder; the time was also noted down. This was repeated with films of different thickness and the results plotted.

4.3 Preparation of hydroxide films on gold films substrate

4.3.1 Principle of the method and sample preparation

(1) A thick film of a non reactive metal such as gold is deposited on a glass substrate and the surface is characterised ellipsometrically by the angles Ψ and Δ determined from the instrument extinction settings. In turn the optical constants can be computed from equation.

A film of aluminium is then superimposed on the gold film. The thickness of aluminium can be determined by an interference method by Tolansky [155] with fringes of equal chromatic order using an interference microscope.

(2) The aluminium films are then exposed to the water vapour environment sufficiently long for all the aluminium to react to form aluminium hydroxide. This state is easily detected since the hydroxide film is non absorbing.

(3) The changes in Ψ and Δ . ($\delta\Psi$ and $\delta\Delta$) from the gold surface due to the presence of the hydroxide film are measured.

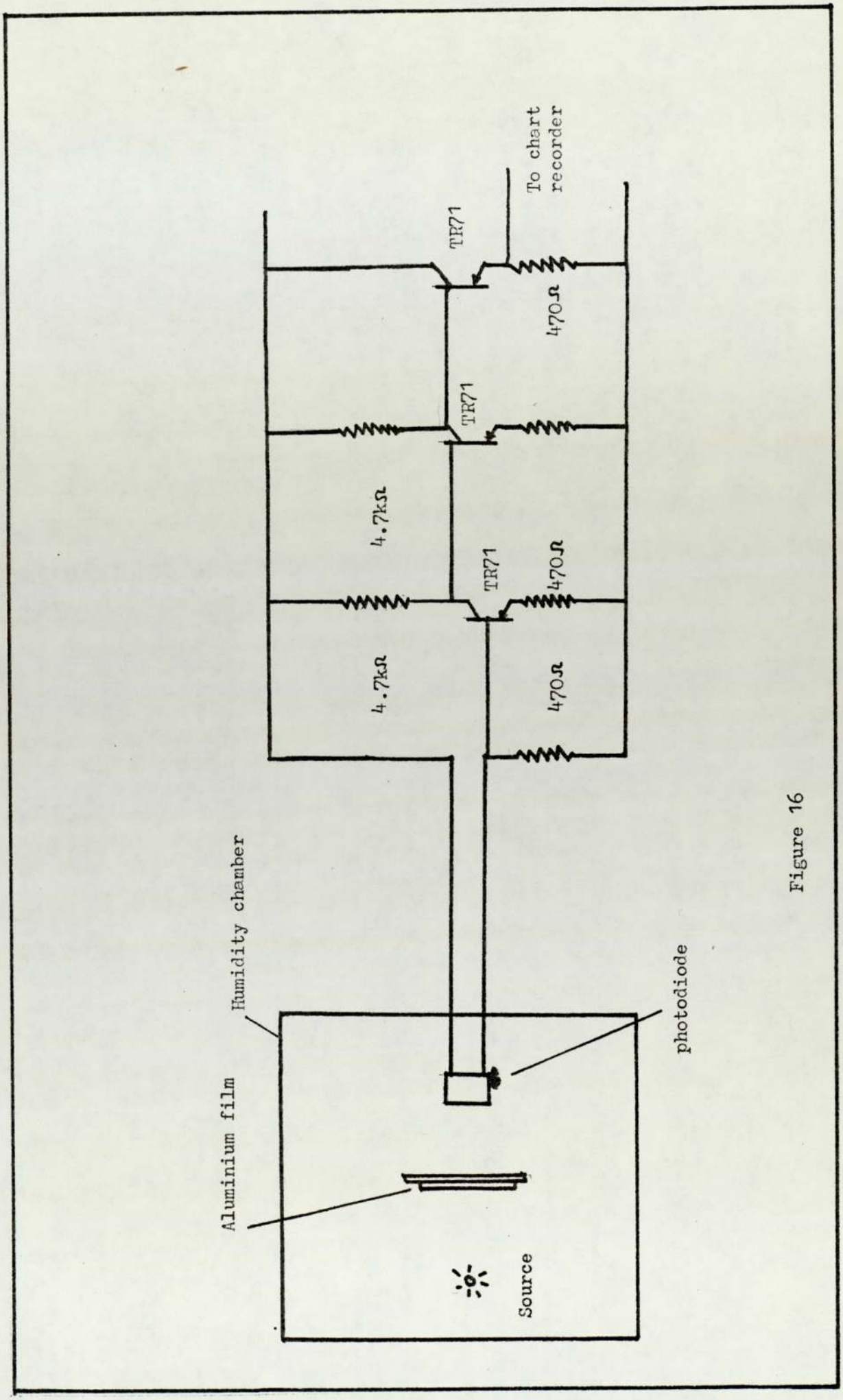
To chart recorder
TR71
470Ω
TR71
4.7kΩ
TR71
470Ω
4.7kΩ
470Ω
Humidity chamber
Aluminium film
photodiode
Source

Figure 16

(4) The hydroxide film is then overlaid by a highly reflecting film of aluminium and the hydroxide thickness determined by the interference microscope.

4.3.2 Experimental Procedure

Glass substrates which were cut from microscope slides were cleaned by immersing in 3% detergent solution in an ultrasonic bath, followed by repeated cleaning in distilled water in an ultrasonic bath. Finally the substrates were boiled in isopropyl alcohol and dried by withdrawing through the vapour. They were then mounted in a vacuum system above a tungsten boat from which gold was evaporated at a base pressure of 5×10^{-7} torr. After evaporation the gold films were removed from the vacuum chamber and annealed at 100°C for 2 hours before ellipsometric readings were taken.

The gold films were replaced in the vacuum system and aluminium films of various thicknesses were evaporated from a tungsten filament. During evaporation it was possible to hold the pressure to 2×10^{-6} torr. For each set of readings two aluminium films of equal thickness were evaporated simultaneously. One was used for ellipsometric tests and the other for thickness measurements. Figure 17 shows cross-sections through the substrates and film system. Figure 17a represents the arrangement used for the measurement of optical properties of gold. Figure 17b shows the system which was used for the measurement of optical properties of aluminium. Figure 17c shows the system which was used for thickness measurement of aluminium films. The specimen for ellipsometric test was placed vertically in a humidity chamber at 70°C and 100% relative humidity. After the reaction was completed an aluminium hydroxide film was formed on the gold film, as shown in Figure 17d. Figure 17f shows the system which was used for the measurement of

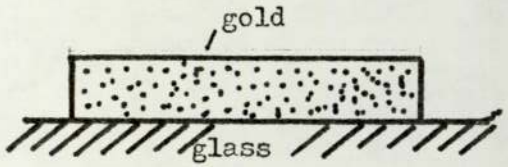

(a) For measurement of optical properties of gold

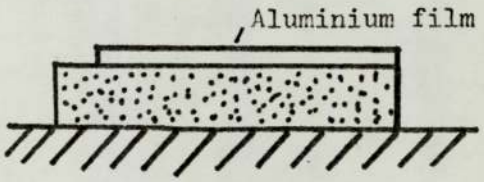

(b) For measurement of optical properties of Aluminium

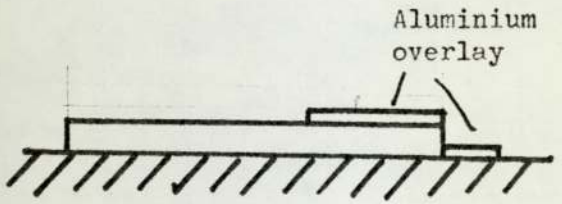

(c) For measurement of Aluminium film thickness

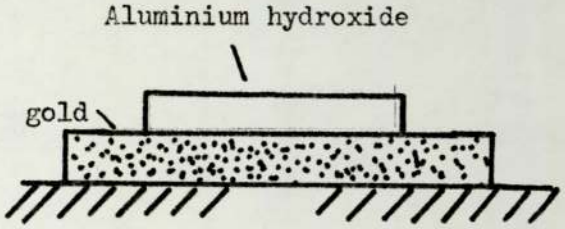

(d) For measurement of optical properties of Aluminium hydroxide

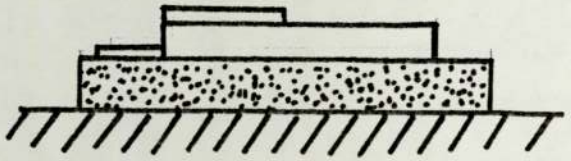

(e) For measurement of Aluminium hydroxide film thickness

Figure 17. Section through film specimens

aluminium hydroxide film thickness.

Details of the type of ellipsometer (with compensator) used in these investigations have been given in 4.72 . A selection from the 32 possible settings was made in the manner described by McCrackin [149] . Ellipsometric readings were made before and after placing the specimens in the humidity chamber. A few sterioscan photographs were also taken to determine the structure of the hydroxide films. The gold films, the aluminium overlay films and the hydroxide films were examined using a step scan X-ray diffractometer.

4.4 Ellipsometry experimental procedure (vacuum)

The aluminium films were prepared by evaporation on to an aluminium sheet substrate from a tungsten wire (0.5mm diameter). The aluminium sheet was mounted onto a sample holder shown in Figure 18, the sample holder was electrically isolated from the vacuum chamber by ceramic. The filament and sample material were first degassed by pre-heating and successively evaporating several small portions of the metal onto the shutter, before preparing films for detailed examination.

The base pressure was 10^{-9} torr but during evaporation, which was carried out in a vacuum chamber as shown in Figure 19 the pressure rose to 2×10^{-8} torr and immediately fell after evaporation to less than 3×10^{-9} torr. The aluminium used for evaporation had bulk impurities, specified at less than 200 ppm.

Pure aluminium foil samples taken from scalped aluminium ingot which had been homogenised and first hot and then cold-rolled to sheet thickness of 0.5 mm were also examined. Some of the aluminium sheet samples were heat treated at $310^{\circ}C$ for 15 minutes and mounted onto the sample holder shown in Figure 19. The sample holder was

attached to a rotary drive. All aluminium sheet samples had protective oxide films. The protective oxide films were removed by Argon ion bombardment using ion tech B10 ion gun Figure 20.

At a pressure of 10^{-6} torr an adsorbed monolayer can form in 1 second assuming the sticking coefficient is one. Therefore in order to study controlled growth of oxide and hydroxide films, one should have base vacuum pressure of the order of 10^{-9} torr. This pressure requirement could be achieved in the vacuum system shown in Figure 19.

Deliberate oxidation of the sample, for experimental requirement, was achieved by exposing the films to oxygen or water vapour at pressure between 10^{-3} torr to 10^{-4} torr within the vacuum chamber. Water was degassed by pumping it continuously in a vacuum of 10^{-3} torr for several hours. The gases were leaked into the vacuum chamber by a non-bakeable valve.

4.5 ESCA experimental procedure

The aluminium films were prepared by evaporation on to a polished Ni substrate from a tungsten wire (0.5 mm diameter). No trace of the wire or substrate material was found in any of the recorded spectra. The filament and sample were first degassed by pre-heating and successively evaporating several small portions of the metal before preparing films for detailed study. For a monatomic gas striking a typical metal surface, with a sticking coefficient of 1.0, the time for formation of an adsorbed monolayer is approximately 1 sec at 10^{-6} torr or 1000 sec at 10^{-9} torr. The ESCA method require measurement times typically of the order of 300 sec for examination of position and shape of a given feature in a spectrum, thus a vacuum at least as good as 10^{-9} torr is required. During the evaporation, which was carried out in sample

Figure 18. Sample holder, electrically isolated from the vacuum chamber by a ceramic joint.

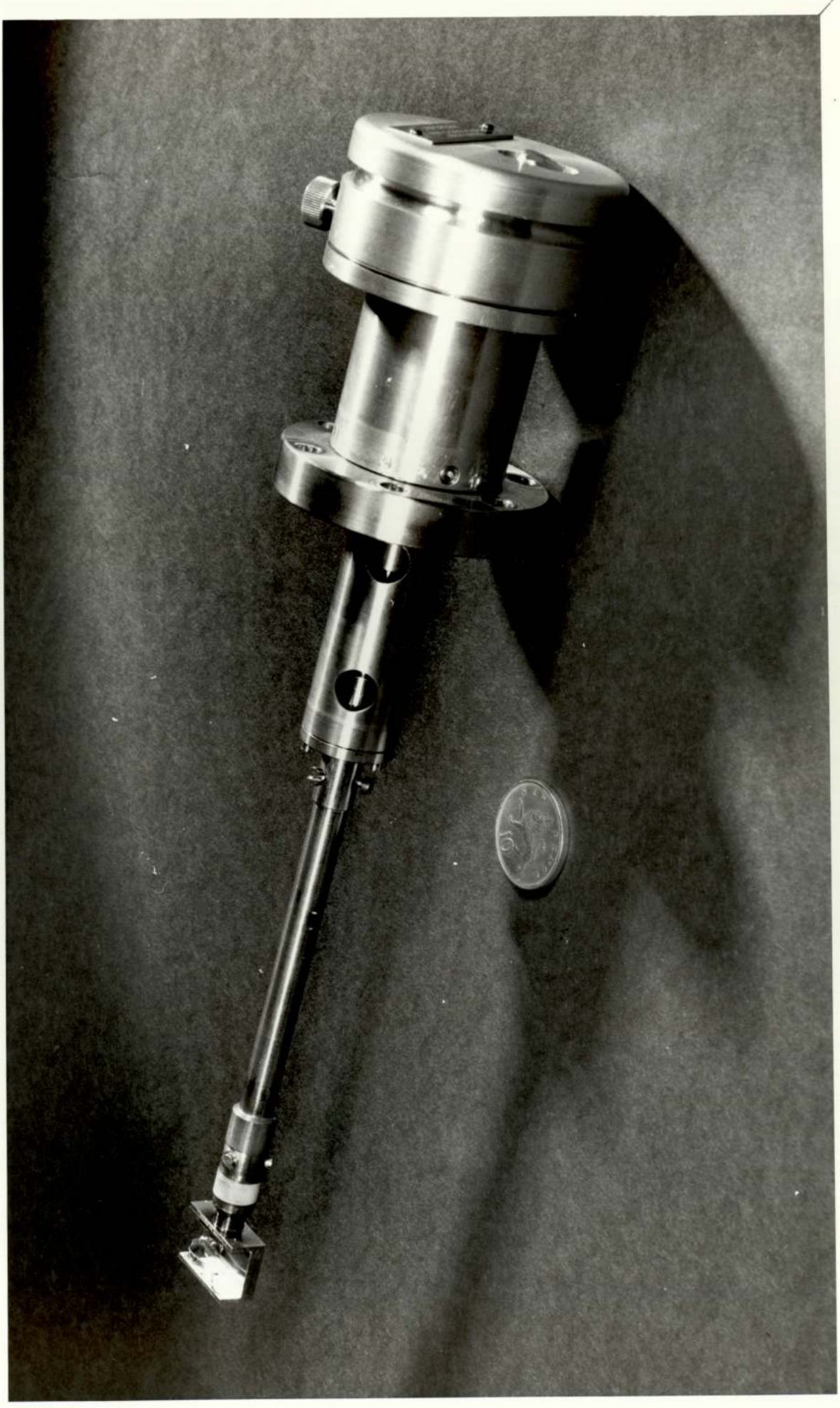

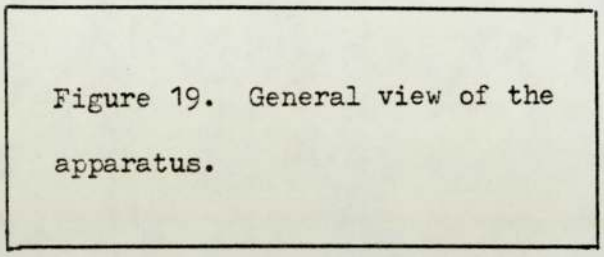

Figure 19. General view of the apparatus.

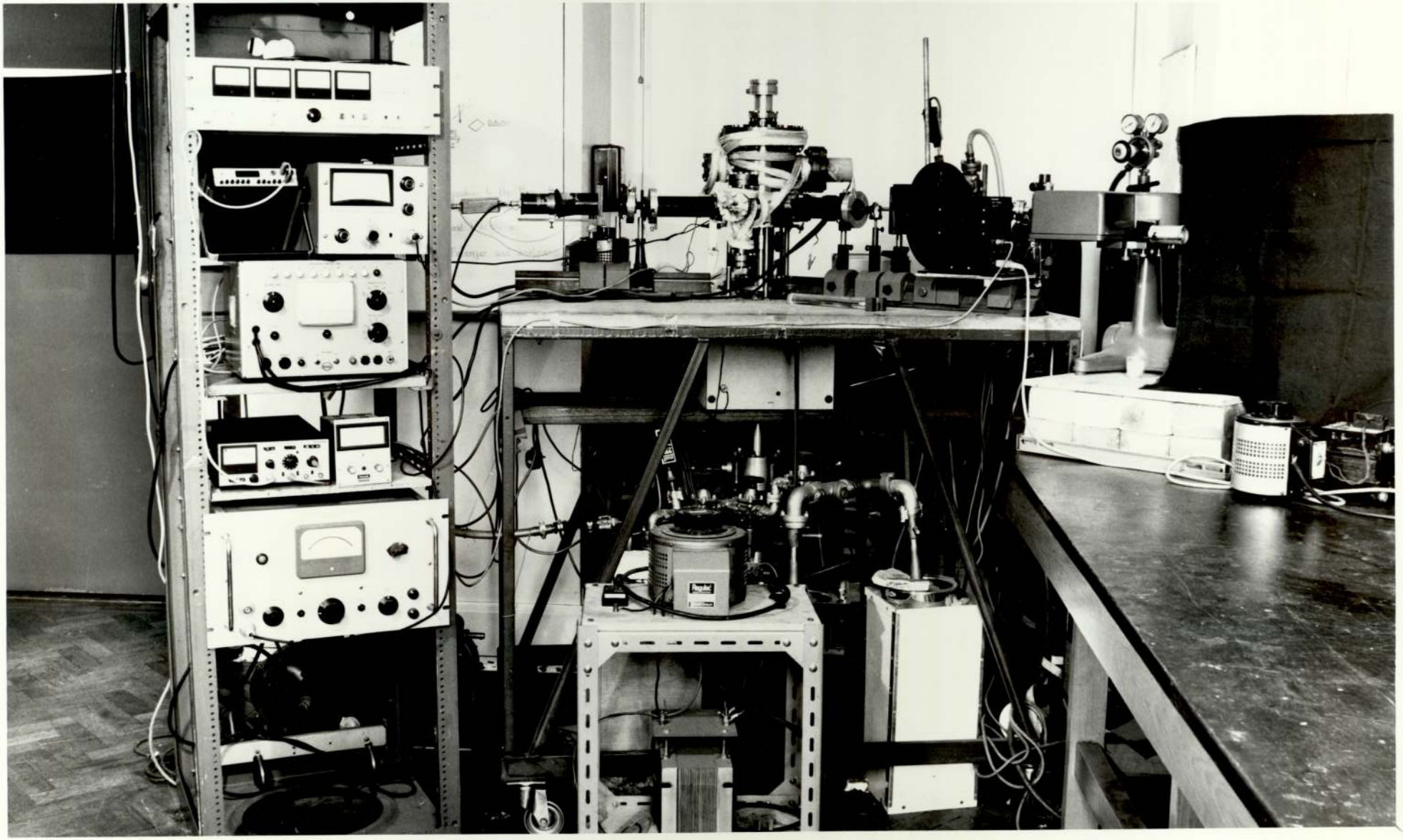

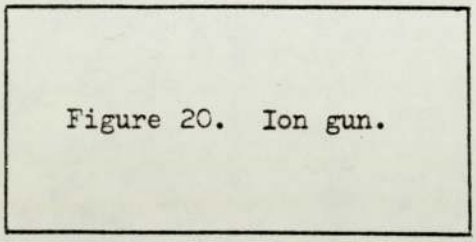

Figure 20. Ion gun.

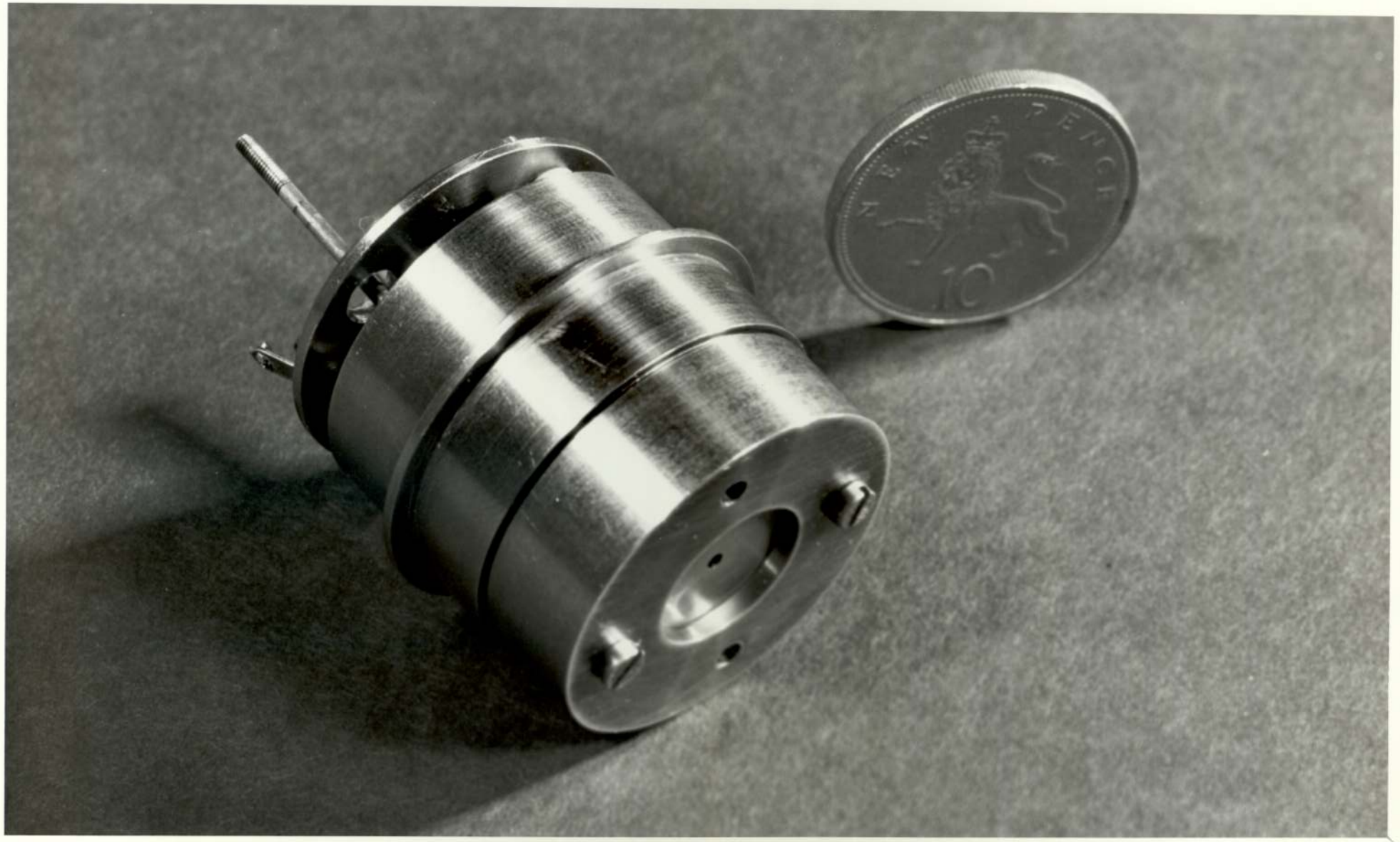
10

preparation chamber of a Vacuum Generators ESCA3 electron spectrometer (Figure 21) the pressure rose to 10^{-8} torr but fell immediately after evaporation to less than 10^{-9} torr. After preparation the sample was transferred under the same vacuum to the analyser chamber, where a pressure of less than 6×10^{-10} torr was maintained. The metals used for evaporation had bulk impurities specified less than 200 ppm. No metallic impurities were seen in the evaporated films in spite of the great sensitivity of ESCA to such contaminants. No surface carbon was detected either, though 10^{14} atoms Ccm^{-2} would have been observable. Oxygen contamination, which was detectable, was very small at the start of a run.

For experimental requirements deliberate oxidation of the sample was achieved by exposing the films to oxygen, or water vapour, at pressures between 10^{-7} and 10^{-4} torr, within the sample preparation chamber. The oxygen was dried by means of a liquid nitrogen cold trap; water was degassed by pumping it continuously, in a vacuum of 10^{-4} torr, for several hours. The purified gases were leaked into the preparation chamber via a non-bakeable valve. When connected to this valve the sample preparation chamber could maintain a vacuum below 2×10^{-9} torr.

Pure aluminium samples taken from scalped aluminium ingot which had been homogenised and first hot and then cold-rolled to sheet thickness of 0.5 mm were also examined. Together with pure aluminium foil, taken from the same sheets as above, heat treated at 310°C for 15 mm and samples which have had their oxide removed by electro-polishing and then stored in a dessicator for 5 days.

All the aluminium foil samples had aluminium oxide films present. In order to study controlled growth of oxide and hydroxide films on aluminium foil the protective oxides have to be removed.

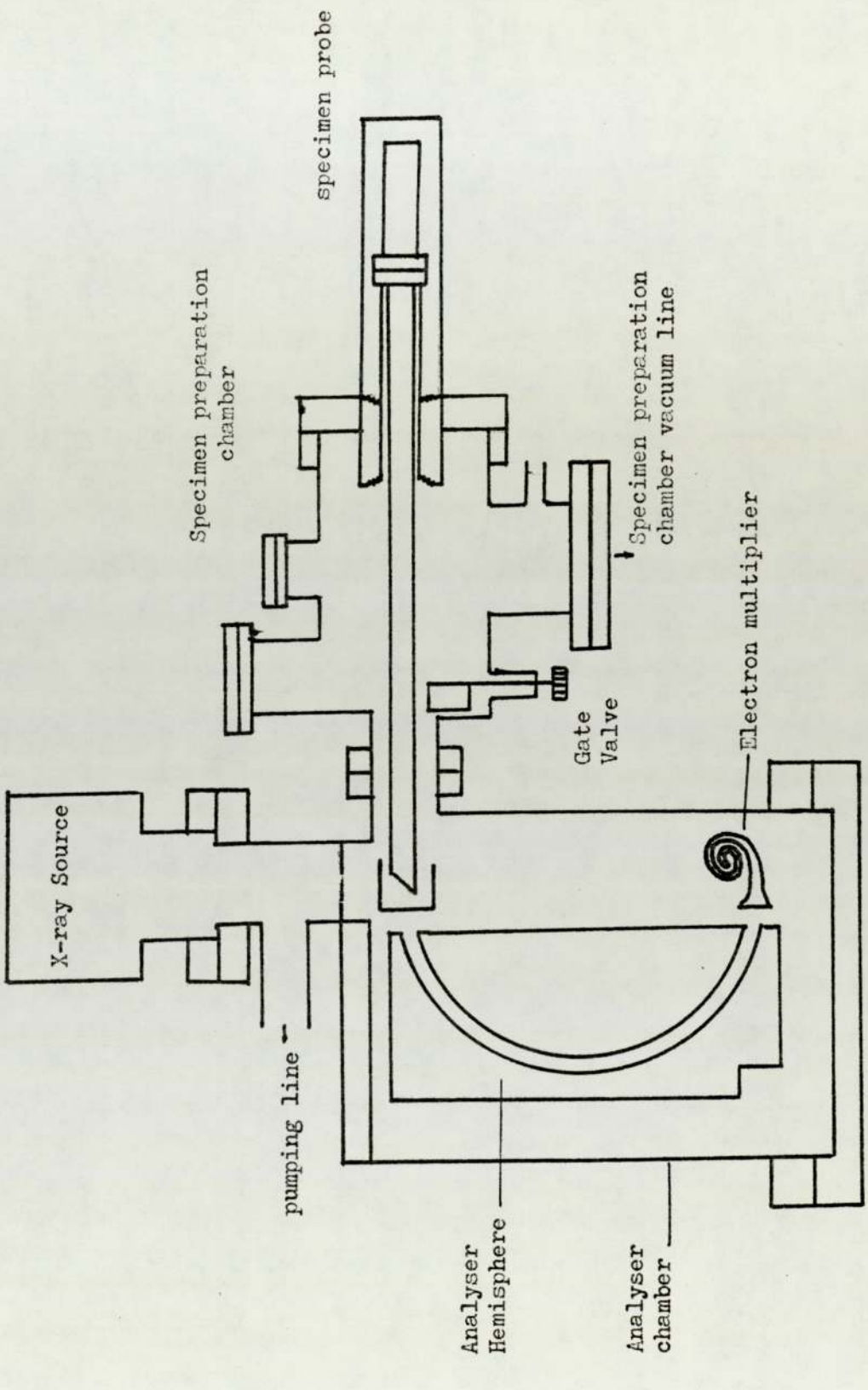

Figure 21: ESCA 3 Analyser - General arrangement

The protective oxide films were removed by Argon ion bombardment in the sample preparation chamber of the ESCA spectrometer.

4.6 Microscopy - experimental procedure

Super-pure base aluminium (99.99%) was used for alloy preparation.

The scalped ingots were homogenised and first hot and then cold rolled to sheet thickness of 0.5 mm Aluminium sheets were annealed at 310°C for 15 min. After heat treatment the sheets were allowed to cool, to room temperature. Aluminium alloy sheets were heat treated at 350°C, 450°C and 550°C for 30 min and cold water quenched

3 mm disc samples were punched out from the sheets. The samples were then electropolished with fresh polishing solution, to render them suitable for electron microscopy. Each sample was checked, by an optical microscope for cleanliness. The samples were stored in a dessicater to be freed from water vapour.

Disc samples were exposed to water vapour at 70°C and 100% relative humidity for different lengths of time. The samples were Then examined in the electron microscope JEOL 100C TEMSCAN.

4.7 Ellipsometer vacuum system

The vacuum system was a conventional one as used by Fane and Neal [156] and is shown in Figure 22a. The stainless steel experimental chamber was pumped by a four-stage diffusion pump charged with DC. 705 oil. This pump was backed through a liquid nitrogen trap by a 42.1 min^{-1} rotary pump. A water-cooled baffle and two liquid nitrogen traps separated the chamber from the pumps, the upper one being positioned so that it could be baked with a heating tape to 250°C. Aluminium wire seals (0.625 mm diam) were used between the chamber and the cold traps, and indium wire seals between the traps and the diffusion pump where the system is

not subject to baking. A plan view of the experimental chamber is shown in Figure 22b along with the optical arrangement and the B10 Ion Tech ion gun, shown in Figure 21.

All flanges used copper gasket seals. A pressure of 10^{-9} torr could be obtained after 24 hours of pumping.

4.7.1 The Ellipsometer

The ellipsometer itself consisted of two triangular section optical benches bolted to fixed plates on the vacuum bench. The light source was a 24 volt, 150 watt tungsten filament projector lamp, operated from a 13 volt transformer. This lamp provided adequate intensity in the visible and near infra-red regions. A lens (L) in Figure 22b is placed such that it produces parallel light which passes through a monochromator. A condenser lens 22 focuses the light on a pin-hole which is arranged to be at the focus of the lens 22, this produces parallel light, which passes through an aperture, to produce the desired size of the beam, and finally through optically flat kodial glass windows. After falling on the specimen film at an angle of approximately 64 degrees, the light was reflected out of the chamber, through the compensator and analyser polaroids to the photomultiplier detector.

4.7.2 Form of Ellipsometer used at 546 nm - The Quarter wave plate

The method of compensation used is that due to Winterbottom[18] and is fully described in section 3.2.1. The polariser and analyser consist of HN22 polaroid in graduated circular vernier scales. These were supplied by the Precision Tool and Instrument Company, and are accurate to within $\pm$ 2 minutes of angle. The quarter wave plate is part of a senarmont compensator and is made of mica sheet also mounted in a circular scale. Essentially quarter wave plates can be constructed of any birefringent material for which the refractive

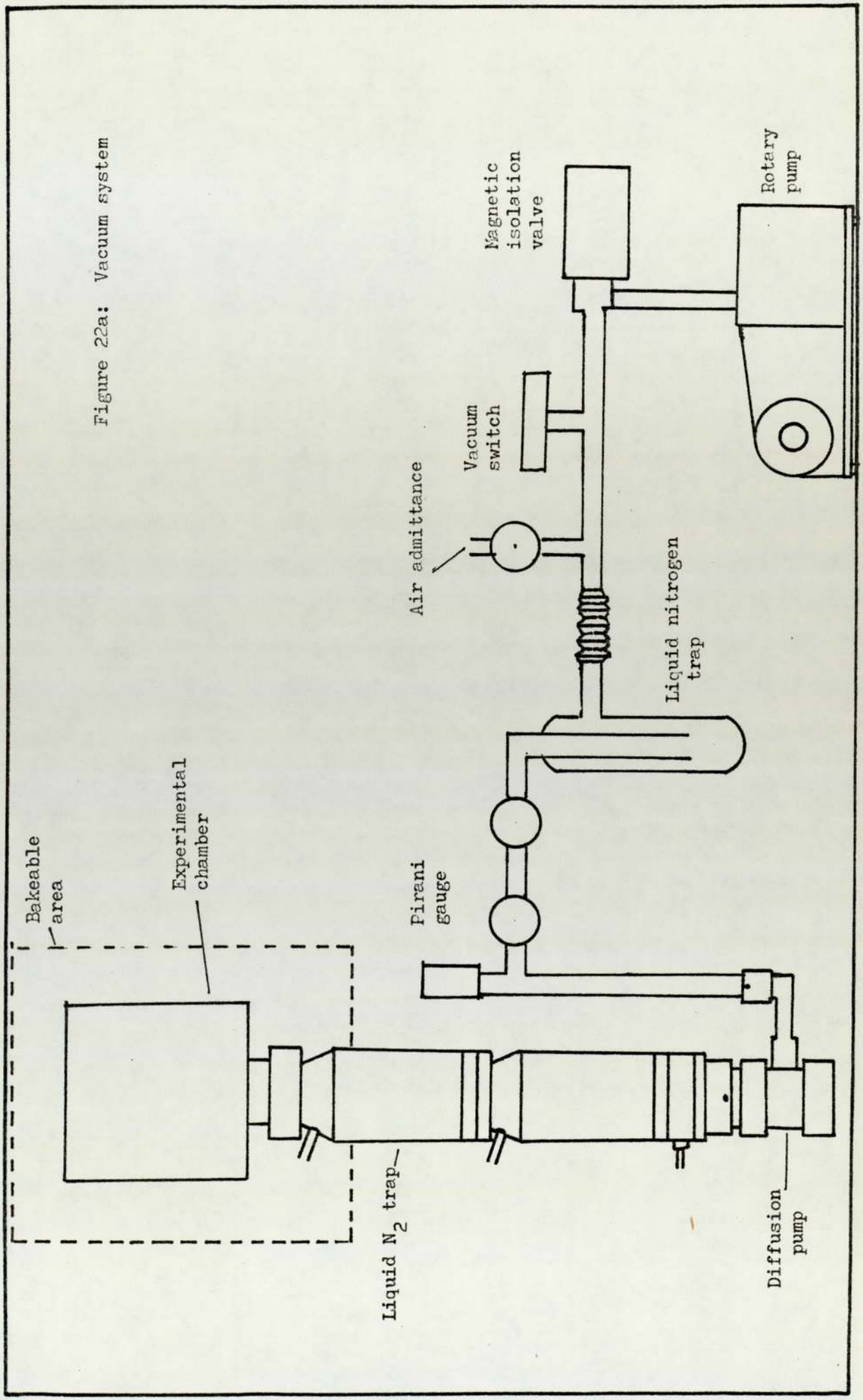

Figure 22a: Vacuum system

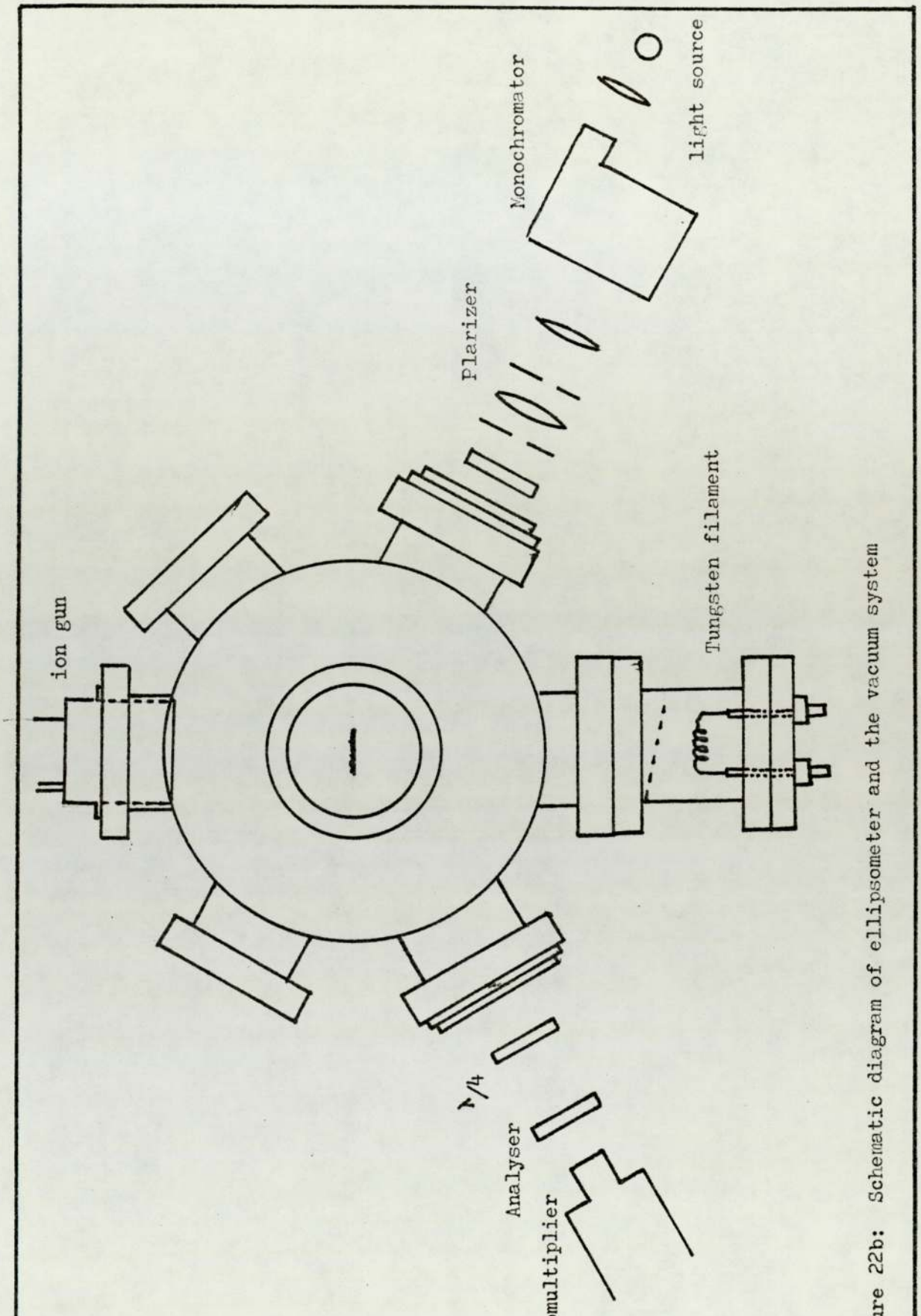

Figure 22b: Schematic diagram of ellipsometer and the vacuum system

indices for the ordinary and extraordinary rays differ. Representing these indices by N_o and n_e respectively, the phase difference between these two rays after passing through the plate will be given by

$$\delta = \frac{2\pi}{\lambda}(N_e - N_o)k \qquad \ldots\ldots 4.1$$

where k is the thickness of the plate. For an exact quarter wave plate δ equals $\frac{\pi}{2}$ and is determined solely by k. The actual thickness of mica required is only 0.000135 mm so that absolutely exact quarter wave plates are difficult to achieve. It is therefore necessary to calibrate them to ensure that the actual phase difference falls within the required limits. In the present work calibration was carried out using the method of Jarrard [156]. Briefly this method requires elliptically polarised light to be passed through the compensator, C and the analyser A. Extinction of the light is achieved for compensator and analyser positions represented by C and A respectively. Compensator and analyser are then moved, first together, and then independently to a new extinction position represented by C_2 and A_2 respectively. As shown by Jarrard the phase difference introduced by the compensator is then given by

$$\cos\delta = \frac{\tan(A_1 - A_2)}{\tan(C_1 - C_2)} \qquad \ldots\ldots 4.2$$

The results obtained for various wavelengths are shown in Figure 22c 24.

The error imparted to the analyser setting if a non-exact quarter wave plate is used is discussed by Seward [159] who shows that if the quarter wave plate is in error by an amount ε (i.e. $\delta = \frac{\pi}{2} \pm \varepsilon$) and if it is used to compensate an ellipticity , then the error in analyser setting, $d\Delta$ is given by

$$\tan 2\alpha\delta = \frac{\varepsilon^2 \sin^2\gamma \cos^2\gamma}{2 - \varepsilon^2 \sin^2 2\gamma} \qquad \ldots\ldots 4.3$$

For the values of ellipticity that occur in the present experiments (typically 70°) calculations show that an error of 2 degrees in the quarter wave plate would lead to an analyser error of less than 1 minute of angle. It may be concluded from Figure 22c therefore, that the quarter wave plate is acceptable over the wavelength range 530 nm to 590 nm. Accordingly a wavelength of 546 nm was chosen for the experiments.

4.8 Procedure for determination of Ψ and Δ for a specimen using the Compensator Method

The essential basis of the method, as explained in section 3.2.1 is that the azimuth of the plane polarised light incident on the specimen is arranged so that the reflected light has equal components in the (p) and (s) direction. (The reflected amplitude ratio $\frac{E_p}{E_s} = 1.0$). Because of the phase difference, Δ between these components, the reflected light will always be elliptically polarised with its major axis at 45° to the plane of incidence, and have an ellipticity that depends on Δ . If the compensator is set with its axes at 45 degrees to a reference position this ensures that the axes of the compensator coincide with the axis of the reflected ellipse. Light of any ellipticity is then compensated, i.e. converted to plane polarised light have an azimuth that depends on the ellipticity, and hence on Δ . The procedure, then, is as follows.

The compensator is locked at 45 degrees to a reference position. As before, the polariser and analyser are successively turned to give minimum light intensity. The polariser extinction position, say P, is then found by "bracketing" the minimum position with the polariser then set at its extinction position, the analyser extinction position, say A, is likewise found be "bracketing". The

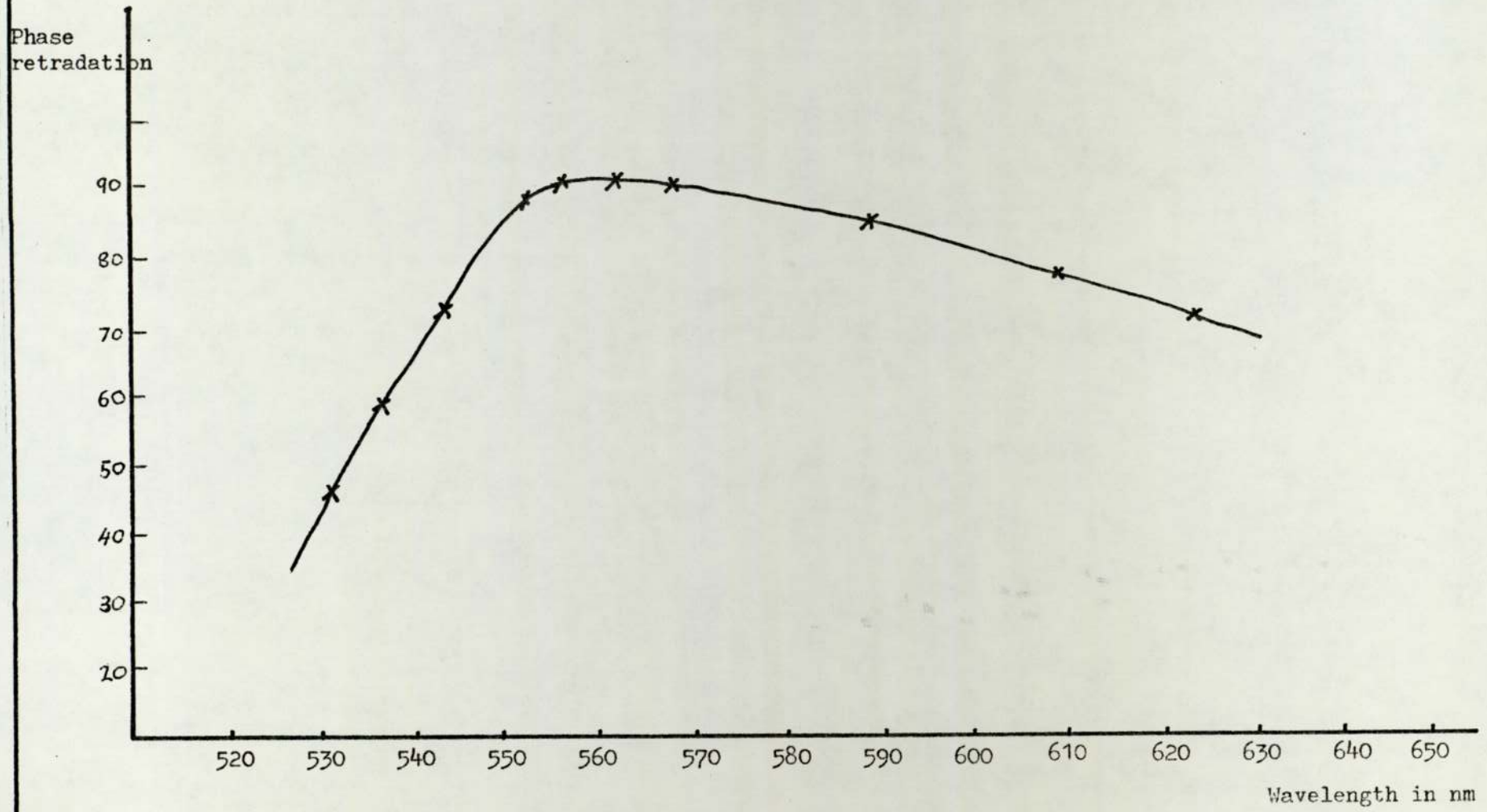
Phase
retradation
90
80
70
60
50
40
30
20
520
530
540
550
560
570
580
590
600
610
620
630
640
650
Wavelength in nm

Figure 22c.

setting procedure is repeated for a polariser azimuth in another quadrant but not 180 degrees away, giving readings P_2 and A_2 on polariser and analyser respectively. Two other polariser positions, P_3 and P_4, together with their corresponding analyser positions A_3 and A_4 are also measured. It is found that P_3 and P_4 are at approximately 180 degrees to P_1 and P_2 respectively. A_3 and A_4 are also at 180 degrees to A_1 and A_2 respectively.

The compensator is then turned through 90 degrees so that the fast axis azimuth is -45 degrees, with respect to the plane of incidence, and four different pairs of polariser and analyser settings obtained in the same way. As explained in Section (3.1.4) time did not allow for measurement to be made in all four zones during some of the experiments.

Consider the polariser readings:

It has been shown in Section (3.2.1) that P_1 and P_2 are symmetrically placed about π_p - p. In general, the polariser settings are symmetrically placed about the plane of incidence. $P_1 - \pi_p$ should equal $\pi_p - P_2$. In general, the average is taken

$$\frac{(P_1 - \pi p) + (\pi_p - P_2)}{2} = \Psi \qquad \ldots\ldots 4.4$$

$\mathrm{Tan}\Psi$ equals the relative amplitude reduction between the (p) and (s) components produced by reflection from the specimen.

Consider the analyser readings:

As shown in Section (2.3), A_1 and A_2 are always separated by approximately 90 degrees. $\alpha_s - A_1$ should equal $\alpha_p - A_2$. In general the average is taken

$$\frac{(\alpha_s - A_1) + (\alpha_p - A_2)}{2} = x \qquad \ldots\ldots 4.5$$

where the angle 2x - 90 degrees gives the relative phase retardation,

Δ between the (p) and (s) components.

4.9 ESCA Apparatus

The vacuum system is shown in Figure 20. The stainless steel preparation and experimental chambers were pumped by separate diffusion pumps Edwards Model E04 charged with Santovac 5 oil (polyphenyl ether). The diffusion pumps were separated from the preparation and experimental chambers by liquid nitrogen traps. The diffusion pumps were backed by rotary pumps.

The X-ray source was pumped by a Ferranti model FJ08 diode ion pump. Both preparation and experimental chambers could be backed. After backing and with the liquid nitrogen traps filled pressures of 10^{-10} torr in the experimental and 10^{-9} torr in the preparation chamber could be obtained. For experimental requirements, deliberate oxidation of the sample was achieved by exposing the films to oxygen, or water vapour, at pressures between 10^{-7} and 10^{-4} torr, within the sample preparation chamber. Oxygen was admitted into the preparation chamber through vacuum generators model GH7 viton sealed valve. A sample could be transferred to the experimental chamber under the same vacuum where it was irradiated with X-rays with the result that electrons are emitted from atoms in the surface layer. Electron energies are characteristic of the atoms from which they have been emitted. The emitted electrons are analysed in the spectrometer and passed through the channel electron multiplier B419AL. The final result is displayed by Bryans 26000 series X-Y recorder.

In order to analyse the sample under the top film and also to study controlled growth of oxide and hydroxide films on films on aluminium foil the protective films were removed by Argon ion bombardment in the sample preparation chamber using ion tech B10 ion gun.

4.10 Electron Microscopes

Bulk samples were examined in a Comberdge steroscan. The vacuum chamber was pumped by a diffusion pump backed by a rotary pump which is separated from the diffusion pump by a liquid nitrogen trap.

The electron transparent samples were examined by JEOL 100C TEMSCAN. Therefore it was possible to study the effect of underlying microstructure on the location of reaction using combined scanning transmission electron microscopy (S.T.E.M) and scanning electron microscopy (S.E.M). The maximum voltage at which the microscope can be operated in the STEM and CTEM modes is 120k volt and 100k volt for SEM. The CTEM image is obtained directly onto the screen whereas the STEM and SEM information is processed before it is displayed on a cathode-ray scope (C.R.S).

Vacuum system is a conventional one, liquid nitrogen trap followed by diffusion pump backed by a rotary pump. A pressure of 10^{-6} torr could be obtained when the liquid nitrogen trap was filled. It was difficult to improve the vacuum because of the rubber seals used. Two samples could be mounted for examination at any one time.

To reduce contamination there was an anti-contaminant system, which was filled with liquid nitrogen thereby producing a temperature difference near the sample. Therefore the carbon contamination was deposited on the cold surface and not the sample.

CHAPTER 5

EXPERIMENTAL RESULTS AND DISCUSSION

5.1 Aluminium hydroxide on aluminium sheet: Ellipsometry Results

The changes in Δ and Ψ with time for exposure of aluminium sheet in the humidity chamber are shown in Figure 23a, b, c, d and in Table 1 and 2. Figure 23a shows the change in Δ against time of exposure at 70°C and 100% relative humidity. From Figure 23a we can see that the hydroxide growth on sample 3, which had a 99.3% purity heat treated at 300°C for 10 minutes had a higher rate of hydroxide growth than sample 4, (99.99%). Figure 23b shows the change in Ψ against time of exposure at 70°C and 100% relative humidity. From the Figure 23c we can see that the value of Ψ first increases significantly due to accumulations on the surface, which could be due to contamination or corrosion.

Figure 23c and 23d shows the change in Δ and Ψ against time of exposure at 70°C and 100% relative humidity for two samples which were first heat treated at 200°C for 10 minutes.

5.1.1 Scanning electron Microscope (SEM) Results

Aluminium sheets which had been exposed to water vapour at 70°C and 100% relative humidity were examined in the SEM. An Figures 24a, b, c and d are typical of the micrographs obtained. Figure 24a was taken from an aluminium sheet which had been cleaned with Phosbite and exposed to water vapour at 70°C for 20 minutes. Figure 24b was taken from an aluminium sheet which had been exposed to water vapour for a much longer period. Higher magnification of the pseudoboehmite island showed islands on island with bayerites included (Figure 24c). Figure 24d was taken in the SEM reflective mode of the same area as

in Figure 24c. This micrograph shows much more clearly the bayerite, growing from the substrate.

Aluminium sheet 99.99 and 99.93 percent pure heat treated 200°C and 300°C for 10 minutes Table 1.

Aluminium sheet (99.93% purity)

heat treated at 200°C — heat treated at 300°C

Sample No.4, exposure to water vapour at 70°C 100% humidity (hours)	Ψ	Δ	Sample No.3, exposure to water vapour at 70°C and 100% humidity (hours)	Ψ	Δ
0	46.95	134.70	0	46.0	133.9
0.5	46.60	134.30	0.5	47.20	133.0
1.0	46.65	133.95	1.0	47.10	132.1
3.0	46.80	133.4	3.0	46.70	130.0
6.0	46.80	132.9	6.0	46.80	127.9
9.0	46.95	132.6	11.0	47.30	126.4
12.0	46.75	132.15	14.0	47.20	125.2
15.0	46.80	131.90	17.0	47.10	124.3
18.0	46.85	131.85			

Aluminium sheet (99.99% purity)

Sample No. 1 heat treated at 200°C			Sample No. 2 heat treated at 300°C		
Exposure to water vapour at 70°C and 100% humidity (hours)	Ψ	Δ	Exposure to water vapour at 70°C and 100% humidity (hours)	Ψ	Δ
0	47.1	134.3	0	46.75	132.4
0.5	46.95	134.0	0.5	46.85	130.9
1.0	47.6	133.7	1.0	46.65	130.0
3.0	47.35	132.5	3.0	46.55	129.2
6.0	47.5	132.0	6.0	46.70	128.6
9.0	47.25	130.5	9.0	47.0	128.2
12.0	46.75	128.10	12.0	46.73	127.8
15.0	46.0	129.50	15.0	46.50	127.6
18.0	45.4	129.2	18.0	46.53	127.2

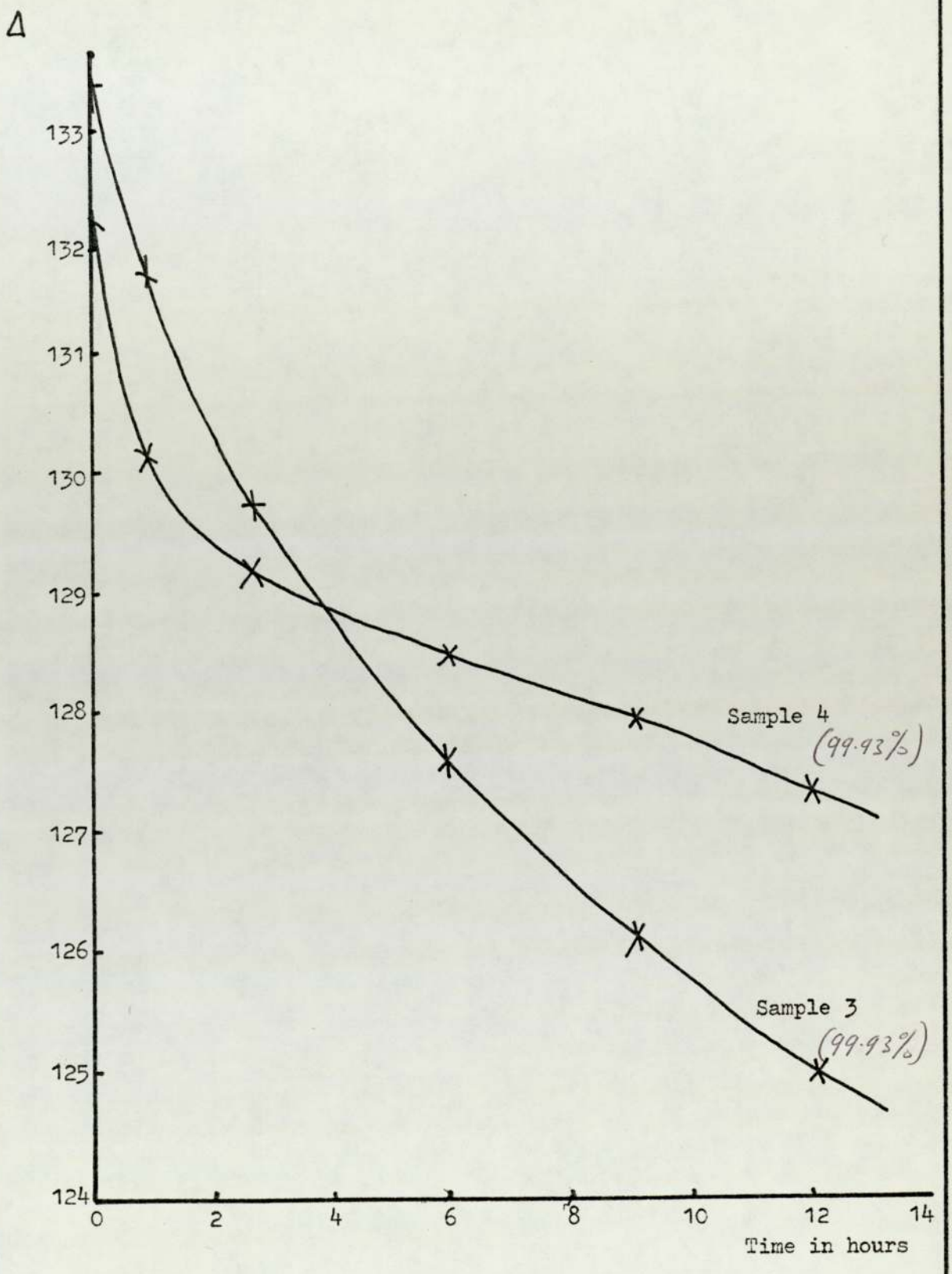

Figure 23a: The graph of Δ against time of exposure to water vapour at 70°C at 100% relative humidity

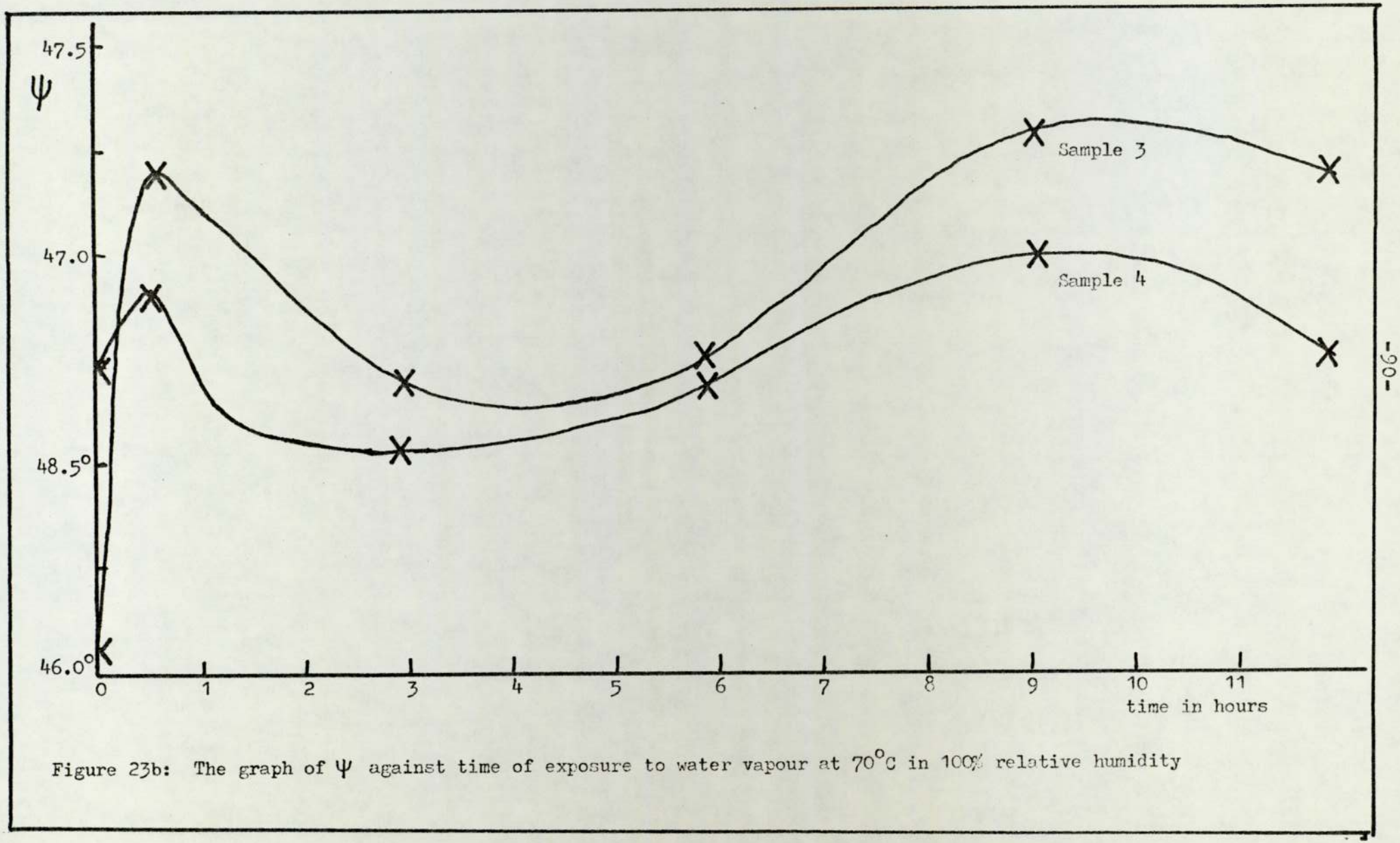

Figure 23b: The graph of Ψ against time of exposure to water vapour at 70°C in 100% relative humidity

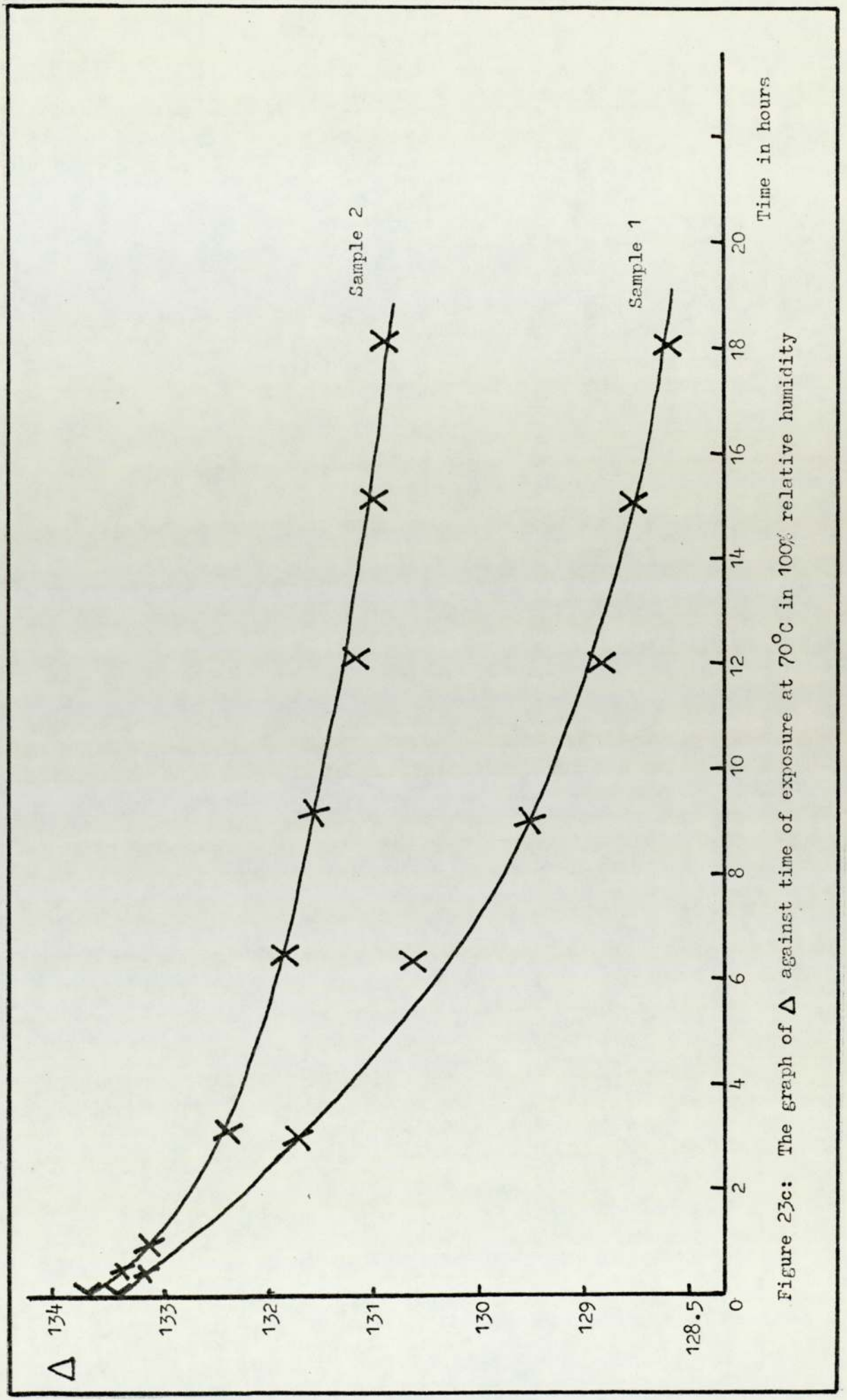

Figure 23c: The graph of Δ against time of exposure at 70°C in 100% relative humidity

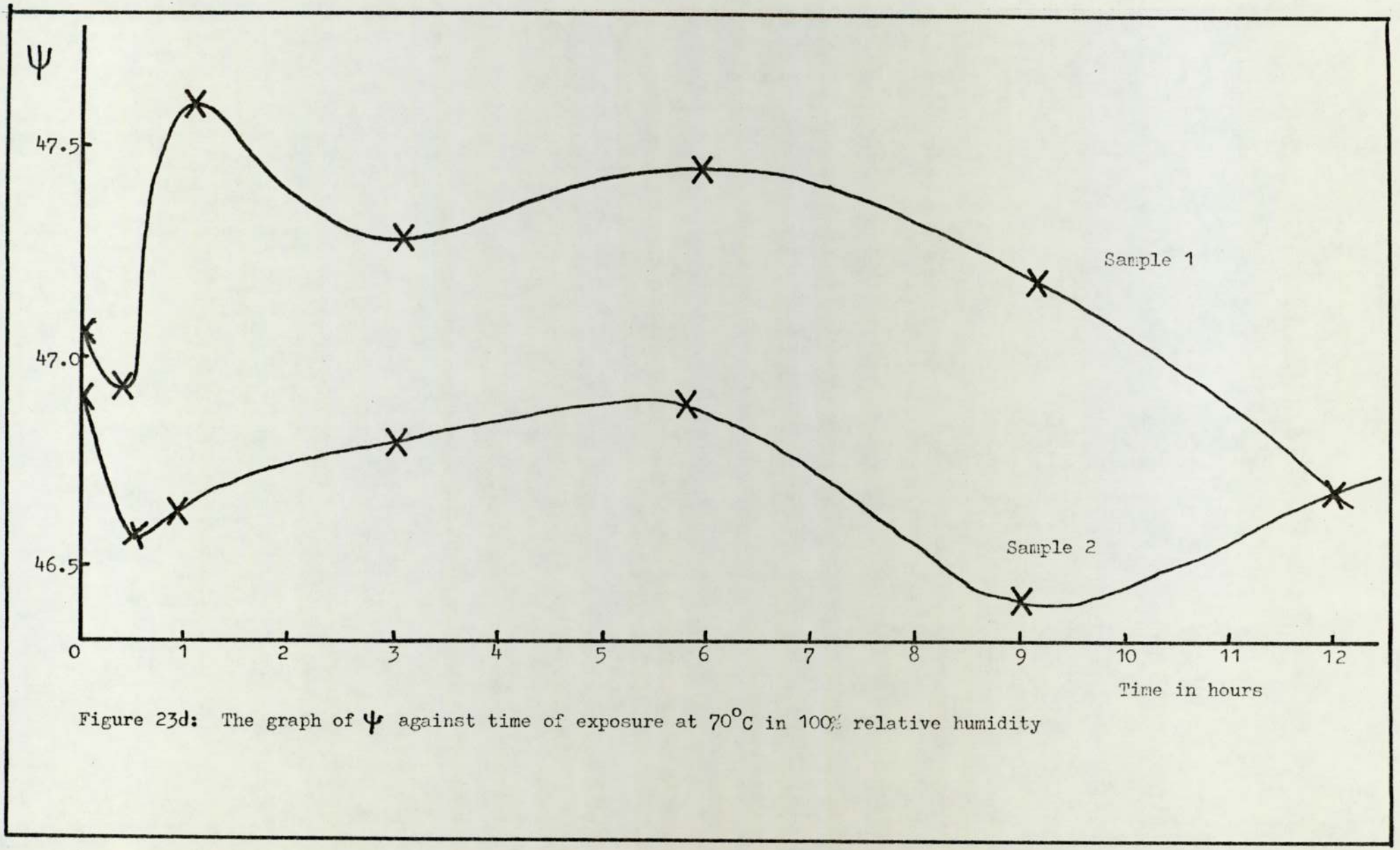

Figure 23d: The graph of Ψ against time of exposure at 70°C in 100% relative humidity

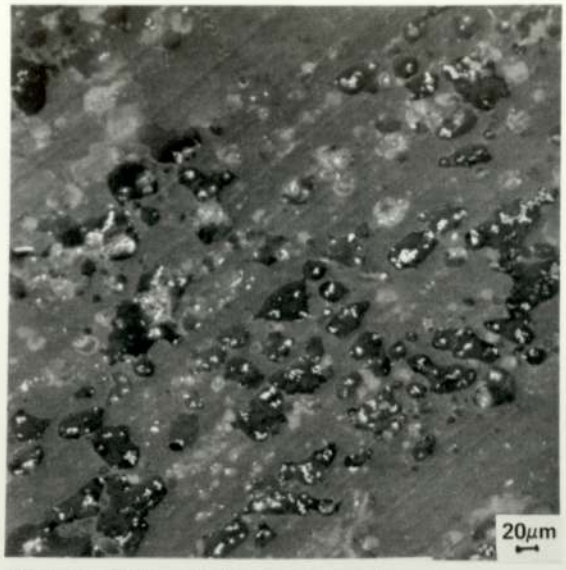

Figure 24a. SEM micrograph. Early stage of aluminium hydroxide film on aluminium sheet.

Figure 24b. SEM micrograph. Aluminium hydroxide film on aluminium sheet, showing boehmite and bayerite.

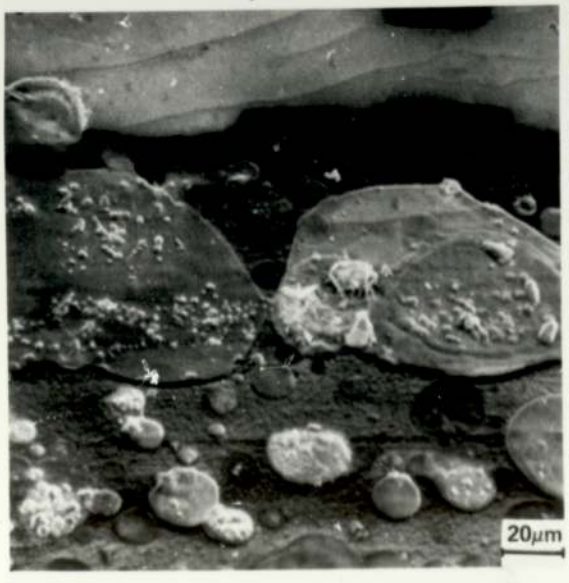

Figure 24C. SEM micrograph. Aluminium hydroxide island with bayerite

Figure 24d. SEM micrograph taken in the reflective mode. Showing bayerite crystals growing from the substrate.

5.2 Discussion: Growth of aluminium hydroxide on aluminium sheet

For sheets of super purity (99.99%) and commercial purity (99.93%) aluminium, two different heat treatments resulted in different grain sizes. These experiments were conducted in order to establish whether differences could be detected by ellipsometry. From examination of Figure 23a, b, c, and d it is clear that different heat treatments do have an effect on the rate of growth of hydroxide films, but before aluminium sheets could be exposed to water vapour, the original protective oxide film formed during rolling, had to be removed to produce a 'clean surface'. Phosbite was used to clean the surface and the action of Phosbite on oxide film is to chemically dissolve them, but it is not clear how and when the new protective oxide film was formed. It could have formed in the phosbite solution, but it is more commonly accepted that it is formed just after removing from the solution.

Aluminium sheets were exposed to water vapour saturated air (WVSA) within 18 hours of cleaning. How thick the new protective oxide film was at that stage, was difficult to say, but later studies showed it to be 2 nm for both purities of aluminium with different heat treatment. It is evident from Figure 23a, b, c and d, that Ψ and Δ changes show rapid changes initially followed by a slow but continuous change. Figure 23b shows Ψ first increases followed by a rapid drop. Whereas Ψ - changes in Figure 23c show a decrease, followed by an increase. These changes were difficult to explain, but after the aluminium sheets had been examined in SEM using EDX analysis, a possibility was suggested, that the starting surface was not 'clean', because when bayerite pillars were examined there were large amounts of copper present and the only source of copper was the phosbite solution. Neal[167] had obtained similar effects with silver films which had been deliberately

contaminated with 1 or 2% copper.

5.2.1 Discussion: (SEM results)

The micrographs showed that the aluminium hydroxide (pseudoboehmite) grows in the form of islands with bayerite within it Figure 24a. The islands grow in two directions Figure 25a, they become thicker and at the same time grow along the surface until they join up to form a continuous film as shown in Figure 24b and Figure 25b. When a higher magnification of one of the islands was examined it was found that there were pseudoboehmite islands on top of pseudoboehmite islands with bayerite crystals Figure 24c.

The same area examined in the reflective mode showed that the bayerite crystals grow from the aluminium substrate. This result was in agreement with the work of Scaman and Tucks [3] on aluminium alloys reaction with WVSA at 70°C. A cross-section through hydroxide film is shown in Figure 25c pseudoboehmite islands joining up to form a continuous film with bayerite pillars growing from the aluminium substrate.

5.3 ESCA results: Aluminium hydroxide on aluminium sheet

Figure 25d shows a general broad scan photo-electron spectrum obtained from an aluminium sheet with an aluminium hydroxide film grown for 50 hours in a humidity chamber at 70°C and 100% relative humidity A1k radiation was employed (hv = 1486 eV) and the electron kinetic energy was scanned from 500 to 1500 eV. The two peaks at 1366.6 eV and 950 eV are readily identified from standard data as corresponding to $A1_{2s}$ and O_{2s} levels respectively. These emissions are not the only ones observed. Emission from other levels and the plasmon effects were also observed Figure 25e shows photo-electron spectra obtained from the same sample as above but from a different expanded range. Figure 25f shows the plots of aluminium,

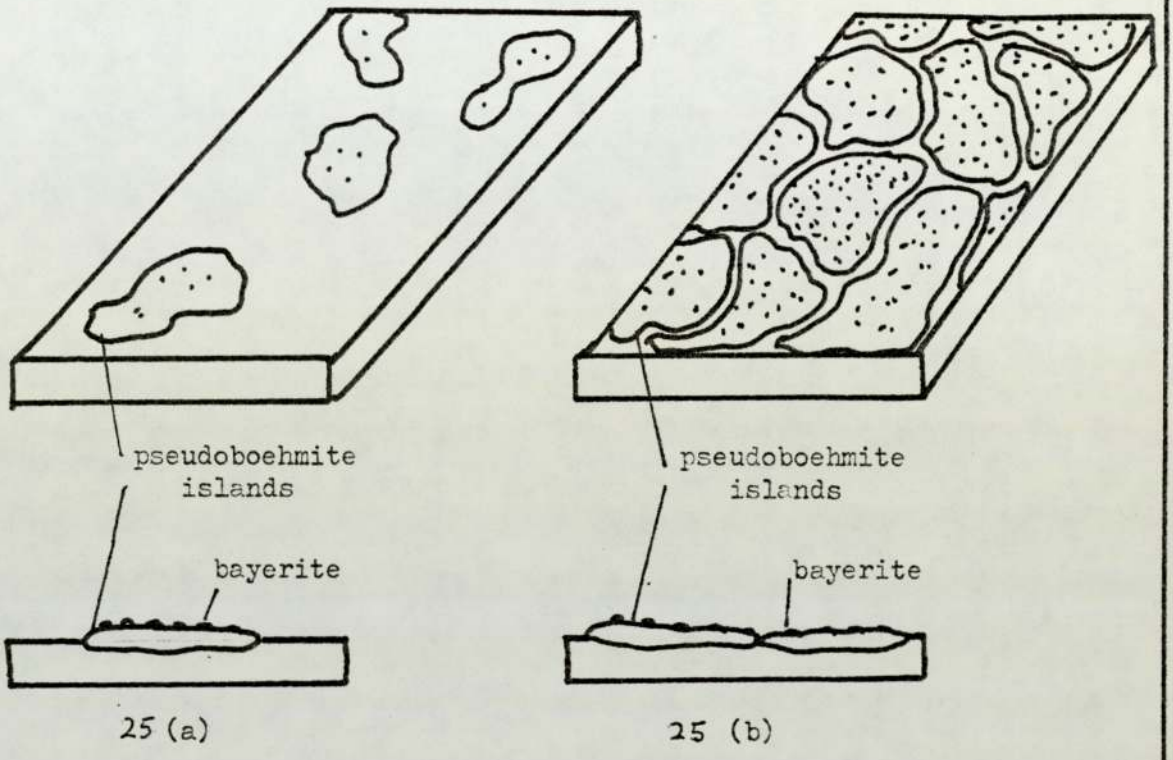

25 (a) 25 (b)

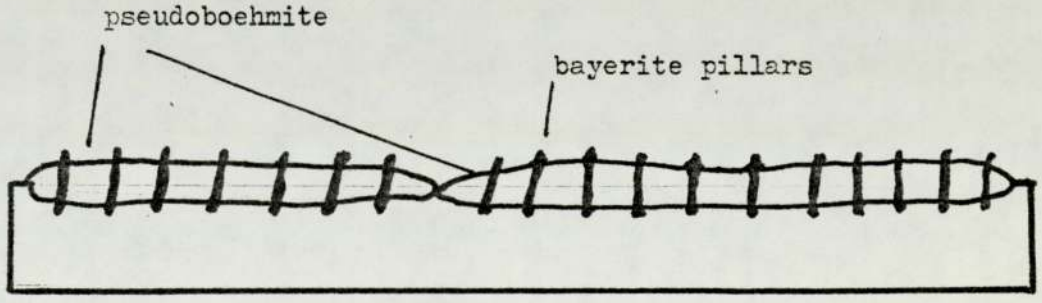

25 (c)

Figure 25

oxygen and carbon peak heights during etching of a sample which had an aluminium hydroxide layer grown on it.

Table 3 gives the detailed results obtained from aluminium hydroxide film on aluminium sheet grown in a humidity chamber at 70°C, 100% relative humidity.

Etch time min	O	Al	O:Al	Al_{2s}		Al_{2p}		O_{1s}	
				Peak posn. eV	½ width eV	Peak posn. eV	½ width eV	Peak posn. eV	½ width eV
0	103	14	2.25	1366.6	2.4	1411.5	1.95	954.0	2.85
0.5	74	12	1.88	1366.6	2.85	1411.5	2.30	954.2	2.85
1.5	77	12	1.96	1366.6	2.90	1411.4	2.30	954.2	2.85
5	62	11	1.73	1366.6	2.90	1411.6	2.40	954.2	2.80
8	59	12	1.58	1366.4	3.00	1411.6	2.30	954.2	2.75
13	119	23	1.59	1366.5	3.10	1411.4	2.30	954.3	2.70
23	52	10	1.60	1366.5	3.10	1911.5	2.30	954.4	2.70

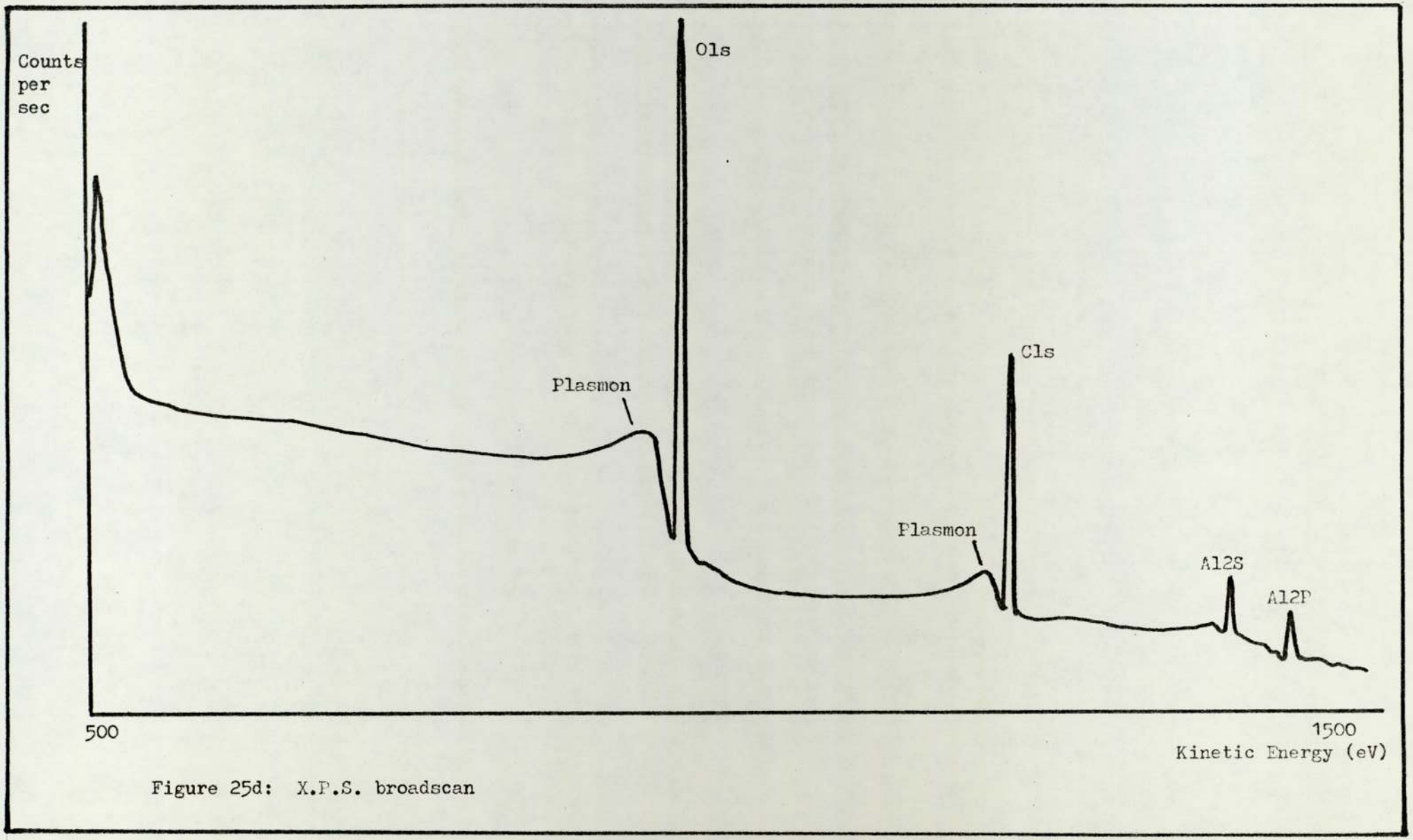

Figure 25d: X.P.S. broadscan

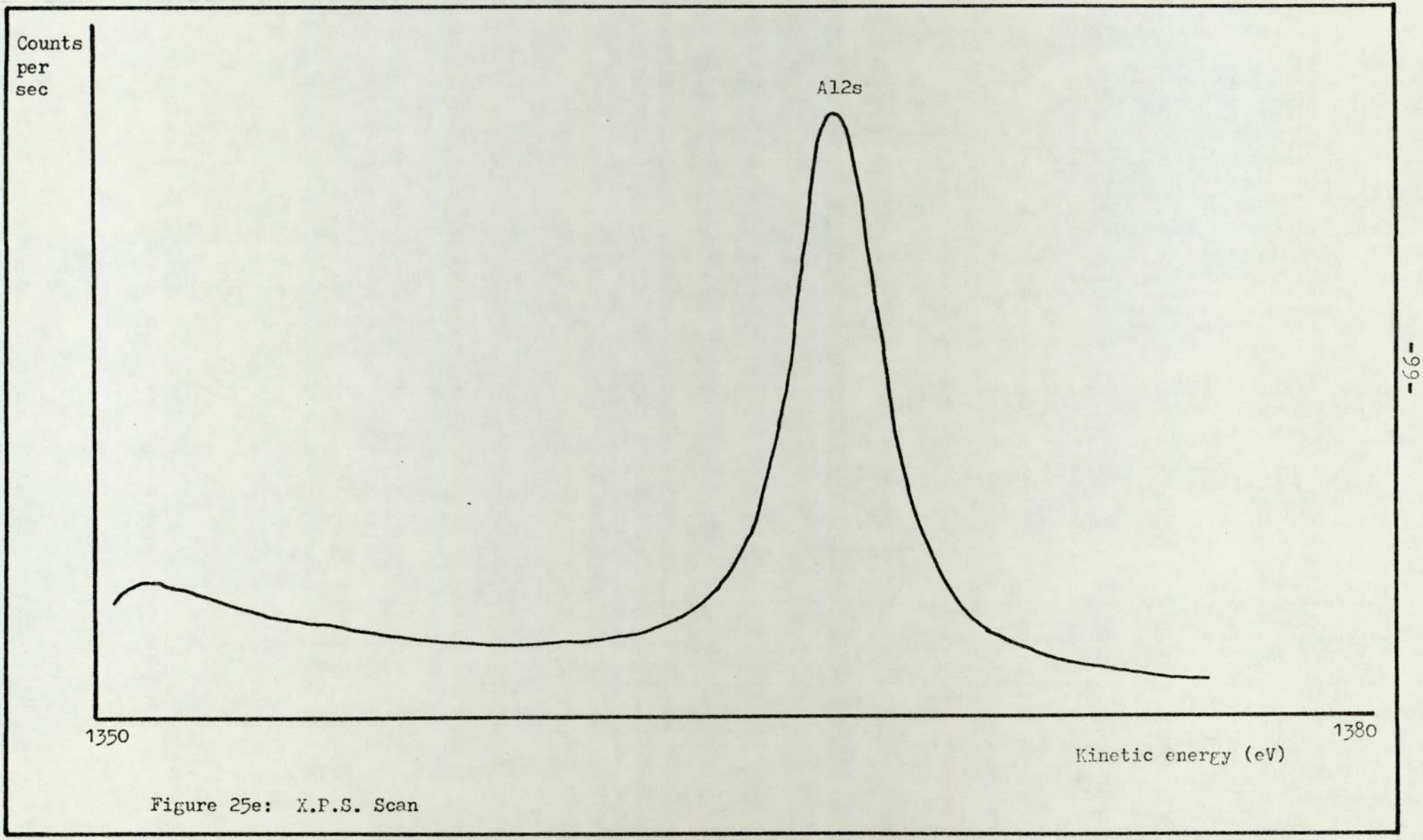

Figure 25e: X.P.S. Scan

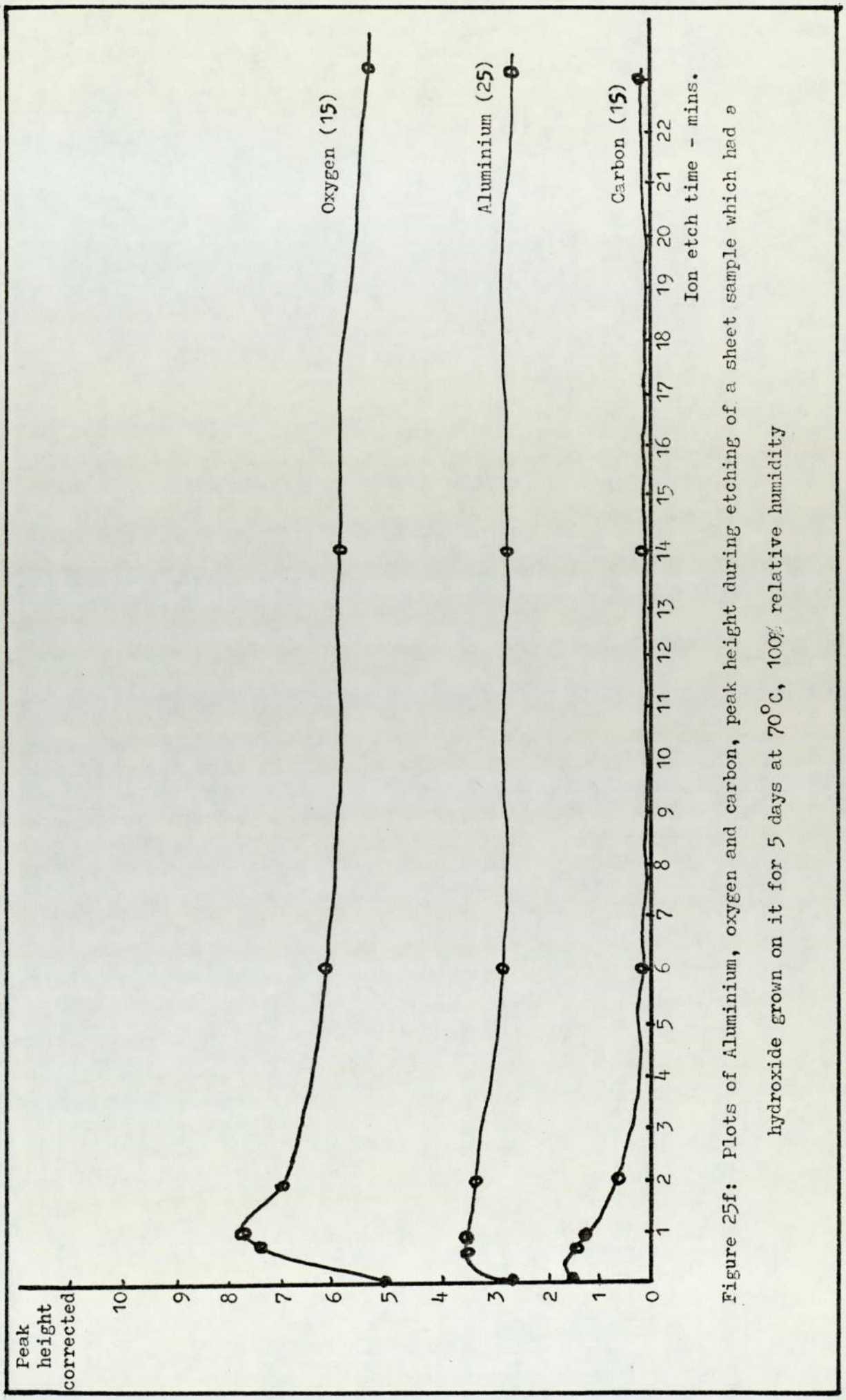

Figure 25f: Plots of Aluminium, oxygen and carbon, peak height during etching of a sheet sample which had a hydroxide grown on it for 5 days at 70°C, 100% relative humidity

5.4 Discussion of ESCA results obtained from aluminium sheet

The results from the ESCA examination of sheets of aluminium which had been exposed to water vapour saturated air (WVSA) for 5 days at 70°C showed that (Figure 25f) there was high level of carbon contamination on the surface, which decreased rapidly as the sample was ion-etched. This contamination had probably arisen from the atmosphere and handling.

The aluminium 2S peak position remained the same throughout etching, but the half-width of the aluminium 2s peak increased in magnitude with increasing etching time. This could have been due to the charging of the surface layer. The ratio of oxygen (corrected level) to aluminium (corrected level) decreased as the sample was etched. This suggests that the structure of aluminium hydroxide could be changing with thickness, but as the sample was further etched the ratio increased, Table 3. This can be explained by trapped aluminium in the hydroxide matrix, isolated from the aluminium substrate. Trapped aluminium in the Al_2O_3 matrix, isolated from the aluminium substrate has been reported by Barr [158].

5.5 Results: Evaporated aluminium films with copper contamination

In previous experiments, aluminium sheets which had been cleaned with Phosbite, were later exposed to WVSA at 70°C and examined in SEM using the EDX analysis. High levels of copper contamination were found in some of the bayerite pillars. Therefore experiments were performed to investigate the effect of copper contamination.

Pure aluminium films were evaporated, from a tungsten boat on to a glass substrate, which was at room temperature and a pressure of 10^{-6} torr. In the same vacuum a thin film 10 nm of copper was evaporated on to the aluminium film. The aluminium film substrate was masked so that not all the aluminium film was covered with copper

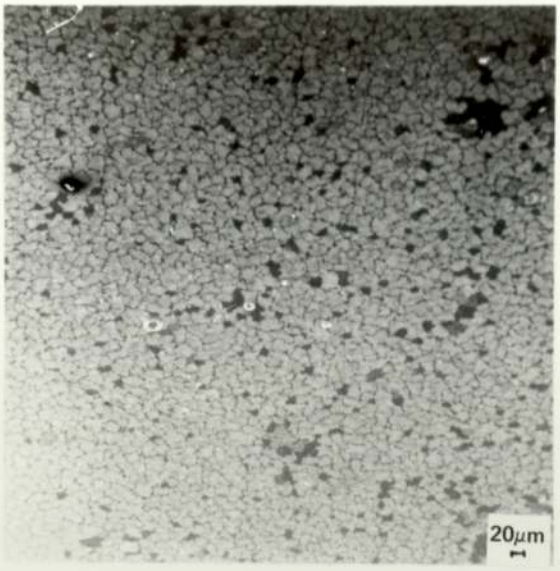

Figure 24e. SEM micrograph. Aluminium hydroxide film on glass substrate with thin (10mm) copper film deposited before reaction with WVSA.

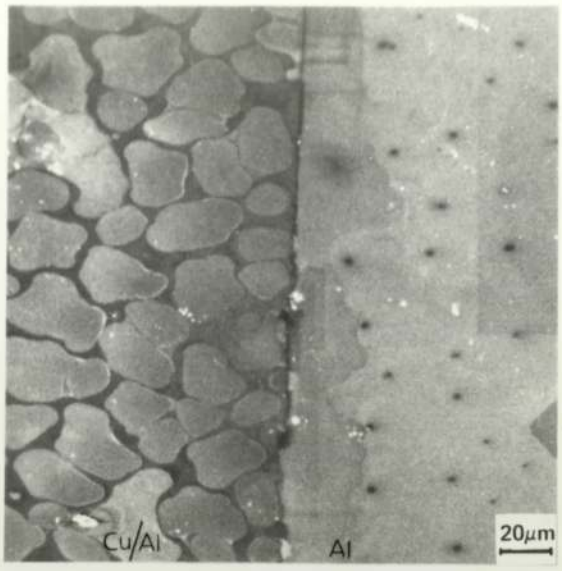

Figure 24f. SEM micrograph. Interface of aluminium/ copper film and aluminium film after reaction with WVSA.

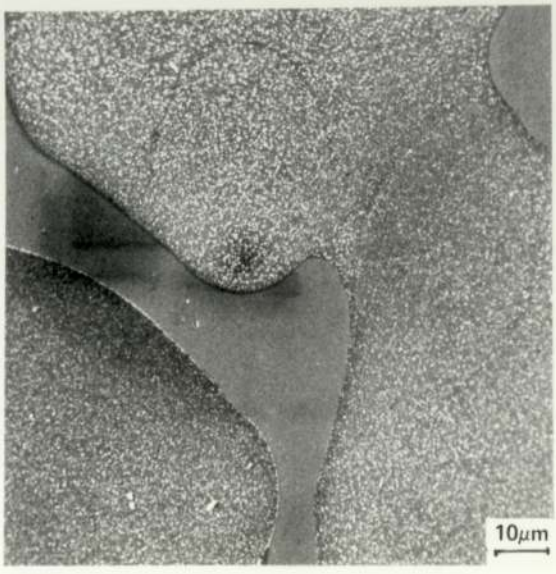

Figure 24g. SEM micrograph. Higher magnification of the aluminium hydroxide island.

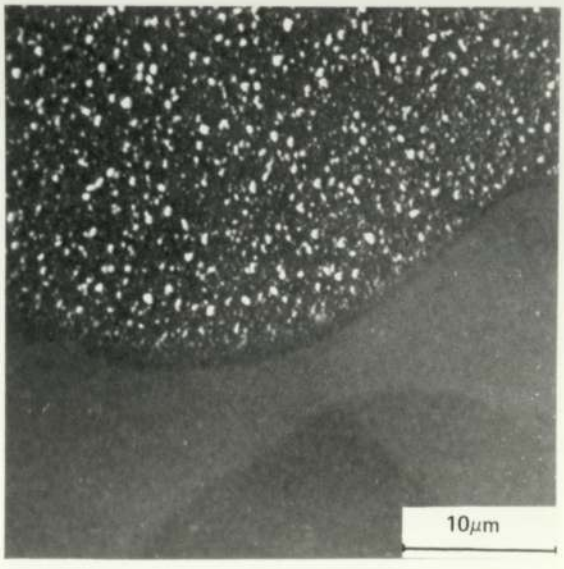

Figure 24h. SEM micrograph. Showing bayrite like crystals on aluminium hydroxide island.

contamination. The samples were then heated in an oven at 100°C for 2 hours. The sample was then exposed to WVSA at 70°C for 5 minutes and examined in SEM. The results are shown in Figure 24e, f, g, h. Figure 24e shows the general view of the aluminium hydroxide film which had been contaminated with a thin 10 nm copper film. Figure 24f shows the aluminium/copper film and aluminium film interface after reaction with WVSA. Figure 24g and 24h shows higher magnification of pseudoboehmite islands with bayerite pillars.

5.6 Results: Measurement of hydroxide film thickness

The hydroxide film thickness measured by ellipsometry did not correlate with hydroxide film thickness estimated by Tuck (Appendix). Therefore it was decided to use an independent method of measuring film thickness. The technique chosen was interferometry as developed by Tolansky [8].

Two aluminium films were simultaneously evaporated on to glass substrate under a vacuum system of a pressure of 10^{-6} torr. Both films were of the same thickness and one of the samples was used for thickness measurement by interferometry. Other pairs of film covering a range of thickness were also prepared. The second sample of each pair was placed in a humidity chamber, examined visually after every 15 minutes. After a certain length of time the film becomes transparent, for aluminium hydroxide k = 0, and the time taken to achieve this was noted. The precise time when the film became transparent was important in determining reaction rates so the technique was refined, Chapter 4.1.

The results are shown in Figure 25g and Table 4 which gives the times for aluminium films of different thickness to react completely to aluminium hydroxide.

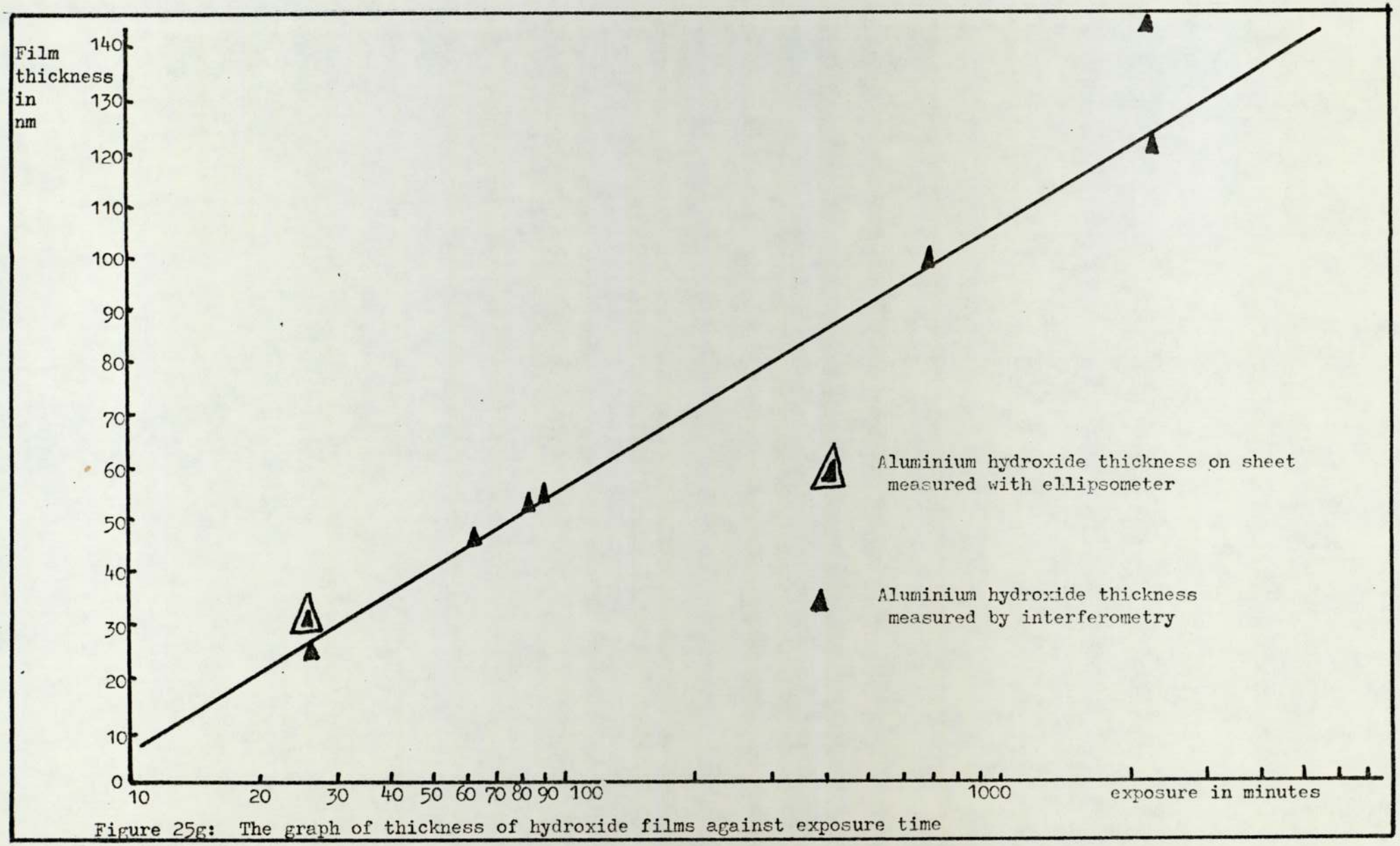

Figure 25g: The graph of thickness of hydroxide films against exposure time

Table 4 Hydroxide film thickness against time of exposure.

Aluminium hydroxide film thickness nm.	Time of exposure to water vapour saturated air at 70°C in minutes.
25	26
44	50
55	80
56	90
102	650
123	2000
154	3200

5.7 Results: Aluminium hydroxide films grown on gold and glass Substrate

Since aluminium is reactive it is difficult to characterise a surface without the presence of an oxide layer. Some experiments were conducted by depositing aluminium on gold, the optical constants of which were first measured. Aluminium hydroxide film thicknesses were measured as indicated by interferometry (Tolansky) [8]. It was also possible to evaluate the thickness from ellipsometer readings since the films were on a gold base, the optical constant (n_2, k_2) of which had previously been measured. By using a value n, for the hydroxide film, values of Ψ and Δ were computed for various hydroxide thicknesses on gold. A "best fit" was found for films of various thicknesses. The increase in thickness from the aluminium metal to the complete hydroxide layer was also measured. Table 5 shows thicknesses of hydroxide measured by ellipsometry and by the interference microscope and the original metal film thickness measured by the interference microscope together with changes in instrument parometers for increased thicknesses of aluminium hydroxide on gold.

The instrument settings for the film free gold base, Ψ and Δ were equal to 40.7° and 119.6° respectively at a wavelength of 546 nm giving $n_2 = 0.48 \pm 0.005$, $k_2 = 2.54 \pm 0.1$ for the gold layer at an angle of incidence of 64.2°.

Figure 26a, b and c show stereoscan photographs of aluminium hydroxide on glass and gold. Examination of the specimens using a step scan X-ray diffractrometer, with Cobalt K radiation showed that both the base gold films and the superimposed aluminium films had a preferred orientation in the (III) direction. Examination of the aluminium hydroxide showed a weak line at $2\theta = 18.4$.

Table 5

	Film No.	1	2	3	4	5	6	7	8
A	Thickness in nm of Aluminium film on gold (Interferometry)	22±3%	25±3%	32±3%	39±3%	42.0±3%	42.5±3%	120.5±3%	127±3%
B	Thickness in nm of Aluminium hydroxide film on gold (Interferometry)	33±5%	39±5%	50±5%	53±5%	61±5%	65±5%	167±2.5%	178±2.5%
C	Ψ changes due to hydroxide film	+3.65	+5.95	+7.72	+8.34	+9.14	+9.44	-1.35	1.56
D	Δ^{o} changes due to hydroxide film	-21.18	-12.78	+7.98	+11.60	+36.69	+52.42	+42.74	+30.12
E	Aluminium hydroxide thickness measured ellipsometrically (nm) using O=1.58	36±4%	43±4%	52±4%	55±4%	65±4%	66±4%	175±2%	185±2%
F	Ratio of $\frac{E}{A}$	1.6	1.7	1.6	1.6	1.5	1.5	1.4	1.4

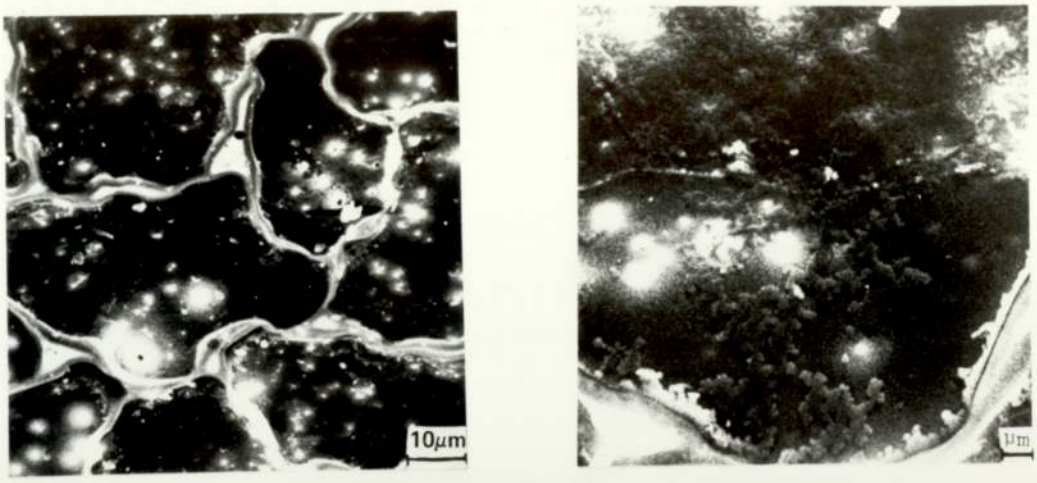

Figure 26a. SEM micrograph.
Aluminium hydroxide film
on gold film substrate.

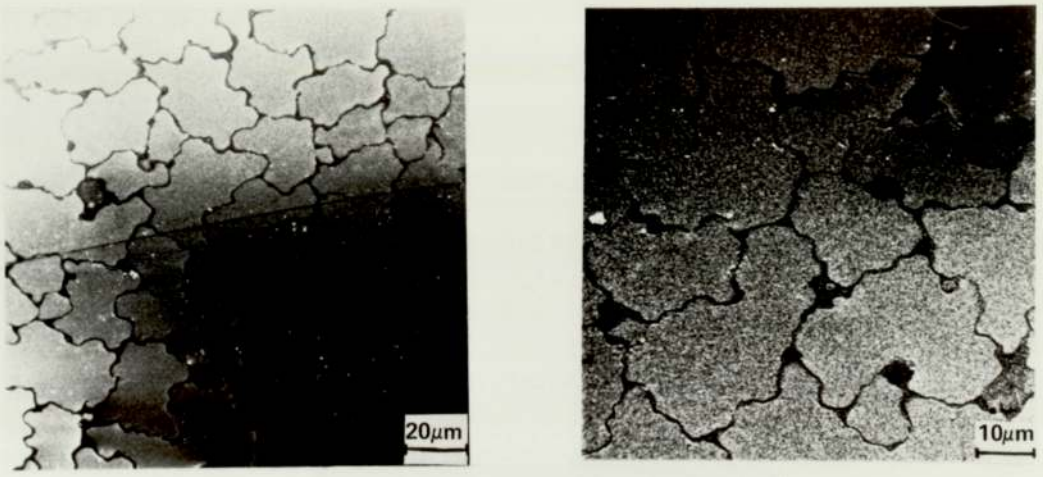

Figure 26b. SEM micrograph.
Thin aluminium hydroxide
film on glass substrate.

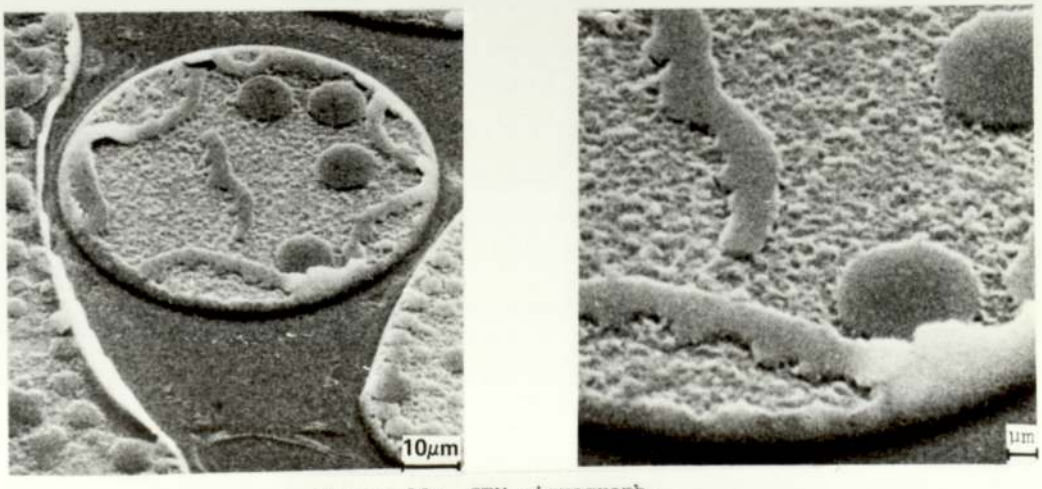

Figure 26c. SEM micrograph.
Thick aluminium hydroxide film
on glass substrate.

5.8 Discussion: Aluminium film with copper contamination

Examination of the SEM micrograph, Figure 26b showed that the aluminium hydroxide on aluminium film was initially in the form of islands, and increasing to form a continuous film similar to the hydroxide film on aluminium sheet, Figure 24b.

Therefore the mechanism with which the hydroxide film grows on aluminium sheet and evaporated aluminium film must also be similar. Presence of copper increases the reaction rate, which can be seen from Figure 24f, showing a higher magnification of the interface of aluminium/copper film and aluminium film, but the structure of islands was similar to the islands on pure evaporated aluminium films and aluminium sheet.

Higher magnification of the pseudoboehmite islands showed bayerite like crystals which were also similar to the bayerite pillars on aluminium hydroxide film grown on aluminium sheet.

5.8.1 Discussion: Measurement of hydroxide film thickness

Since the hydroxide film thickness measured by ellipsometry did not correlate with hydroxide films thickness estimated by Tuck, an independent method, interferometry as developed by Tolansky, for measuring film thickness was used.

One of the reasons why there was an apparent discrepancy between the measurement of hydroxide film thicknesses, was that Tucks estimation of hydroxide film thickness values, in the same range as ellipsometry values, were based on thick hydroxide film which had been developed by exposure to WVSA at 70°C for 20 days. Tuck repeated his technique using aluminium film, as in this work, in the thickness range of 10 nm to 300 nm. His results obtained from these experiments confirmed the results in Table 4. Therefore it was concluded that a different mechanism operated for the development of

thick layers of hydroxide film. The film thickness reaches a limit by one mechanism and the process is taken over by another mechanism. It is difficult to say which are the mechanisms operating for film growth of less than 0.5 μm.

Film thicknesses measured by the Transparency technique and ellipsometry agreed within experimental errors, Figure 25g. Therefore it is concluded that ellipsometry can be satisfactorily used for measuring hydroxide film thickness in the early stages of growth.

5.8.2 Discussion: Aluminium hydroxide films on gold and glass substrate

The film free gold base yielded initial values of Ψ and Δ which were substituted into equation 3.22 and 3.23 to evaluate the optical constants n_2 and k_2 for the surface. Using these computed constants and a two layer programme, values of the angles Ψ and Δ, were computed for composite surfaces of varying aluminium hydroxide thicknesses on gold and on assumed value of refractive index for the hydroxide. Figure 27a shows a plot of measured Ψ and Δ for the eight Aluminium hydroxide films together with computed values of Ψ and Δ using various values of refraction index for aluminium hydroxide assuming $k = 0$. It can be seen from Figure 27a that in all cases where $k = 0$ a complete loop is formed in that when very thick films are measured Ψ and Δ values repeated themselves.

There are two samples (7 and 8) for which the measured ellipsometric parameters do not lie on any of the computed closed loops. Figure 27b shows similar plots but in each case with a value of $k_1 = 0.0009$ (i.e. a small absorption is assumed). It can now be seen that 7 and 8 lie on curves with n_1 values between 1.55 to 1.60 and $k_1 = 0.0009$. This represents the best fit for thicker aluminium

hydroxide film i.e. thicker than about 80 nm. When the optical parameter Ψ and Δ for films less than 80 nm are plotted on the computed graph where $k_1 = 0$ there is better agreement between the computed thickness and measured thickness by interferometry. It would appear therefore that in these early stages of growth the optical constants for the hydroxide at a wavelength of 546 nm are $n_1 = 1.58 \pm 0.03$ and $k_1 = 0$ and for thicker films the constants are given by $n_1 = 1.58 \pm 0.03$ and $k_1 = 0.0009$.

The optical constant of aluminium hydroxide film, prepared under these conditions have not been reported in the literature. However, the optical constants of electro-polished aluminium, reacting with hot circulating water has been reported by Barrett [161] to be $n_1 = 1.60$ $k_1 = 0$.

Alwitt [7] has shown that the reaction of water with aluminium for temperatures less than 90°C produces an outer layer of bayerite crystals with an inner layer of pseudo-boehmite and the other forms of aluminium hydroxide are only produced at higher temperatures.

As already mentioned the step scan X-ray diffractrometer showed a weak line at $2\theta = 18.4^\circ$ using Cobolt α radiation which was assumed to be pseudo-boehmite, since the aluminium hydroxide in this was formed at 70°C.

The structure of aluminium hydroxide on glass and on gold films can be seen from Figure 26a, b and c. The micrographs 26a, 26c shows the island structure and also the porous nature of the hydroxide films. Figure 26c shows thin aluminium hydroxide film on glass substrate this micrograph also illustrates the island structure of early stage of growth.

The sensitivity of the method for determining the constants of the superimposed hydroxide layer depends on the relative optical constants of the base and film. It is also important that the base

material is non reactive and this was the reason for suggesting either gold or platinum. Calculations have been made for four base materials and the results are illustrated in Figure 27c. A glass substrate is least sensitive followed by gold, tantulum and platinum. Although an oxide layer of the order of 1 nm forms on tantulum when exposed to the atmosphere (Ayuado-Bombin and Neal [162]) it could be employed as a base since it has been shown by Kurivek and Melmed [163] that in many cases of film growth on metal it is possible to use pseudo constants for a surface prior to subsequent film growth subject to certain limitations.

5.9 ESCA Results: Samples exposed in vacuum

Aluminium sheets and evaporated aluminium film evaporated on to etched sheet, (vacuum pressure during evaporation refer to section 4.5) exposed to water vapour 'in situ' were examined in ESCA, using MgK_{α} radiation, Table 5 shows ESCA results of tests obtained from aluminium sheet which had been electro-polished and stored in dry air for 5 days and subsequently etched to get profile analysis. The results show film thickness calculated using Fadley's expression:

$$ln\left[\left[\frac{Nt\ (\Theta)}{N\ t\ (\Theta)}\right] \cdot \frac{(E)(A1)}{(E)(A1_2O_3)} + 1\right] \Lambda'_e(E)\ \text{Sin}\ \Theta = t$$

$Nt'(\Theta)$ area under the aluminium oxide peak

$N_{\infty}\, t'(\Theta)$ area under the aluminium metal peak

$\Lambda_e(E)A1$ escape depth of electron in aluminium metal

$\Lambda'_e(E)(A1_2O_3)$ escape depth of electron in alumin oxide

t = film thickness

It was possible to calculate film thickness using different values of electron-escape depth in aluminium oxide and metal.

Table 6 shows data obtained from an aluminium sheet which had

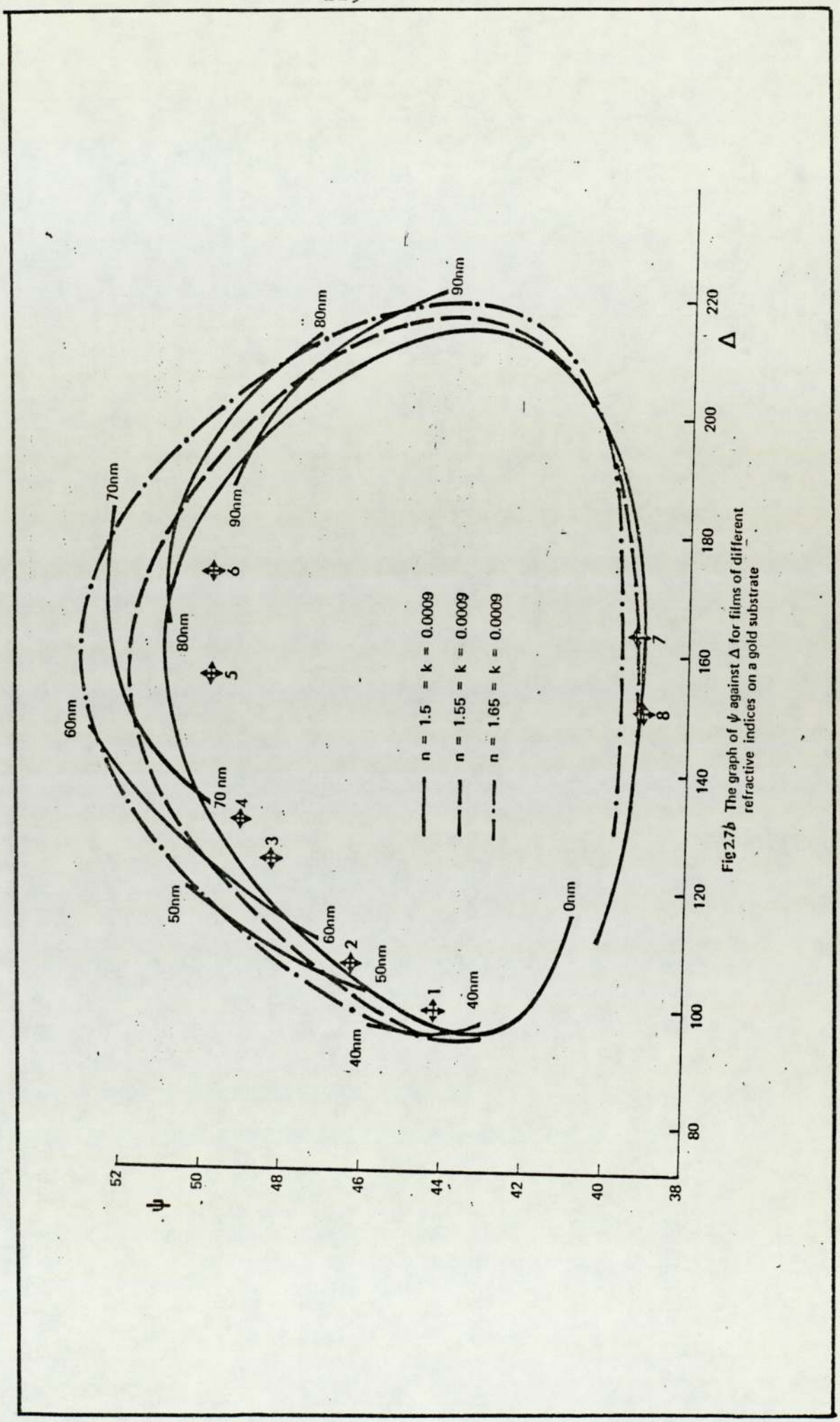

Fig 2.7*b* The graph of ψ against Δ for films of different refractive indices on a gold substrate

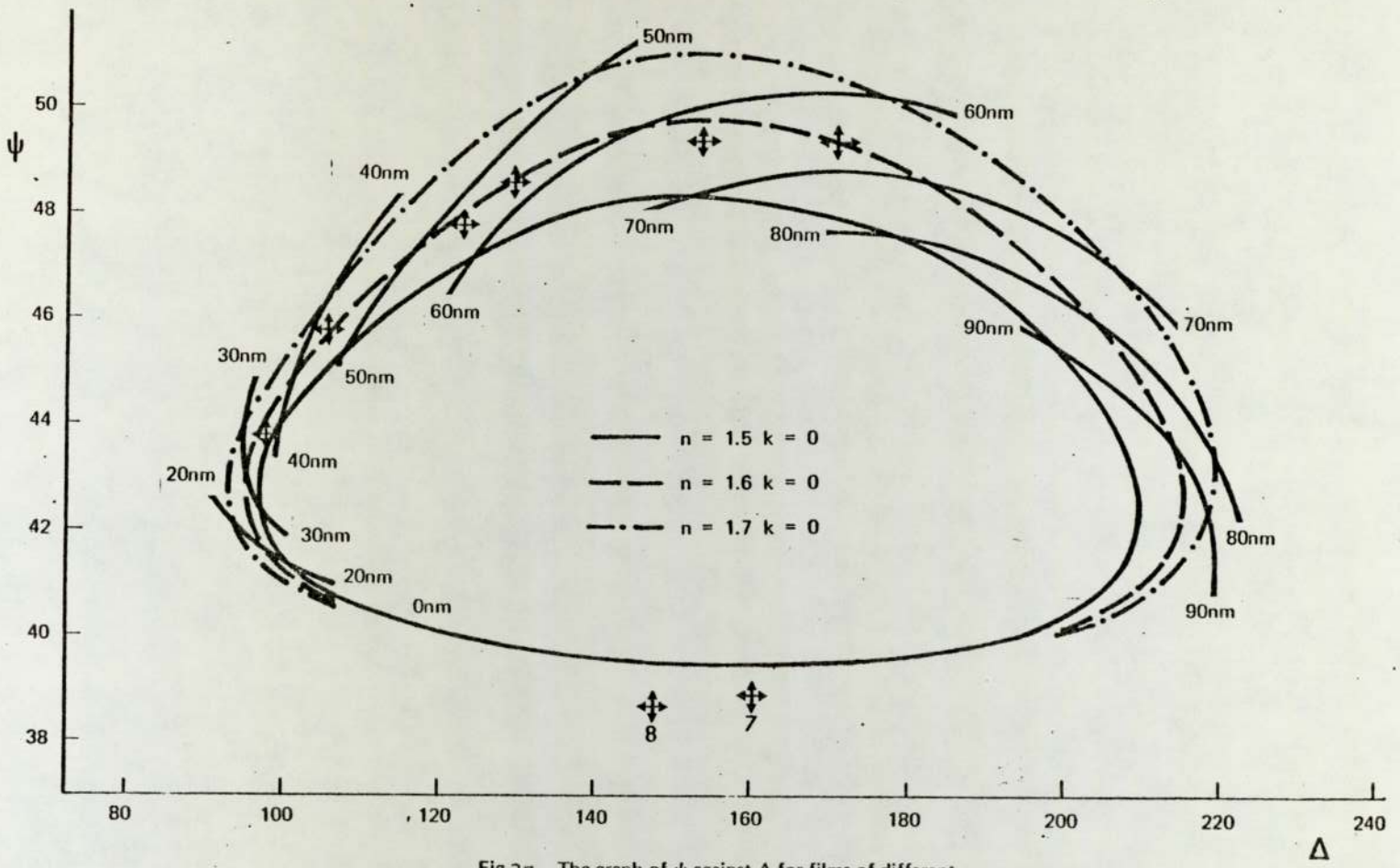

Fig 27a The graph of ψ against Δ for films of different refractive indices on a gold substrate

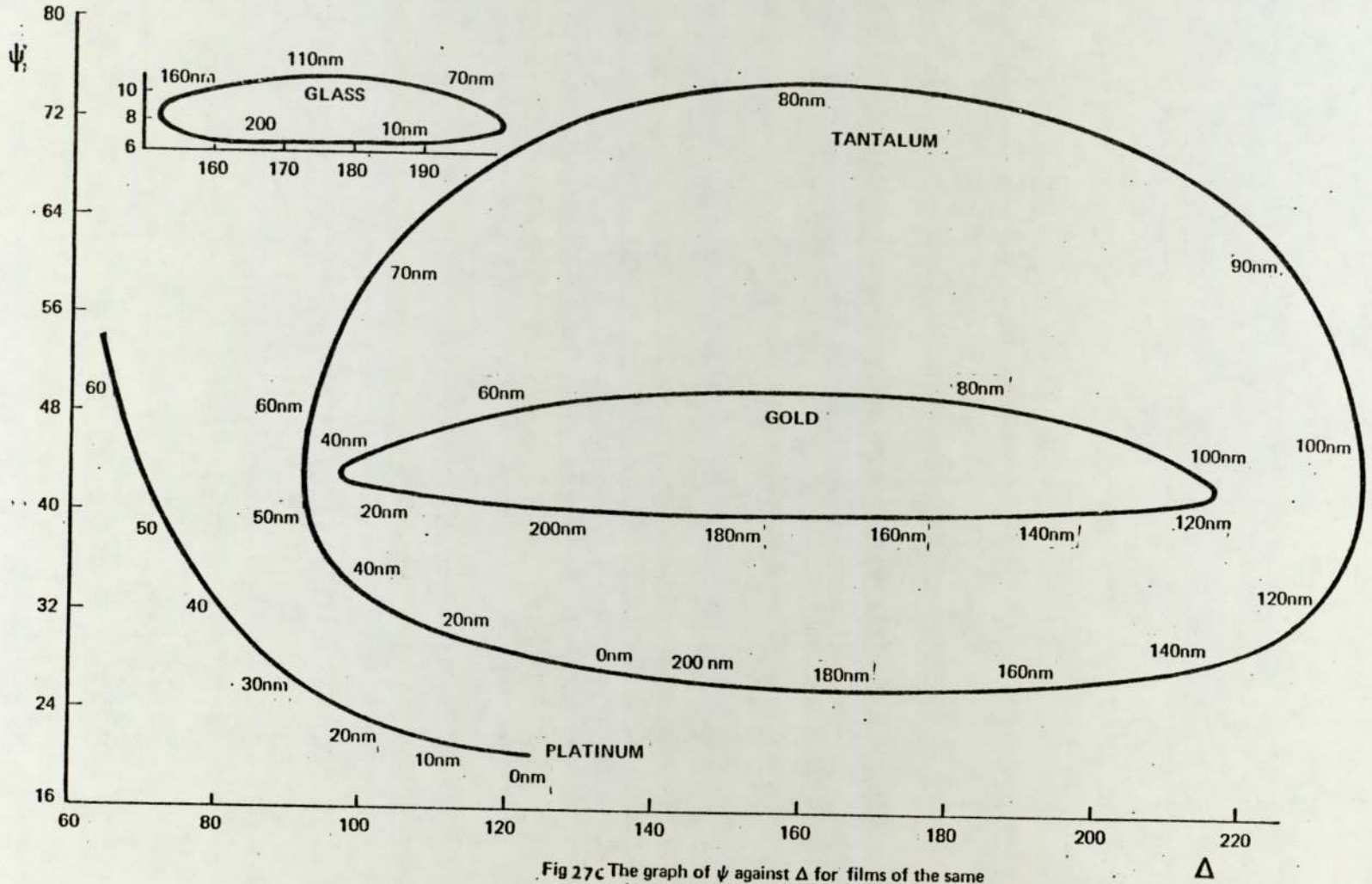

Fig 27c The graph of ψ against Δ for films of the same refractive index, but different substrates

been 'cleaned' by ion etching and exposed to water vapour 'in situ'. The exposures are in Langmiurs where one langmiur = 10^6 torr sec exposure.

Table 7 shows ESCA data obtained from evaporated aluminium 'in situ' and exposed to oxygen. Film thicknesses were obtained by assuming different escape depths.

Table 8 shows ESCA data obtained from evaporated aluminium film which have been ion etched and exposed to water vapour and oxygen 'in situ'.

Figure 28 shows the aluminium 2p peak obtained from an aluminium sheet which had been electropolished and stored in dry air for 5 days. The sheet was then ion etched, Figure 28a shows the aluminium oxide and aluminium metal peak after various etching periods. Figure 28b shows the aluminium metal peak with a small aluminium oxide peak but after further etching the only peak which remains is the aluminium metal peak. Figure 28c shows the aluminium metal and oxide peaks after exposure to oxygen in Langmuirs. The aluminium oxide peak increased in magnitude. Figure 28d shows aluminium metal and oxide peaks after longer exposures.

Figure 28a to 28b are of aluminium oxide and hydroxide film thickness against exposures in Langmuirs. Film thicknesses are calculated by assuming different values for the electron escape depth.

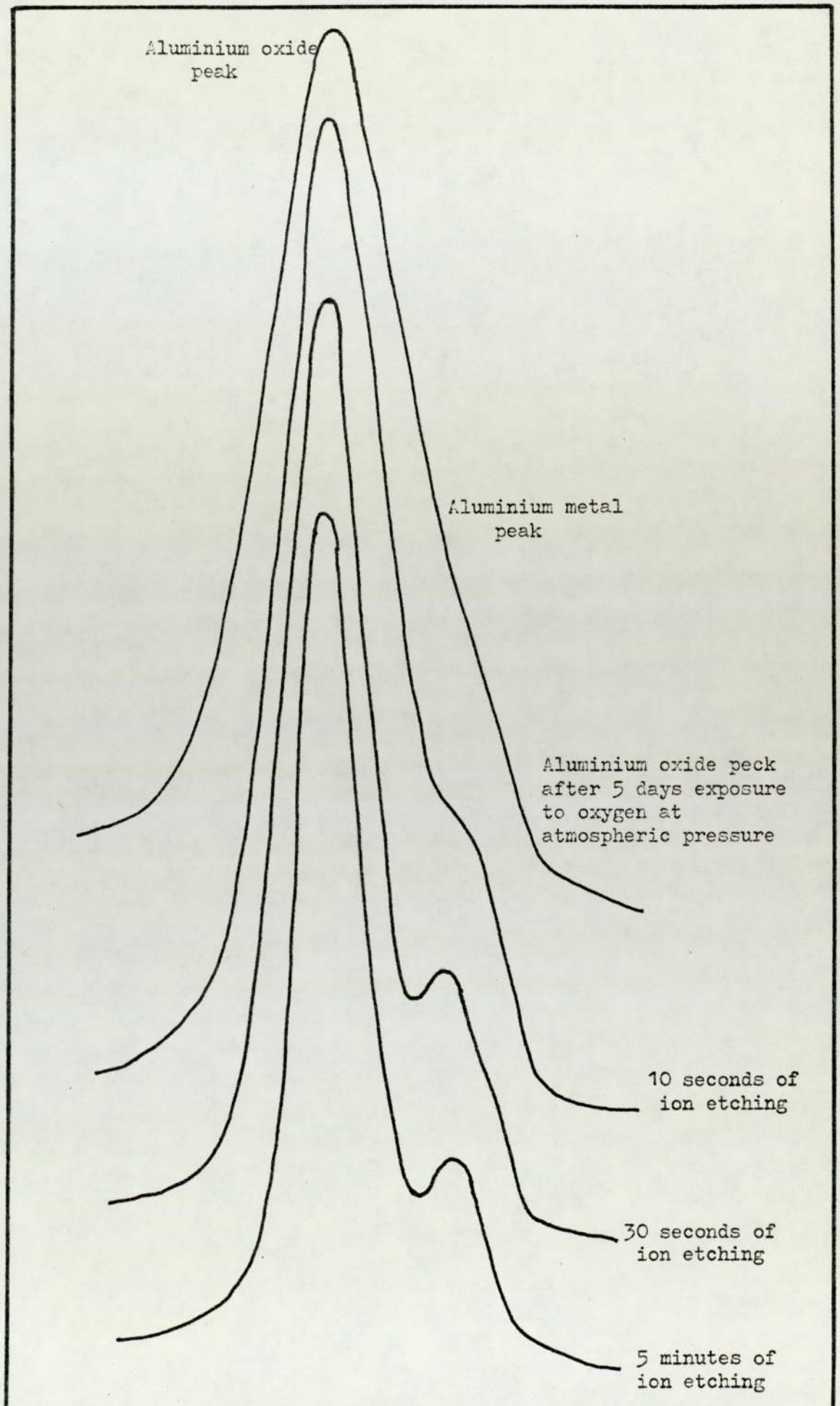

Figure 28a: Aluminium oxide and metal 2p peaks after various stages of ion etching

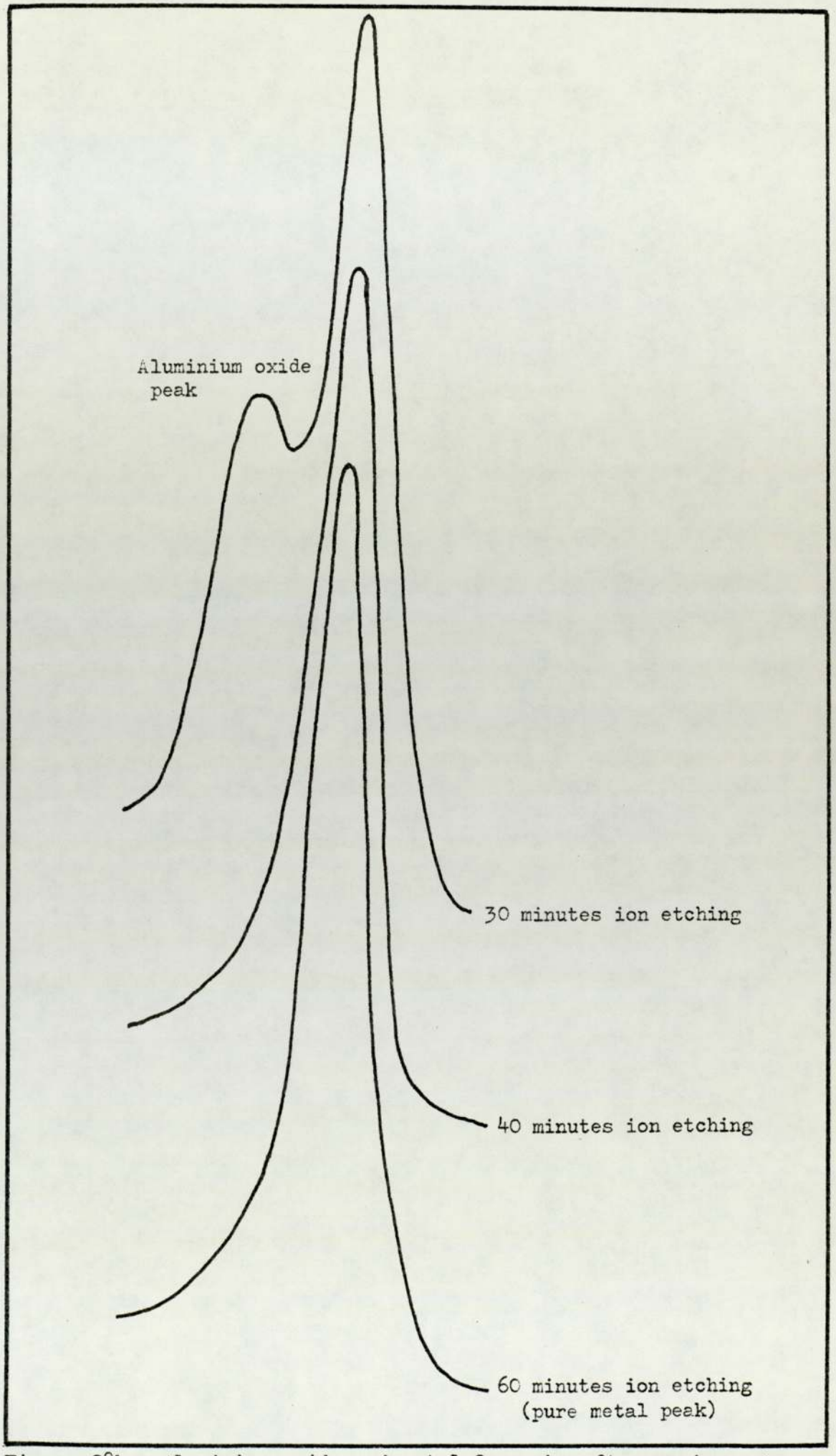

Figure 28b: Aluminium oxide and metal 2p peak, after various stages of ion etching

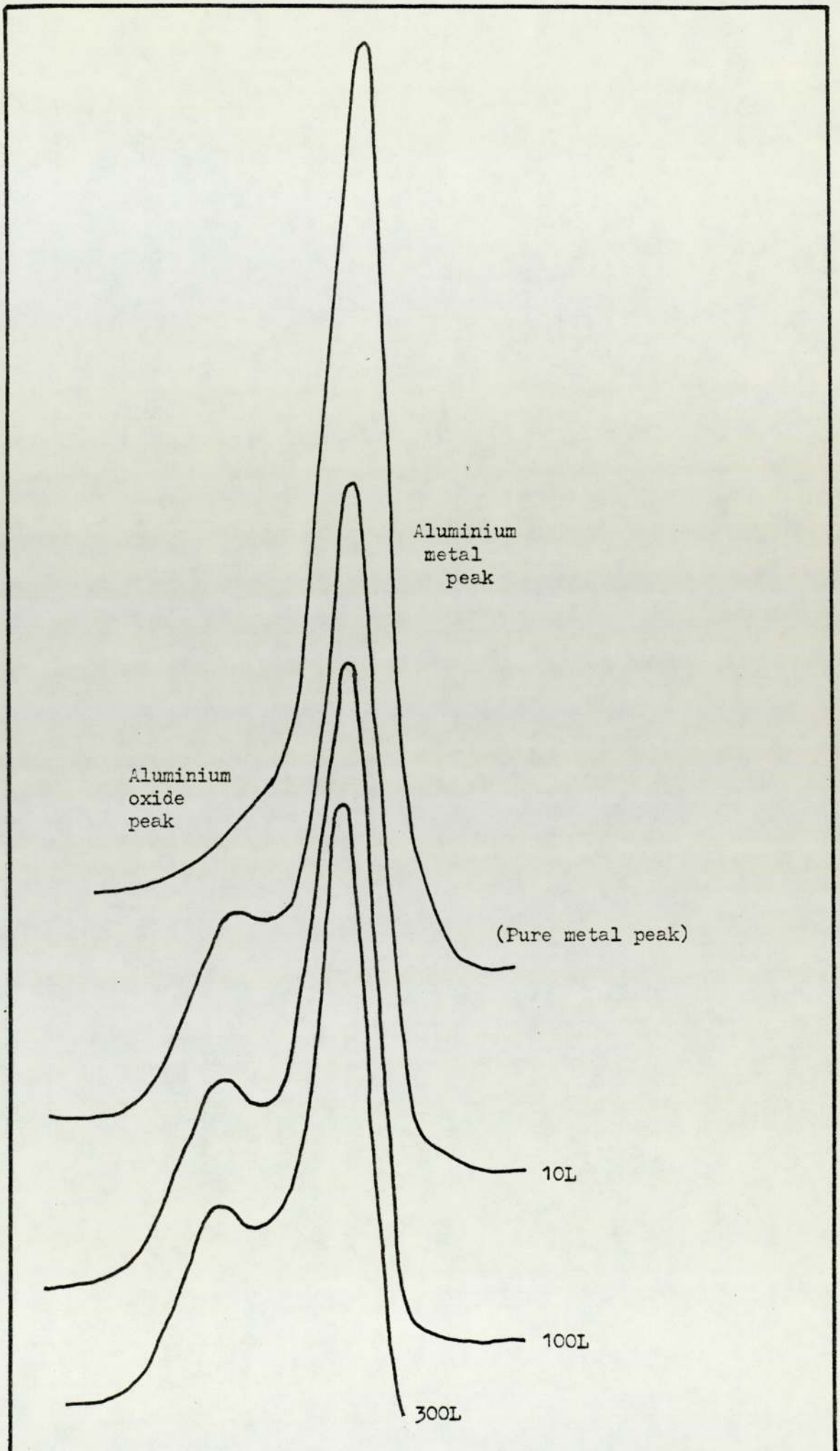

Figure 28c: Aluminium oxide and metal 2p peak, after various stages of exposure to oxygen

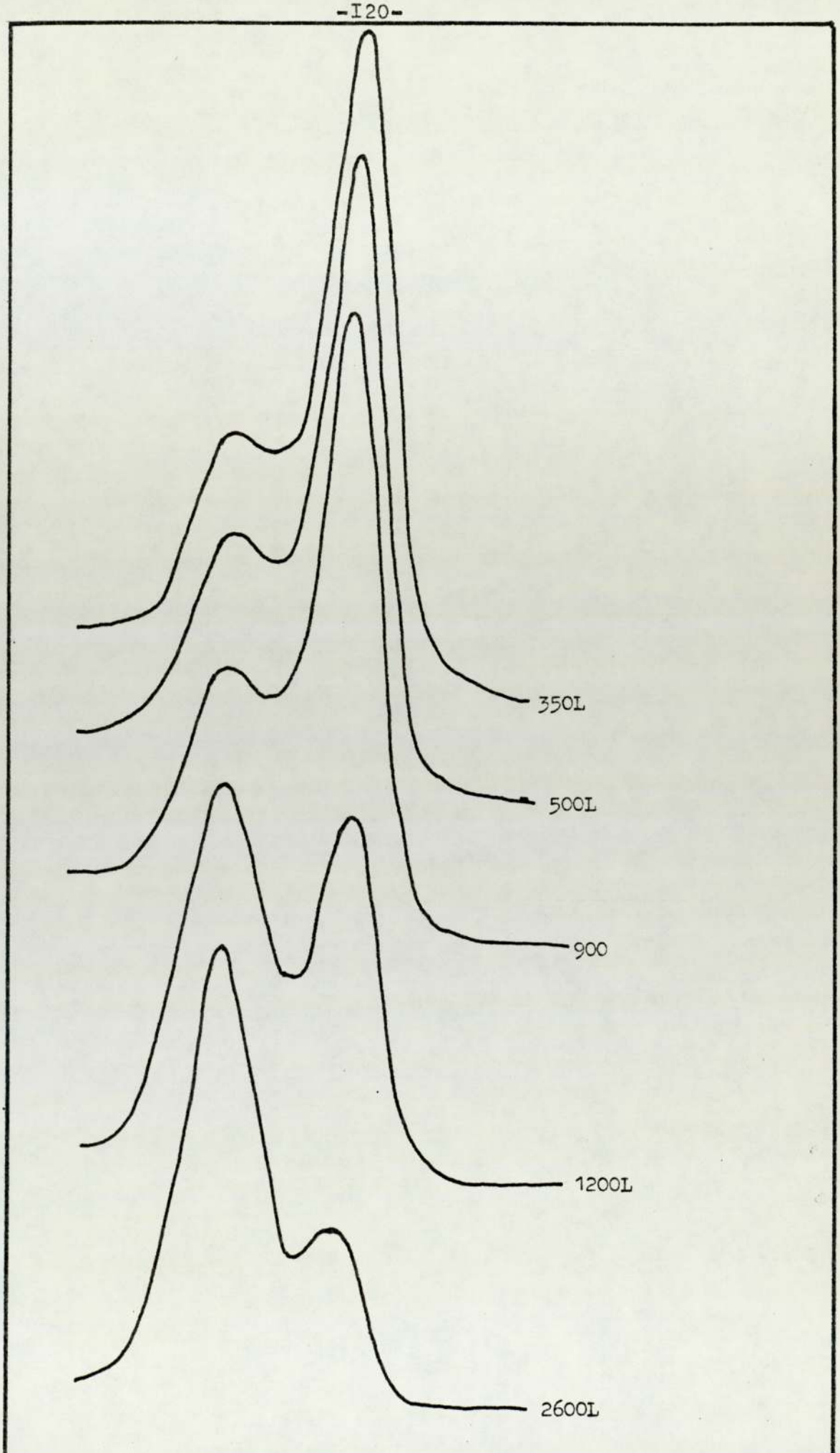

Figure 28d: Aluminium oxide and metal 2p peak, after various stages of exposure to oxygen

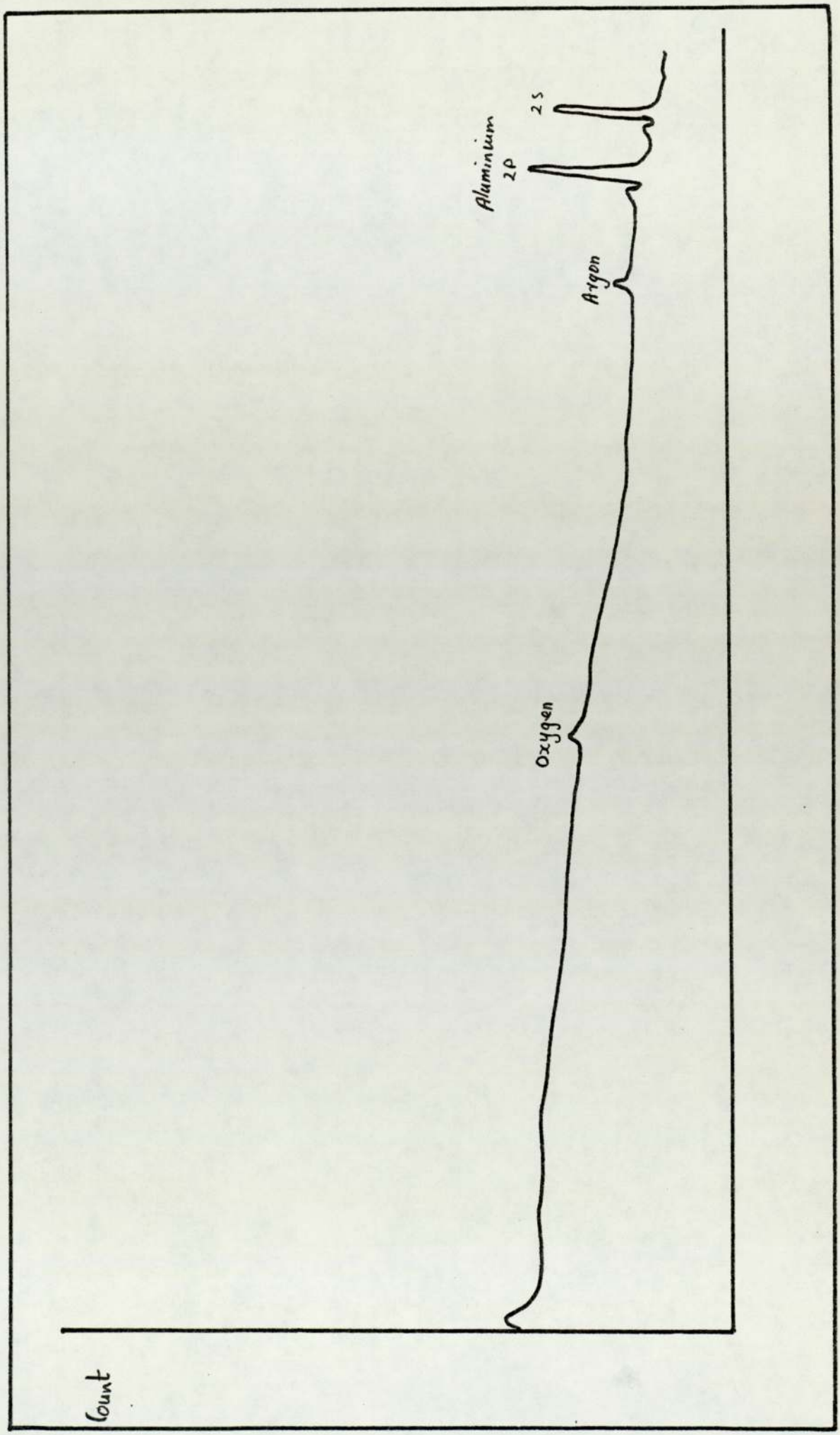

Figure 28e X.P.S. broadscan

TABLE 5a

Sample Treatment		A	B	C	D
Area of Al_{2p} Peak	Al_2O_3 Peak	78	100	100	76
	Al Peak	13	13	26	59
Al Metal Peak Position eV		1180.4	1179.8	1180.0	1180.
Al Metal $\frac{1}{2}$ width eV		1.40	1.40	1.40	1.40
Aluminium oxide peak position eV		1177.0	1177.0	1177.4	1178.4
Aluminium oxide $\frac{1}{2}$ width eV		1.80	2.04	2.04	2.16
Oxygen peak position eV main		722.5	722.5	722.5	722.6
Oxygen $\frac{1}{2}$ width eV main		2.4	2.3	2.25	2.4
Film Thickness	(Al_2O_3)=1.63nm (Al)=2.36nm	0	2.45	2.0	1.2
using Fadleys	(Al_2O_3)=1.63nm (Al)=2.5nm	0	3.09	2.3	1.4
Expression for $\Theta = 45^\circ$	$(Al_2O)_3$=2.5nm (Al)=2.5nm	0	3.82	2.8	1.5
Ellipsometric data Film thickness in nm		-	3.90	-	-

A = Aluminium sheet which had been electropolished and kept in oxygen for 5 days,

B = Etched for 6 seconds, C = Etched for 40 seconds,

D = Etched for 60 seconds.

TABLE 5b

Sample Treatment		E	F	G
Area of Al_{2p} Peak	Al_2O_3 Peak	60	9	7
	Al Peak	78	44	43
Aluminium Metal Peak Position eV		1181.48	1182.08	1182.0
Aluminium Metal ½ width eV		1.68	1.44	1.44
Aluminium oxide peak position eV		1179.1	1180.0	1180.0
Aluminium oxide ½ width eV		2.16	2.16	2.16
Oxygen peak position eV main		722.4	722.6	722.5
Oxygen ½ width eV main		2.3	2.4	2.4
Film thickness using Fadleys Expression for $\Theta=45^\circ$	(Al_2O_3)=1.63nm (Al)=2.36nm	0.8	0.27	0.26
	(Al_2O_3)=1.63nm (Al)=2.5nm	0.95	0.32	0.31
	(Al_2O_3)=2.5nm (Al)=2.5nm	1.01	0.33	0.32
Ellipsometric data Film thickness in nm		-	-	-

E = Etched for 160 seconds, F = Etched for 40 minutes

G = Etched for 60 minutes

TABLE 6b

Sample Treatment		E	F	G
Area of Al_{2p} Peak	Al_2O_3 Peak	14	15	14
	Al Peak	33	30	28
Area of O1s Peak	Main peak	31	32	30
	Secondary peak	22	21	24
Aluminium Metal Peak Position eV		1181.6	1181.0	1181.1
Aluminium Metal ½ width eV		1.44	1.40	1.40
Aluminium oxide Position eV		1179.08	1178.2	1178.6
Aluminium oxide ½ width eV		2.16	2.04	2.16
Oxygen peak position eV	Secondary	720.5	719.6	720.3
	Main	722.2	721.4	721.8
Oxygen ½ width eV main		2.22	2.04	2.04
Film thickness using Fadleys Expression $\Theta=45^\circ$	(Al_2O_3)=1.63nm (Al)=2.36nm	0.51	0.6	0.6
	(Al_2O_3)=2.0nm (Al_2O_3)=2.5nm	0.60	0.69	0.69
	(Al_2O_3)=2.5nm (Al)=2.5nm	0.63	0.72	0.72
Ellipsometric data film thickness in nm		0.65	0.85	1.0

E = 30L exposure (H_2O), F = 60L exposure (H_2O)

G = 120L exposure (H_2O)

TABLE 6a

Sample Treatment		A	B	C	D
Area of Al_{2p} Peak	Al_2O_3 Peak	12	16	18	12
	Al Peak	35	29	32	41
Area of O1s Peak	Main Peak	100	46	46	23
	Secondary Peak	9	18	22	22
Aluminium Metal Peak Position eV		1180.64	1181.4	1182.0	1181.36
Aluminium metal $\frac{1}{2}$ width eV		1.50	1.44	1.40	1.44
Aluminium oxide peak position eV		1178.3	1178.9	1179.6	1178.7
Aluminium oxide $\frac{1}{2}$ width eV		2.16	2.28	2.1	1.8
Oxygen peak position eV	Secondary	717.5	720	721.4	721.1
	main	721.0	722.0	722.8	722.8
Oxygen $\frac{1}{2}$ width eV main		2.4	2.3	2.16	2.04
Film thickness using Fadleys Expression $\theta=45^\circ$	$(Al_2O_3)=1.63nm$ $(Al)=2.36nm$	0.43	0.62	0.63	0.37
	$(Al_2O_3)=2.0nm$ $(Al_2O_3)=2.5nm$	0.5	0.74	0.75	0.44
	$(Al_2O_3)=2.5nm$ $(Al_2O_3)=2.5nm$	0.52	0.78	0.79	0.45
Ellipsometric data film thickness in nm		0.55	0.80	-	0.55

A = Aluminium sheet, etched clean and 10L exposure (H_2O)

B = 60L exposure

C = Sample was etched clean and given 60L exposure total (H_2O)

D = Sample was etched clean and given 10L exposure total (H_2O)

TABLE 6c

Sample Treatment		H	I	J
Area of Al_{2p} Peak	Al_2O_3 Peak	15	15	20
	Al Peak	27	25	34
Area of O1S Peak	Main peak	29	30	89
	Secondary peak	20	23	36
Aluminium Metal Peak Position eV		1180.6	1180.9	1180.9
Aluminium Metal ½ width eV		1.40	1.40	1.40
Aluminium oxide position eV		1178.1	1178.3	1178.1
Aluminium oxide ½ width eV		2.0	2.04	2.04
Oxygen peak position eV	Secondary	719.8	719.9	719.7
	Main	721.4	721.7	721.6
Oxygen ½ width eV main		2.1	2.1	2.04
Film thickness using Fadleys Expression $\theta=45^\circ$	(Al_2O_3)=1.63nm (Al)=2.36nm	0.63	0.66	0.65
	(Al_2O_3)=2.0nm (Al)=2.6nm	0.75	0.79	0.78
	(Al_2O_3)=2.5nm (Al)=2.5nm	0.78	0.83	0.82
Ellipsometric data film thickness in nm		1.18	1.48	-

H = 300L exposure (H_2O), I = 1800 exposure (H_2O)

J = Sample was etched clean and given 300L exposure total (H_2O)

TABLE 7a

Sample Treatment		A	B	C	D
Area of Al_{2p} Peak	Al_2O_3 Peak	23	21	19	18
	Al Peak	5	7	7	8
Area of O1s Peak	Main Peak	40	50	54	67
	Secondary Peak	14	16	18	18
Aluminium Metal Peak Position eV		1181.0	1181.1	1181.0	1181.0
Aluminium Metal $\frac{1}{2}$ width eV		1.4	1.5	1.5	1.4
Aluminium oxide position eV		1178.5	1178.3	1178.3	1178.3
Aluminium oxide $\frac{1}{2}$ width eV		2.2	2.3	2.2	2.3
Oxygen peak position eV	Secondary	719.7	720.2	719.6	719.5
	Main	721.4	722.2	721.6	721.4
Oxygen $\frac{1}{2}$ width eV, main		2.6	2.7	2.5	2.6
Film thickness using Fadleys Expression $\theta=45^\circ$	(Al_2O_3)-1.63nm (Al)=2.36nm	0.31	0.45	0.49	0.57
	(Al_2O_3)=2.0nm (Al)=2.5nm	0.34	0.49	0.54	0.63
	(Al_2O_3)=2.5nm (Al)=2.5nm	0.35	0.51	0.56	0.65
Ellipsometric data film Thickness in nm		-	0.5	0.62	0.9

A = Aluminium film, evaporated in ESCA system

B = 10L exposure of oxygen

C = 30L exposure of oxygen

D = 140L exposure of oxygen

TABLE 7b

Sample Treatment		E	F	G
Area of Al_{2p} Peak	Al_2O_3 Peak	17	16	16
	Al Peak	8	9	10
Area of O1s Peak	Main Peak	58	67	70
	Secondary Peak	18	18	20
Aluminium Metal Peak Position eV		1181.0	1181.0	1181.0
Aluminium Metal $\frac{1}{2}$ width eV		1.4	1.4	1.4
Aluminium Oxide Position eV		1178.3	1178.2	1178.2
Aluminium oxide $\frac{1}{2}$ width eV		2.2	2.2	2.2
Oxygen Peak position eV	Secondary	719.2	720.2	719.5
	Main	721.4	722.2	721.4
Oxygen $\frac{1}{2}$ width eV, main		2.5	2.5	2.6
Film thickness using Fadleys Expression for $\theta=45^\circ$	(Al_2O_3)=1.63nm (Al)=2.36nm	0.6	0.69	0.74
	(Al_2O_3)=2.0nm (Al)=2.5nm	0.65	0.75	0.82
	(Al_2O_3)=2.5nm (Al)=2.5nm	0.68	0.79	0.86
Ellipsometric data film Thickness in nm		1.1	1.3	1.5

E = 320L exposure of oxygen

F = 1220L exposure of oxygen

G = 7000L exposure of oxygen

TABLE 8a

Sample Treatment		A	B	C	D
Area of Al_{2p} Peak	Al_2O_3 Peak	28	20	18	16
	Al Peak	-	7	8	9
Area of O1s Peak	Main Peak	13	53	60	70
	Secondary Peak	2	12	12	15
Aluminium Metal Peak Position eV		1181.2	1181.1	1181.1	1181.1
Aluminium metal ½ width eV		1.4	1.4	1.4	1.4
Aluminium oxide position eV		-	1178.5	1178.5	1178.5
Aluminium oxide ½ width eV		-	2.2	2.2	2.2
Oxygen Peak position eV	Secondary	719.5	719.1	719.2	719.4
	Main	722.2	722.2	721.8	721.5
Oxygen ½ width eV, main		2.7	2.7	2.7	2.7
Film thickness using Fadleys Expression for $\theta=45^\circ$	(Al_2O_3)=1.63nm (Al)=2.36nm	-	0.47	0.57	0.69
	(Al_2O_3)=2.0nm (Al)=2.5nm	-	0.51	0.63	0.75
	(Al_2O_3)=2.5nm (Al)=2.5nm	-	0.53	0.65	0.79
Ellipsometric data, Film Thickness in nm		-	0.55	0.90	1.15

A = Aluminium film evaporated in ESCA system and etched for 5 minutes

B = 10L exposure of oxygen

C = 120L exposure of oxygen

D = 1200L exposure of oxygen

TABLE 8b

Sample Treatment		E	F	G	H
Area of Al_{2p} Peak	Al_2O_3 Peak	26	18	16	16
	Al Peak	-	8	8	9
Area of O1s Peak	Main Peak	40	68	70	73
	Secondary Peak	7	17	19	16
Aluminium metal peak position eV		1181.0	1181.0	1181.0	1181.0
Aluminium metal $\frac{1}{2}$ width eV		1.4	1.4	1.4	1.5
Aluminium oxide position eV		-	1178.2	1178.2	1178.2
Aluminium oxide $\frac{1}{2}$ width eV			2.2	2.2	2.2
Oxygen Peak position eV	Secondary	719.4	719.2	719.2	719.3
	Main	721.8	721.4	721.4	721.4
Oxygen $\frac{1}{2}$ width eV, main		2.7	2.7	2.7	2.7
Film thickness using Fadleys Expression for $\theta=45^\circ$	(Al_2O_3)=1.63nm (Al)=2.36nm	-	0.57	0.63	0.69
	(Al_2O_3)=2.0nm (Al)=2.5nm	-	0.63	0.69	0.75
	(Al_2O_3)=2.5nm (Al)=2.5nm	-	0.65	0.72	0.79
Ellipsometric data, Film thickness in nm		-	0.60	1.10	1.50

E = Aluminium film evaporated in ESCA system and etched for 5 minutes,

F = 15L exposure (H_2O),

G = 300L exposure (H_2O),

H = 1200L exposure (H_2O)

5.10 Ellipsometry Results obtained from aluminium sheets and evaporated aluminium films in vacuum

Aluminium sheets and evaporated aluminium films which had been exposed to water vapour or oxygen 'in situ' were examined by ellipsometry at a wavelength 546 nm and an angle of incidence of 64.1°.

Table 9 shows the variation of Ψ and Δ for samples of 99.99% pure aluminium sheet which has been etched with Ar^+ ions (4k volts 40 A beam current).

Sample 1

Δ ±.05	122.02	138.76	141.56	143.84	143.55
Ψ ±.05	39.75	43.1	43.32	43.50	43.60
Etch time (mins)	0	80	120	190	240

Sample 2

Δ ±.05	122.60	132.66	140.45	143.8	143.48
Ψ ±.05	41.81	40.93	43.37	43.4	43.6
Etch time (mins)	0	35	110	180	250

Sample 3

Δ ±.05	123.4	138.95	138.80	143.37	143.56
Ψ ±.05	39.9	42.29	42.85	42.89	43.0
Etch time (mins)	0	30	60	150	210

Sample 4

Δ ±.05	121.30	137.20	142.40	143.4	143.60
Ψ ±.05	38.6	37.0	43.2	43.4	43.8
Etch time (mins)	0	90	116	195	260

Sample 5

Δ ±·05	125.35	132.10	139.6	142.9	143.45
Ψ ±·05	40.80	43.1	43.0	43.8	44.1
Etch time (mins)	0	40	70	175	285

Sample 6

Δ ±·05	120.2	134.15	140.2	143.0	143.65
Ψ ±·05	37.4	39.75	42.17	43.2	44.0
Etch time (mins)	0	65	90	185	295

Sample 7

Δ ±·05	121.7	137.2	142.1	143.35	143.75
Ψ ±·05	41.2	40.8	42.6	43.35	43.65
Etch time (mins)	0	80	110	185	285

Table 10 shows the variation of Ψ and Δ for samples of 99.99% pure aluminium sheet which had first been heated at 350°C for 15 mins in air and then etched with Ar^+ ions.

Sample 8

Δ ±.05	115.15	138.68	139.67	142.33	143.61
Ψ ±.05	43.34	43.09	42.03	43.1	43.2
Etch time (mins)	0	150	185	210	285

Sample 9

Δ ±.05	115.13	138.9	140.09	141.43	143.45
Ψ ±.05	39.9	42.29	43.41	43.41	43.42
Etch time (mins)	0	160	205	230	290

Sample 10

Δ ±.05	115.13	138.90	139.45	140.10	191.43	143.47
Ψ ±.05	37.2	42.85	42.90	42.86	93.0	43.0
Etch time (mins)	0	90	120	150	210	300

Sample 11

Δ ±.05	107.9	127.61	135.39	140.06	142.50	143.50
Ψ ±.05	42.67	41.37	43.41	43.29	43.40	43.8
Etch time (mins)	0	20	85	145	230	310

Sample 12

Δ ±.05	119.22	137.4	141.65	141.958	142.35	143.42
Ψ ±.05	40.12	41.2	42.46	42.91	43.32	43.3
Etch time (mins)	0	65	105	165	245	325

Table 11 shows the variations in Ψ and Δ as etched 99.99% pure aluminium sheet was exposed to water vapour at pressures between 10^{-4} to 10^{-8} torr.

Sample 1

$\Psi \pm .05$	$\Delta \pm .05$	Exposure Langmuirs	Hydroxide thickness in nm Ellipsometry ± 5%
43.60	143.55	0	0
43.55	142.99	10	0.54
43.60	142.86	30	0.65
43.62	142.72	90	0.80
43.68	142.42	250	1.10
43.70	142.36	900	1.15
43.74	142.01	2×10^3	1.50

Sample 2

$\Psi \pm .05$	$\Delta \pm .05$	Exposure Langmuirs	Hydroxide Thickness in nm Ellipsometry ± 5%
43.60	143.48	0	0
43.64	142.95	10	0.51
43.68	142.84	30	0.60
43.70	142.69	90	0.74
43.70	142.46	200	1.00
43.67	142.36	900	1.06
43.75	142.02	1.2×10^3	1.42

Sample 3

$\Psi \pm .05$	$\Delta \pm .05$	Exposure Langmuirs	Hydroxide Thickness Ellipsometry ± 5%
43.00	143.56	0	0.0
43.20	143.00	10	0.53
43.24	142.87	30	0.66
43.30	142.73	90	0.78
43.40	142.47	300	1.03
43.45	142.39	800	1.12
43.40	142.1	1.2×10^3	1.42

Sample 4

$\Psi \pm .05$	$\Delta \pm .05$	Exposure Langmuirs	Hydroxide Thickness Ellipsometry ± 5%
43.80	143.60	0	0.0
43.90	143.04	10	0.54
43.85	142.91	30	0.67
43.90	142.77	90	0.78
43.94	142.48	250	1.06
44.00	142.41	900	1.13
44.05	142.03	2×10^3	1.31

Sample 8

$\Psi \pm .05$	$\Delta \pm .05$	Exposure Langmuirs	Hydroxide Thickness Ellipsometry ± 5%
43.20	143.61	0	0.0
43.27	143.05	10	0.53
43.32	142.92	30	0.65
43.30	142.52	200	0.96
43.40	142.42	900	1.15
43.45	142.12	1.2×10^3	1.45

Sample 9

$\Psi \pm .05$	$\Delta \pm .05$	Exposure Langmuirs	Hydroxide Thickness Ellipsometry ± 5%
43.42	143.45	0	0
43.45	142.89	10	0.54
43.40	142.76	30	0.66
43.50	142.61	90	0.78
43.50	142.36	300	1.04
43.50	142.29	800	1.14
43.55	141.95	1.2×10^3	1.48

Sample 10

$\Psi \pm .05$	$\Delta \pm .05$	Exposure Langmuirs	Hydroxide Thickness Ellipsometry ± 5%
43.0	143.47	0	0
43.1	142.92	10	0.52
43.15	142.78	30	0.66
43.18	142.65	90	0.80
43.18	142.40	200	1.06
43.20	142.29	900	1.17
43.20	141.94	2×10^3	1.30
43.25	141.77	7×10^3	1.70

Sample 11

$\Psi \pm .05$	$\Delta \pm .05$	Exposure Langmuirs	Hydroxide Thickness nm Ellipsometry ± 5%
43.80	143.50	0	0
43.80	142.95	10	0.55
43.85	142.86	30	0.64
43.90	142.60	200	0.90
43.85	142.49	300	1.0
43.90	142.16	1×10^3	1.34

Sample 12

$\Psi \pm .05$	$\Delta \pm .05$	Exposure Langmuirs	Hydroxide Thickness nm Ellipsometry ±5%
43.3	143.42	2	0.2
43.31	143.21	10	0.5
43.30	142.89	30	0.62
43.40	142.78	200	0.90
43.45	142.51	300	1.00
43.47	142.41	1×10^3	1.32
43.5	142.08	4×10^3	1.50
43.5	141.68	3×10^4	1.72

Table 12 shows the variations in Ψ and Δ as etched 99.99% pure aluminium foil was exposed to oxygen at pressures between 10^{-4} to 10^{-2} torr.

Sample 5

$\Psi \pm .05$	$\Delta \pm .05$	Exposure Langmuirs	Hydroxide Thickness Ellipsometry nm ± 5%
44.10	143.45	0	0
44.10	142.92	10	0.51
44.15	142.82	30	0.60
44.00	142.55	200	0.88
44.20	142.45	300	0.98
44.20	142.13	1×10^3	1.28

Sample 6

$\Psi \pm .05$	$\Delta \pm .05$	Exposure Langmuirs	Hydroxide Thickness Ellipsometry nm ± 5%
44.0	143.65	0	0
44.10	143.09	10	0.54
44.10	143.01	30	0.61
44.15	142.87	90	0.74
44.20	142.71	250	0.90
44.15	142.42	900	1.21
44.20	142.17	4×10^3	1.40

Sample 7

$\Psi \pm .05$	$\Delta \pm .05$	Exposure Langmuirs	Hydroxide Thickness Ellipsometry nm ± 5%
43.65	143.75	0	0.0
43.70	143.19	10	0.54
43.80	143.09	30	0.63
43.85	142.80	200	0.93
43.90	142.68	300	1.05
43.95	142.38	1×10^3	1.34

Table 13 shows the variations in Ψ and Δ for an evaporated aluminium film, on aluminium foil as a substrate, and exposed to oxygen.

$\Psi \pm .05$	$\Delta \pm .05$	Exposure Langmuirs	Hydroxide Thickness nm Ellipsometry ± 5%
44.10	144.12	0	0.0
44.10	143.6	10	0.50
44.16	143.41	50	0.75
44.20	143.03	400	1.08
44.20	142.82	2×10^3	1.32
44.30	142.52	1×10^4	1.60

Table 14 shows the variations in Ψ and Δ for an evaporated aluminium film, on aluminium foil as a substrate, and exposed to water vapour

$\Psi \pm .05$	$\Delta \pm .05$	Exposure Langmuirs	Hydroxide Thickness nm Ellipsometry ± 5%
44.13	144.23	0	0
44.18	143.69	10	0.52
44.20	143.36	70	0.85
44.25	143.09	300	1.12
44.30	142.9	1×10^3	1.33
44.40	142.58	6×10^3	1.62

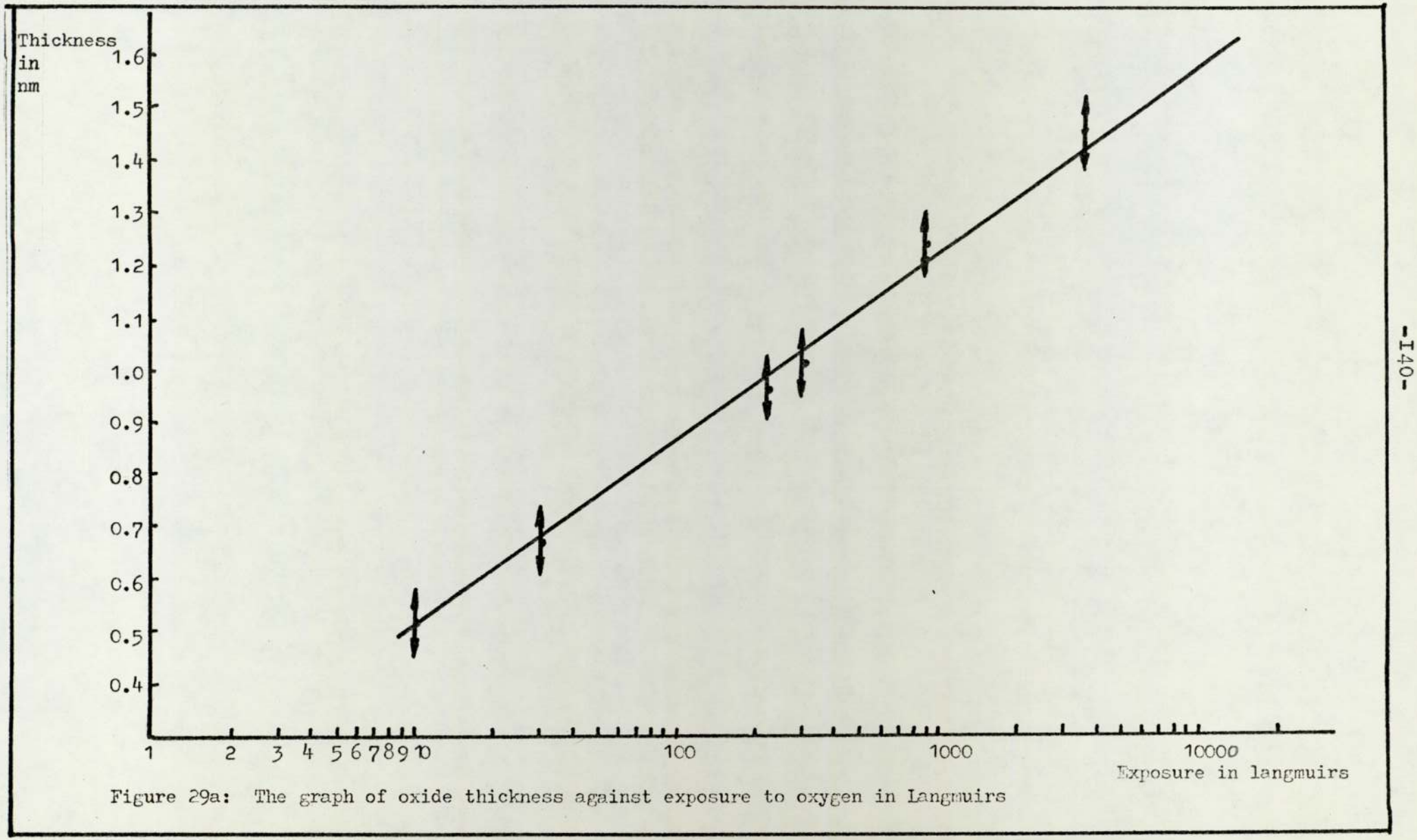

Figure 29a: The graph of oxide thickness against exposure to oxygen in Langmuirs

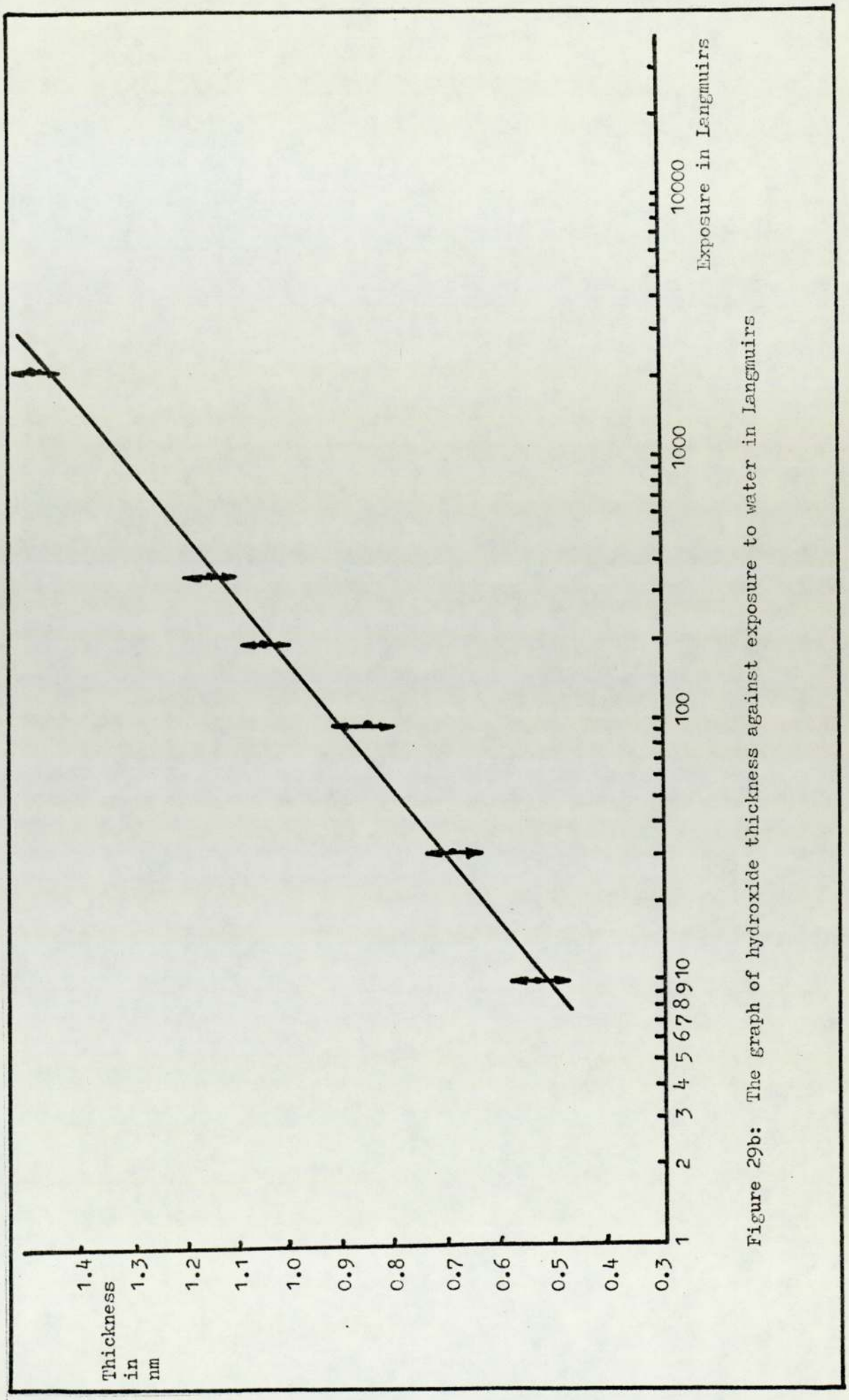

Figure 29b: The graph of hydroxide thickness against exposure to water in Langmuirs

5.11 Discussion of ESCA results

In situ experiments in the ESCA apparatus were performed to measure the thickness of oxide and hydroxide films and their structure on aluminium sheets and evaporated aluminium films.

For experimental purposes oxide and hydroxide films were grown under controlled conditions. Before these experiments could be performed on aluminium sheets, the protective oxide films were removed, 'in situ' by Argon ion etching with an accelerating voltage of 4kV and ion beam current of 40 uA. After etching the sample was transferred to the analysing chamber where the aluminium 2p peak was examined. As can be seen from aluminium 2p peak Figure 28a, etching removed the aluminium oxide film. Etching was continued until the aluminium metal peak was the only peak observable Figure 28b, but when the oxygen peak was examined, oxygen was still found to be present on the surface Figure 28e.

The origin of oxygen on the surface could be due to the oxygen in the solution of the metal (Hansen and Anderko[164]) or it could be due to the adsorption from the vacuum system. The second possibility can be ruled out because the pressure in the analysing chamber was 10^{-9} torr or less and at this pressure it would take approximately 10^{3} seconds to form a monolayer of adsorped oxygen. There is another possibility to explain the origin of the oxygen present on surface. During ion etching a number of different mechanisms are operating (McCraken). One of them is the knocking of surface atoms into the matrix. This could be one explanation of the oxygen presence even after the aluminium oxide peak had disappeared. But with continual etching, oxygen from this origin should also be reduced to undectectable levels. This was found not to be the case.

For experimental purposes the sample was etched until the level of oxygen peak reached a plateau and this was taken to be the

starting surface. Producing a 'clean' starting surface by ion etching technique may give a clean surface from the point of view of the surface composition. But structurally it is different, in that there are dislocations and vacancies induced by ion etching (McCraken).

Deliberate oxidation, for experimental purposes, was achieved by bleeding in dry oxygen between pressures of 10^{-8} to 10^{-4} torr. This pressure range was chosen because, Haber and Kirk [79] believed that the oxide formed within the pressure range of 10^{-3} to 10^{-4} torr was structurally different to oxide formed at higher pressures. As will be discussed, there was no evidence for it. Hydroxide films were grown by bleeding in (H_2O) water vapour from a water reservoir which had been continuously pumped for 3 hours at a pressure of 10^{-4} torr. This removed the adsorbed oxygen in water.

After each exposure in Langmuirs, the sample was transferred to the analysing chamber, under the same vacuum, where it was analysed for the growth of oxide and hydroxide film by recording the spectra of oxygen and aluminium 2p peak.

During exposure to X-ray radiation there was a temperature rise but this was small compared to the initial heat treatment given to the aluminium sheet, therefore damage caused by X-ray radiation to the sample must have been minimal.

5.11.1 Discussion: Oxide and hydroxide films on aluminium sheet

To calculate the oxide and hydroxide film thickness from the ESCA results the first step was to resolve the aluminium 2p peak into aluminium oxide and aluminium metal peaks, Figure 29e. This was done by using a curve resolver. Once the peak was resolved it was possible to measure the relative areas of aluminium oxide and aluminium metal under the peaks. When one examines the equation 3.9 which is simplified from Fadleys expression [142], to calculate the

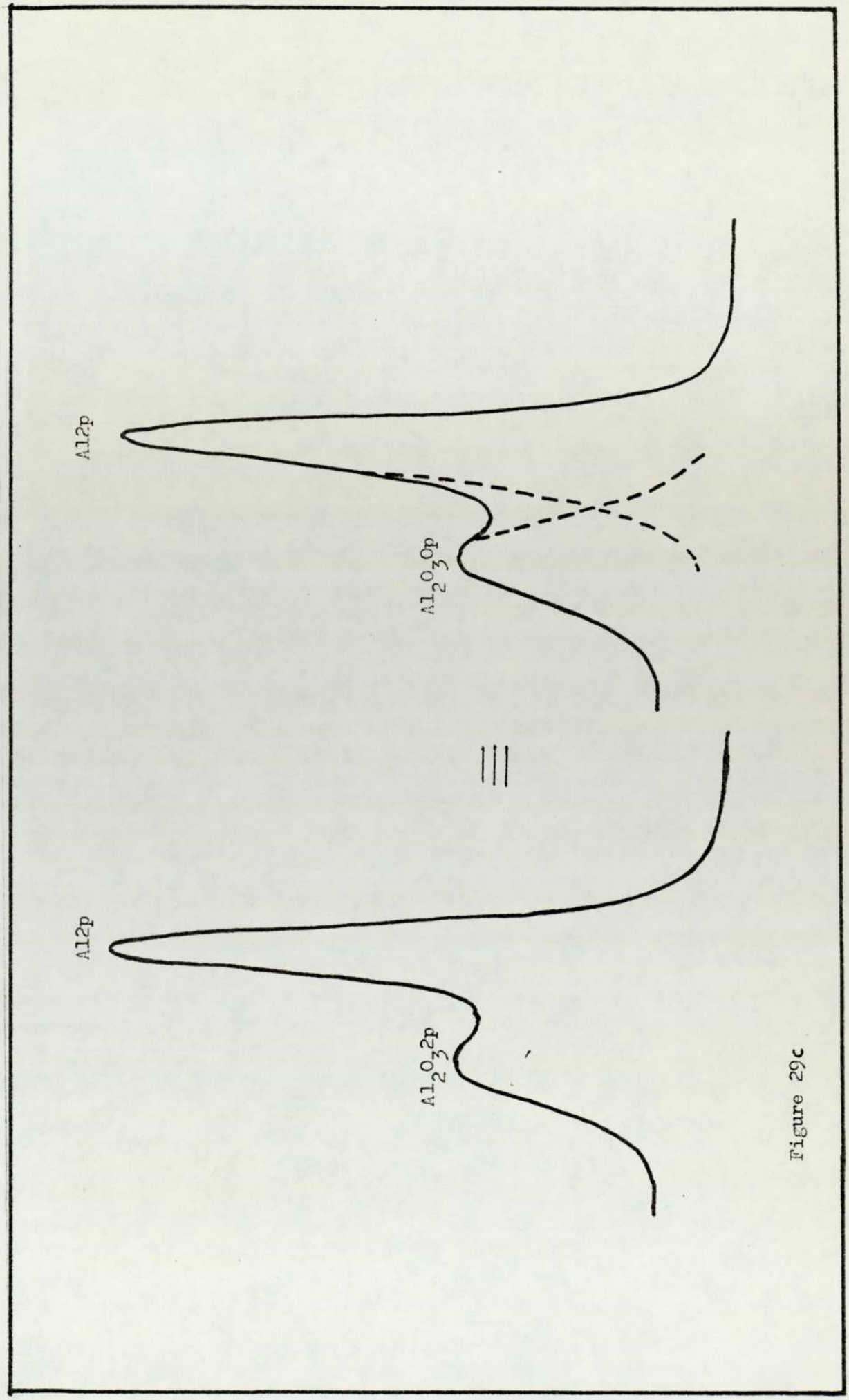

Figure 29c

oxide of hydroxide film thickness only the ratio of the area under the aluminium oxide and aluminium metal peaks is required.

$$\ln \left[\frac{\text{area under the aluminium oxide peak}}{\text{area under the aluminium metal peak}} \frac{\Lambda_e(E)(Al)}{\Lambda_e(E)(Al_2O_3)} + 1 \right] \Lambda'_e(E) \sin 45^\circ$$

$$= t \text{ (Film thickness)}$$

The other parameters required to calculate film thickness, are the attentuation length or escape depths of electron in aluminium metal and aluminium oxide.

These were taken from the literature (Powell) [165] 1.63 nm for aluminium oxide and 2.36 nm for aluminium metal and the results presented in Table 5 and 6. An exposure of 10L, of water vapour, only produced a film thickness of 0.37nm. The sticking coefficient calculated from these results agreed quite well with Fort and Wells [126].

Later experiments on oxide film growth, on aluminium sheet for longer exposures (7000L). Table 7 shows that the oxide film grows to 0.74 nm With further exposures at atmospheric pressure for 21 sec (1.5×10^{10}L), the film thickness was found to be 1.8nm, but when the sample was exposed for longer periods at atmospheric pressure (under dry conditions) the oxide film thickness was such that the aluminium 2p metal peak could not be observed. The oxide film thickness after such exposures was much greater than the escape depth of electron in aluminium oxide.

The thickness of aluminium hydroxide film was found to be greater than the oxide films, for same exposure time, using the same values for the escape depth (Figure 30b) as for the aluminium oxide. One of the reasons for using the escape depth of aluminium oxide for calculating the hydroxide film thickness was, that no values of escape depth for aluminium hydroxide have been reported in the

literature. The second reason was that, no difference could be detected by ESCA, in the peak position of the aluminium oxide and hydroxide or the half-width of aluminium oxide and hydroxide peaks.

When the aluminium oxide and aluminium metal peaks were resolved, using a curve resolver there was some difficulty in the measurement of the areas under the aluminium oxide peak, because for a pure aluminium metal the 2p peak is not symmetrical (Figure 28b).

When the aluminium sample is exposed to oxygen or water vapour, the oxide and hydroxide peaks are on the same side, on which the aluminium metal peak has the shoulder. With all these problems, it was still possible to compare the results from evaporated aluminium film and aluminium sheets. For the same exposure in Langmuirs the calculated thicknesses of aluminium oxide film on evaporated aluminium film and aluminium sheet are comparable tables 15, 16, 17.

It can be seen that an exposure of 10L on evaporated aluminium film gives an oxide thickness of 0.45nm. The same exposure of aluminium sheets give an oxide thickness of 0.45nm. To compare the rate of growth of aluminium oxide film, on ion etched aluminium films to clean aluminium evaporated film, the aluminium films were ion etched in the preparation chamber for 5 minutes after which the specimen was transferred to the analysing chamber under the same vacuum conditions.

The examination of the aluminium 2p peak, showed only the aluminium metal peak at a peak position of 1181.2 eV. But when the oxygen peak was examined, oxygen was still found to be present on the surface in small amounts. Further ion etching did not reduce the level of oxygen. The presence of oxygen throughout the evaporated aluminium films could be possibly due to volume oxidation arising from the increase in pressure to 5×10^{-7} torr,

during evaporation. The pressure fell to 1×10^{-9} torr soon after evaporation. Neal et al[31] have argued that there was a possibility of volume oxidation, during evaporation. The only other element which could be detected by the ESCA method, after ion etching was Argon, in very small amounts arising from the ion etching process.

For the same exposures, oxide growth on etched and unetched evaporated aluminium films showed very little difference (Table 7 and 8). Therefore any vacancies and dislocation caused by ion etching had little effect on the rates of growth.

Different values of escape depth for electrons in aluminium and aluminium oxide at 1180 eV energy and at an angle of 45° were used to calculate the film thickness. The results were ploted on Figure 30. As can be seen from the Figure 30, increasing the escape depth from 1.63nm increases the calculated film thickness by 0.1nm.

There are small variations in the half-widths of the aluminium metal and aluminium oxide peaks. It is difficult to draw conclusions whether these variations were due to change in oxide structure or were just random variations.

In all the experiments either oxygen or water vapour exposure, the oxygen peak could be resolved into two separate peaks. When the specimens were exposed to oxygen the peaks were separated by 1.7 eV. The conclusion one reaches is, that oxygen on the surface is in two states, oxides and the other adsorped oxygen. When the samples were exposed to water vapour, oxygen peaks could still be resolved into two peaks. Furthermore there were a few oxygen peaks which could be resolved into three peaks. The conclusion one reaches in this case is, that the oxygen was present on the surface of the specimen in three states, oxide, hydroxide and adsorbed oxygen in the form of water vapour molecules. But this situation was found only in a few cases. In most cases the two oxygen peaks were separated by 1.9 eV.

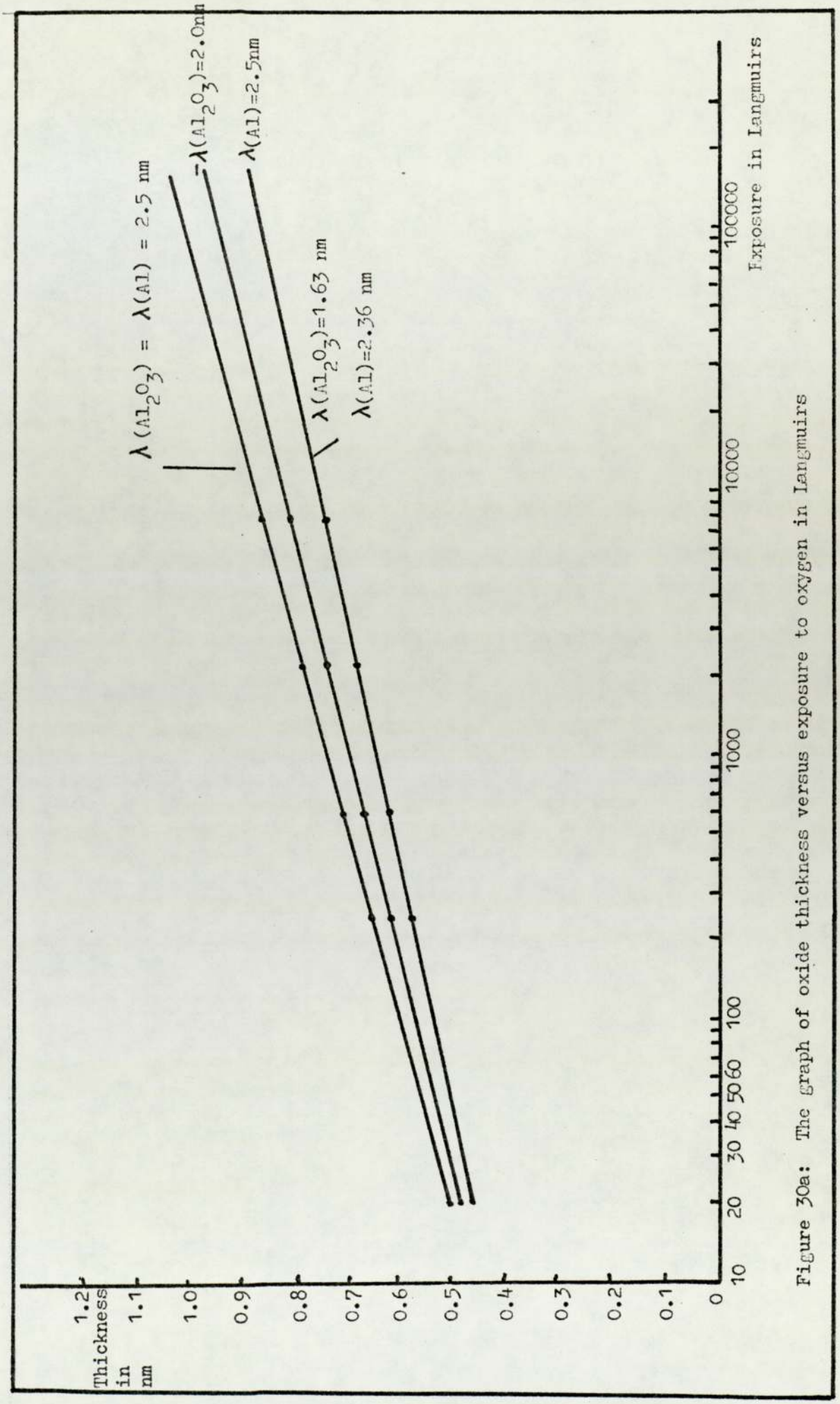

Figure 30a: The graph of oxide thickness versus exposure to oxygen in Langmuirs

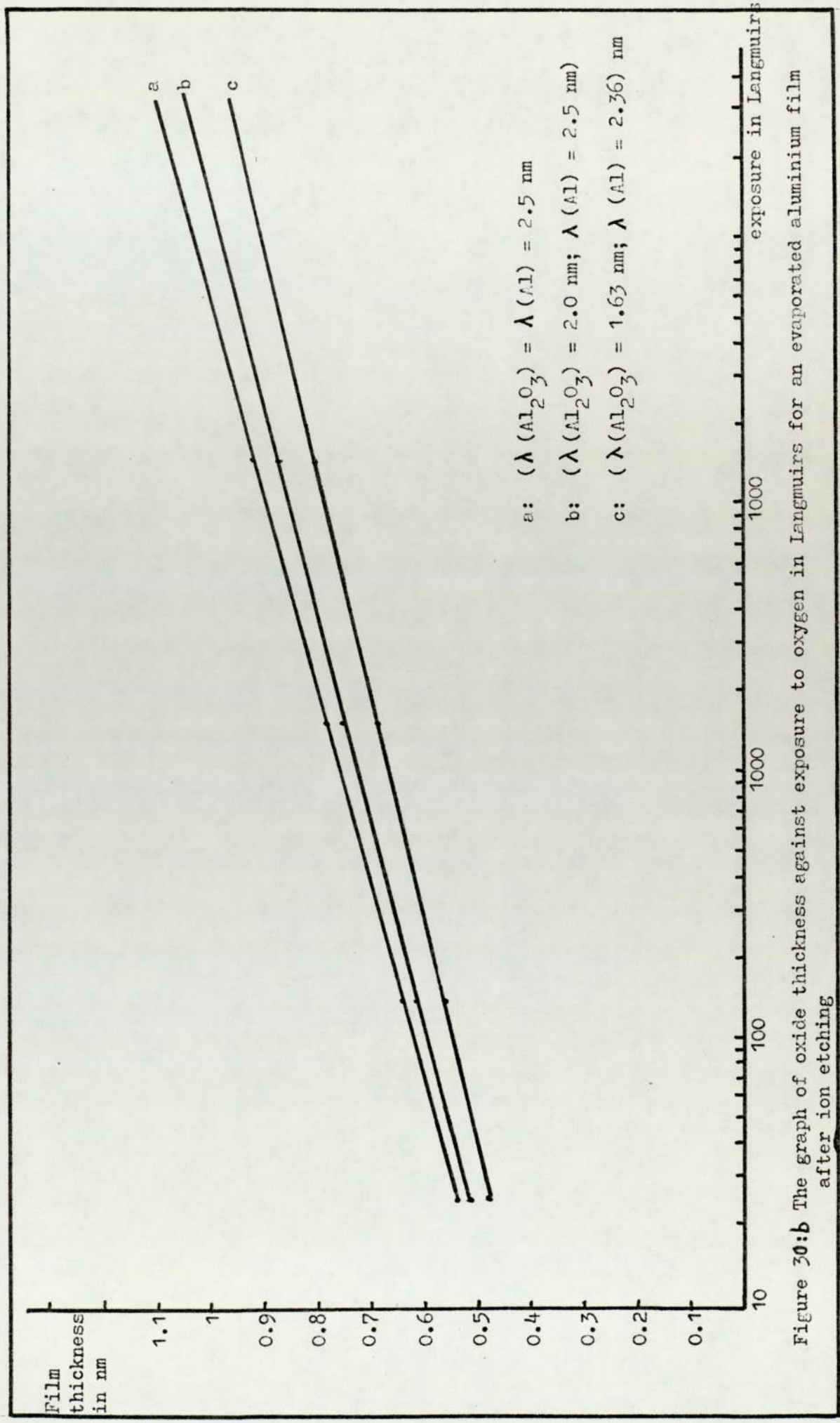

Figure 30:b The graph of oxide thickness against exposure to oxygen in Langmuirs for an evaporated aluminium film after ion etching

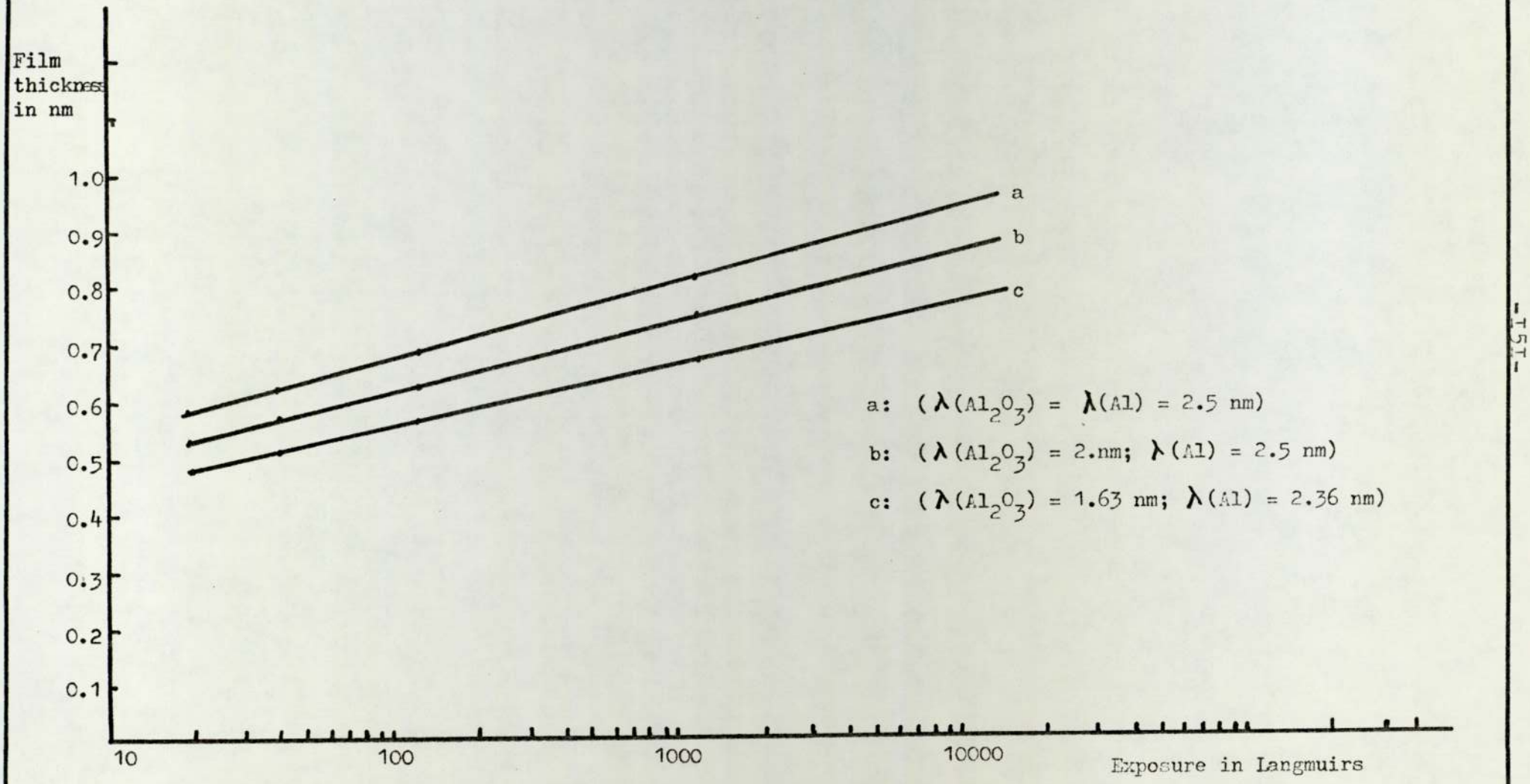

Figure 30:c The graph of Hydroxide film thickness against exposure to water vapour in Langmuirs (sheet)

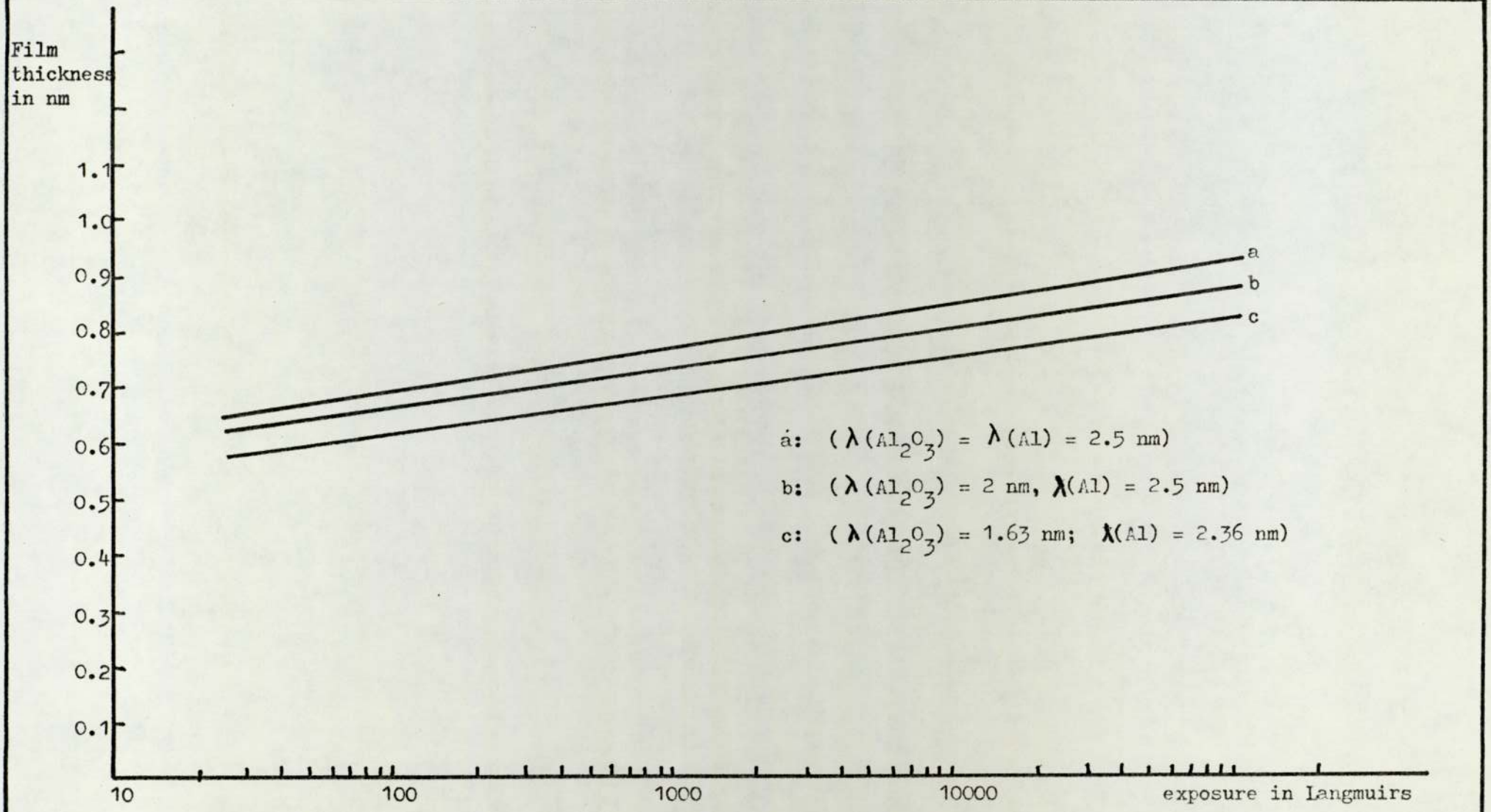

Figure 30:d The graph of Hydroxide film thickness against exposure to water vapour in Langmuirs

Fuggle et al [127] have reported similar work on evaporated films. In their studies, they also found oxygen present on the surface in three different states, but their experimental conditions were different. In their experiments the sample was cooled to -77°C. Therefore oxygen peaks were assigned to condensed water (ice) and the other two oxygen peaks assigned to aluminium oxide and tentatively to aluminium hydroxide. Therefore in the case of water vapour exposure in the present work aluminium oxide and aluminium hydroxide were present together.

5.11.2 Discussion: Ellipsometry (vacuum)

Ellipsometry was used as a complementary technique, to measure oxide and hydroxide film thicknesses grown 'in situ' under ultra high vacuum conditions on aluminium sheets and evaporated aluminium films.

Before aluminium sheets could be exposed to oxygen or water vapour for experimental purposes, protective oxide films were removed 'in situ' by Argon ion etching, the sample was rotated to a position previously determined by alignment in the ellipsometry i.e. detected by the photomultiplier of the instrument after reflection from the sample. Ellipsometry readings were taken and the parameters Ψ and Δ were calculated and corrected for effects of the windows. For further ion etching the sample was rotated back to the position where Argon ion etching could take place.

Since ellipsometry was being used as a complementary technique, the same experimental conditions had to be obtained as in ESCA experiment. Ion etching was therefore conducted at the same accelerating voltage, ion beam current and angle as in ESCA. From ESCA experience, it was calculated how much ion etching was required to produce a chemically 'clean' surface. In ellipsometry experiments

Ψ and Δ parameters were used to obtain a starting surface. Further ion etching was continued until no further noticable change in ellipsometric parameters Ψ and Δ was detected. In all the cases, the period of ion etching was longer, by 40 minutes, than the time required in the ESCA method to produce a chemically 'clean' surface.

Therefore the sample for ellipsometric experiments were chemically 'clean' and also perhaps with more vacancies and dislocations. To reduce the number of vacancies and dislocations, the sample was left in vacuum (10^{-9} torr) for 18 hours. During this time, two different processes were taking place. One a thin oxide film grew on the surface of the sample and second, since aluminium anneals at low temperature (O'Shea)[148] (25°C room temperature), the number of vacancies and dislocations were reduced.

Finally to produce the starting surfaces, which were chemically 'clean' and structurally similar to the starting surface in ESCA experiments, the sample was ion etched for a further 5 minutes. This etch time would produce less damage after the annealing stage.

Deliberate oxidation, for experimental purposes was achieved by bleeding in dry oxygen between pressures of 10^{-8} to 10^{-4} torr. This pressure range was chosen in order to perform the experiments under similar conditions as in the ESCA tests. Hydroxide films were grown by bleeding in water vapour, from a water reservoir between a pressure range of 10^{-8} to 10^{-4} torr which had been continuously pumped for 5 hours at a pressure of 10^{-3} torr.

The time taken for each ellipsometric pair of readings was small compared to the time required for an ESCA spectrum. This reduced the error in the exposure time. In this technique the amount of energy which interacts with the sample, is very small. Therefore the complication produced, in the study of oxide and hydroxide film thickness by ESCA, due to surface heating in the ESCA equipment is

negligible in ellipsometry.

5.11.3 Discussion: Oxide thickness

Aluminium sheet samples heated at 250°C and 350°C for 10 minutes, were ion etched to produce 'clean' starting surfaces. From ellipsometric readings it was possible to calculate the original aluminium oxide film thicknesses which were found to be 20nm and 2.8nm respectively. With the ESCA technique original oxide thickness greater than the escape depth can only be estimated by ion etching.

Oxide and hydroxide film thicknesses were calculated by assuming n = 1.58 and k = 0. The optical constant of the aluminium oxide films, prepared under these conditions have not been reported in the literature. However, the optical constants of thicker films have been reported to be between (n = 1.58 - 1.65) and k = 0. To calculate the thickness of thin oxide films, the spread of optical constant has little effect on the thickness i.e. for films less than 15.0 nm.

In the ellipsometric apparatus, there was a shutter in front of the substrate, to reduce contamination when the aluminium film was evaporated from the tungsten filament. Ellipsometric parameters, Ψ and Δ , when measured were found to be lower than the reported values, by Alan, Fane and Neal [137] . This again could be due to the increase in pressure to 6×10^{-7} torr during evaporation despite the rapid decrease to 5×10^{-9}, soon after evaporation. There was some volume oxidation which was found through the evaporated film, in that similar values of Ψ and Δ were obtained as the film was etched.

Comparison of the film thicknesses obtained by ellipsometric and ESCA techniques showed that thickness measured by the ellipsometry techniques were constantly higher for all exposures, Table 15 to 17. For low exposures the differences were small, well within the

Treatment to the sample	ESCA. Film thickness using Fadleys expression ± 10% (a) (Al_2O_3)=1.63nm, Al=2.36nm, θ=45°	(b) (Al_2O_3)=2.00nm Al=2.5nm, θ=45°	(c) (Al_2O_3)=2.5nm θ=45°	Ellipsometric data (d) Film thickness in nm ± 5%	Difference in film thickness, nm (d-a)	(d-b)	(d-c)
Aluminium film, evaporated in ESCA system and etched for 5 minutes 10L exposure (oxygen)	0.47	0.51	0.53	0.55	0.08	0.04	0.02
120L exposure (oxygen)	0.57	0.63	0.65	0.40	0.33	0.27	0.25
1200L exposure (oxygen)	0.69	0.75	0.79	1.15	0.46	0.40	0.36
Aluminium film, evaporated in ESCA system and etched for 5 minutes 15L exposure (H_2O)	0.57	0.63	0.65	0.60	0.03	-0.01	-0.05
300L exposure (H_2O)	0.63	0.69	0.72	1.10	0.47	0.41	0.38
1200L exposure (H_2O)	0.69	0.75	0.79	1.50	0.81	0.75	0.71

TABLE 15

Treatment to the sample	ESCA. Film thickness using Fadleys expression ±10% (a) (Al_2O_3)=1.63nm Al=2.36nm, θ=45°	(b) (Al_2O_3)=2.00nm Al=2.5nm, θ=45°	(c) (Al_2O_3)=2.5nm θ=45°	Ellipsometric data (d) Film thickness in nm ± 5%	Difference in film thickness, nm (d-a)	(d-b)	(d-c)
Aluminium film, evaporated in ESCA system 10L exposure (oxygen)	0.45	0.49	0.51	0.5	0.05	0.01	-0.01
30L exposure (oxygen)	0.49	0.54	0.56	0.62	0.13	0.08	0.06
140L exposure (oxygen)	0.57	0.63	0.65	0.9	0.33	0.27	0.25
320L exposure (oxygen)	0.6	0.65	0.68	1.1	0.5	0.45	0.42
1220L exposure (oxygen)	0.69	0.75	0.79	1.3	0.61	0.55	0.51
7000L exposure (oxygen)	0.74	0.82	0.86	1.5	0.76	0.68	0.64

TABLE 16

Treatment to the sample	ESCA. Film thickness using Fadleys expression ± 10% (a) (Al_2O_3)=1.63nm, Al=2.36nm, Θ=45°	(b) (Al_2O_3)=2.00nm Al=2.5nm, Θ=45°	(c) (Al_2O_3)=Al=2.5nm Θ=45°	Ellipsometric data (d) Film thickness in nm ± 5%	Difference in film thickness, nm (d-a)	(d-b)	(d-c)
Aluminium sheet, which had been electropolished and kept in dry air for 15 days and ion etched 'clean' 10L exposure (H_2O)	0.43	0.5	0.52	0.55	0.12	0.05	0.03
60L exposure (H_2O)	0.62	0.74	0.78	0.80	0.18	0.06	0.02
Sample was etched clean and given 60L exposure total (H_2O)	0.63	0.75	0.79	-	-	-	-
Sample was etched clean and given 10L exposure. (H_2O)	0.37	0.44	0.45	0.55	0.18	0.11	0.10
30L exposure (H_2O)	0.51	0.60	0.63	0.65	0.14	0.05	0.02
60L exposure (H_2O)	0.60	0.69	0.72	0.85	0.25	0.16	0.13
120L exposure (H_2O)	0.60	0.69	0.72	1.0	0.4	0.31	0.28
300L exposure (H_2O)	0.63	0.75	0.78	1.18	0.55	0.43	0.4
1800L exposure (H_2O)	0.66	0.79	0.83	1.48	0.82	0.69	0.65

experimental errors, but for longer exposures the differences in film thickness were large and could only be reduced by increasing the value of escape depth for electron in aluminium oxide and thereby increasing the calculated film thickness obtained by the ESCA technique. Chang and Boulin [167] have recently reported a disagreement between thicknesses measured by ellipsometry and Auger spectroscopy. They measured the oxide thickness on Si by using Auger electron spectroscopy, without ion etching depth profiling, by using the ratio of the chemically shifted and unshifted peaks from the oxide and substrate. They concluded that, with the estimated absolute accuracy for their technique of 10%, comparisons of the Auger measurements of the thickness, with ellipsometric determinations revealed a discrepancy which was larger than their estimated limits of error. They found no way of reducing the observed disagreement without introducing other less acceptable, contradictions.

Chang and Boulin reached the conclusion that a large part of the discrepancy originated from a fundamental difference in the definitions of the interface plane because of the different physical parameters measured.

The one possibility Chang and Boulin did not look into was that the initial oxide films grow in the forms of islands as shown in Figure 31. As can be seen from the Figure 31 the island height may be larger than the escape depth of the electron in aluminium oxide. Therefore the oxide at the base is not detected by ESCA, but this is not the case with ellipsometry because there is no limit to the thickness of the film it can detect as long as k=0 or very small as is the case in aluminium oxide films. In practice the substrate may not be planar. Therefore the island could be represented as shown in Figure 32. Here again the oxide film may be too thick, in places,

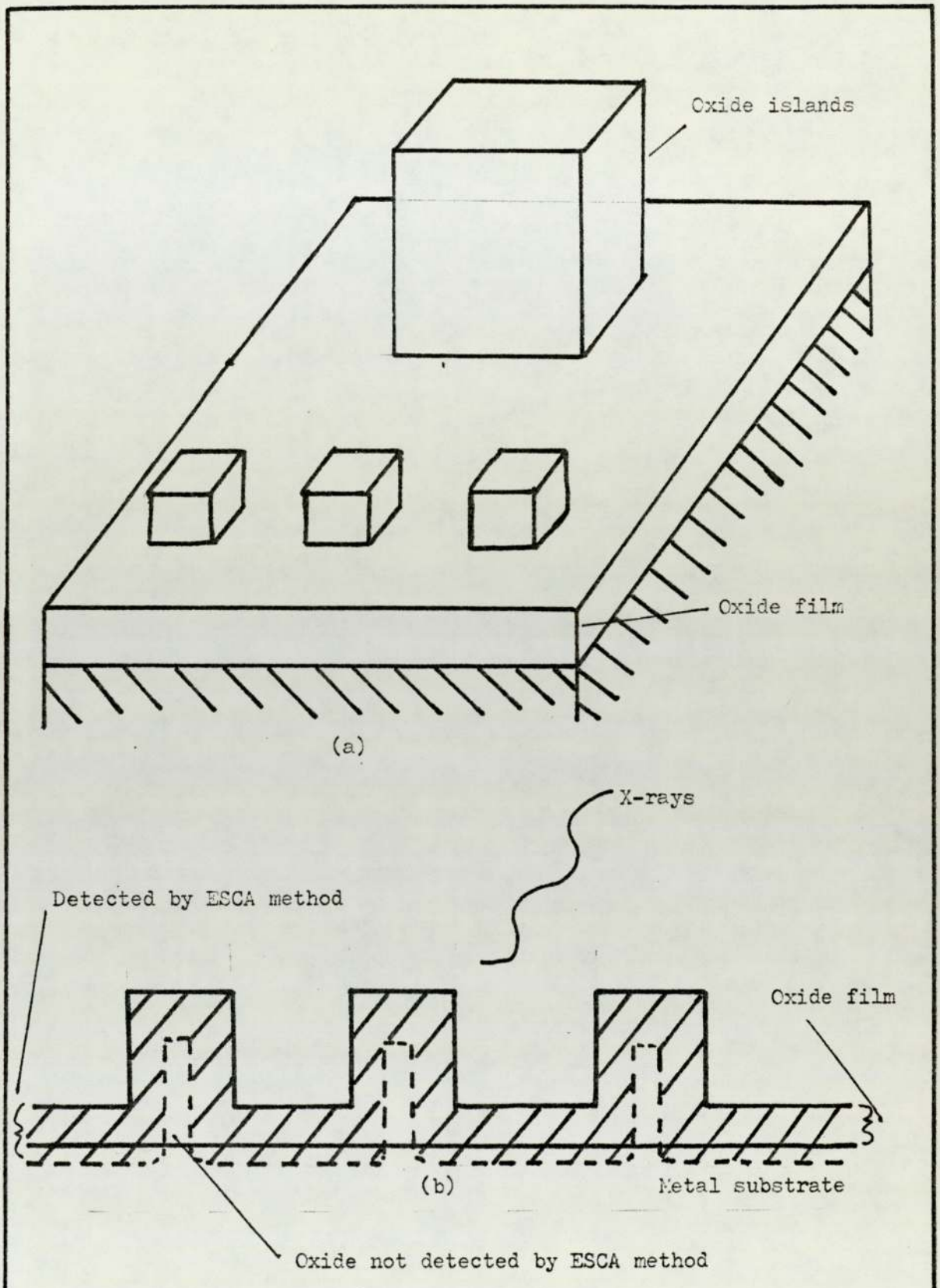
Oxide islands
Oxide film
(a)
X-rays
Detected by ESCA method
Oxide film
(b)
Metal substrate
Oxide not detected by ESCA method

Figure 31

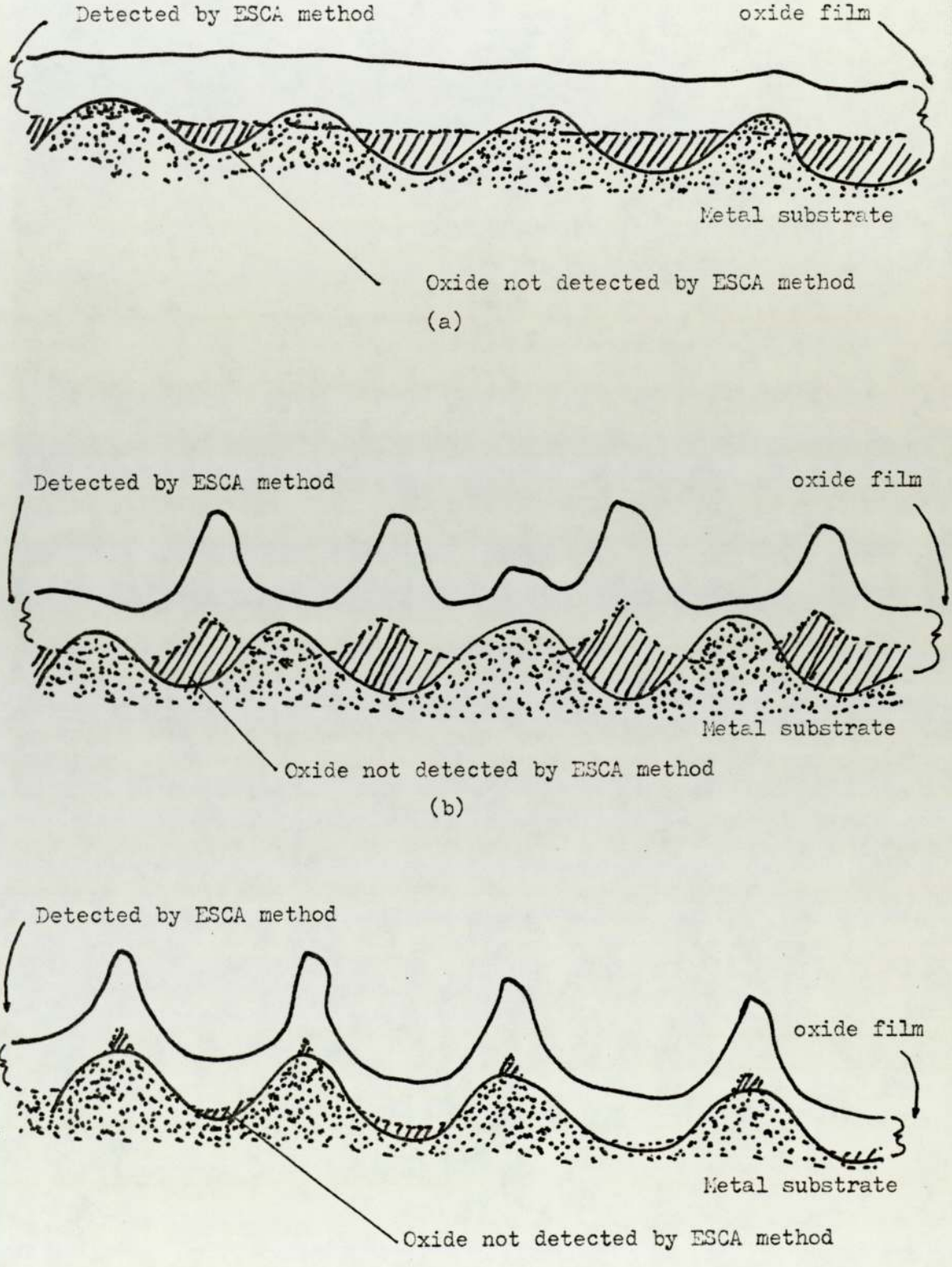
Detected by ESCA method
oxide film
Metal substrate
Oxide not detected by ESCA method
(a)
Detected by ESCA method
oxide film
Metal substrate
Oxide not detected by ESCA method
(b)
Detected by ESCA method
oxide film
Metal substrate
Oxide not detected by ESCA method

Figure 32

for the ESCA technique to detect. From the data obtained it is difficult to obtain the height and number of island present on any sample because of the number of variables, such as, substrate structure, locations of the islands, dimensions and the number of islands on any area. This aspect of the effect of the growth mechanism on measured film thickness needs further investigation.

5.12 Summary

In order to study the rate of growth of aluminium oxide and hydroxide films, on aluminium sheets with ellipsometry, the original protective oxide film formed during rolling was removed by Phosbite etching. The changes in the ellipsometry parameters Ψ and Δ were difficult to explain. Further investigation using EDX analysis, showed that the new oxide film contined copper contamination and the source of this copper copper contamination was bound to be in Phosbite solution. Neal[167] had obtained similar effects with silver films which had been deliberately contaminated with 1% or 2% copper.

SEM results showed that the aluminium hydroxide (pseudoboehmite) grows in the form of islands, with bayerite within it. The islands grow in two directions, becoming thicker and at the same time growing along the surface until they join up to form a continuous film. Examination in the reflective mode showed that the bayerite crystals grow from the aluminium substrate.

ESCA examination of the aluminium hydroxide grown on aluminium sheets showed high levels of carbon contamination on the surface, which decreased rapidly as the sample was ion etched. This contamination had probably arisen from the atmosphere and sample handling. The ratio of oxygen (corrected level) to aluminium (corrected level) decreased as the sample was etched, but as the sample was further etched the ratio increased. This can be

explained by trapped aluminium in the hydroxide matrix and isolated from the aluminium substrate. Barr[158] has reported similar results.

The examination in SEM, of aluminium film with copper contamination after exposure to water vapour saturated air (WVSA) for 5 minutes showed islands, which were similar to the islands on pure evaporated aluminium films and aluminium sheet. Further examination showed that the presence of copper increases the reaction rate, which could be seen from the interface of aluminium/copper film and aluminium film.

For the measurement of hydroxide film thickness, an independent method (interferometry) was used. The reason why an independent method was used was because of an apparent discrepancy between the measurement by ellipsometry and by Tucks method[4]. Tuck repeated his technique using evaporated aluminium film - as in this work, in the thickness range of 10nm to 300nm. His results obtained from these experiments agreed with the film thickness measured by the Transparency technique.

Film thickness measured by the Transparency technique and ellipsometry agreed to within experimental errors. Therefore it was concluded ellipsometry could be satisfactorilly used for measuring hydroxide film thickness in the early stages of growth.

The refractive index of the aluminium hydroxide was measured ellipsometrically by, first evaporating gold films. The gold base (gold film) yielded initial values of ψ and Δ which were substituted into equation 3.22 and 3.23 to evaluate the optical constants n_2 and k_2 for the surface. Using these computed constants and a two layer programme, values of the angles ψ and Δ were computed for composite surfaces of varying aluminium hydroxide thicknesses on gold and on assumed value of refractive index for the hydroxide. When the optical parameter ψ and Δ for films less

than 80nm were plotted on the computed graph were k=0 there was agreement between the computed thickness and measured thickness by interferometry. There were two samples (7 and 8) for which the measured optical parameter Ψ and Δ did not lie on the computed closed loops (k=0), but with a value of $k_1 = 0.0009$ (small absorption) 7 and 8 were found to lie on the computed loops. It would appear therefore that in early stages of growth the optical constants for the hydroxide at a wavelength of 546nm are $n_1 = 1.58 \pm 0.03$ and $k_1 = 0$ and for thicker films the constants are better given by $n_1 = 1.58 \pm 0.03$ and $k_1 = 0.0009$.

Aluminium hydroxide films formed on glass and on gold film substrate were in the form of islands. The sensitivity of the method for determining the constants of the superimposed hydroxide layers depends on the relative optical constants of the base and film. It is also important that the base material is non reactive and this was the reason for using gold.

ESCA and Ellipsometry (vacuum)

Before experiments could be performed on aluminium sheets, the protective oxide films were removed 'in situ' by Argon ion etching. In ESCA experiments, continuous etching removed the aluminium oxide 2p peak, but when the oxygen peak was examined, oxygen was still found to be present on the surface. The origin of oxygen on the surface could be due to the oxygen in the solution of the metal ((Hansen and Anderko)

For experimental purposes the sample was etched until the level of oxygen peak reached a plateau. For ellipsometric experiments the changes in parameter Ψ and Δ were used. Producing a 'clean' starting surface by an etching technique may give a clean surface from the point of view of the surface chemical composition, but structurally it is different, in that there are dislocations and

vacancies induced by ion etching. Examination of the results from evaporated aluminium films and etched evaporated aluminium showed no difference therefore any change in the rate of growth, in oxide and hydroxide films induced by dislocation and vacancies was negligible or it could indicate that the ion bombardment did not affect the structure significantly to produce any change.

To calculate the oxide and hydroxide film thickness from the ESCA results the aluminium 2p peak was resolved into aluminium oxide and aluminium metal peaks. The relative areas under the aluminium oxide and aluminium metal peaks were measured and substituted into Fadleys expression [142] . Ellipsometry film thicknesses were measured by, assuming n = 1.58 and k=0, but for small thicknesses less than 10nm a large charge in n, k have very little change on the calculated film thickness.

Comparison of the film thicknesses obtained by ellipsometric and ESCA techniques showed, that thicknesses measured by the ellipsometry technique were consistently higher for all exposures. For low exposure the differences were small, but for longer exposure, the differences in film thicknesses were large. The discrepancy could be explained by assuming that, the initial oxide and hydroxide films grow in islands and the height of the islands may be larger than the escape depth of the electron. Therefore the oxide or hydroxide at the base was not detected by ESCA, but this was not the case with ellipsometry.

CHAPTER 6

RESULTS AND DISCUSSIONS (TEMSCAN)

The effects of exposing a freshly prepared aluminium specimen to WVSA at 70°C, without filling the anticontamination chamber are shown in Figure 33a, Figure 33b, c and d show other features which are produced by the interaction of the electron beam and the specimen. Figure 34a shows reaction sites developed during exposure to WVSA for 5 minutes at 70°C: this micrograph was taken away from the electron transparent area. Micrographs taken on or near electron transparent areas also showed reaction sites, Figure 34b. When the reaction sites were examined at higher magnification they appeared to be blisters, Figure 34c. Figure 34d is a STEM micrograph of the same area as Figure 34c. The underlying microstructure can be clearly seen and closer examination revealed the blister. In most cases, reaction sites were randomly distributed and not associated with any underlying microstructure, but Figure 35a and b shows a reaction site associated with crystal particles.

In the case of freshly prepared aluminium specimen, even when the exposure time to WVSA at 70°C was increased it was difficult to see the reaction sites in STEM, Figure 35c and d. Figure 36a shows the effect of increasing the oxide film thickness until it is possible to observe complete blisters randomly distributed. When the oxide film thickness was increased it was possible to observe the blisters in the STEM, TEM and SEM modes, (Figure 36b and 36c). Figure 37a and 37b show the random

distribution of blisters. Figure 38a and 38b show the effect of increasing the exposure to water vapour until the reaction product was randomly distributed to take a diffraction pattern. Figure 38c and 38d show the reaction product and the diffraction pattern taken from a bayerite particle. Further examination of the bayerite particle, Figure 39a and Figure 39b showed it to be more than a single crystal. Figure 39c shows the boehmite reaction product developed during exposure to WVSA for 180 minutes at 70°C on pure aluminium.

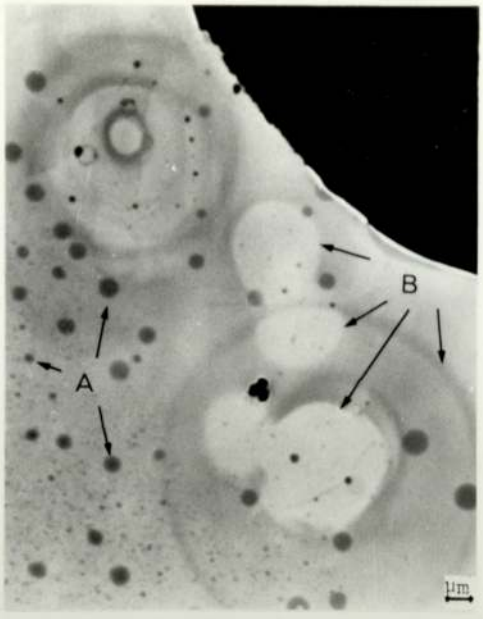

Figure 33a. High resolution SEM micrograph showing reacted areas (A) with carbon contamination (B) caused by 100 Kev electron beam on pure aluminium electron transparent specimen.

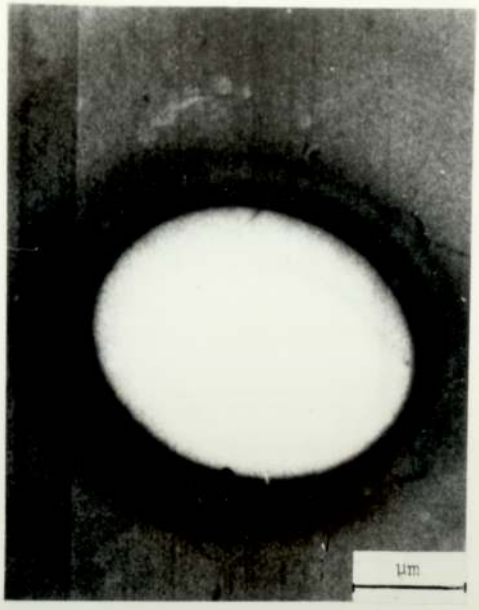

Figure 33b. Higher magnification of one of the carbon contamination marks.

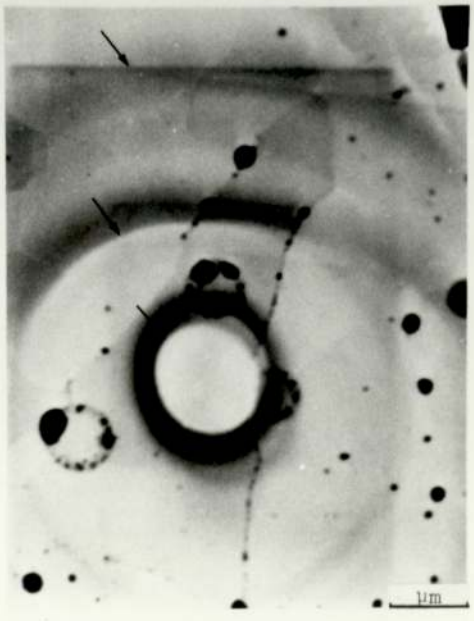

Figure 33c. SEM micrograph with carbon contamination marks due to focusing on and near grain boundary.

Figure 33d. STEM micrograph of the same area as Figure 33c. No carbon contamination marks are noticable.

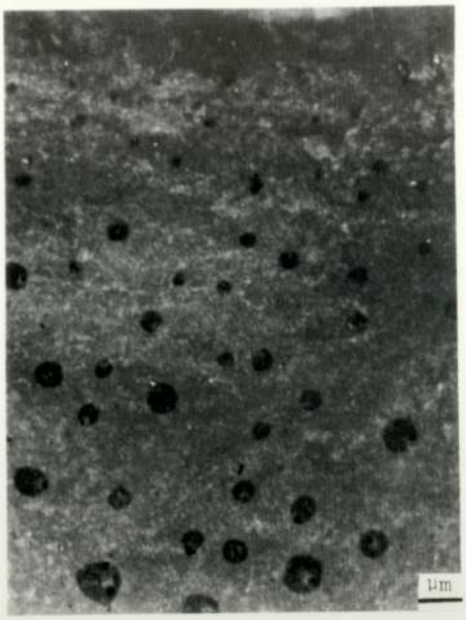

Figure 34a. High resolution SEM micrograph with reacted areas developed during exposure to water-vapour-saturated air (WVSA) for 5 minutes at 70°C. Reacted sities were observed away from the electron transparent area.

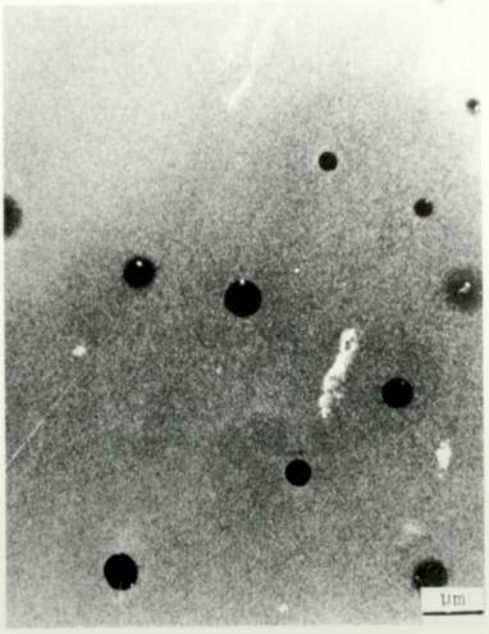

Figure 34b. High resolution SEM micrograph with reacted sities near and on the electron transparent area.

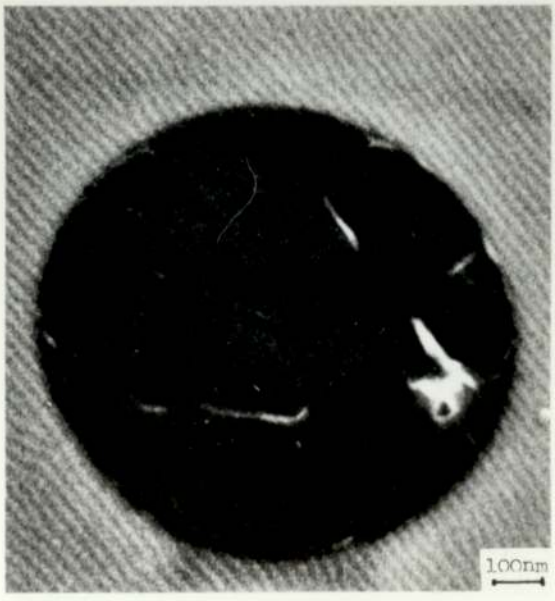

Figure 34c. High magnification SEM micrograph of one of the reaction sities, closer examination shows it to be a blister.

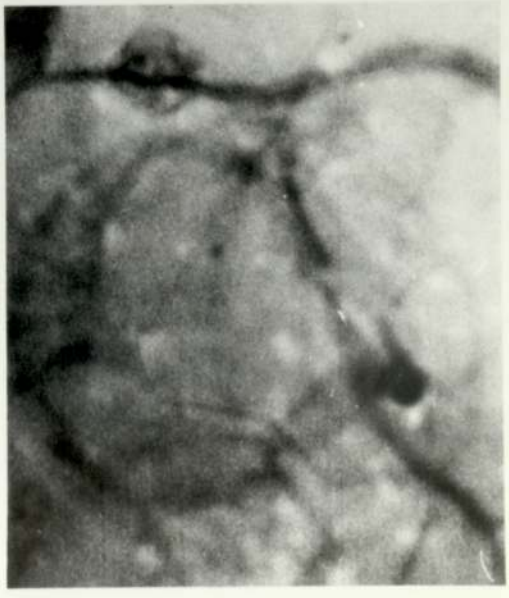

Figure 34d. STEM micrograph of the same area as Figure 34c, it is just possible to observe the reaction site on the underlying microstructure.

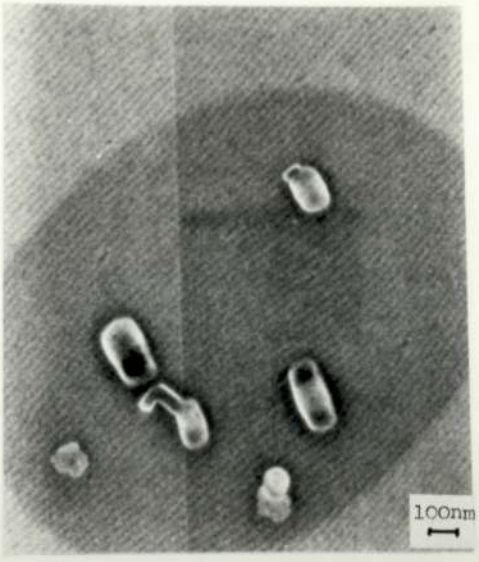

Figure 35a. High resolution SEM micrograph. A reaction site associated with crystal particles.

Figure 35b. STEM micrograph of the same area as Figure 35a. The only features which are observable in both modes are the crystal particles on and near grain boundaries.

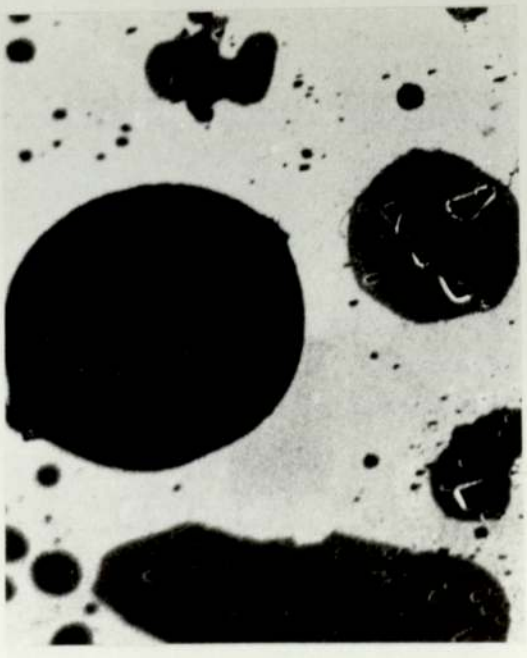

Figure 35c. High resolution SEM micrograph with reacted areas developed during exposure to water-vapour-saturated air (WVSA) for 15 minutes at 70°C on pure aluminium electron transparent specimen.

Figure 35d. STEM micrograph of the same area as Figure 35c. The only features which are noticable are grain boundaries and etch pites.

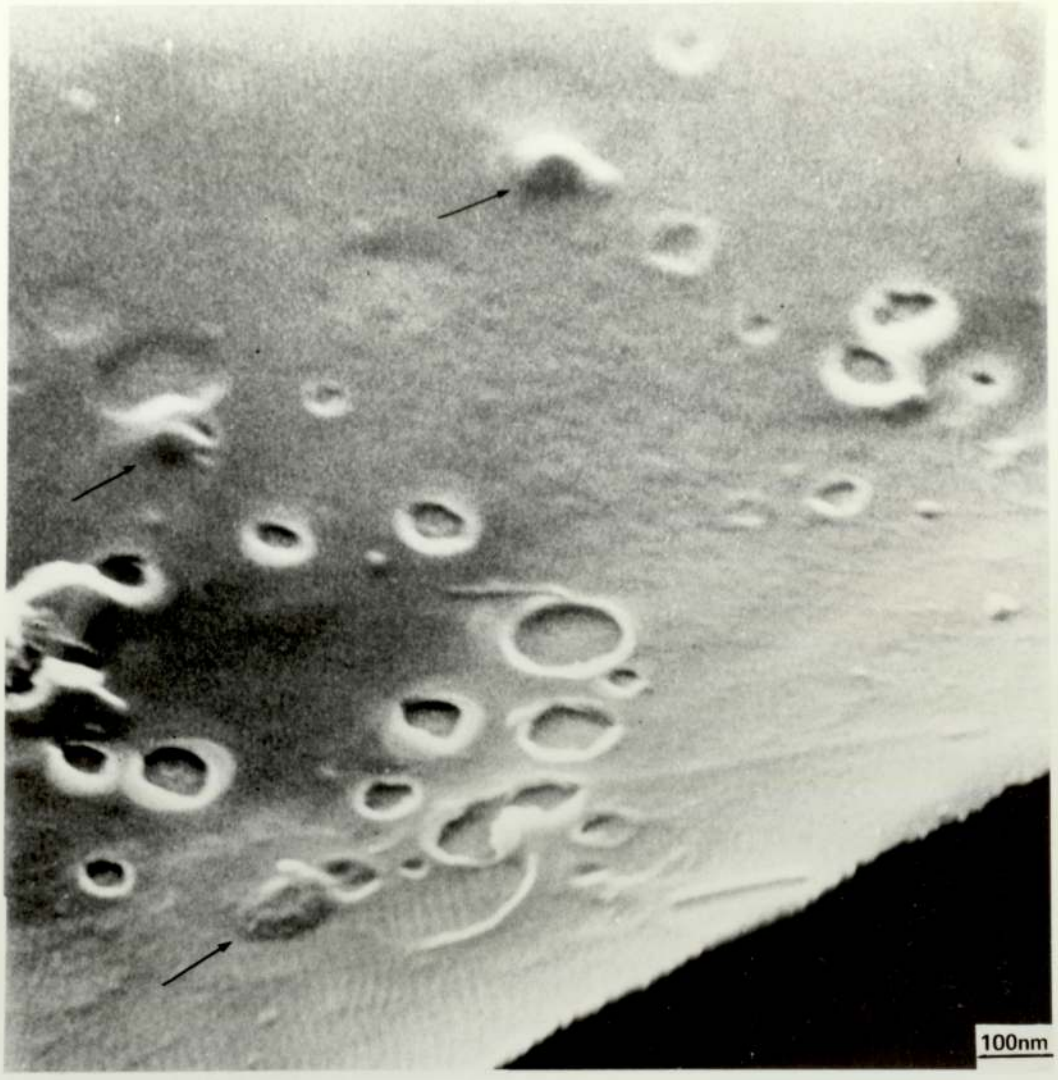

Figure 36a. High resolution, high magnification SEM micrograph with reacted areas, randomly distributed in the form of blisters, developed during exposure to WVSA for 5 minutes at 70°C on pure aluminium electron transparent specimen which had been stored in dry air for 22 days.

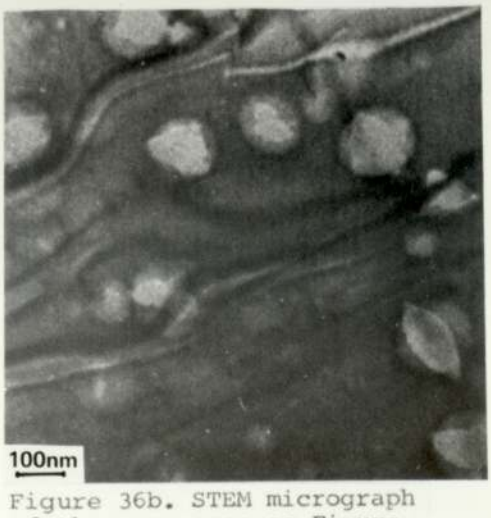

Figure 36b. STEM micrograph of the same area as Figure 36c. Because of the thicker oxide film, it is possible to observe blisters in STEM mode.

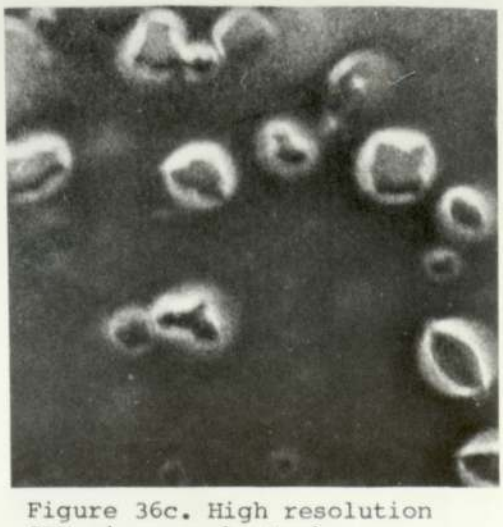

Figure 36c. High resolution SEM micrograph. Broken blisters randomly distributed.

Figure 37a. TEM micrograph. Because of the thicker oxide film it is possible to observe the blisters in TEM mode, which are randomly distributed and not associated with grain boundaries.

Figure 37b. Higher magnification TEM micrograph, randomly distributed broken blisters.

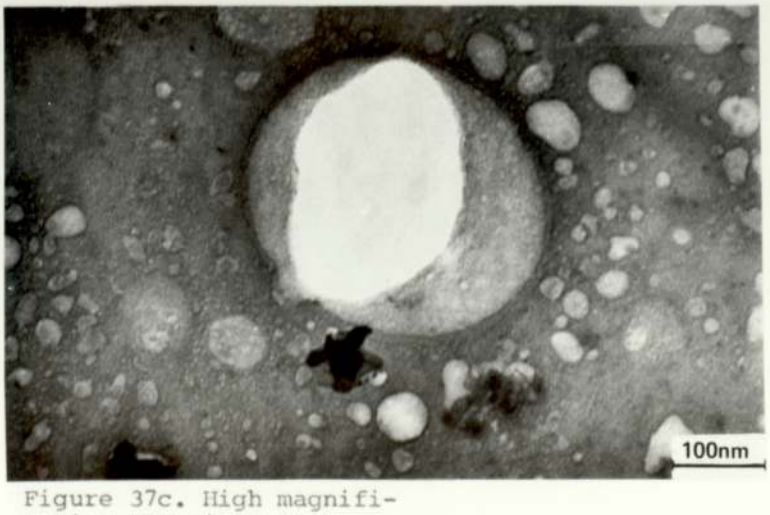

Figure 37c. High magnification TEM micrograph single broken blister with thin base.

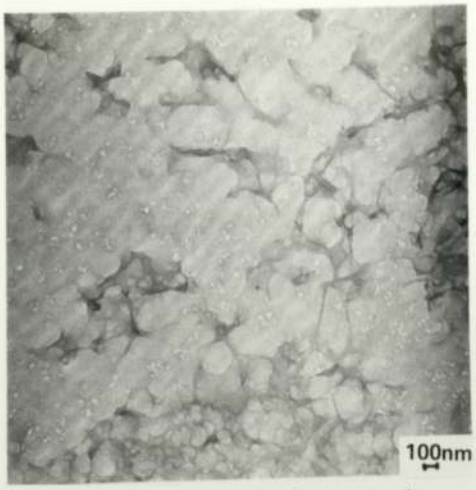

Figure 38a. TEM micrograph. Randomly distributed boehmite, developed during exposure to WVSA for 2 hours at 70°C on pure aluminium electron transparent specimen which had been stored in dry air for 18 hours.

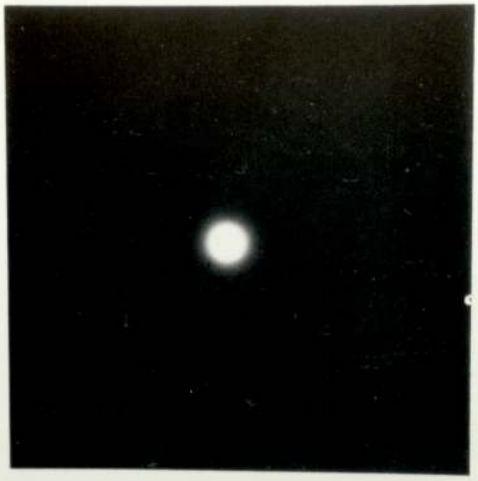

Figure 38b. Ring diffraction parthern taken from an area with boehmite as a reaction product.

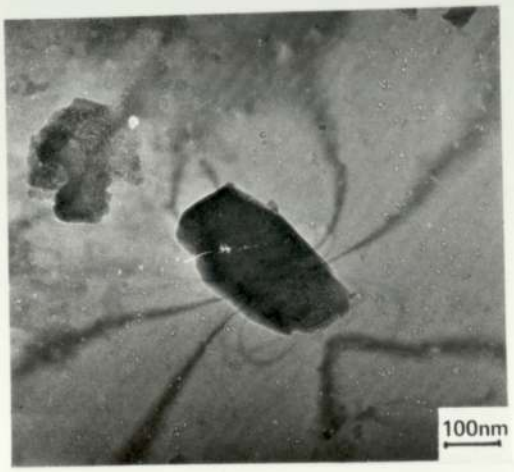

Figure 38c. TEM micrograph. Crystal (Bayerite) with stress field.

Figure 38d. Diffraction parthern taken from the crystal in Figure 38c.

Figure 39a. TEM micrograph taken in the dark field mode, crystal particle with some internal structure.

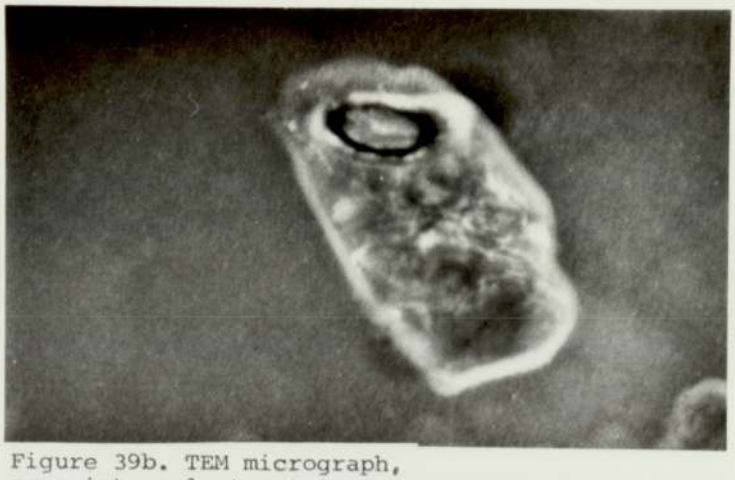

Figure 39b. TEM micrograph, more internal structure suggesting particle is not a single crystal.

Figure 39c. TEM micrograph. Boehmite reaction product developed during exposure to WVSA for 180 minutes at 70°C on pure aluminium electron transparent specimen.

6.2 Exposure of electron transparent specimen to water vapour saturated air at 70°C: Aluminium alloys

Aluminium alloy specimens prepared from sheets of aluminium 5% magnesium which had been heat treated at 350°C, were exposed to WVSA for 10 minutes and examined. Figure 40a shows the reaction sites along grain boundary, surface-interface developed during exposure to WVSA at 70°C. Blisters similar to the one seen on pure aluminium can be seen on aluminium alloy. Figure 40b, c and d show that the reaction sites are only a surface phenomenon. These reaction sites can also be observed in the TEM mode, Figure 41a, but upon closer examination it is possible to see two rows of reaction sites. This is because one row of reaction sites are on the lower side and the other on the top side. As a result of a few seconds of beam irradiation, hydrogen bubbles form on the grain boundaries, Figure 41b, c, d, e and f.

Figure 42a shows a high magnification TEM micrograph. It is possible to have hydrogen bubbles nucleated away from the grain boundaries and be joined by dislocation to larger bubbles. Hydrogen bubbles are normally viewed by their stress field contrast and Figure 42b shows how this can be improved by tilting the specimen. In some cases hydrogen bubbles may be viewed by the further interaction of 120 kV electron beam with the hydrogen bubbles. Figure 43a, b, c and d show a dynamic sequence and the associated phenomena which make it easy to observe hydrogen bubbles.

Figure 44a, b, c, d, e and f show that by changing the heat

treatment it is possible to change the location of reaction sites. Figure 45a, b, c, d, 46a, b show further examples of different heat treatments and their effect on reaction site locations. Figure 46c shows carbon contamination marks after EDX analysis. The volume from which the X-Ray information was obtained was about 50nm in diameter. Aluminium 5% Znic samples, which had been prepared from sheets of aluminium 5% Znic, heat treated at 350°C, 450°C, 550°C and CWQ were also examined. No grain boundary surface interface reaction sites were observed. Figure 41d shows a typical reaction product developed during exposure to WVSA at 70°C.

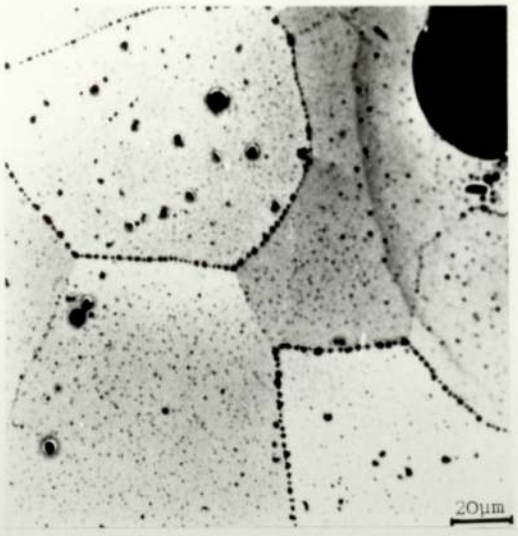

Fig. 40a. High resolution, low magnification SEM micrograph, reaction sites along grain boundaries developed during exposure to WVSA for 10 minutes at 70°C on aluminium 5% magnesium electron transparent specimen which had been heat treated at 330°C for 30 minutes.

Figure 40b. High resolution SEM micrograph, large single broken blister surrounded by small complete blisters.

Figure 40c. STEM micrograph, triple point with no reaction product along grain boundaries.

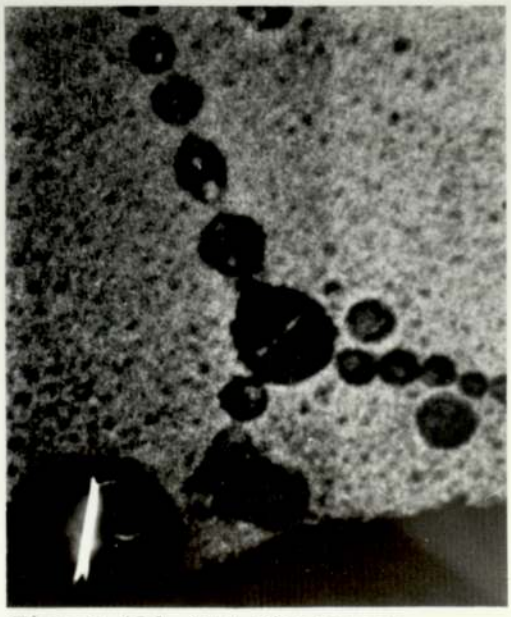

Figure 40d. SEM micrograph, same triple point as in Figure 40c, but in this mode it is possible to see reaction product along grain boundaries.

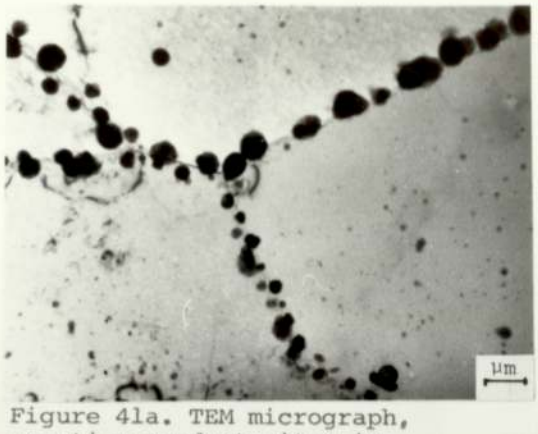

Figure 41a. TEM micrograph, reaction product sites in two rows along grain boundaries.

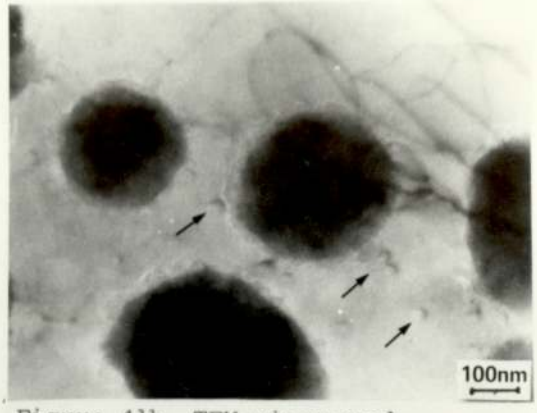

Figure 41b. TEM micrograph. Two rows of reaction product sites with hydrogen bubble in between.

Figure 41c. After 5 seconds under 120 Kev electron beam. Increase in size and number of bubbles.

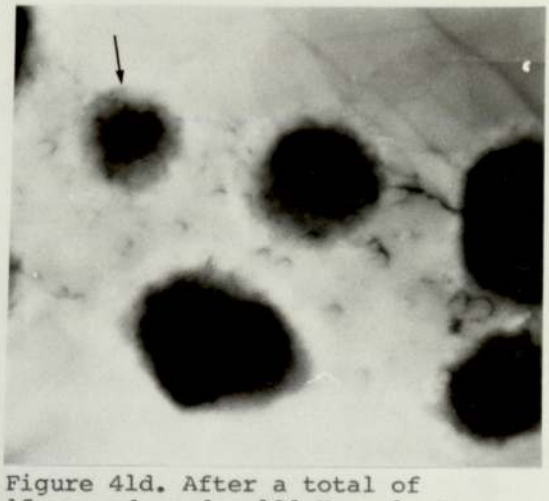

Figure 41d. After a total of 15 seconds under 120 Kev electron beam. No further increase in number or size of bubble but the reaction product sites decomposed.

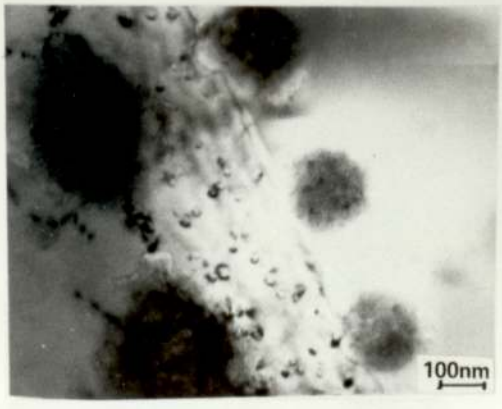

Figure 41e. Another example of rows of reaction sites with hydrogen bubbles.

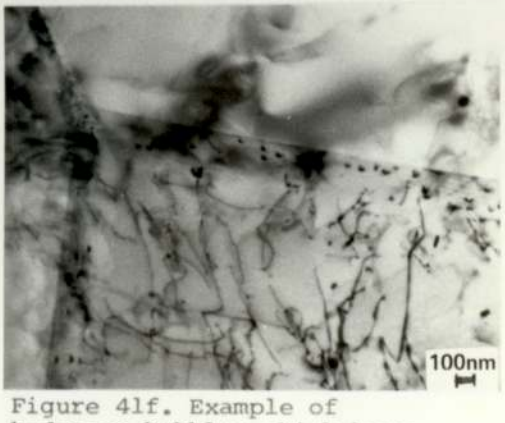

Figure 41f. Example of hydrogen bubbles which have formed under the action of electron beam without any reaction sites near the grain boundary.

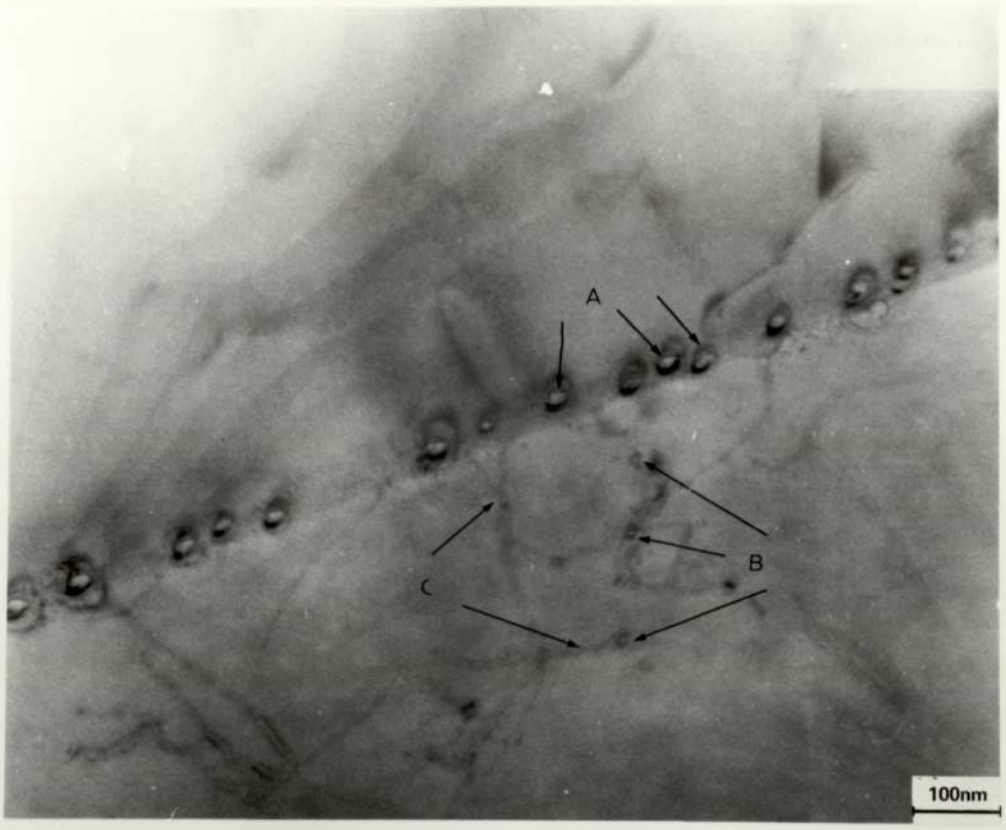

Figure 42a. High magnification TEM micrograph. Hydrogen bubbles along the grain boundaries (A) are joined to smaller hydrogen bubbles (B) which have nucleated away from the grain boundary, by dislocations. (C)

Figure 42b. TEM micrograph. Variation in hydrogen bubble contrast on tilting.

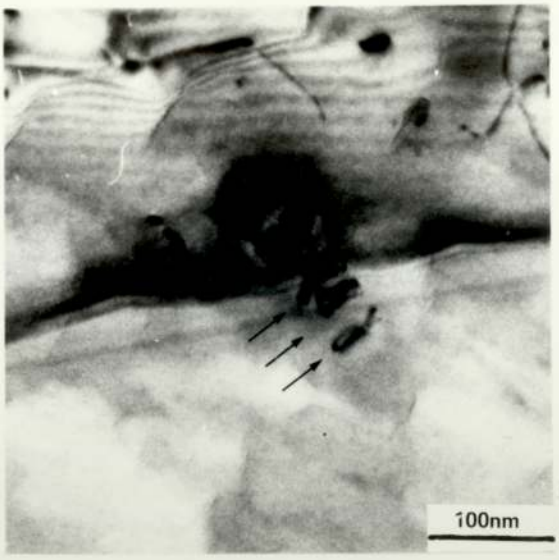

Figure 43a. Dynamic Sequence showing the interaction of 120 Kev electron beam with hydrogen bubble 43a hydrogen bubble with three dislocation loops.

Figure 43b. After 10 seconds, hydrogen bubble with four dislocation loops.

Figure 43c. After 20 seconds, hydrogen bubble with six dislocation loops.

Figure 43d. After 30 seconds the first four loops near to the hydrogen bubble have joined up to form a screw loop.

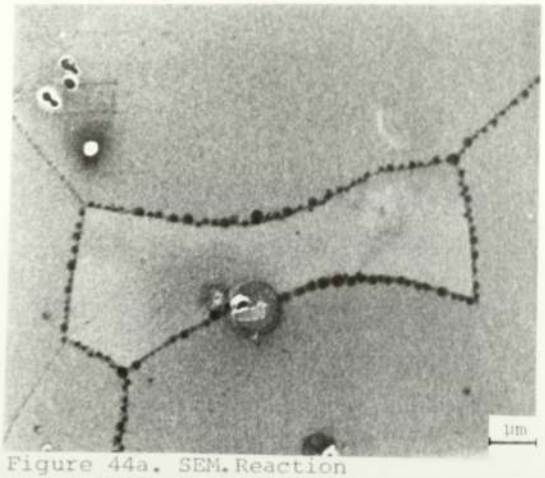

Figure 44a. SEM. Reaction sites along grain boundaries on alloy specimen which was prepared from a sheet, heat treated at 350°C for 30 minutes and CWQ.

Figure 44b. STEM micrograph. Grain boundaries and a few extra features which are on the lower surface.

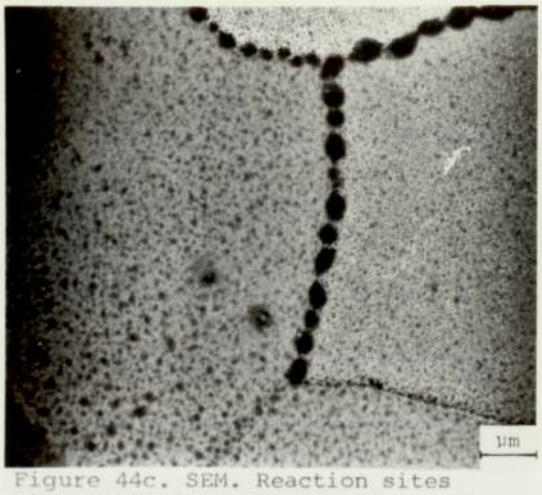

Figure 44c. SEM. Reaction sites along grain boundaries and matrex on alloy specimen which was prepared from a sheet, heat treated at 450°C for 30 minutes and CWQ.

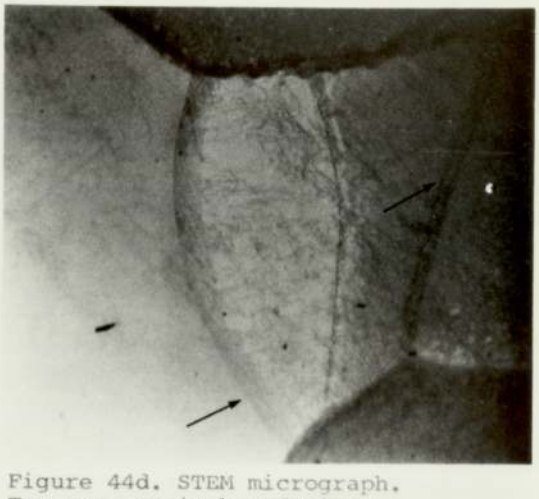

Figure 44d. STEM micrograph. Two more grain boundaries which are not noticable in Figure 44c.

Figure 44e. SEM micrograph. Reaction sites randomly distributed on alloy specimen which was prepared from a sheet, heat treated at 550°C for 30 minutes and CWQ.

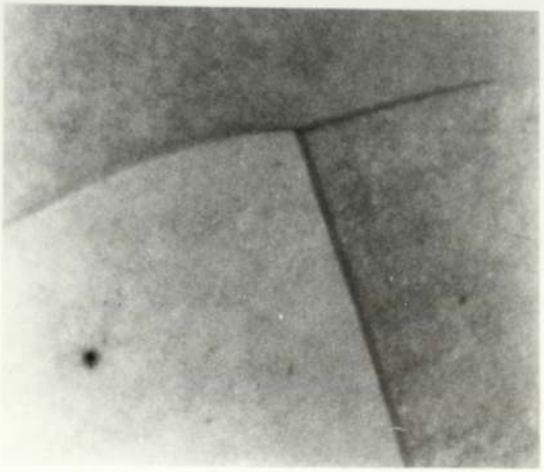

Figure 44f. STEM micrograph. Grain boundaries.

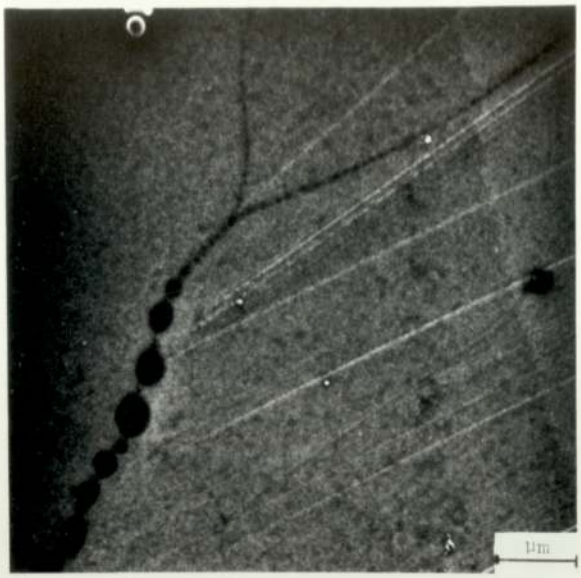

Figure 45a. SEM micrograph. Reaction sites, along a grain boundary, decreasing in size on alloy specimen which was prepared from a sheet, heat treated at 350°C for 30 minutes and CWQ.

Figure 45b. STEM micrograph. Shows another grain boundary which is not noticable in Figure 45a.

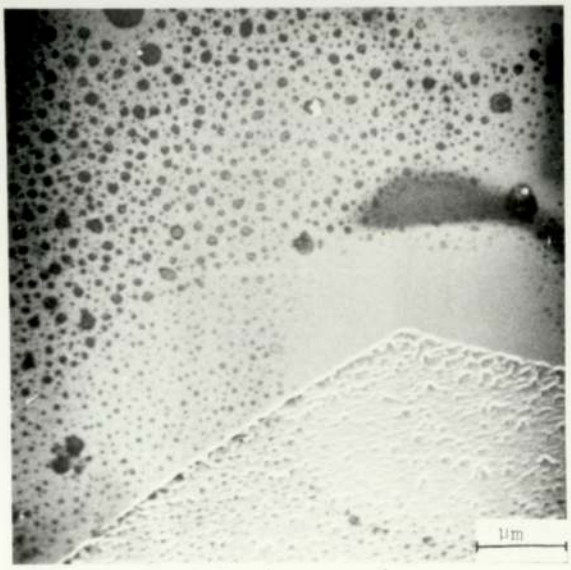

Figure 45c. SEM micrograph. Reaction sites randomly distributed on alloy specimen which was prepared from a sheet, heat treated at 450°C for 30 minutes and CWQ.

Figure 45d. STEM micrograph. Shows a grain boundary which is not noticable in Figure 45c.

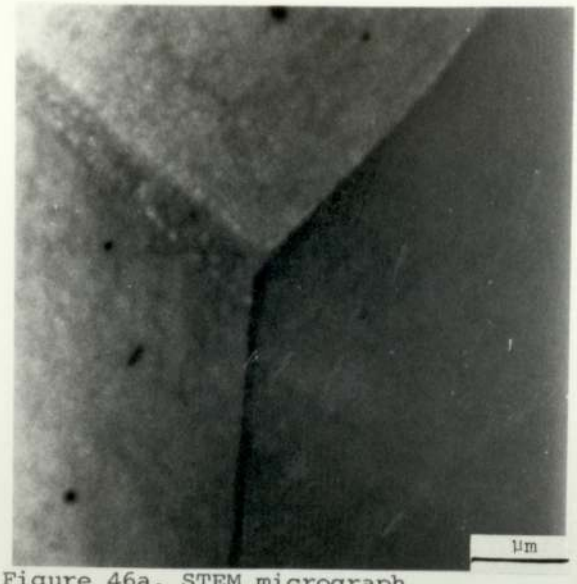

Figure 46a. STEM micrograph. A triple point with no reaction sites on alloy specimen which was prepared from a sheet, heat treated at 450°C for 30 minutes and CWQ.

Figure 46b. SEM micrograph of the same area as in Figure 46a, showing one grain boundary with reaction sites.

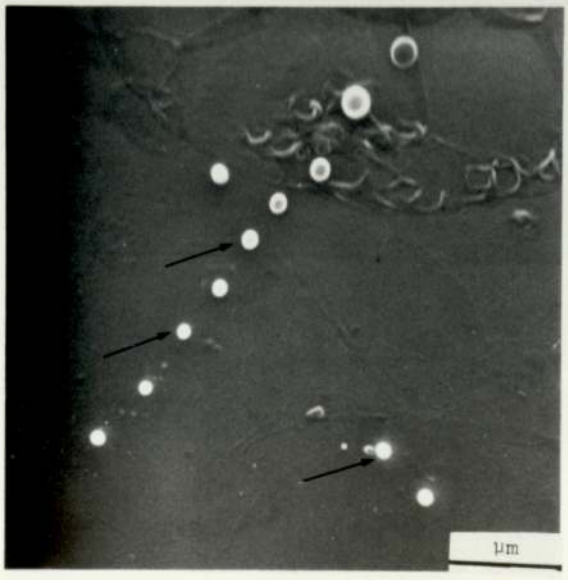

Figure 46c. SEM micrograph showing carbon contamination marker after EDX analysis.

Figure 46d. SEM micrograph. Randomly distributed reaction sites in the form of blister on (Al5%Zn) specimen which was prepared from a sheet, heat treated at 350°C for 30 minutes and CWQ.

6.3.1 Discussion: Pure aluminium (TEMSCAN)

TEMSCAN was used as an additional technique to obtain further information on the reaction of aluminium and alloys with water vapour. The electron transparent specimens were prepared from sheets of aluminium and aluminium alloys which had been heated at various temperatures. Each of the specimen, after electro-polishing, was examined for cleanliness using an optical microscope.

Aluminium samples heated at different temperatures showed different degrees of crystalization but initial experiments showed very little difference in the rate of reaction with different heat treatments, using the TEM mode. Therefore for further experiments samples were prepared from sheets of pure aluminium which had been heated at 350°C for 10 minutes. Before exposing to WVSA at 70°C, samples were stored in a dessicator for 18 hours. The thickness of oxide film present on the specimen, estimated from ellipsometry was 2.5 to 2.9 nm.

After the specimen had been exposed to WVSA at 70°C for 5 minutes, it was examined in TEMSCAN, in the transmission electron mode (TEM). No reaction sites or any other features which could be associated with aluminium - water vapour reaction were observed. The examination of the specimen in scanning transmission electron mode (STEM), also showed no reaction sites. When the sample was examined in scanning electron mode (SEM), there were several features which could be observed (Figure 33a).

Some of them could be readily identified as contamination marks, due to the electron beam during focusing, but there were several other features (Figure 33a and 33b) which were initially thought of as reaction products.

When combined, high resolution STEM and SEM microscopy of precisely located areas in the electron transparent region were

performed. Features which were thought to be reaction sites Figure 33c could not be observed Figure 33d. The only explanation for this, is that the features (reaction sites) are a few nm thick and therefore it is only a surface phenomenon.

After reexamination of the micrograph Figure 33a, it was concluded that some of the 'reaction' sites may be caused by the interaction of the electron beam during examination of the specimen in TEM and STEM modes, since carbon is always present as a residual product, due to hydrocarbons in the vacuum from the rotary and diffusion pump.

The vacuum was improved by filling the liquid nitrogen trap and the anti-contamination device in the system with liquid nitrogen. The anti-contamination device was operated by lowering the temperature of the material near the specimen. The second method of reducing the carbon contamination was by adopting a procedure by which specimen was examined. Al specimens were first examined in SEM mode and then followed by STEM and TEM. Taking all these precautions into consideration, electron transparent pure aluminium samples were examined, which had previously been exposed to WVSA at 70°C Figure 34a. The micrograph was taken away from the electron transparent area. It shows randomly distributed reaction sites. When Figure 34a was compared with Figure 33a, features A and B were not observed. Similar reaction sites were observed near and on electron transparent areas. When one of the reaction sites was examined at higher magnification Figure 34c, in the SEM mode, it was found to be, on closer examination, a broken blister. It was possible to observe broken walls of blisters. Examination of the same area in the STEM mode showed only, at first sight, the underlying microstructure. On closer examination however, it was possible to observe the blister. This can again be explained by

assuming, that blistering is a surface phenomenon. These blisters were found randomly distributed and with no association with the underlying microstructure. But in some cases reaction sites were associated with crystal particles (Figure 35a). Further examination in the STEM mode revealed them to be grown from the substrate.

Several electron transparent aluminium specimens were given longer exposures of WVSA at 70°C and upon examination in SEM mode showed a greater number of reaction sites. During further examination in the STEM mode (Figure 35d), the only features observable were the etch pits. Again underlying the fact that features observed in SEM are only surface phenomenon.

Since the blisters observed in the earlier work were broken it was decided to attempt to obtain unbroken blisters by starting with thicker oxide film prior to exposure.

From ellipsometry work it was found, that the oxide film thickness after 18 hours was only 2.0 to 2.5 nm, but increased to 3.8 - 4.5 nm after 20 days.

Therefore after electro-polishing, a number of electron transparent aluminium specimens were stored in dry air for 22 days. They were then exposed to WVSA for 5 minutes at 70°C upon examination, randomly distributed broken blisters were seen (Figure 36a), but there were a few blisters which were still complete. This was because the protective oxide film was thicker, i.e. with thicker blister walls. It was possible to observe the blister in the TEM and STEM modes.

The reaction of water vapour with electron transparent aluminium specimens, under these conditions, has not been reported in the literature. However, Flower [163] has reported the reaction of aluminium with water vapour after the specimen had been

exposed to electron irradiation in the energy range 100-1000 kV. These experiments were carried out 'in situ'. Flower [168] reached the conclusion, that the reaction was due to ionization rather than atomic displacement. The ionization lowered the oxide/metal bond strength and as the oxide grows it decohered from the metal to form blisters. Therefore the mechanism with which the blisters in the present work were formed was different. In order to understand the mechanism of blister formation more clearly, the structure of the protective oxide films needs to be looked at more closely. Barr [159] using ESCA obtained evidence of trapped aluminium in the Al_2O_3 matrix isolated from the aluminium substrate. His observations have also been confirmed in the present work. Protective oxide film may be represented as in Figure 47a, which shows the oxide film with trapped aluminium ions. The water molecule is attracted to the aluminium ions by the negative charge on the oxygen atoms. The reaction of water molecule or hydroxide ion produces aluminium oxide, hydroxide and hydrogen. The presence of hydrogen near the metal/oxide bond weakens the bond and also provides the internal pressure. The increase in surface area of oxide film, due to the blister formation, is compensated by the oxide of hydroxide formation in the oxide film.

The internal pressure required to produce the blister can be calculated from the force required to break the oxide/metal bond.

After the blister is formed, the internal pressure increases. Due to further reaction of aluminium substrate with water vapour the pressure increases until the blister breaks, (Figure 47e). Further reaction continues until there are islands of pseudo-boehmite with Bayerite pillars, Figure 24d. As the reaction

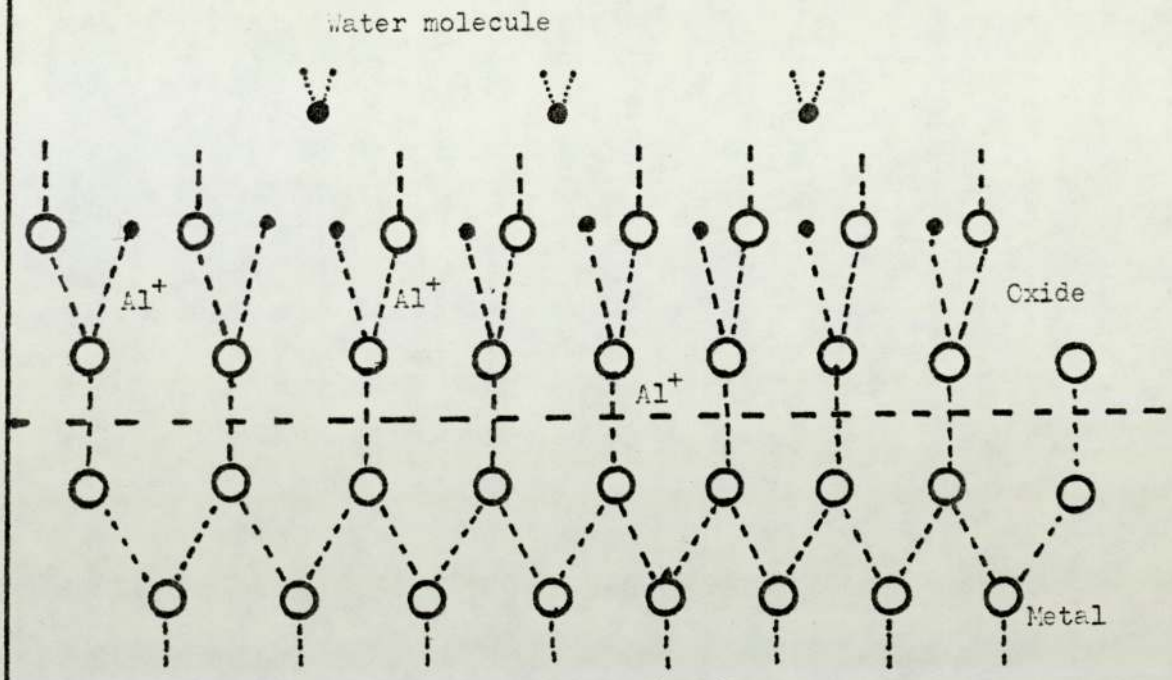

Figure 47(a)

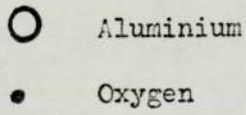

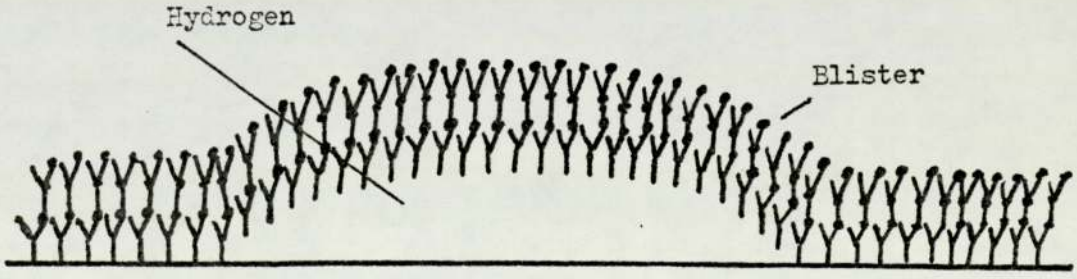

(b)

Figure 47b

proceeds the islands join up to form a continuous film. To obtain information about the structure of pseudoboehmite and Bayerite crystals, aluminium electron transparent specimens were exposed to WVSA at 70°C for 2 hours - ring diffraction patterns were obtained from areas with pseudoboehmite reaction product, together with diffraction patterns taken from Bayerite crystals. In both cases it was difficult to establish the structure. When a Bayerite particle was examined in the dark field mode (Figure 39a and 39b) the single particle showed internal structure suggesting that the particle was not a single crystal.

6.3.1 Discussion: Aluminium alloys

Sheets of aluminium 5% magnesium were heated at 350°C for 30 minutes and cold water quenched (CWQ). From the work of Taylor and Edgers [168], it is known that heat treatment at this temperature produces grain boundary segregation. Electron transparent specimens were prepared, examined for clealiness, exposed to WVSA at 70°C and examined in TEMSCAN. To avoid carbon contamination, due to the electron beam, the procedure which had been established previously, for pure aluminium specimen was used. Figure 40a shows reaction sites randomly distributed on the matrix but along the grain boundary surface interface the reaction was much more advanced. Upon closer examination, broken blisters were seen (Figure 40b). At higher magnification, examination of one of the grain boundaries, in STEM mode, Figure 40c, showed that no reaction was produced, but when the same area was examined in the SEM mode (Figure 40d) reaction sites along grain boundary surface interfaces were seen:- suggesting that it is also a surface phenomenon.

In the TEM mode, Figure 41a, it was possible to see two rows of reaction sites on the grain boundary surface interfaces. Upon closer examination of the two rows of reaction sites, Figure 41b, it was

noticed that hydrogen bubbles appeared under the action of electron beam. Figure 41c shows the development of hydrogen bubbles which are viewed by their stress field contrast. The other phenomenon noticed, which was also produced by the action of the electron beam on the specimen, was the decomposition of reactions sites, Figure 41d.

Hydrogen bubbles, viewed by stress field contrast, in Al-Zn-Mg alloys have been reported by Scaman and Scaman [1], Alani and Swann. In the present work, a closer examination of hydrogen bubbles on grain boundaries, it revealed that there were smaller hydrogen bubbles which had nucleated away from the grain boundary. These small hydrogen bubbles were joined to larger hydrogen bubbles on the grain boundary by dislocations, Figure 42a. The smaller bubbles could have nucleated away from the grain boundaries where there was higher concentration of magnesium or vacancies.

Hydrogen bubbles were only observed after the interaction of the electron beam, in this case 120 kV and it could be that the hydrogen bubble phenomenon is only found in thin foils. The molecular hydrogen, within the bubble, generates a significant stress, as the yield stress of the surrounding matrix is soon exceeded, and dislocation generation and propagation are observed. This can be seen in dynamic sequence, Figure 43, which shows the interaction of 120 kV electron beam with an accumulated grain-boundary hydrogen bubble. The hydrogen bubble first generates three dislocation loops and after further exposure to the electron beam more dislocation loops are generated and finally a screw dislocation loop was formed.

In order to form a hydrogen bubble it is necessary that the chemisorbed hydrogen be recombined to form a hydrogen molecule and be desorbed. The hydrogen atom can be highly mobile and may rapidly migrate to grain boundary sites and with the energy required

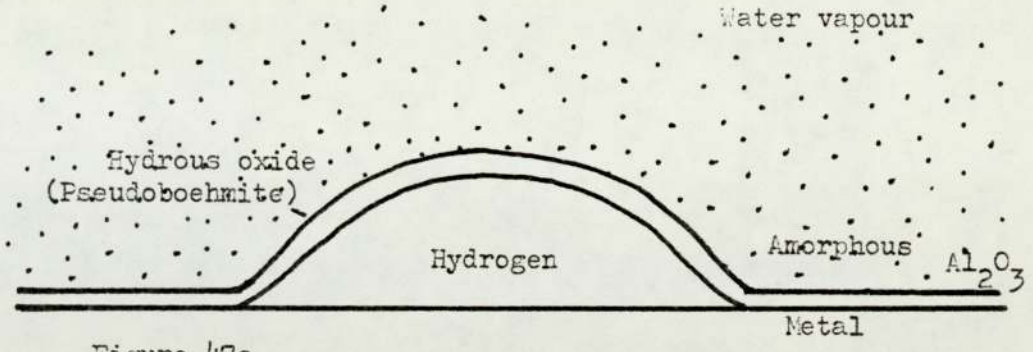

Figure 47c

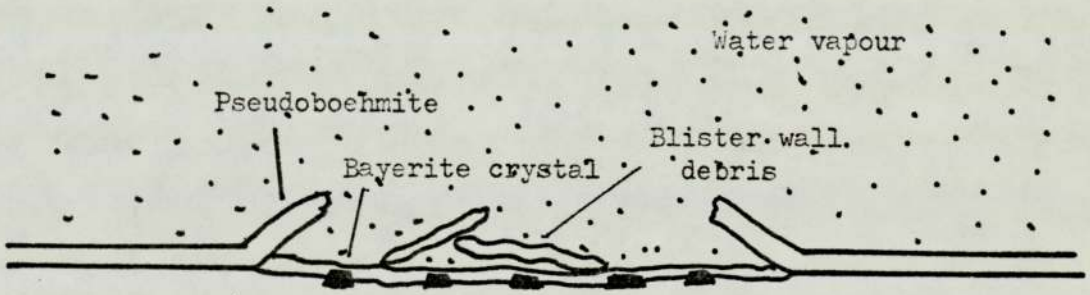

Figure 47d

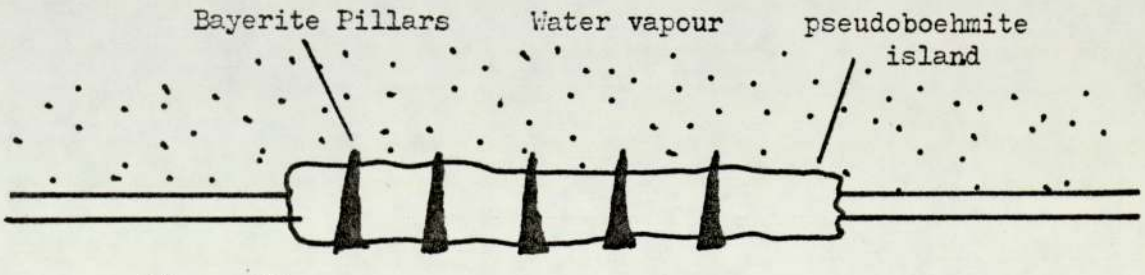

Figure 47e

for the formation of the hydrogen molecule coming from the 120 kV electron beam.

Formation of the hydrogen bubble can be schematically represented by, Figure 48. Hydrogen atoms migrate to the grain boundary under the action of the beam and recombine to form hydrogen molecules. Grain boundary bonds are broken by the build up of pressure, and also by the weakening of the bonds by the physical presence of hydrogen. With further exposure to the electron beam, more hydrogen atoms form hydrogen molecules to increase the pressure until the yield stress of the surrounding matrix is exceeded and the bubble may be viewed by the associated phenomenon, i.e. dislocation, dislocation loops and more commonly the stress field contrast.

Pressure inside the hydrogen bubble can be calculated by amount of force required to break the bounds and the area of the bubble.

The consideration of reaction sites and therefore hydrogen bubbles associated with grain boundaries on the aluminium 5% magnesium is very important because hydrogen penetration of grain boundaries in Al-Zn-Mg alloys results in a loss of grain-boundary adhesive strength and promotes intergranular embrittlement and stress-corrosion crack propagation.

The precise chemical composition of the grain-boundary is therefore extremely important. Changes in the composition of magnesium on the grain boundary plane can be controlled by the heat treatment and quenching.

Sheets of aluminium 5% magnesium were heat treated at 350°C, 450°C, 550°C and cold water quenched (CWQ). Electron transparent specimens were prepared and exposed to WVSA at 70°C for 5 minutes. The samples which had been heated at 350°C showed grain boundary surface interface reaction sites (Figure 44a). When the same area was examined in STEM, Figure 44b, only the grain boundaries were

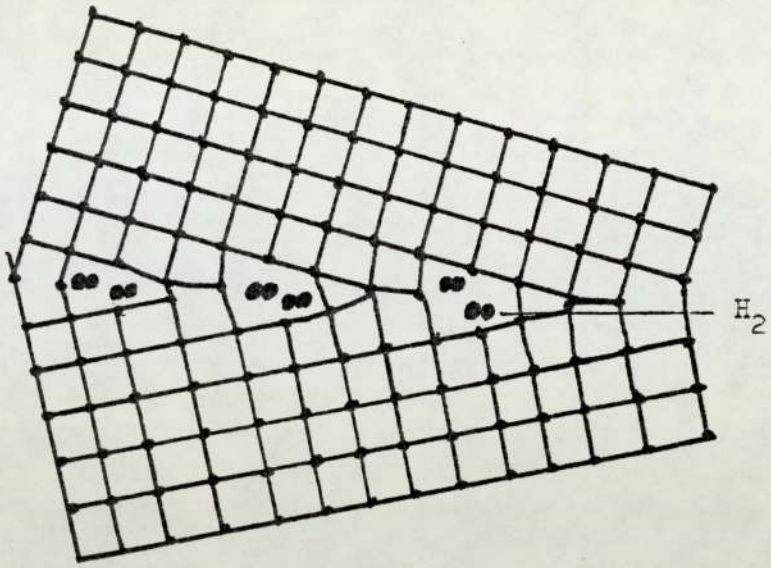

Figure 48a: Burgers dislocation model of a symmetrical grain boundary

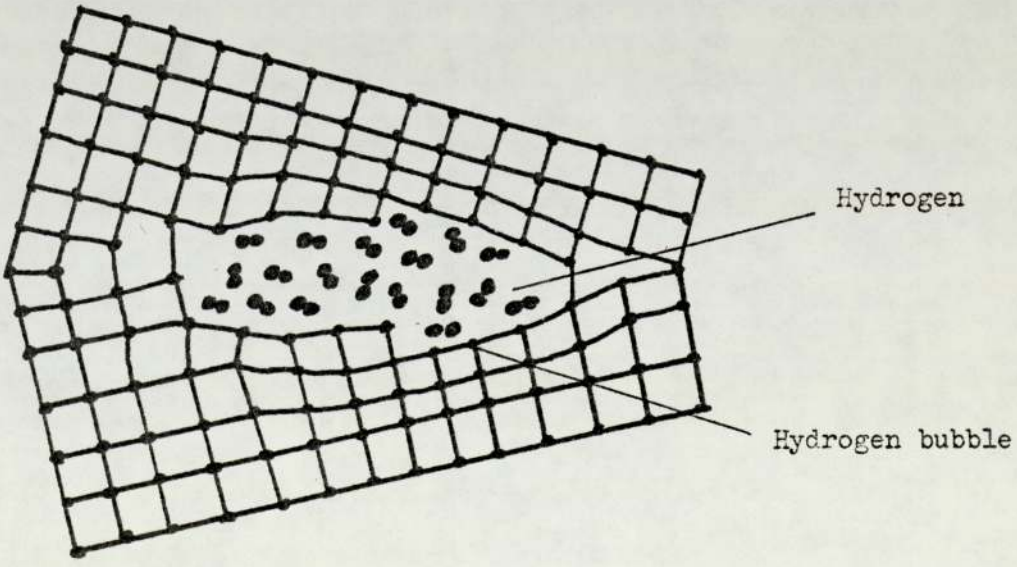

Figure 48b: Formation of hydrogen bubble

seen. Examination of the 450°C heat treatment sample showed grain boundary surface interface and matrix reaction sites, but when the sample was examined in the STEM mode, Figure 44d, it revealed two more grain boundaries which had no reaction sites along them. When the 550°C heat treated sample was examined, only randomly distributed reaction sites were seen. Further examination in the STEM mode showed the grain boundaries more clearly but revealed no new information. It was possible therefore to change the composition of magnesium on the grain boundary plane. This shows up in the way WVSA reacts on samples, with different heat treatments. When grain boundary analysis of the samples, prepared from sheets heat treated at different temperatures, was carried out using EDX analysis, the results were inconclusive because there was no difference between the amount of magnesium detected at the grain boundary and the matrix. The micrograph, Figure 44a, b, c, d, e, f, shows different degrees of grain boundary surface interface attack for different heat treatments and since the only elemental composition which can vary with heat treatment is magnesium the conclusion one reaches is that the concentration gradient $\frac{c}{x}$ of magnesium on the grain boundary plane is sharp and too narrow for the EDX detector to resolve.

The resolution of the EDX detector is about 50 nm and magnesium concentration at the grain boundary width x may be much smaller.

Scaman [1] has shown that hydrogen bubbles interact both with the grain-boundary precipitate and with the intermetallic particles formed during casting or during homogenization. The role of grain-boundary precipitates is therefore important. Scaman has tried the additions of Fe, Si, Fe + Si + (r), Fe + Sc + Mn, Fe + Si + Zn none of which do not prevent grain-boundary hydrogen penetration.

It would be interesting to include Lithium in the cast, because

Lithium adsorbes hydrogen very readily. Precipitates of Li on grain boundaries would readily adsorb hydrogen and prevent penetration of hydrogen into grain boundaries in Al-Zn-Mg and stop the loss of grain-boundary adhesive strength and promote intergranular embrittlement and stress-corrosion.

6.4 Summary

Further information on the reaction of aluminium and aluminium alloys was obtained by using TEMSCAN as an additional technique. All the specimens had regions which were electron transparent. Initial examination of the aluminium electron transparent specimen, after 5 minutes exposure to WVSA, in the TEM mode showed no reaction sites. Further, combined high resolution STEM and SEM microscopy of precisely located areas in the electron transparent region showed features of aluminium reaction with WVSA. These features could only be observed in SEM, but further observation showed that some of the features were carbon contamination due to the interaction of the electron beam with the specimen.

Carbon contamination marks were reduced first by filling the liquid nitrogen trap and the anti-contamination device in the system with liquid nitrogen and secondly, by first examining the specimen in SEM mode and then followed by STEM and TEM. Taking all these precautions, examination of the electron transparent specimen, after exposure to WVSA for 5 minutes showed randomly distributed reaction sites in the form of blisters. Examination of the same area in the STEM mode showed only, at first sight, the underlying microstructure. On closer examination however, it was possible to observe the blister. This could be explained by assuming that blistering was a surface phenomenon. These blisters were found to be randomly distributed and with no association with the underlying microstructure.

By starting with a thicker oxide film, prior to exposure to WVSA it was possible to observe in the STEM and TEM modes. The reaction of water vapour with electron transparent aluminium specimens, under these conditions has not been so far reported in the literature. However Flower [168] has reported on the reaction of aluminium with water vapour, after the specimen had been exposed to electron irradiation in the energy range of 100-1000 kV. These experiments were carried out 'in situ'. Flower reached the conclusion that the reaction was due to ionization rather than atomic displacement. The ionization lowered the oxide/metal bond strength and as the oxide grows it decohered from the metal to form blisters. Therefore the mechanism with which the blisters in the present work were formed was different. In the light of present experiments we can conclude that the water molecule was attracted to the aluminium ions by the negative charge on the oxygen atom. The reaction of water molecule or hydroxide ion produces aluminium oxide, hydroxide and hydrogen. The presence of hydrogen near the metal/oxide bond weakens the bond and also provides the internal pressure. After the blister had formed, the internal pressure increased, due to further reaction of the aluminium substrate with water vapour.

The pressure increases until the blister burst. Further reaction continues until there are islands of pseudoboehmite with Bayerite pillars. As the reaction proceeds the islands join up to form a continuous film.

Aluminium Alloys

Reaction of aluminium 5% magnesium electron transparent specimens (prepared from sheets of aluminium 5% magnesium heated at 350°C for 30 minutes and cold water quenched (CWQ), with WVSA, showed reaction sites not randomly distributed on the matrix but along the grain

boundary surface interface. The reaction was much more advanced than on the matrix. Examination in the STEM mode again only showed the underlying microstructure, suggesting that the reaction sites (blisters) were a surface phenomenon.

In the TEM mode it was possible to see two rows of reaction sites on the grain boundary surface interface. Upon closer examination of the two rows of reaction sites it was noticed that hydrogen bubbles appeared under the action of the electron beam. The hydrogen bubbles were viewed by their stress field contrast. The other phenomenon noticed which was also produced by the action of the electron beam on the specimen, was the decomposition of reaction sites. Hydrogen bubbles were normally seen on the grain boundaries but in a few cases smaller hydrogen bubbles which had nucleated away from the grain boundary were observed. These smaller hydrogen bubbles were joined to larger hydrogen bubbles on the grain boundary by dislocations.

Hydrogen bubbles were only observed after the interaction of the electron beam. In this case (120 kV) it could be that the hydrogen bubble phenomenon is only found in thin foils. Hydrogen bubbles associated with grain boundaries, on the aluminium 5% magnesium are very important because hydrogen penetration of grain boundaries in Al-Zn-Mg alloys results in a loss of grain-boundary adhesive strength and promotes intergranular embrittlement and stress-corrosion crack propagation.

The chemical composition of the grain boundary was changed by heat treating and water quenching sheets of aluminium 5% magnesium after heating at 350°C, 450°C and 550°C. The sample which had been heated at 350°C showed grain boundary surface interface reaction sites. Examination of the 450°C heat treated sample showed grain boundary surface interface and matrix reaction sites, but when the

550°C heat treated sample was examined only randomly distributed reaction sites were seen. When grain boundary analysis of the samples prepared from sheets heat treated at different temperatures was carried out using EDX analysis the results were inconclusive because there was no difference between the amount of magnesium detected at the grain boundary and in the matrix.

CHAPTER 7

CONCLUSIONS AND RECOMMENDATIONS

In this Chapter, a summary of the conclusions reached and some possible extensions to the present work are presented.

Conclusions

In all the experiments conducted to evaluate surface film growth, the state of the starting surface was very significant. Ellipsometry experiments with aluminium sheet showed that copper contamination gave rise to results which were difficult to explain. SEM investigation of the aluminium films deliberately contaminated with copper showed that the rate of growth on the surface with copper contamination was much greater. Similar difficulties were encountered in TEMSCAN work where surface contamination (carbon) was difficult to detect in STEM and TEM and the only way it was detected was by the combined high resolution STEM and SEM microscopy of precisely located areas in the electron transparent region.

Examination of aluminium hydroxide on aluminium sheet by SEM showed that the aluminium hydroxide (pseudoboehmite) grows in the form of islands with bayerite within it. The islands grow in two directions becoming thicker and at the same time growing along the surface until they join up to form a continuous film. Examination in the reflective mode showed that the bayerite crystals grow from the aluminium substrate. Aluminium hydroxide films on glass and on gold film substrate were also in the form of islands.

When an independent interferometric technique was used for measuring the thickness of hydroxide films on gold it was possible

to show that ellipsometry could be used to measure both the hydroxide film thickness and the refractive index.

The refractive index of aluminium hydroxide was found to be, at a wavelength of 549 nm, for film thickness less than 80 nm $n = 1.58 \pm 0.03$, $k = 0$ but for film thickness greater than 80 nm it was necessary to assume an absorption ($k = 0.0009$).

For 'in situ' experiments in ESCA, continuous etching of the aluminium sheet removed the aluminium oxide 2p peak, but when the oxygen peak was examined, oxygen was still found to be present on the surface. The origin of oxygen on the surface was due to oxygen in the solution of the metal. For experimental purposes the sample was etched until the level of oxygen peak reached a plateau. For ellipsometric experiments a reference surface was defined in terms of constant values for the parameter Ψ and Δ. Examination of the results from evaporated aluminium films and etched evaporated aluminium films showed no difference in the rate of film growth. Therefore any change in the rate of growth, in oxide and hydroxide films induced by dislocation and vacancies was negligible.

Comparison of the film thicknesses obtained by ellipsometric and ESCA techniques showed that thicknesses measured by the ellipsometric technique were consistently higher for all exposures. The discrepancy was explained by assuming that initial oxide and hydroxide films grow in islands and when the height of the islands is larger than the escape depth of the electron, the oxide or hydroxide at the base was not being detected by ESCA.

Further examination, of the reaction of aluminium with WVSA, using TEMSCAN showed that the initial oxide breaks away from the substrate and forms blisters, therefore further reaction can continue. These blisters were only observed in the SEM mode. When the same area was examined in STEM, the only features

observed were the underlying microstructure. This suggested that the blistering was a surface phenomenon. By increasing the oxide film thickness prior to exposure to WVSA it was possible to observe unbroken blisters. These blisters could also be observed in STEM and TEM modes. The reaction of aluminium with WVSA proceeds by the blistering of the initial oxide film.

Reaction of aluminium 5% magnesium electron transparent specimen prepared from sheets of aluminium 5% magnesium heated at 350°C for 30 minutes and (CWQ), with WVSA, showed reaction sites randomly distributed on the matrix more concentrated along the grain boundary surface interface. The reaction on the grain boundary was much more advanced than on the matrix. Examination in STEM mode again only showed the underlying microstructure indicating that the reaction sites (blisters) were a surface phenomenon.

Hydrogen bubbles were produced by the action of the electron beam on the specimen and viewed by their stress field contrast. Hydrogen bubbles were normally seen on the grain boundaries but in a few cases smaller Hydrogen bubbles which had nucleated away from the grain boundary were observed. These smaller hydrogen bubbles were joined to larger hydrogen bubbles on the grain boundary by dislocation. The smaller hydrogen bubbles may have nucleated away from the grain boundary because of the vacancies, dislocation or higher concentration of magnesium.

Changes in the chemical composition of the grain boundary for samples which had been heated at 350°C, 450°C and 550°C were examined using EDX analysis, but the results were inconclusive because there was no difference between the amount of magnesium detected at the grain boundary and in the matrix.

Recommendation for future work

There are a number of aspects of the present work which would merit further investigation:

(a) The refractive index of aluminium hydroxide, which was measured using gold film as the substrate, could be investigated further using platinum or another non-reactive material as the substrate.

(b) The rate of growth of hydroxide films on aluminium alloy sheets, could be investigated at atmospheric pressure, using ellipsometry.

(c) In the present work the rate of growth of oxide and hydroxide film thickness, under ultra high vacuum conditions was measured using ellipsometry. It would be interesting to measure the rate of growth of oxide and hydroxide film thickness on aluminium alloy sheets.

(d) Recently Dares [168] has pointed out that Auger emission at 1396 eV, using X-rays of Mg (1250 eV) gives a separation between aluminium metal and aluminium oxide peak of 7 eV. This may be advantageous to study the rate of growth of oxide, hydroxide film thickness and the structure, because of the large oxide, metal peak separation.

(e) Since the role of grain-boundary precipitates is very important it would be interesting to include lithium in the cast, because lithium adsorbes hydrogen very readily. Precipitates of Li on grain boundaries would readily adsorb hydrogen and prevent penetration of hydroxide into grain boundaries in Al-Zn-Mg and stop the loss of

grain-boundary adhesive strength and promote intergranular embrittlement and stress-corrosion. Therefore it would be interesting to carry out some TEMSCAN experiments on specimens prepared from such sheets.

REFERENCES

1. G.M. SCAMANS, Journal of materials science, 13, (1978) 27-36

2. G.M. SCAMANS, R. ALANI and P.R. SWANN, Corrosion Science 16, (1976), 443

3. G.M. SCAMANS and C.D.S. TUCK, Proceedings of the International Conference of Mechanisms of Environment Sensitive Cracking of Materials, Guildford 1977 edited by P.R. Swann.

4. C.D.S. TUCK and G.M. SCAMANS, Second International Conference of Hydrogen in Metals, Paris 1977

5. L. MONTRAIN and SWANN, Proceedings of the International Conference on Hydrogen in Metals, Seven Springs 1973 edited by I.M. Bernstein and A.W. Thompson (A.S.M., Metals Park Ohio, 1974) P.575

6. G.W. LORIMER and R.B. NICHOLSON, Acta Met 4 (1966) 41

7. R.S. ALWITT, "The Aluminium-water system" in "oxides and oxide films", Vol.4 edited by J.W. Diggle, published Marcel Dekker (1976) 169-254

8. S. TOLANSKY, Multiple Beam Interferometry (Oxford Univ. Press) 1948

9. H. MURMANN Z. Physik 80, 161, 1933
   S. Physik 101, 643, 1936

10. O. HEAVENS 'Optical Properties of Thin Solid Films' (Dover, New York) 1965

11. L. RAYLEIGH, Phil. Mag. 33 (1892) 1

12. P. DRUDE, Weid.Ann (Leipzig) 39, 1890, 421
Weid.Ann (Leipzig) 43, 1891, 125

13. L. TRWOSTAD and C.W. BORGMAN, J.Opt.Soc.Am. 30 (1934) 349

14. L. TROWSTAD and C.G.D. FEACHEM, Proc.Roy.Soc. 145A (1934) 115

15. L. TRONSTAD and T. HOVERSTAD, Trans.Farad.Soc. 30 (1934) 1114

16. C.E. LEBERNIGHT and B. LUSTMAN, J.Op.Soc.Am. 29 (1939) 59

17. A. ROTHEN, Rev.Sci.Instr. 16 (1945) 26

18. A. ROTHEN and M. HANSON, Rev.Sci.Instr. 28 (1957) 283

19. A.B. WINTERBOTTOM, Norske Videnskabers Selskab (Trondheim) 1955

20. J.R. BEATTIE, Phil.Mag. 46 (1955) 235

21. P.C.S. HAYFIELD and G.W.T. WHITE, Ellipsometry in the measurement of surfaces and thin films, Washington Symposium 1963

22. F.L. McCRACKIN, E. PASSACAGLIA, R. STROMBERG and H.L. STEINBERG. J.Research Nat.Bur. of Standards 67 (1963) 363

23. R.J. ARCHER, J.Opt.Soc.Am. 52 (1962) 970

24. E.J. GILHAM, Nature (G.B.) 178 (1956) 1412

25. R.J. SEWARD, Ph.D Thesis, Univ. of Southampton 1967

26. B.D. CAHAN and R.F. SPANIER, Suf.Sci. 16 (1969) 166

27. S.N. JASPERSON, D.K. BURGE and R.C. O'HANDLEY, Surf.Sci. 37 (1973) 548

28. B.D. CAHAN, J. HORKANS and E. YEAGER, Surf.Sci. 37 (1973) 559

29. R.H. MULLER and H.J. MATHIEU, App.Optics, 13 (1974) 2222

30. R.H. MULLER, Surf.Sci. 56 (1976) 19

31. W.E.J. NEAL, Physics in Technology, November (1977) 238

32. T.H. ALLEN, J.Vac.Sci.Technol. Vol.13 (1975) 112

33. N.J. CHOU, Y.J. VANDER MUELEN, R. HAMMER and J.CAHILL, App.Phys.Lett. 24 (1974) 200

34. R.V. LATHAM and A.S. BRAH, J.Phys.D, App.Phys. 10 (1977) 151

35. H. ROBINSON and W.F. RAWLINSON, Phil.Mag. 28 (1914) 277

36. H. ROBINSON, Proc.Roy.Soc. A 104 (1923) 455

37. H. ROBINSON, Phil.Mag. 50 (1925) 241

38. M. DE BROGLIE, C.R. 172, (1921) 274

39. K. SIEGBAHN, "Alpha, Beta-and Gamma-Ray Spectroscopy" Chapter III, Ed.K Siegbahn, North Holland Publ.Co. Amsterdam 1965

40. K. SIEGBAHN, C. NORDLING, S.E. KARLSSON, S. HAGSTROM and A. FAHLMAN, Nucl.Instr. and Meth 27 (1964) 173

41. K. SIEGBAHN, C.L. NORDLING and J.M. HOLLANDER J.M. UCRL - 10023, (1962) 232

42. R.L. GRAHAM, G.T. EWAN and J.S. GEIGER, Nucl.Instr. and Meth. 9 (1960) 345

43. E. RUDBERG, Proc.Roy.Soc. A127 (1930) 111

44. K. SIEGBAHN, Chapter III, Ed. K. Siegbahn. North-Holland Publ.Co. Amsterdam 1965

45. A. FAHLMAN, K. HAMRIN, R. NORDBERG, C. NORDLING, Phys.Rev. Lett 14 (1965) 127

46. K.E. EASTERLING and A.R. THÖLEN, Asta Met 20 (1972) 1001

47. K.E. EASTERLING and A.R. THÖLEN, Electron microscopy and structure of materials (ed. G. Thomas), 427, 1972, University of California Press

48. H. CONRAD et al. ibid, 438

49. P.B. HIRSCH, ibid 60

50. L.E. THOMES et al: High voltage electron microscopy; (eds. P.R. Swann et al) 255 1974, London, Academic Press

51. P.B. HIRSCH: ibid 2

52. G. THOMAS, Physical aspects of electron microscopy and microbeam analysis (eds. B.M. Siegel and D.R. Beaman) 81, 1975, Wiley

53. M. HENDERSON-BROWEN and K.F. HALE, High voltage electron microscopy: (eds P.R. Swann et al) 206, 2974, London Academic Press

54. T.E. MITCHELL, Microstructural analysis, (eds. J.L. McCall and W.M. Mueller) 125 1973, New York, Plenum

55. V.E. COSSLETT, Modern diffraction and imaging techniques in material science (eds. S. Amelinckx et al) 391, 1930, Amsterdam

56. C.J. HUMPHREYS, Jernkontorets Ann, 155 (1971) 459

57. H. HASHIMOTO, High voltage electron microscopy, (eds. P.R. Swann et al) 9 (1974) London, Academic Press

58. G.W. LORIMER and P.E. CHAMPNESS, High voltage electron microscopy: (eds P.R. Swann et al) 301, 1974, London, Academic Press

59. S. WHITE, ibid 317

60. J. NUTTING, Electron microscopy and structure of materials (ed. G. Thomas) 617, 1972, University of California Press

61. W.L. BELL and G. THOMAS, ibid, 23

62. P.B. HIRSCH et al: Phil. Mag. 1, (1956) 667

63. P.B. HIRSCH et al, Electron microscopy of thin crystals, 1965, London, Butterworths

64. S. AMELINCKY et al, Modern diffraction and imaging techniques in material science, 1970, Amsterdam, North-Holland

65. V.A. PHILLIPS, Modern metallographic techniques and their applications, 1971, New York, Wiley

66. D.J.H. COCKAYNE et al: Phil. Mag. 20, 1969, 1256

67. E. ZEITLER and M.G.R. THOMSON, Optik, 31 (1970) 258, 359

68. E. RUSKA, J.Roy.Microscop.Soc. 84 (1965) 77

69. M.G.R. THOMSON, Ibid 39 (1973) 15

70. D.O. HAYWARD, 1971 Chemisorption and Reactions on Metallic Films, ed. J.R. Anderson (New York Academic Press) p. 226

71. R.V. CULVER and F.C. TOMPKINS, 1959 Advances in catalysis Vol XI (New York: Academic Press), p.67

72. G.C. BOND 1962 Catalysis by Metals (New York: Academic Press)

73. D.O. HAYWARD and B.M.W. TRAPNELL, Chemisorption (London: Butterworths) 1964

74. G.C. WOOD, Techniques in Metals Research, Vol.4, Ed. R.A. Rapp (New York: Interscience)

75. G. EHRLICH, 1963a Metal Surface: Structure, Energetics, and Kinetics (Metals Park: ASM) p. 221

76. M.W. ROBERTS and B.R. WELLS, 1966 Disc. Faraday Soc. 41, 162

77. M.W. ROBERTS, 1967 Surface Sci. 8, 453

78. M.W. ROBERTS, 1969 Surface Sci. 15, 325

79. E.E. HUBER and C.T. KIRK, 1966 Surface Sci. 5, 447

80. M.J. BENNETT and F.C. TOMPKINS 1960, Proc.R.Soc. A259, 21

81. L.H. GERMER and J.W. MAY, 1966, Surface Sci. 4, 452

82. E. BAUER, 1965 Adsorption of croissance cristalline Colloq. Int.Cent.Nat.Rech.Sci. No.16, p.20

83. J.W. MAY, 1972 Adv.Catalysis 21, 151

84. T.H. GEORGE and P.M. STIER 1962 ChemPhys 37 (1935)

85. M.A.H. LANYON and B.M.W. TRAPNELL, 1955, Proc.R.Soc. A217, 387

86. J.W. MAY, 1969, Adv.Catalysis, 21, 151

87. D.F. MITCHELL and K.R. LAWLESS 1966, I.Paint Tech. 38, 575

88. G.W. SIMMONS, D.F. MITCHELL and K.R. LAWLESS, 1967, Surface Sci. 8, 130

89. M. HANSEN and K. ANDERKO, 1958 Constitution of Binary Alloys (New York: McGraw-Hill)

90. P. KOFSTAD, K. HAUFFE and H. KJOLLESDAL 1958 Acta Chem. Scand., 12, 259

91. I.M. RITCHIE and G.L. HUNT, 1969, Surface Sic. 15, 524

92. N.F. MOTT, 1940 Trans. Faraday Soc. 36, 472

93. N. CABRERA, 1949, Phil.Mag, 40, 175

94. N. CABRERA and N.F. MOTT, 1948, Rep.Proy.Phys. 12, 163

95. D.D. ELEY and P.R. WILKINSON, 1959, Structure and Properties of Thin Films, ed. C.A. Neugebauer et al (New York: John Wiley) P.508

96. K.R. LAWLESS, Rep.Prog.Phys. 1974, 34, 231-316

97. O. KUBASCHEWSKI and B.E. HOPKINS 1962, Oxidation of Metals and Alloys (London: Butterworths)

98. F.F. VOL'KENSHTEIN, 1967, Sov.Phys.Usp. 9, 743

99. T.I. BARRY and F.S. STONE, 1960, Proc.R.Soc. A255, 124

100. K. HAUFFE and H.J. ENGELL, 1952, Z.Elektrochem., 56, 366

101. F.P. FEHLNER and N.F. MOTT, 1970, f. Oxidation Metals, 2 59

102. A.F. BECK, M.A. HEINE, E.J. CAULE and M.J. PRYOR, 1967, Corrosion Sci. 7 1

103. J.A. DAVIES, B. BOMEIJ, J.P.S. PRINGLE and F. BROWN, J. Electrochem.Soc. 112, 675

104. M.A. HEINE and M.J. PRYOR, 1963, J.Electrochem.Soc. 110, 1205

105. R.K. HART, 1956, Proc.Roy.Soc. A236, 68

106. T.N. RHODIN, J.Am.Chem.Soc. 73, 3143

107. P.K. KRISHNAMOORTHY and S.C. SIRCAR, 1970, J.Oxidation of Metals, 2, 349

108. R.S. ALWITT, 1976, "The Aluminium-water System in oxide and oxide films," Vol.4, edited by J.W. Diggle, published Marcel Dekker, 169-254

109. W. VEDDER and D.A. VERMILYEA, 1969, 'Aluminium and Water Reaction" Trans.Faraday Soc. 65, 561-584

110. R.K. HART, 1957, Trans.Faraday Soc., 53, 1020

111. R.S. ALWITT and L.C. ARCHIBALD, (1973), Corrosion Sci. 13, 687

112. M. KAWASAKI, S. WOMURA, H. ITAMI, Y. KONO, Japan Atomic Energy Res.Inst.Rept. 1035 (1962)

113. H.H. PODGURSKI, 1948, Metal.Progr. 54, 195

114. M. MORIZE and P. LACOMBE, 1946, C.R.Acad.Sci., Paris, 222, 658

115. G. HASS, 1949, J.Opt.Soc.Amer., 39, 532

116. N. Cabrera, 1949, Rep.Progr.Phy. 12, 163

117. N. HACKERMAN and E.H. LEE, 1955, J.Phys.Chem. 59, 900

118. J. WUSTENHAGEN, 1957, Naturwissens chaften, 44, 228

119. L.P. THIEN, Phys.Rev. 53 (1938) 287

120. L. GRUNGERG and K.H.R. WRIGHT, 1954, Nature, 174, 657

121. L. GRUNGERG and K.H.R. Wright, 1955, Proc.Roy.Soc. (London) A232, 403

122. F. FIANDA and E. LANGE, 1951, Elektrechem 55, 237

123. H. MULLER and F. WEINBERER, 1957, Acta Phys. Austriaca, 10,409

124. E.E. HUBER and C.T. KIRK, 1966, Surface Sci. 5, 447

125. R.J. BATT and C.H.B. MEE, 1970, Appl.opt. 9, 79

126. T. FORT and R.L. WELLS, 1972, Surface Sci. 32, 543

127. J.C. GUFFLE, L.M. WATSON and D.J. FABIAN, 1975, Surface Sci. 49, 61

128. W.H. KRUEGER and S.R. POLLACK, 1972, Surface Sci. 43, 526

129. D.D. ELEY and P.R. WILKINSON, 1960, Proc.Roy.Soc. (London) A254, 327

130. I.M. BERNSTEIN and A.W. THOMPSON, eds. Hydrogen in Metals, ASM, Metals Park, Ohio (1974)

131. R.E. McCRIGHT, J.E. SLATER and R.W. STAEHLE, eds. Stress Corrosion and Hydrogen Embrittlement of Iron-based Alloys, NACE, Houston, Texas (1975)

132. R.P. JEWETT, R.J. WALTER, W.T. CHANDLER and R.P. FROHMBERG, Hydrogen Environment Embrittlement of Metals, Rocketdyne, NASA (R-2163, NASA, Washington, D.C. March (1973)

133. T.B. GROENEVELT, E.E. FLETCHER and A.R. ELSEA; Summarized in W. Beck, E.J. Jankowsky, and P. Fischer, Hydrogen stress cracking of High Strength Steels, NADC-MA-7140, WAVAL Air Dev.Cent. Warminster Da, (1971) December

134. A.R. TROIANO, Trans.Asm.,,Vol.52, p.54 (1960)

135. R.A. ORIANI and P.H. JOSEPHIC, Acta Met, Vol.22, p.1065,(1974)

136. K. SIEGBAH, C. WORDLING, A. FAHLMAN, R. WOROBERA, K. HAMRIN, J. HEDMAN, G. JOHANSSON, T. BERGMARK, S. KARLSSON, I. LINDGREN, B. LINDBERG,

ESCA, Atom, Molecular and Solid State Structure studied by means of electron spectroscopy presented to the Royal Society of Sciences of Uppsala, Dec.3rd, 1965.

137. L.G. PARRATT, Mod.Phys. 31, (1959) 616

138. B. HENKE, J.Phys. (paris), 4 (1971) 115

139. B. HENKE, Phys.Rev. A6 (1972) 94

140. W.A. FRASER, J.V. FLORIO, W.N. DELGASS and W.O. ROBERTSON, Surf.Sci. 36 (1973) 661

141. C.S. FADLEY, R.J. BAIRD, W. SIEKHAUS, T. NOVAKOV, S.A.L. BERGSTROM, Journal of Electron Spectroscopy and Related Phenomena, 4 (1974) 93-137

142. C.S. FADLEY and S.A.L. BERGSTROM, Phys.Lett. 35A (1971) 375; in D.A. Shirley (editor) Electron spectroscopy North Holland Publishing Co., Amsterdam 1972, p. 233

143. H. EBEL, M.F. EBEL and E. HILLBRAND, J.Electron Spectrosc 2 (1973) 277

144. F. ABELES, Ann.de Physique, 3 (1948) 504

145. R. DITCHBURN, Light (Blackie, London) 1952, p.480

146. P. ROUARD, Ann.de Physique, 7, (1937) 291

147. A. VASICEK, J. de Physique, 7 (1950) 342

148. K.R. O'SHEA, Ph.D. Thesis, Univ.of Aston (1971)

149. F.L. McCRACKIN, E. PASSACAGLIA, R. STROMBERG and H.L. STEINBERG: J. Research Nat.Bar of Standards, 67A, 363, (1963)

150. E. ZEITLER and M.G.R. THOMSON, Optik, 31, (1970), 258

151. M.G.R. THOMSON, Ibid, 39 (1975) 15

152. O. ALMEN and G. BRUCE 1961 Nucl.Instrum.Methods, 11, 257

153. G.M. McCRACKEN, Rep.Prog.Phys. 38 (1975) 241

154. J. LINDHARD and M. SCHARFF, Phys.Rev. 34, (1961) 128-130

155. R.W. FANE and W.E.J. NEAL, J.Opt.Soc.Amer, 60 (1970) 760

156. H.G. JARRARD, J.Opt.Soc.Am. 42 (1952) 159

157. P.V. ANDREWS, Phil.Mag. 19 (1969) 99

158. T.L. BARR, J.Vac.Sci.Technol, Vol.14 Vol Jan/Feb 1977

159. C. TUCK, Private communication

160. M.A. BARRETT, Ellipsometry in the measurement of surfaces and thin film, Ed. (E.Passaglia), National Bureau of Standards, Washington, 1964

161. R.M. AGUOAD BOMBIN and W.E.J. NEAL, Thin Solid Film, 42, (1977) 91-96

162. J. KUCIVEK and A.J. MELMED, J.Opt.Am, 65 (1976) 611

163. M. HANSEN and K. ANDERKO 1958 Constitution of Binary Alloys (New York: McGraw-Hill)

164. C.J. POWELL, Surface Science, 44 (1974) 29-46

165. C.C. CHANG and D.M. BOULIN, Surface Science, 69 (1977) 385-402

166. FLOWER To be published (1977)

167. W.E.J. NEAL, Private communication

168. TAYLOR and EDGER, Met.Trans. Vol.2 1971 133

169. N.C. DARES Private communication

ACKNOWLEDGMENTS

I should like to thank my Supervisor, Dr. W.E.J. Neal, for his invaluable guidance and help throughout the course of this work.

Thanks are due to T. Thomas, G. Scaman and N.Daves who gave advice and encouragement for the part of the work carried out at Alcan Laboratories, Banbury.

I wish to express my gratitude to the technical staff of the Alcan Laboratory. I am particularly indebted to C. Wiseman.

To be submitted for
Publication.

Measurement of Optical Constants and Thickness of Aluminium Hydroxide Films Grown in Water Vapour.

A. S. Rehal and W. E. J. Neal

Physics Department, University of Aston in Birmingham,

Birmingham B4 7ET.

Abstract

The optical constants of aluminium hydroxide films grown in a humidity chamber at 70°C and 100% relative humidity, on gold film substrates have been measured ellipsometrically at a wavelength of λ = 546 n.m. For thin films of aluminium hydroxide less than 80 n.m. the best fit for optical constants were found to be $n_1 = 1.58 \pm 0.03$ and $k_1 = 0$, but for films more than 80n.m. thick, a better fit was found with $n_1 = 1.58 \pm 0.03$ and $k_1 = 0.0009$. Interferometry was used as an independent method for measuring aluminium and aluminium hydroxide film thicknesses. The effect on ellipsometric parameters Ψ and Δ of changing the base optical constants were also studied by computer simulation.

REFERENCES

(1) J. R. Ambrose and J. Kruger. Corrosion 28 30 (1972)

(2) R. S. Alwitt, Oxide and Oxide Films, Vol. 4, edited by J. W. Diggle and A. K. Vijh. Publ. by Maral Dekker, (1976) p.169

(3) W. Vedder and D. A. Vermilyea,J. Electrochem.Soc. 115 561 (1968)

(4) O. Heavens Optical Properties of Thin Solid Film, (Dover, New York) 1965

(5) W. E. J. Neal. Surface Technology 6 81 (1977)

(6) R. W. Ditchburn J. Op.Soc.Am. 45 743 (1955)

(7) S. Tolansky. Multiple Beam Interferometry,Clarendon Press, Oxford (1969)

(8) W. E. J. Neal, R. W. Fane, and N. W. Grimes. Phil. Mag.21 167 (1970)

(9) A. B. Winterbottom, in Ellipsometry in the Measurement of Thin Films. E. Passglia, R. Stromberg and J. Kruger Eds. Nationial Bureau of Standards (U.S.). Misc.Pub/256 (U.S. Govt. Printing Office Washington D.C. (1961) p. 97

(10) F. L. McCrackin, E. Passaglia, R.R. Stromberg and A. L. Steinberg, J Res.Nat.Bur.Std. (U.S.) A37 363 (1963)

(11) R. M. Aguado Bombin and W. E. J. Neal. Thin Solid Films 42 91-96 (1977)

(12) J. Kucivek and A. J. Melmed. J.Opt.Am. 65 611 (1976)

(13) M. A. Barrett. Elipsometry in the Measurement of Surfaces, and Thin Film, Ed. (E. Passaglia), Nationial Bureau of Standards Washington 1964.

Measurement of Optical Constants and Thickness of Aluminium Hydroxide Films Grown in Water Vapour

A. S. Rehal and W. E. J. Neal

Physics Department,

University of Aston in Birmingham

B4 7ET

1. Introduction

The properties of corrosion layers of hydroxides or oxides on metals are of considerable interest in all branches of science and engineering. In some cases surface layers form a protection against further corrosion and the susceptibility of a metal to stress corrosion cracking could be related to the rupture of a protective surface film and the repassivation rate of the freshly exposed metal to the environment as has been suggested by Ambrose and Kruger (1). The increased interest in surface properties during the last decade has prompted investigations using a wide range of analytical techniques. The work reported here forms part of a programme of investigation using the complementary techniques of E.S.C.A.(X.P.S.),electron microscopy and ellipsometery to study the composition optical and structural properties of films grown on aluminium exposed to various environmental conditions. Of particular interest has been the growth of aluminium hydroxide films on commercial and pure aluminium when exposed to saturated water vapour. The reaction of aluminium with water in the liquid phase (as opposed to the vapour phase) has been studied extensively by Alwitt(2) and Vedder and Vermilyea (3). It has been found that for aluminium hydroxide films formed at a temperature less than 90^{o}C the structure consists of an outer layer of bayerite crystals with an inner layer of pseudo boehmite. To date little work has appeared in the literature on the reaction of aluminium

Measurement of Optical Constants and Thickness of Aluminium Hydroxide Films Grown in Water Vapour.

A. S. Rehal and W. E. J. Neal

Physics Department, University of Aston in Birmingham,

Birmingham B4 7ET.

Abstract

The optical constants of aluminium hydroxide films grown in a humidity chamber at 70°C and 100% relative humidity, on gold film substrates have been measured ellipsometrically at a wavelength of λ = 546 n.m. For thin films of aluminium hydroxide less than 80 n.m. the best fit for optical constants were found to be n_1 = 1.58±03 and k_1=0, but for films more than 80n.m. thick, a better fit was found with n_1 = 1.58±03 and k_1=0.0009. Interferometry was used as an independent method for measuring aluminium and aluminium hydroxide film thicknesses. The effect on ellipsometric parameters Ψ and Δ of changing the base optical constants were also studied by computer simulation.

with water vapour and this report deals with a technique which has been developed for investigating the optical properties and density of aluminium hydroxide films, particularly during the early stages of growth. A discussion on thin film optics and the several methods by which optical properties have been measured by various authors can be found in a book by Heavens (4).

2. Optical Measurements

A review of the application of ellipsometry to the investigation of surface films and film growth has been given by Neal (5) and need not be described in detail here. The basic equation for the instrument is:

$$r_p/r_s = \tan \psi \exp i\Delta \qquad (1)$$

where r_p and r_s are the Fresnel coefficients for light with its electric vector parallel and perpendicular to the plane of incidence respectively. The two angles ψ and Δ are obtained from the instrument settings of the polariser and analyser at extinction. The optical constants n and k for a film free surface were given by Ditchburn (6) in terms of the angles ψ and Δ and the angle of incidence ϕ_o:-

$$n^2 - k^2 = \sin^2 \phi_o \left[1 + \tan^2 \phi_o (\cos^2 2\psi - \sin^2 2\psi \sin^2 \Delta)/(1 + \sin 2\psi \cos\Delta)^2 \right] \qquad (2)$$

$$2nk = (\sin^2 \phi_o \tan^2 \phi_o \sin 4\psi \sin\Delta)/(1 + \sin 2\psi \cos\Delta)^2 \qquad (3)$$

For a film covered surface (see Figure 1) the Fresnel reflection coefficients are

$$r_p = \left\{ (r_{01})_p + (r_{12})_p \exp D \right\} \left\{ 1 + (r_{01})_p (r_{12})_p \exp D \right\}^{-1} \qquad (4)$$

with a similar expression for r_s.

For a non absorbing film

$$D = 4 \pi n_1 (\cos \phi_1) \, t/\lambda_o \qquad (5)$$

For an absorbing film:

$$D = 4 \pi i n_1 (\cos \phi_1) t/\lambda_o \qquad (6)$$

where λ_o is the radiation wavelength and t the film thickness.

For a non absorbing film when $k_1 = 0$, which is the case for most oxides and hydroxides, in order to obtain both n_1 and t it is necessary to know the optical constants (n_2, k_2) of the underlying metal base. For a reactive metal such as aluminium it is difficult to measure n_2 and k_2 in the absence of a film unless the surface film can be removed in U.H.V. by ion bombardment and the optical measurements also made in U.H.V. An alternative is to evaporate a thin film of the metal at a pressure of the order of 10^{-10} torr and measure the optical properties before a film has had time to grow. Both these approaches have been used by the authors in the course of the present investigations with success but another technique has also been adopted and shown to be applicable. It could for example be used in circumstances where the alternatives mentioned above and which require U.H.V. equipment are not always available.

3. Principle of the Method and Sample Preparation

(1) A thick film of a non reactive metal such as gold (or platinum) is deposited on a glass substrate and the surface is characterised by the angles ψ and Δ determined from the instrument extinction settings. In turn the optical constants can be computed from equation (2) and (3). A film of aluminium is then superimposed on the gold film. The thickness of aluminium can be determined by an interference method suggested by Tolansky (7) with fringes of equal chromatic order using an interference microscope.

(2) The aluminium film is then exposed to the water vapour environment sufficiently long for all the aluminium to react to form aluminium hydroxide. This state is easily detected since the hydroxide film

is non absorbing or nearly so in visible light (see later).

(4) The changes in ψ and Δ ($\delta\psi$ and $\delta\Delta$) from the gold surface due to the presence of the hydroxide film are measured.

(5) The hydroxide film is then overlaid by a highly reflecting film of aluminium or silver and the hydroxide thickness determined by the interference microscope.

4. Experimental Procedure

Glass substrates which were cut from microscope slides were cleaned by immersing in 3% detergent solution in an ultrasonic bath, followed by repeated cleaning in distilled water in an ultrasonic bath. Finally the substrates were boiled in isopropyl alcohol and dried by withdrawing through the vapour. They were then mounted in a vacuum system above a tungsten boat from which gold was evaporated at a base pressure of 5×10^{-7} torr. After evaporation the gold films were removed from the vacuum chamber and annealed at $100^{\circ}C$ for 2 hours before ellipsometric readings were taken.

The gold films were replaced in the vacuum system and aluminium films of various thicknesses were evaporated from a tungsten filament. During evaporation it was possible to hold the pressure to 2×10^{-6} torr. For each set of readings two aluminium films of equal thickness were evaporated simultaneously. One was used for ellipsometric tests and the other for thickness measurements. Fig. 2 shows cross sections through the substrates and film systems. Fig. 2.1. represents the arrangement used for the measurement of optical properties of gold. Fig. 2.2a shows the system which was used for the measurement of optical properties of Aluminium. Fig. 2.2b shows the system which was used for thickness measurement of Aluminium films.

The specimen for ellipsometric tests was placed vertically in a humidity chamber at 70°C and 100% relative humidity. After the reaction was completed an aluminium hydroxide film was formed on the gold film, as shown in Figure 2.3. Fig. 2.4 shows the system which was used for the measurement of aluminium hydroxide film thickness.

Details of the type of ellipsometer (with compensator) used in these investigations have been given elsewhere (8,9). A selection from the 32 possible settingswas made in the manner described by McCrackin (10). Ellipsometric readings were made before and after placing the specimens in the humidity chamber. A few stereoscan photographs were also taken to determine the structure of the hydroxide films. The gold films, the aluminium overlay films and the hydroxide films were examined using a step scan x-ray diffractometer.

5. Results

Aluminium hydroxide film thicknesses were measured as indicated by interferometry. It was also possible to evaluate the thickness from ellipsometer readings since the films were on a gold base the optical constants (n_2, k_2) of which had previously been measured. By using a value n_1 for the hydroxide film, values of ψ and Δ were computed for various hydroxide thicknesses on gold. A "best fit" was found for films of various thicknesses. The increase in thickness from the aluminium metal to the complete hydroxide layer was also measured. Table 1 shows thicknesses of hydroxide measured by ellipsometry and by the interference microscope and the original metal film thickness measured by the interference microscope together with changes in instrument parameters for increased thicknesses of aluminium hydroxide on gold.

The instrument settings for the film free gold base, ψ and Δ were equal to 40.7° and 119.6° respectively at a wavelength of 546 nm giving $n_\lambda = 0.48 \pm 005$ $k_\lambda = 2.54 \pm 0.1$ for the gold layer at an angle of incidence of 64.2°.

Table I

Film No.	1	2	3	4	5	6	7	8
Thickness in n.m. of Aluminium film on gold (Interferometry)	22±3%	25±3%	32±3%	39±3%	42.0±3%	42.5±3%	120.5±3%	127.±3%
Thickness in n.m. of Aluminium hydroxide film on gold (Interferometry)	33±5%	39±5%	50±5%	53±5%	61 ±5%	65±5%	167±2.5%	178.5±2.5%
$\delta\psi^\circ$ changes due to hydroxide film	+3.65	+5.95	+7.72	+8.34	+9.14	+9.44	-1.35	-1.56
$\delta\Delta^\circ$ changes due to hydroxide film	-21.18	-12.78	+7.98	+11.60	+36.69	+52.42	+42.74	+30.12
Aluminium hydroxide thickness measured ellipsometrically(n.m) using n = 1.58	36±4%	43±4%	52±4%	55±4%	65±4%	66±4%	175±2%	185±2%
Ratio of $\frac{E}{A}$	1.6	1.7	1.6	1.6	1.5	1.5	1.4	1.4

Fig. 3 a,b,c,d,e,f,g,h, show stereoscan photographs of Aluminium hydroxide on glass and gold. Examination of the specimens using a step scan X-ray diffractrometer, with Cobalt k_α radiation showed that both the base gold films and the superimposed Aluminium films had a preferred orientation in the (111) direction. Examination of the Aluminium hydroxide showed a weak line at $2\theta = 18.4^\circ$.

6. Discussion

As has been pointed out in section 3 the ellipsometric measurements involve changes in the instrument parameters ψ and Δ due to the presence of varying thicknesses of aluminium hydroxide on the gold base. The film free gold base yielded initial values of ψ and Δ which were substituted into equations (2) and (3) to evaluate the optical constants n_2 and k_2 for the surface. Using these computed constants, and a two layer programme, values of the angles ψ and Δ were computed for composite surfaces of varying aluminium hydroxide thicknesses on gold and an assumed value of refractive index for the hydroxide.

Fig. (4) shows a plot of measured ψ and Δ for the eight Aluminium hydroxide films together with computed values of ψ and Δ using various values of refraction index for Aluminum hydroxide assuming $k_1 = 0$. It can be seen from Fig. (4) that in all cases where $k_1 = 0$, a complete loop is formed in that when very thick films are measured ψ and Δ values repeat themselves.

There are two samples (7 and 8) for which the measured ellipsometric parameters do not lie on any of the computed closed loops. Fig. (5) shows similar plots but in each case with a value of $k_1 = 0.0009$ (i.e. a small absorption is assumed). It can now be seen that 7 and 8 lie on curves with n_1 values between 1.55 to 1.60 and $k_1 = 0.0009$. This represents the best fit for thicker aluminium hydroxide films i.e. thicker than about 80 n.m. When the optical parameter ψ and Δ for films less than 80 n.m. are ploted on the computed graph where $k_1 = 0$ there is better agreement between the computed thickness and measured thickness by interferometry). It would appear therefore that in these early stages of growth the optical constants for the hydroxide at a wavelength of 546 n.m. are $n_1 = 1.58 \pm 03$ and $k_1 = 0$ and for thicker films the constants are

given by $n_1 = 1.58 \pm .03$ and $k_1 = 0.0009$. It is also interesting to note that thicker films are more compact as can be seen in Table I(F).

The optical constant of Aluminium hydroxide films, prepared under these conditions have not been reported in the literature. However, the optical constants of electropolished Aluminium, reacting with hot circulating water has been reported by Barrett (13) to be $n_1 = 1.60$, $k_1 = 0$.

Alwitt (2) has shown that the reaction of water with Aluminium for temperatures less than 90°C produces an outer layer of bayerite crystals with an inner layer of pseudo boehmite and the other forms of aluminium hydroxide are only produced at higher temperatures.

As already mentioned the step scan X-Ray diffractrometer showed a weak line at $2\theta = 18.4^\circ$ using Cobalt α radiation which we assumed to be pseudo boehmite since the aluminium hydroxide in this was formed at 70°C.

The structure of aluminium hydroxide on glass and on gold films can be seen from Figs. 4a, b, e and f which are of thicker films and with magnifications 2.1K, 5.2K, 0.42K and 1.7K respectively. The micrographs b and f show the porous nature of the hydroxide. Micrographs c, d, g and h are of thinner aluminium hydroxide films on glass and gold and illustrate the island structure of early growth stages in all cases. The sensitivity of the method for determining the constants of the superimposed hydroxide layer depends on the relative optical constants of the base and film. It is also important that the base material is non reactive and this was the reason for selecting gold in this work. However values have been computed for four base materials and the results are illustrated in Figure 6. A glass substrate is least sensitive, followed by gold, tantalum and platinum. Although an oxide layer of the order of 1 n.m. forms on tantalum when exposed to the atmosphere

(Aguado-Bombin and Neal[11]) it could be employed as a base since it has been shown by Kucirek and Melmed[12] that in many cases of film growth on metals it is possible to use pseudo constants for a surface prior to subsequent film growth subject to certain limitations.

Acknowledgments

One of us A.Rehal acknowledges a grant in the form of a CASE award from the Science Research Council and appreciates the help given by personnel and the opportunity to use equipment at the research laboratories of the collaborating body, Alcan International Ltd. of Banbury.

REFERENCES

(1) J. R. Ambrose and J. Kruger. Corrosion 28 (1972) 30

(2) R. S. Alwitt, Oxide and Oxide Films, Vol. 4, edited by J. W. Diggle and A. K. Vijh. Publ. by Maral Dekker, (1976) p.169

(3) W. Vedder and D. A. Vermilyea,J. Electrochem.Soc. 115 (1968) 561.

(4) O. Heavens Optical Properties of Thin Solid Film, (Dover, New York) 1965

(5) W. E. J. Neal. Surface Technology 6 (1977) 81

(6) R. W. Ditchburn J. Op.Soc.Am. 45 (1955) 743

(7) S. Tolansky. Multiple Beam Interferometry,Clarendon Press, Oxford (1969)

(8) W. E. J. Neal, R. W. Fane, and N. W. Grimes. Phil. Mag.21 (1970) 167

(9) A. B. Winterbottom, in Ellipsometry in the Measurement of Thin Films. E. Passglia, R. Stromberg and J. Kruger Eds. National Bureau of Standards (U.S.). Misc.Pub/256 (U.S. Govt. Printing Office Washington D.C. (1961) p. 97

(10) F. L. McCrackin, E. Passaglia, R.R. Stromberg and A. L. Steinberg, J Res.Nat.Bur.Std. (U.S.) A37 (1963) 363

(11) R. M. Aguado Bombin and W. E. J. Neal. Thin Solid Films 42 (1977) 91-96

(12) J. Kucivek and A. J. Melmed. J.Opt.Am. 65 (1976) 611.

(13) M. A. Barrett. Elipsometry in the Measurement of Surfaces, and Thin Film, Ed. (E. Passaglia), National Bureau of Standards Washington 1964.

FIGURE LEGENDS

Fig 1 Reflection and Transmission of light by a single film

Fig 2 Section through film specimens

2.1 For measurement of optical properties of gold

2.2a For measurement of optical properties of Aluminium

2.2b For measurement of Aluminium film thickness

2.3 For measurement of optical properties of Aluminium hydroxide

2.4 For measurement of Aluminium hydroxide film thickness

Fig 3a Magnification X1000 Thick Aluminium hydroxide film on glass Substrate

Fig 3b Magnification X5200 Thick Aluminium hydroxide film on glass Substrate

Fig 3c Magnification X400 Thin Aluminium hydroxide film on glass Substrate

Fig 3d Magnification X1000 Thin Aluminium hydroxide film on glass Substrate

Fig 3e Magnification X2500 Thick Aluminium hydroxide film on gold film

Fig 3f Magnification X5600 Thick Aluminium hydroxide film on gold film

Fig 3g Magnification X350 Thin Aluminium hydroxide film on gold film

Fig 3h Magnification X10000 Thin Aluminium hydroxide film on gold film

Fig 4 The graph of Ψ against Δ for films of different refractive indices on a gold substrate

Fig 5 The graph of Ψ against Δ for films of different refractive indices on a gold substrate

Fig.6 The graph of Ψ against Δ for films of the same refractive index but different substrates.

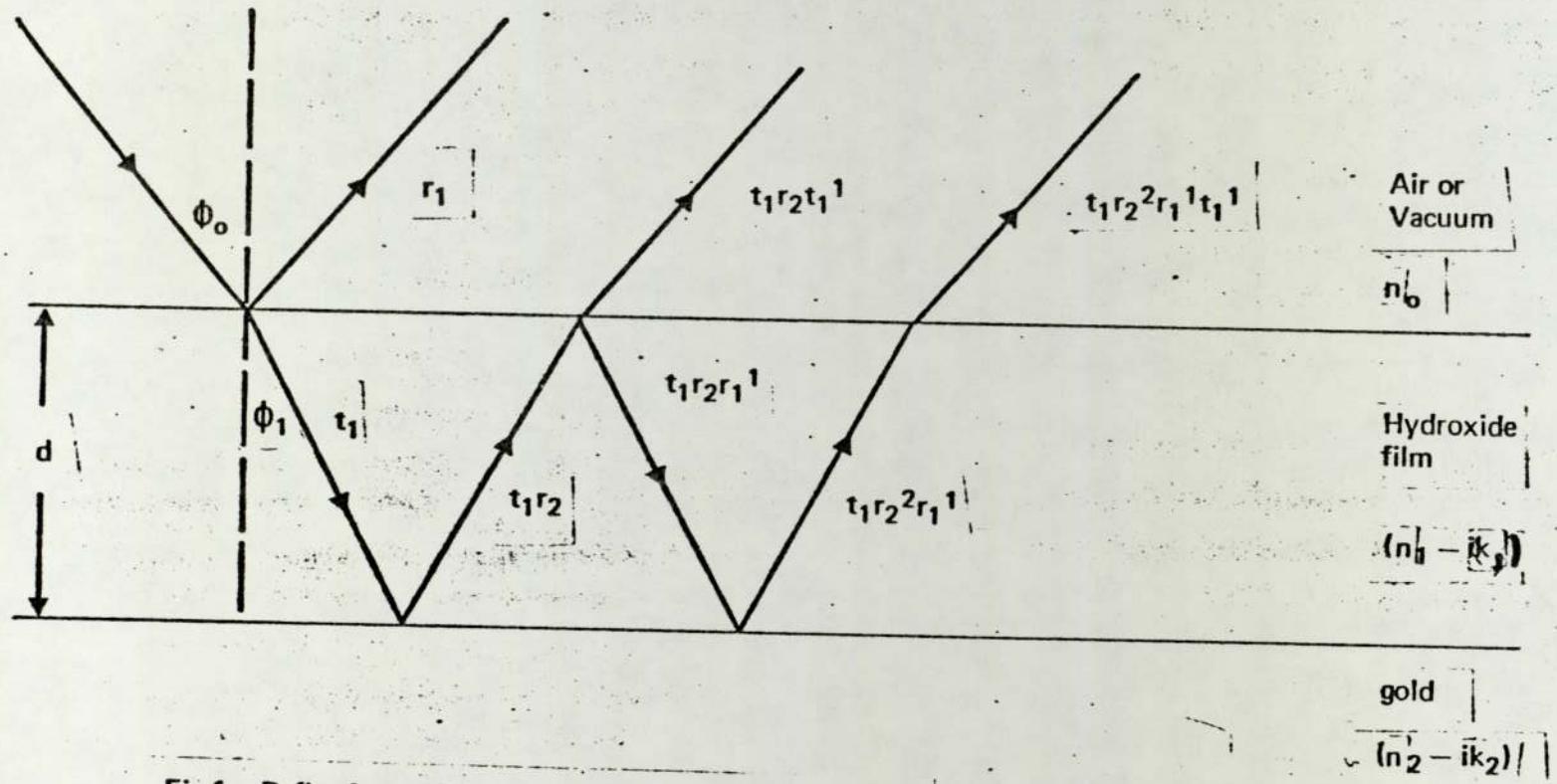

Fig 1 Reflection and Transmission of light by a single film

Fig 2 Section through film specimens

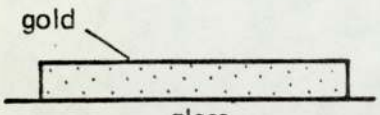

Fig. 2.1

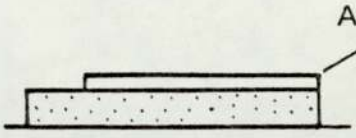

Fig. 2.2a

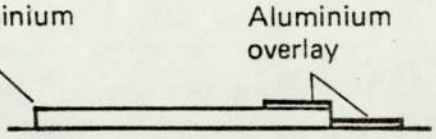

Fig. 2.2b

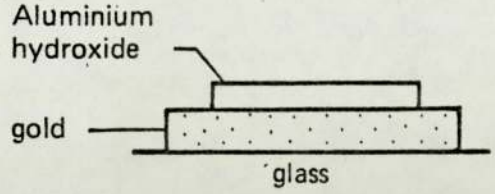

Fig. 2.3

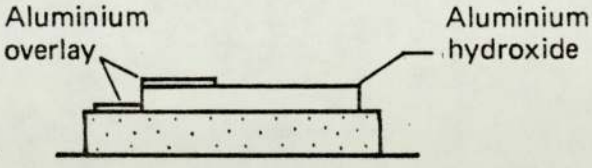

Fig. 2.4

2.1 For measurement of optical properties of gold

2.2a For measurement of optical properties of Aluminium

2.2b For measurement of Aluminium film thickness

2.3 For measurement of optical properties of Aluminium hydroxide

2.4 For measurement of Aluminium hydroxide film thickness

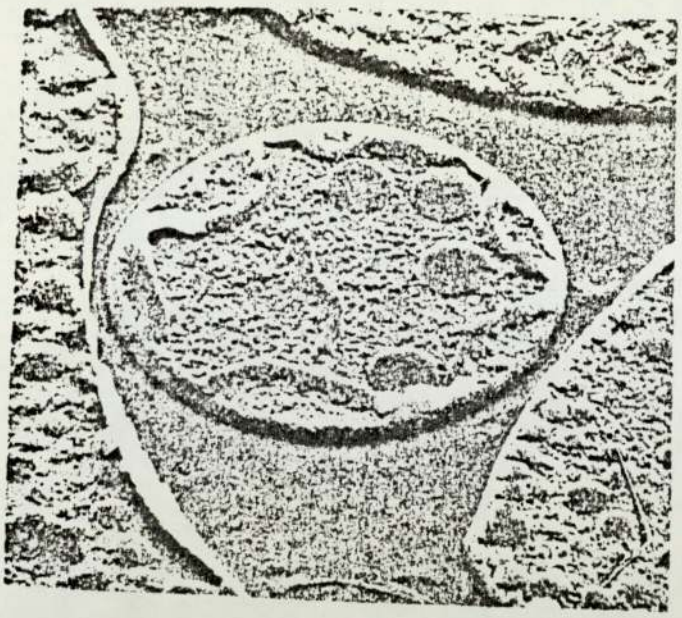

Fig3a Magnification X1000: Thick Aluminium hydroxide film on glass substrate

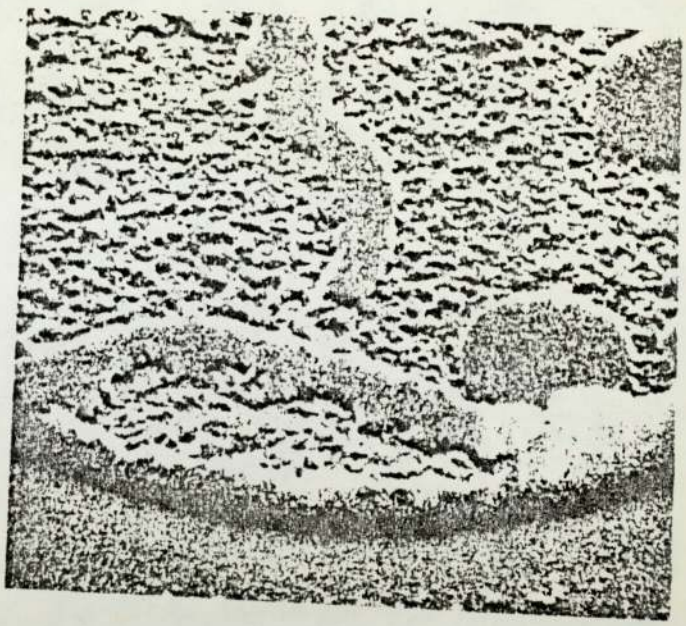

Fig3b Magnification X 5200 Thick Aluminium hydroxide film on glass substrate

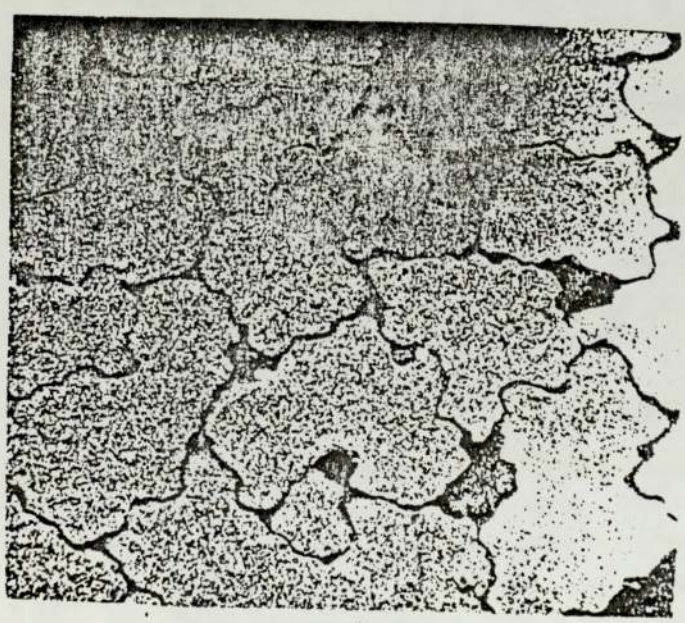

Fig3c Magnification X400 Thin Aluminium hydroxide film on glass substrate

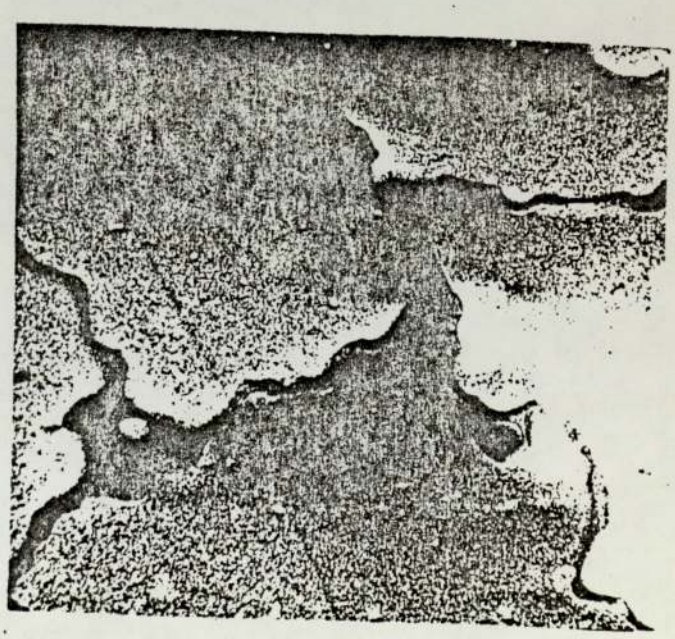

Fig3d Magnification X1000 Thin Aluminium hydroxide film on glass substrate

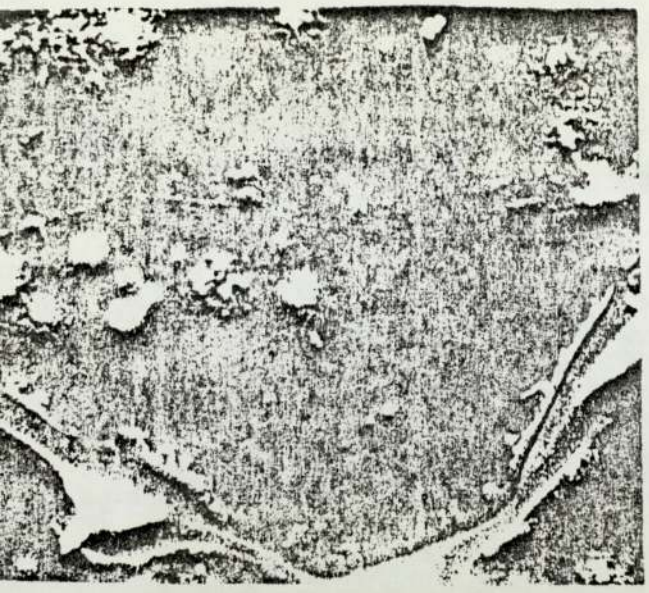

g3e Magnification X2500Thick
uminium hydroxide film on
old film

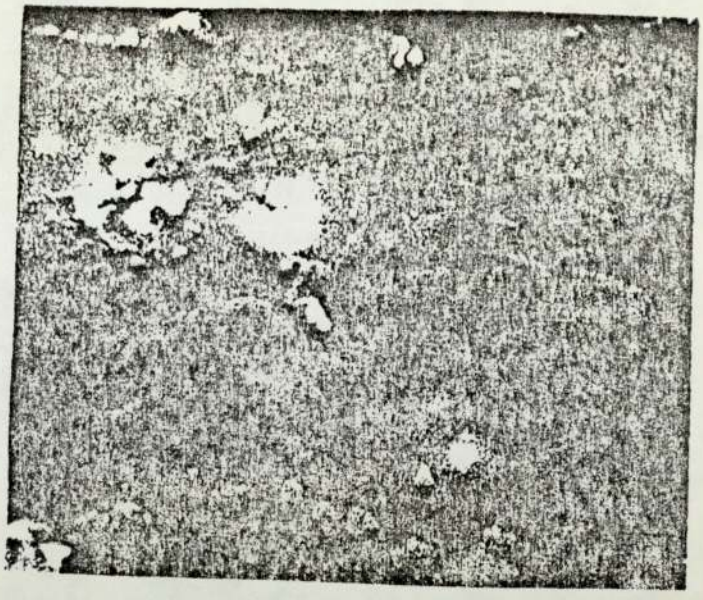

Fig3 Magnification X5600 Thick
Aluminium hydroxide film on
gold film

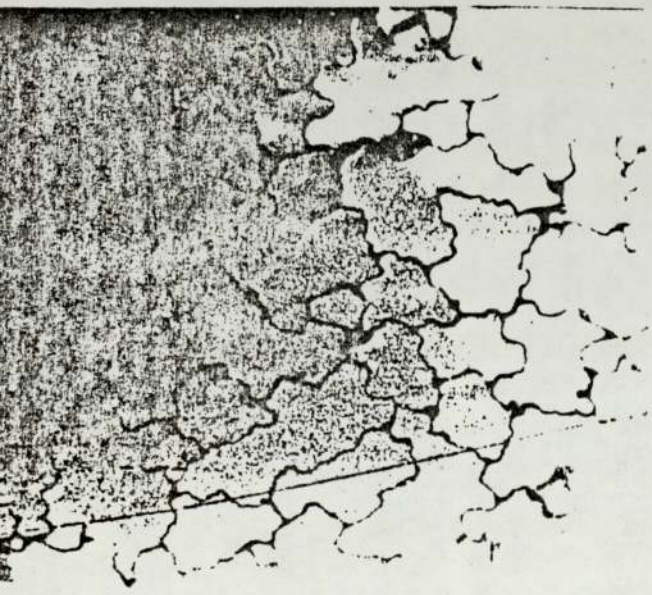

g3g Magnification X350 Thin
Aluminium hydroxide film on
gold film

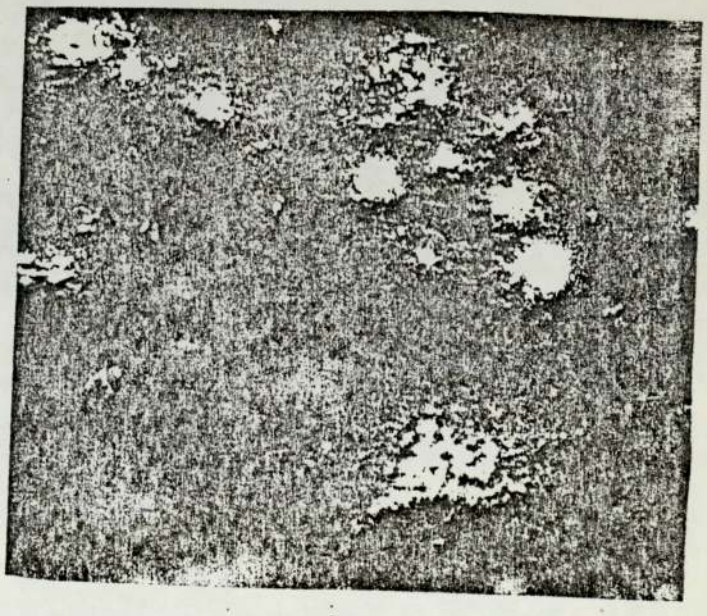

Fig3h Magnification X10000 Thin
Aluminium hydroxide film on
gold film

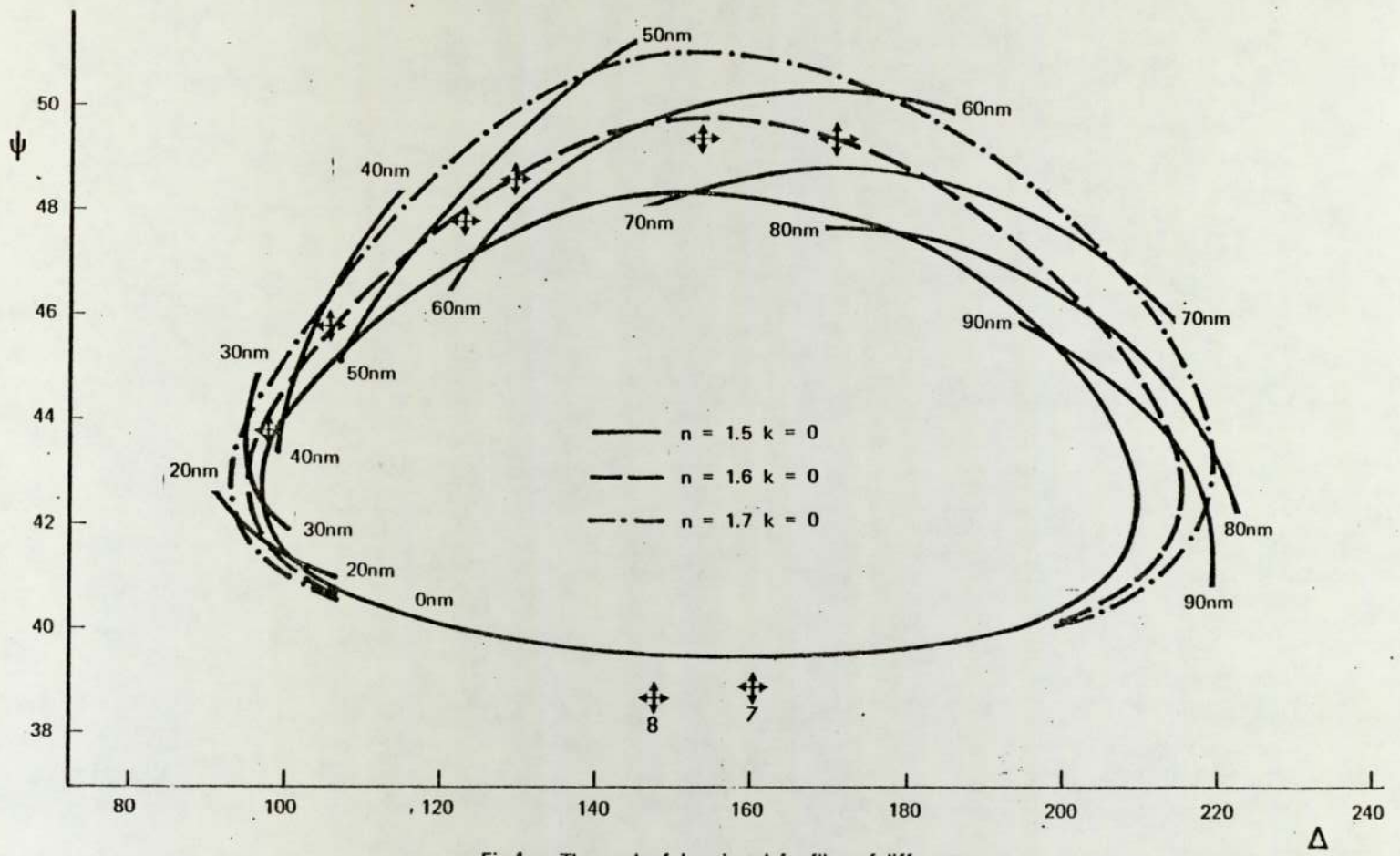

Fig 4 The graph of ψ against Δ for films of different refractive indices on a gold substrate

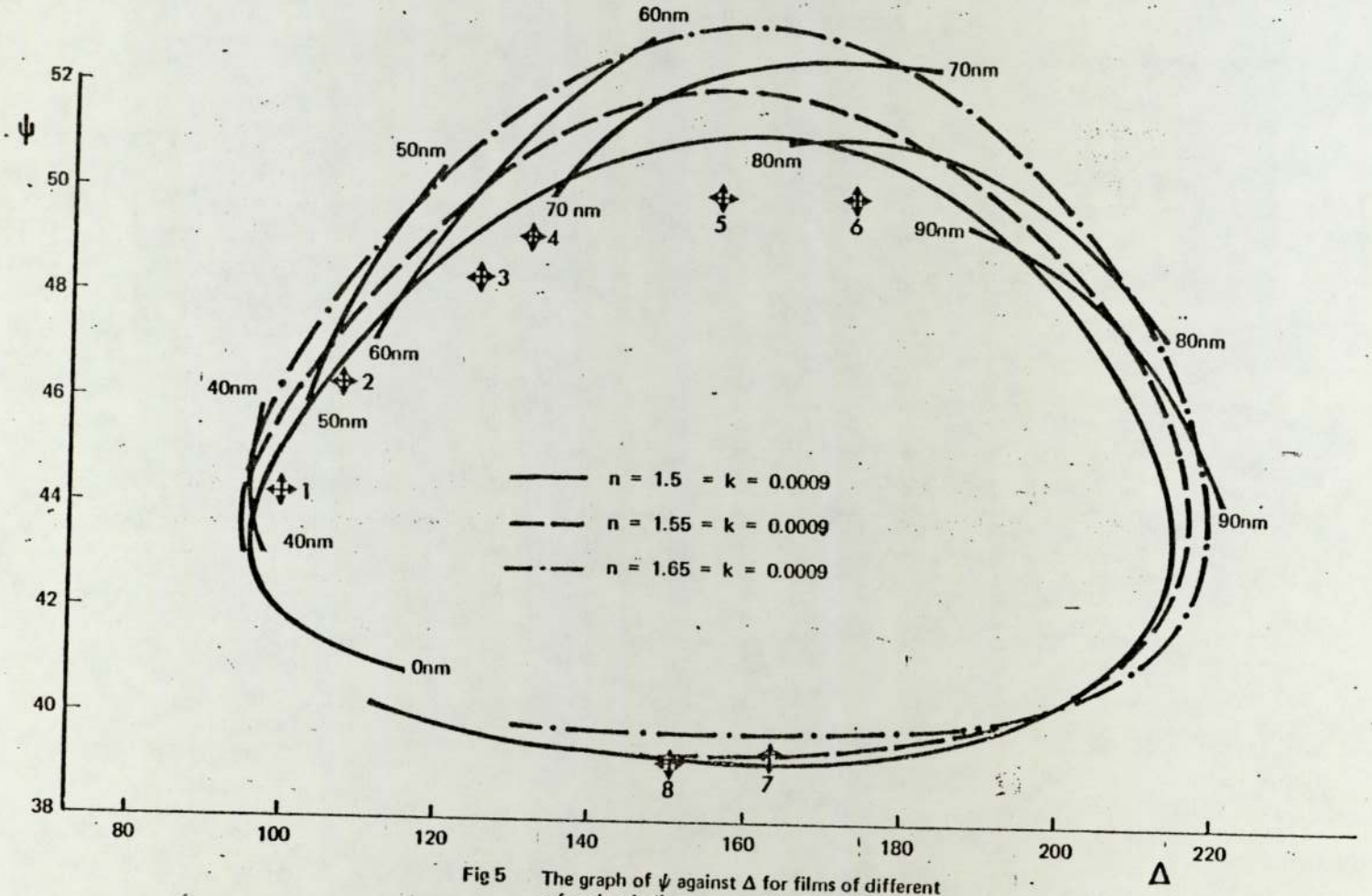

Fig 5 The graph of ψ against Δ for films of different refractive indices on a gold substrate

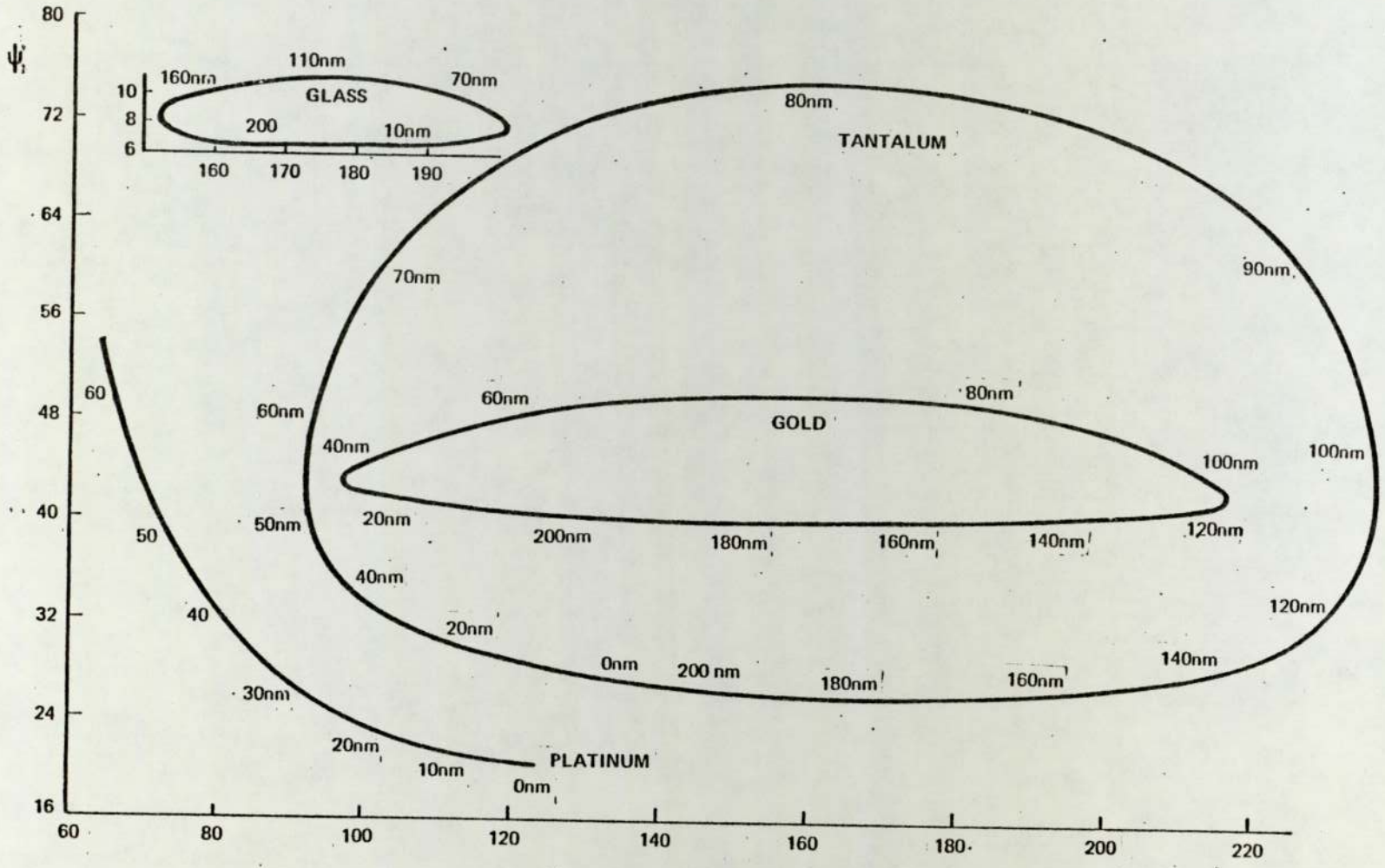

Fig 6 The graph of ψ against Δ for films of the same refractive index, but different substrates

Presented at the Washington
Conference on Contamination
Control, September 1978

ELLIPSOMETRIC OBSERVATIONS OF ALUMINIUM HYDROXIDE FILMS GROWN IN WATER VAPOR

W.E.J.Neal and A.S.Rehal

The University of Aston in Birmingham,
Gosta Green,
Birmingham, B4 7ET, United Kingdom.

The paper describes ellipsometric investigations of aluminium hydroxide films grown on aluminium surfaces which have been exposed to water vapor. The types of samples used for the investigations have been:-

1. Commercial aluminium sheet which had been etched by Argon ions and exposed to water vapor in a vacuum system at 25 °C.
2. As supplied commercial aluminium sheet which had been chemically or mechanically cleaned and exposed to saturated water vapor at 70 °C.
3. Freshly deposited films exposed to water vapor in a vacuum system at 25 °C.

The optical constants for aluminium hydroxide at a wavelength of 549 nm for films up to 65 nm thick were found to be n = 1.55 to 1.60, k = 0.

For hydroxide films which were grown on gold surfaces (by depositing aluminium films on gold and then exposing to saturated water vapor at 70 °C) the best values of optical constants were found to be:-

$n_1 = 1.58 \pm 0.03$, $k_1 = 0$ for films < 80 nm thick
$n_1 = 1.58 \pm 0.03$, $k_1 = 0.0009$ for films > 80 nm thick

INTRODUCTION

The susceptibility of Aluminium-Zinc-Magnesium alloys to stress corrosion often restricts their more widespread use with the result that much research effort has been put into determining the mechanism of stress-corrosion cracking. The properties of corrosion layers of hydroxides or oxides on metals are therefore of interest to workers in many branches of science and engineering. Tronstad[1] was one of the earliest workers to study the growth of corrosion layers on materials by ellipsometry. Following his pioneering work the technique has been employed by many authors [2,3,4,5] in conjunction with oxidation and corrosion studies.

The work reported here forms part of a programme of investigation using the combined techniques of ESCA (XPS) electron microscopy and ellipsometry to study the composition, optical and structural properties of films grown on aluminium and aluminium alloys exposed to various environmental conditions. The optical properties of aluminium hydroxide films grown on pure aluminium when exposed to saturated water vapour will be considered here, particularly in the early stages of growth. Alwitt[6] and Vedder and Vermilyea[7] have made extensive studies on the reaction of aluminium with water (in the liquid phase). The reaction of aluminium with water at 70 °C produces a duplex film consisting of pseudo-boehmite on aluminium oxyhydroxide, similar to boehmite (AlOOH) but containing more water, and bayerite ($Al(OH)_3$). Bayerite crystals take the form of pillars or cones and pseudo-boehmite appears as needles when viewed by transmission electron microscopy or platelets when viewed by scanning electron microscopy[6].

There has been much less reported work on the reaction of aluminium with water vapour or the formation and structure of aluminium hydroxide films on aluminium formed at low exposures. Such studies require ultra high vacuum facilities and surface sensitive techniques and we have used the complementary techniques of ESCA with ellipsometry. In some instances it has also been possible to combine transmission electron microscopy (TEM), scanning transmission electron microscopy (STEM) and scanning electron microscopy using the JEOL 100C Temscan Instrument. It is possible with the instrument to compare surface features with underlying microstructure for precisely located areas.

OPTICAL MEASUREMENTS

An outline of the technique of ellipsometry is included in a review on the "application of ellipsometry to surface films and film growth" by Neal[8]. Essentially, in measurements on

surface film growth, the optical properties of a surface are determined before, during and after the growth of the layer or film and the instrument is particularly appropriate in studies of highly reflecting materials such as metals. In most circumstances when an incident beam of plane polarized light is reflected from a metal surface the reflected beam is elliptically polarized. The two exceptions are when the electric vector of the incident radiation is vibrating parallel or perpendicular to the plane of incidence. In both cases the reflected light is then plane polarized with the same vibrational direction as in the incident beam and these directions are used as reference directions. The optical constants of a surface can be determined from the orientation of the ellipse with respect to the plane of incidence and the ratio of the major to minor axis. The presence of a thin layer on the surface modifies the optical constants and in turn the characteristics of the elliptically polarized light in the reflected beam.

The basic ellipsometer for measurements in the visible region of the spectrum is made up of the following basic components: 1. - a filtered light source or monochromator, 2. - a polarizer comprising Polaroid, a Nicol or Glan Thomson prism to produce plane polarized light, 3. - a specimen holder, 4. - a compensator, sometimes referred to as a quarter wave plate, to convert elliptically polarized light to plane polarized light, 5. - an analyzer, as in the polarizer, to detect plane polarized light, 6. - a light detector. The optical components polarizer, compensator and analyzer are set for extinction when a surface is examined. In the present work a chopped light source was used in conjunction with a phase sensitive detector. For most of the investigation the radiation wavelength was kept at 549 nm. On occasions when a range of wavelengths was used the compensator was removed and the method of analyses due to Beattie and Conn[9] was used.

The basic equation of the instrument is given by:

$$r_p / r_s = \tan \psi \exp i \Delta \quad (1)$$

where r_p and r_s are reflection coefficients for light with electric vectors parallel and perpendicular to the plane of incidence respectively. The parameters ψ and Δ are obtained from instrument settings of polarizer and analyzer at extinction. The refractive index is written as $n - ik$ and the optical constants n and k for a film free surface can be computed from ψ and Δ and the angle of incidence ϕ_o. The angles ψ and Δ can be used to characterise a surface. The parameters change with the growth of a surface layer and are indicative of changes in the characteristics of the elliptically polarized light, i.e. in the ratio of

minor to major axes of the ellipse and its orientation with respect to the plane of incidence. In the early stages of growth the changes in ψ and Δ are proportional to film thickness (t) and can be written:

$$\psi = \overline{\psi} + At \quad (2)$$

$$\Delta = \overline{\Delta} + Bt \quad (3)$$

where $\overline{\psi}$ and $\overline{\Delta}$ relate to a clean surface and ψ and Δ to a film covered surface. A and B are constants and depend on the optical constants of the film and base metal and on the angle of incidence. For films thicker than about 10 nm, more exact equations, derived by Drude[10] almost 100 years ago, and given by Ditchburn[11] in a suitable form for computation, must be used. Figure 1. illustrates reflections from an ideal film covered surface in which multiple reflections take place in the film. The phase of the reflected beam is thus dependent on film thickness. In the case of a non absorbing film in which $k_1 = 0$ on a substrate of known optical constants (n_2 and k_2) two unknown quantities n_1 and t for a surface film can be determined. In the case of films which absorb the electromagnetic radiation there is a basic difficulty in that three unknown quantities n_1, k_1 and t need to be determined and only two instrument parameters (ψ and Δ) are measured. Several methods have been suggested to increase the number of instrument readings and these are discussed by McCrackin and Colson.[12]

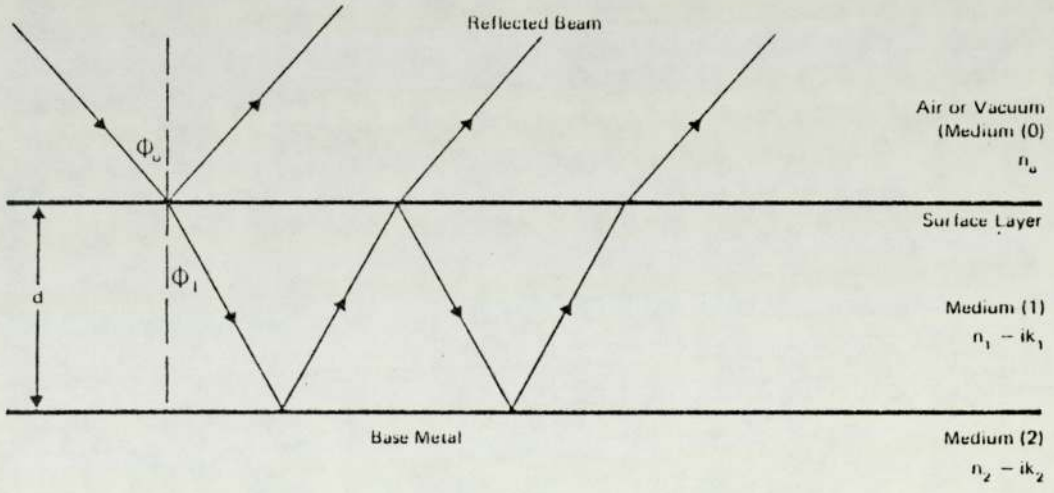

Figure 1. Reflection and Transmission of Light by a Surface Layer.

Figure 2 shows a plot of computed variations in ψ and Δ as a layer of aluminium hydroxide ($n_1 = 1.58$, $k_1 = 0$) forms on aluminium for light of wavelength 549 nm (the angle of incidence = 64.20).

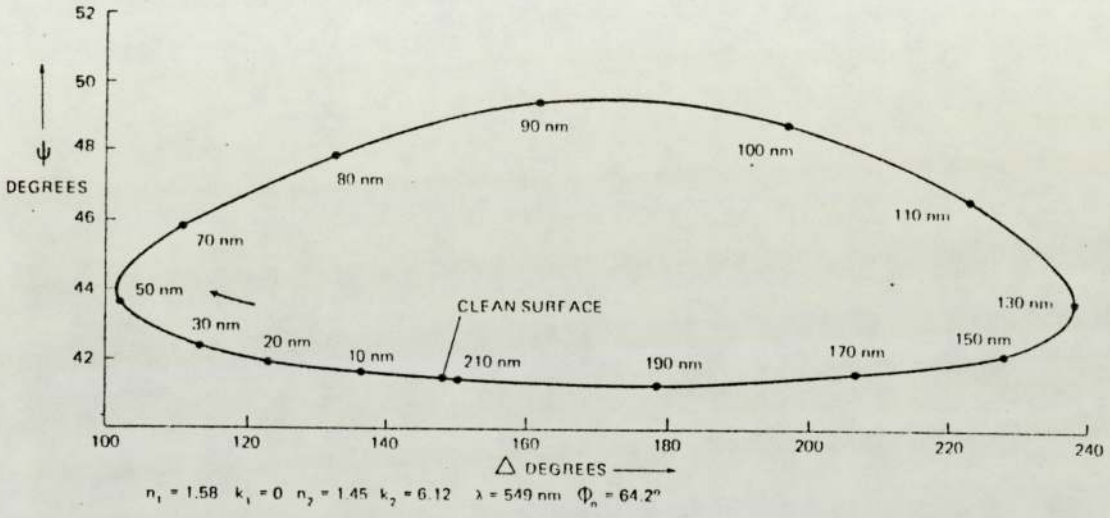

Figure 2. Aluminium Hydroxide Layer Growth on Aluminium.

Figure 3 shows the effect for a similar film on gold. For a non absorbing corrosion layer a closed loop is formed as the layer thickness increases in that the ψ and Δ values repeat themselves. For the growth of an absorbing layer a spiral would be formed. Even for non-absorbing films which is the case for most oxides and hydroxides, in order to obtain both n_1 and t it is necessary to know the optical constants n_2 and k_2 of the underlying base metal, i.e. the film free surface instrument readings ψ and Δ (equations (2) and (3)) need to be known. In studies of corrosion layers particularly on reactive metals such as aluminium, problems are experienced in obtaining the characteristics of a film free surface. Even in a vacuum system held at a pressure of 10^{-6} Pa layers form on a freshly evaporated film in a matter of minutes. This poses a problem when values of corrosion thicknesses are required in the early stages of growth. Various approaches have been made to produce film free surfaces in order

to measure subsequent growth of corrosion layers when exposed to different environments. In some cases fresh surfaces have been prepared by evaporating a metal in ultra high vacuum[13, 14]. In other instances clean surface areas have been prepared by bombarding a corroded surface with positive argon ions to remove existing corrosion layers, prior to subsequent growth in a chosen environment. We have carried out this procedure for sheets of commercial aluminium. In addition we have used freshly evaporated aluminium films, on aluminium sheet. The films were then exposed to an oxygen or water vapour environment. Ellipsometric observation on fresh films or bombarded surfaces provides information from which n_2 and k_2 can be directly calcualted. We have also employed a procedure of using a non reactive metal such as gold or platinum on which to form a corrosion layer. This enables the optical constants and thickness of corrosion layer growth to be determined without the need for optical measurements in an ultra high vacuum system.

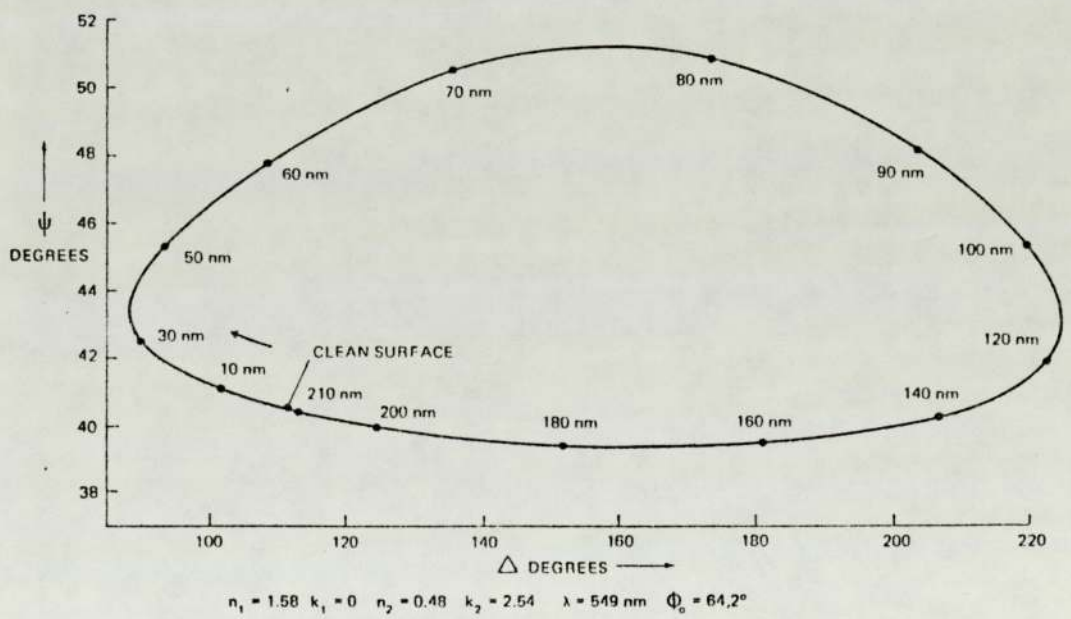

Figure 3. Aluminium Hydroxide Layer Growth on Gold.

CORROSION LAYERS GROWN ON NON REACTIVE METALS

The procedure can be briefly described as follows: Thick films of a highly reflective, non reactive metal such as gold or platinum are deposited on substrates of glass, quartz or sapphire. The film forms the base and the optical constants n_2 and k_2 for the base are determined ellipsometrically. The surface will be characterised by the instrument parameters ψ_S and Δ_S (corresponding to $\overline{\psi}$ and $\overline{\Delta}$ of equations (2) and (3)). A film of the reactive metal whose corrosive properties are to be examined is then superimposed on the non reactive base. Its thickness can be determined during deposition by a quartz crystal monitor or after deposition by an interference method suggested by Tolansky[15] using fringes of equal chromatic order. We used the latter method. The reactive metal is then exposed to the appropriate environment and the corrosive reaction permitted to proceed until all the reactive metal has been converted to films of the corrosion material. The instrument parameters ψ_F and Δ_F for the composite surface of base material plus corrosion films are determined. Since n_2 and k_2 are known from values of ψ_S, Δ_S and ϕ_o (the angle of incidence) if the corrosion layer is non-absorbing both its refractive index n_1 and its thickness t can be determined. A check on the thickness of the corrosion layer can also be made by the Tolansky[15] method. In the case of absorbing layers it is necessary to determine the thickness independently of the ellipsometer if the refractive index of the layer is not known, as mentioned earlier. Measurement of the reactive metal thickness and the corrosion thickness enables volume changes from the metal to corrosion layer to be estimated. In the present investigations the base metal was gold and aluminium hydroxide films of various thicknesses were grown by exposing aluminium films (deposited on the gold) to water vapour at 70 °C.

RESULTS AND DISCUSSION

Aluminium Hydroxide Grown on Aluminium

Table I shows the variation of ψ and Δ for a sample of commercial aluminium sheet which has been etched with Ar^+ ions. The radiation wavelength was 549 nm.

Table I. Etching of 'As Received' Aluminium Sheet.

Δ	123.4	138.95	138.80	143.37	143.56
ψ	39.9	42.29	42.85	42.89	43.0
Etch time (mins)	0	30	60	150	210

The total oxide thickness on "as received" sheet was calculated to be 20 nm.

Table II shows the variation of ψ and Δ for a sample of commercial aluminium sheet which had first been heated at 350 °C for 15 mins. in air and then etched with Ar^+ ions. The radiation wavelength was 549 nm.

Table II. Etching of Pre-heated Aluminium Sheet.

Δ	115.13	138.90	139.45	140.09	141.43	143.47
ψ	37.2	42.85	42.90	42.86	43.0	43.0
Etch time (mins)	0	90	120	150	210	300

The total oxide thickness prior to etching was calculated to be 28 nm.

In both cases the accelerating voltage was 4kV and the beam current 20μA.

Table III shows the variations in ψ and Δ as the etched aluminium sheet (from Table II) was exposed to water vapour at 25 °C. Values of hydroxide layer thickness calculated from ellipsometry and ESCA measurements are also given.

Table III. Hydroxide Growth on Aluminium Sheet.

ψ	Δ	Exposure (Langmuirs)	Hydroxide Thickness nm Ellipsometry	ESCA*
43.0	143.47	0	0	0
43.1	142.92	10	0.52	0.51
43.15	142.78	30	0.66	0.56
43.18	142.65	90	0.8	0.65
43.18	142.40	200	1.06	0.69
43.20	142.29	900	1.17	
43.20	141.94	2×10^3	1.50	0.86
43.25	141.77	7×10^3	1.70	1.01

*These thicknesses were obtained assuming electron escape depths of 2.0 nm and 1.65 nm from pure aluminium and aluminium hydroxide respectively.

Table IV shows the variations in ψ and Δ for hydroxide growth at 25 °C on aluminium film which had been deposited on etched aluminium sheets with a system base pressure of 10^{-8} Pa.

Table IV. Hydroxide Growth on Aluminium Film.

ψ	Δ	Exposure (Langmuirs)	Thickness nm Ellipsometry
44.18	144.1	0	0
44.18	143.56	10	.52
44.12	143.33	70	.85
44.25	142.96	300	1.12
44.26	142.77	10^3	1.33
44.4	142.45	6×10^3	1.62

From tables I and II it can be seen that it is possible to obtain values of ψ and Δ, after etching which can be used to characterise a surface prior to subsequent tests. In some samples of sheet which were not previously heat treated differing values of ψ could be obtained and was attributed to differences in surface structure. The rates of hydroxide growth on films and etched surfaces in the early stages of growth were similar.

A series of tests was also made on aluminium films and on commercial aluminium sheets which were either chemically or mechanically cleaned and then exposed to saturated water vapour at 70 °C for between 150 and 200 minutes. The average values of refractive index for aluminium hydroxide films up to 65 nm thick at a wavelength of 549 nm with k assumed to be zero were:

Etched Sheet and Films n = 1.55±0.05
Sheet (Chemically Cleaned) n = 1.55±0.05
Sheet (Mechanically Cleaned) n = 1.60±0.05

ALUMINIUM HYDROXIDE GROWN ON GOLD

Figures 4 and 5 show computed variations in the values of ψ and Δ as films of differing refractive indices formed on a gold surface. The experimental values found for films of 8 different thicknesses are also given. The instrument settings for a film free gold base were $\psi_S = 40.7°$ and $\Delta_S = 119.6°$ at a radiation wavelength of 549 nm and an angle of incidence of 64.2°. Values of the optical constants of the gold base were computed using the measured values of ψ_S and Δ_S and found to be $n_2 = 0.48$ and $k_2 = 2.54$. The experimental points were obtained by exposing the aluminium films to saturated water vapour at 70 °C.

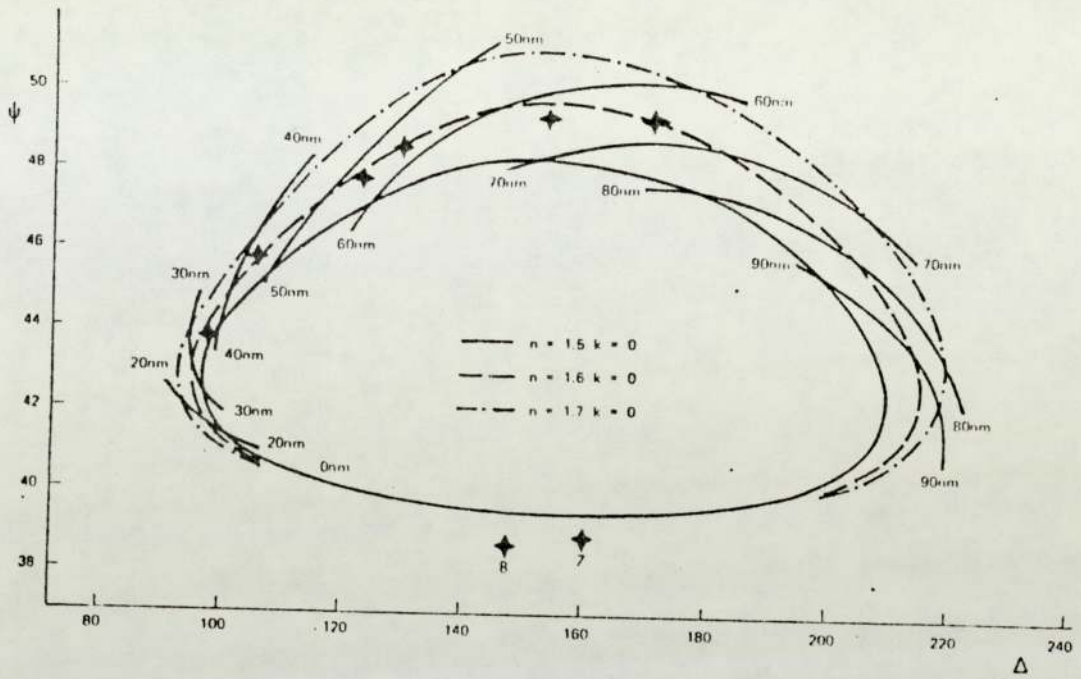

Figure 4. The graph of ψ against Δ for films of different refractive indices on a gold substrate.

The values of ψ_F and Δ_F, given in figures 4 and 5, were then computed using a two layer programme and assumed values for the hydroxide optical constants. In all cases in figure (4) $k_1 = 0$ and a complete loop is formed and values of ψ_F and Δ_F repeat themselves for hydroxide films greater than 212 nm.

The experimental points for two films (7 and 8) do not lie on any of the computed closed loops. Figure 5 shows similar plots but with an assumed slight absorption, with $k_1 = 0.0009$ in each case.

The optical constants for aluminium hydroxide which best fit the experimental results for a wavelength of 549 nm are:

For films < 80nm $n_1 = 1.58 \pm 0.03$, $k_1 = 0$
For films > 80nm $n_1 = 1.58 \pm 0.03$, $k_1 = 0.0009$

These results compare well with those obtained for growth on etched sheet and on fresh aluminium films deposited on etched sheet.

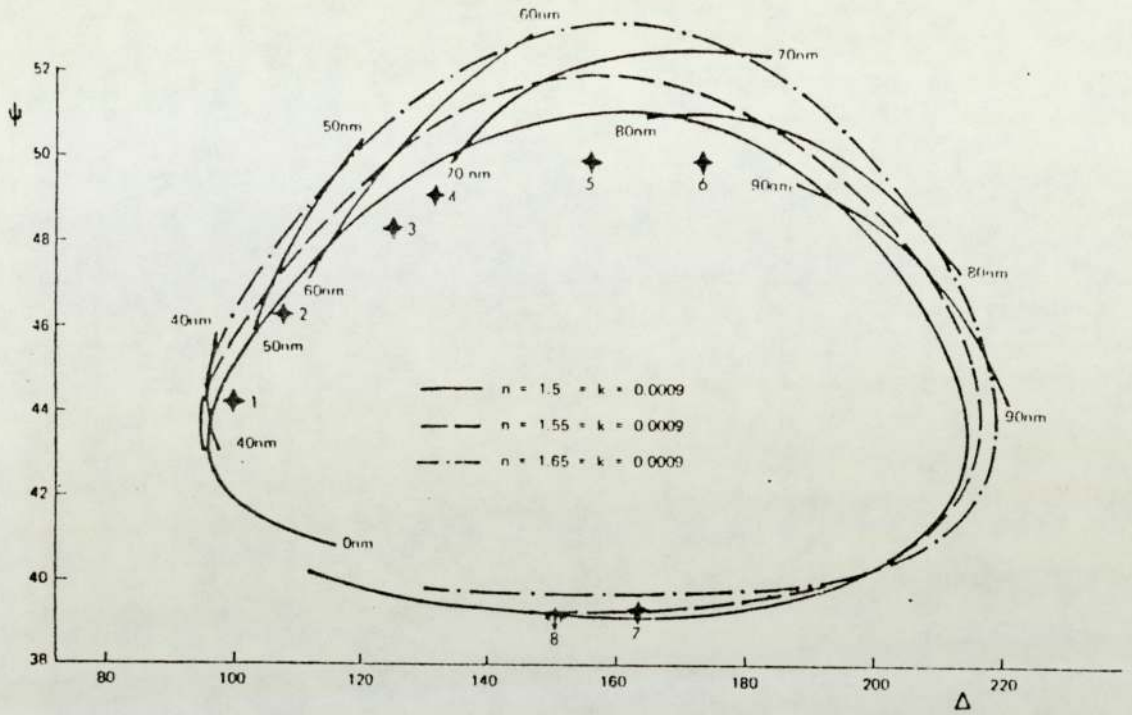

Figure 5. The graph of ψ against Δ for films of different refractive indices on a gold substrate.

In this work it was also found that the ratio of hydroxide layer thickness to metal thickness decreased from 1.6 for films 3 nm thick to 1.4 for films 18 nm thick.

Values of optical constants for aluminium hydroxide which we have obtained from growth on aluminium films and sheet and on gold can be compared with films prepared by reacting electropolished aluminium with hot water and given by Barrett[16] as $n = 1.60$, $k_1 = 0$. As already mentioned the latter technique could be used with any non reactive base metal but gold and platinum would be preferable since with most other metals thin oxide layers would always be present. Computer calculations show that by using platinum (as the base) for the examination of aluminium hydroxide corrosion layers the ψ sensitivity would be improved in the early stages of growth whilst the Δ sensitivity would not be greatly reduced. We have also examined aluminium hydroxide films prepared directly on glass substrates. In such cases $n_2 = 1.5$, $k_2 = 0$ and the ψ and Δ sensitivities are greatly reduced. Figures 6 and 7 are typical scanning electron microscopy (SEM) micrographs of aluminium hydroxide grown on thick aluminium films which were deposited on gold and glass. The aluminium was exposed to

saturated water vapour at 70 °C. The spongy nature and island growth of the hydroxide films can be seen.

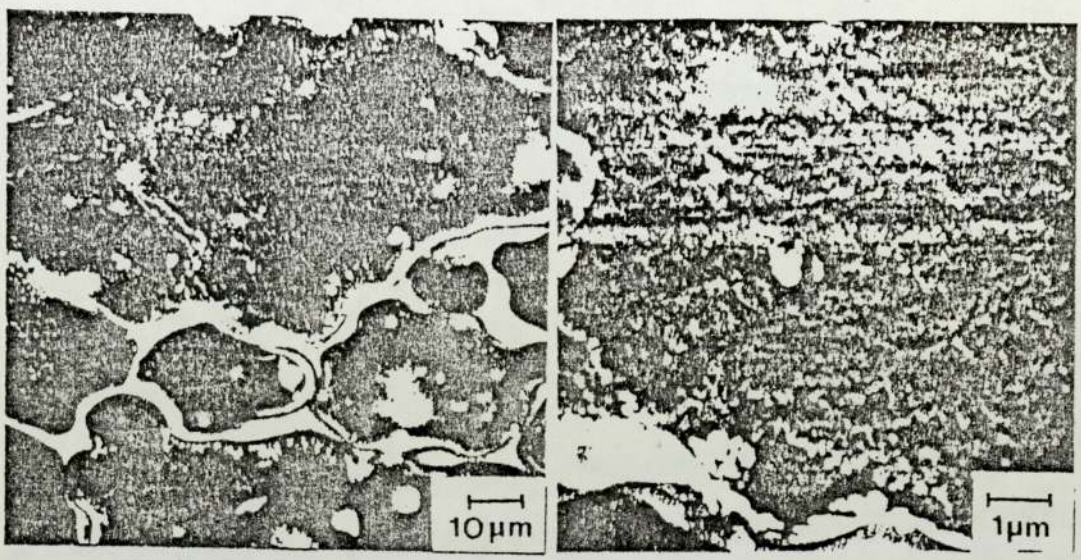

Figure 6. SEM Micrograph of Aluminium Hydroxide on Gold.

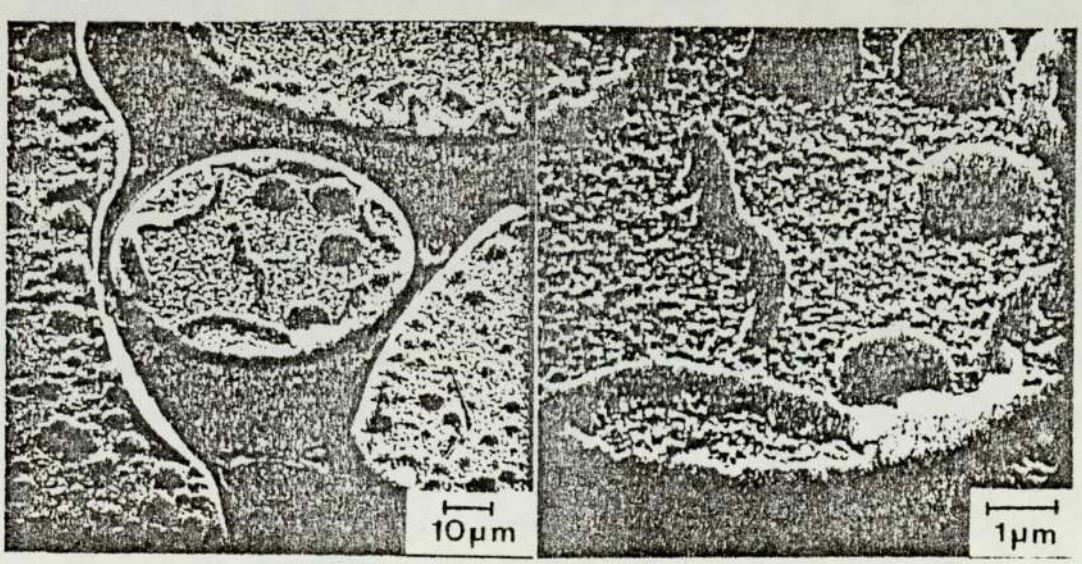

Figure 7. SEM Micrograph of Aluminium Hydroxide on Glass.

Figure 8 shows SEM micrographs of aluminium hydroxide growth on aluminium sheet formed when the sheet was exposed to saturated water vapour at 70 C. Figure 8a was taken after 20 minutes exposure and shows islands of aluminium hydroxide with pillars of bayerite. Figure 8b was taken after a 1 hour exposure and shows the joining together of islands to form a continuous hydroxide film. Figures 8c and 8d are higher magnifications of an island. Figure 8c shows boehmite (island) together with bayerite pillars. Figure 8d is a micrograph taken in the reflective mode and shows the bayerite growing into the aluminium substrate.

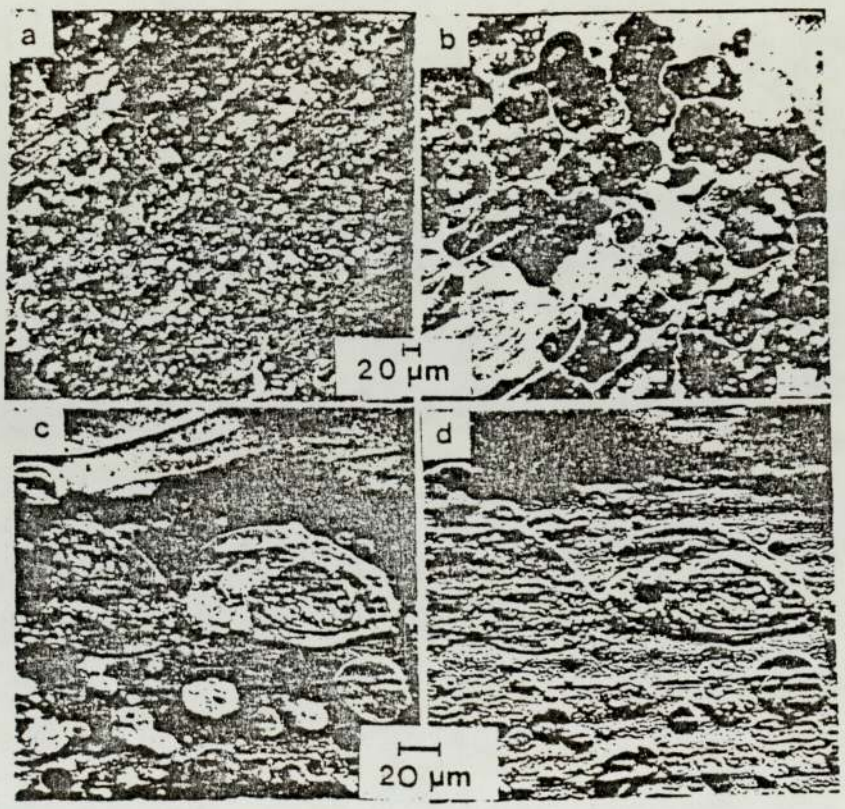

Figure 8. Hydroxide growth on aluminium sheet.

SUMMARY

Two methods have been used for the optical characterisation of aluminium surfaces prior to the growth of aluminium hydroxide layers by exposure to water vapour:-

1. Freshly deposited aluminium films.
2. Ion etched aluminium sheet.

For films less than 65 nm thick and assuming no absorption the refractive index for aluminium hydroxide was found to lie between 1.55 and 1.60 for a wavelength of 549 nm.

Another method for determining the optical constants of hydroxide films was employed by depositing films of aluminium on gold and subsequently exposing them to water vapour. The optical constants of aluminium hydroxide for a wavelength of 549 nm were found to be:

(a) For films < 80nm, $n_1 = 1.58 \pm 0.03$, $k_1 = 0$
(b) For films > 80nm, $n_1 = 1.58 \pm 0.03$, $k_1 = 0.0009$

The latter technique has been shown to be a viable alternative in the determination of optical constants of corrosion layers of reactive metals when problems of surface characterisation exist and when optical measurements in ultra high vacuum systems are not possible.

In addition to the work described, another part of the experimental programme has been to make measurements on oxide growth on aluminium in vacuo, and the investigations will be extended in the next phase to include oxide and hydroxide growth on aluminium alloys, again with the emphasis being on the early stages of growth. The investigations have been undertaken as part of a collaborative programme with the Alcan Research Laboratories, Banbury, U.K.

ACKNOWLEDGEMENTS

The authors wish to thank Dr.G.M.Scamans for his assistance in preparing the electron micrographs and to Alcan Research Laboratories for permission to reproduce Figures 6, 7 and 8. One of us, A.Rehal, wishes to acknowledge a studentship from the Science Research Council.

REFERENCES

1. L.Tronstad, Trans.Faraday Soc. 29 (1933) 502.

2. M.A.Barrett and A.B.Winterbottom, First International Congress on Metallic Corrosion, London, Butterworths 1962, p.657.

3. J.Kruger and P.C.S.Hayfield, Handbook on Corrosion Testing, Ed. W.H.Ailor, Pub.Wiley, 1971, P.783.

4. P.C.S.Hayfield, Surface Science 1976, 56, 488.

5. R.Aguado-Bombin and W.E.J.Neal, Thin Solid Films 1977, 42, 91.

6. R.S.Alwitt, "The Aluminium-Water System" in Oxides and Oxide Films, Vol.4, ed. J.W.Diggle and A.K.Vijh, Pub.Maral Dekker 1976, p.169.

7. W.Vedder and D.A.Vermilyea, J.Electrochem.Soc. 115 (1968) 561.

8. W.E.J.Neal, Surface Technology, 1977, 6, 81.

9. J.R.Beattie and G.K.T.Conn. Phil.Mag 1955, 46, 222.

10. P.Drude, Ann.Phys.Leipzig, 1887, 32, 584; 1888, 34, 489; 1890, 39, 481.

11. R.W.Ditchburn, 1955, J.Opt.Soc.Am. 45, 743.

12. F.L.McCrackin and J.P.Colson. "Ellipsometry in the Measurement of Surfaces and Thin Films". Ed.Passaglia 1964 (Washington: National Bureau of Standards) p.61.

13. R.W.Fane and W.E.J.Neal, J.Opt.Soc.Am. 1970, 60, 790.

14. J.H.Halford, F.K.Chin and J.E.Norman, J.Opt.Soc.Am. 1973, 63, 786.

15. S.Tolansky. "Multiple Beam Interferometry" Clarendon Press, Oxford 1969.

16. M.A.Barrett "Ellipsometry in the Measurement of Surfaces and Thin Films" Ed.Passaglia 1964 (Washington: National Bureau of Standards) p.213.